



# Kent Academic Repository

**Wang, Jingyu (2012) *Optical coherence tomography methods using 2-D detector arrays*. Doctor of Philosophy (PhD) thesis, University of Kent.**

## Downloaded from

<https://kar.kent.ac.uk/94718/> The University of Kent's Academic Repository KAR

## The version of record is available from

<https://doi.org/10.22024/UniKent/01.02.94718>

## This document version

UNSPECIFIED

## DOI for this version

## Licence for this version

CC BY-NC-ND (Attribution-NonCommercial-NoDerivatives)

## Additional information

This thesis has been digitised by EThOS, the British Library digitisation service, for purposes of preservation and dissemination. It was uploaded to KAR on 25 April 2022 in order to hold its content and record within University of Kent systems. It is available Open Access using a Creative Commons Attribution, Non-commercial, No Derivatives (<https://creativecommons.org/licenses/by-nc-nd/4.0/>) licence so that the thesis and its author, can benefit from opportunities for increased readership and citation. This was done in line with University of Kent policies (<https://www.kent.ac.uk/is/strategy/docs/Kent%20Open%20Access%20policy.pdf>). If you ...

## Versions of research works

### Versions of Record

If this version is the version of record, it is the same as the published version available on the publisher's web site. Cite as the published version.

### Author Accepted Manuscripts

If this document is identified as the Author Accepted Manuscript it is the version after peer review but before type setting, copy editing or publisher branding. Cite as Surname, Initial. (Year) 'Title of article'. To be published in *Title of Journal*, Volume and issue numbers [peer-reviewed accepted version]. Available at: DOI or URL (Accessed: date).

## Enquiries

If you have questions about this document contact [ResearchSupport@kent.ac.uk](mailto:ResearchSupport@kent.ac.uk). Please include the URL of the record in KAR. If you believe that your, or a third party's rights have been compromised through this document please see our [Take Down policy](https://www.kent.ac.uk/guides/kar-the-kent-academic-repository#policies) (available from <https://www.kent.ac.uk/guides/kar-the-kent-academic-repository#policies>).

# **Optical Coherence Tomography Methods**

## **Using 2-D Detector Arrays**

by

Jingyu Wang

Submitted for the degree

of

Doctor of Philosophy

in

the Subject of Physics

University of Kent

2012



F 226737

# ABSTRACT

Optical coherence tomography (OCT) is a non-invasive, non-contact optical technique that allows cross-section imaging of biological tissues with high spatial resolution, high sensitivity and high dynamic range. Standard OCT uses a focused beam to illuminate a point on the target and detects the signal using a single photo-detector. To acquire transverse information, transversal scanning of the illumination point is required. Alternatively, multiple OCT channels can be operated in parallel simultaneously; parallel OCT signals are recorded by a two-dimensional (2D) detector array. This approach is known as Parallel-detection OCT.

In this thesis, methods, experiments and results using three parallel OCT techniques, including full-field (time-domain) OCT (FF-OCT), full-field swept-source OCT (FF-SS-OCT) and line-field Fourier-domain OCT (LF-FD-OCT), are presented. Several 2D digital cameras of different formats have been used and evaluated in the experiments of different methods. With the LF-FD-OCT method, photography equipment, such as flashtubes and commercial DSLR cameras have been equipped and tested for OCT imaging.

The techniques used in FF-OCT and FF-SS-OCT are employed in a novel wavefront sensing technique, which combines OCT methods with a Shack-Hartmann wavefront sensor (SH-WFS). This combination technique is demonstrated capable of measuring depth-resolved wavefront aberrations, which has the potential to extend the applications of SH-WFS in wavefront-guided biomedical imaging techniques.

# ACKNOWLEDGMENT

There are many people for whom I would like to thank for the help and friendship they have offered me in the last few years.

Firstly, I would like to thank my supervisor Prof. Adrian Podoleanu for his enormous support and patience. Without his guide, knowledge and encouragement, none of this would have been possible. I would also like to thank to Prof. Chris Dainty from NUIG, for his advice, hospitality in Galway and expensive camera on loan.

To Prof. David Jackson, Dr. George Dobre, Dr. Adrian Bradu, Dr. Ramona Cernet, Dr. Radu Cucu, Dr. John Rogers, Dr. Mark Hathaway, Dr. Harald Gnewuch, Dr Xiang Zhou and all current members of AOG and ex-colleagues for all the wonderful advices, discussion and selfless help.

To Irina Trifanov, Simon Tuohey, Liviu Neagu, Michael Hughes, Erika Odlund, Michael Leitner, Sabine Chiesa and all other students in the HIROSOMI network for the wonderful time they have spend with me, in Kent, Galway, Orsay and Porto.

I am extremely grateful to Marie Curie Grant and ERC Grant for the generous funding for my research. Also, I would like to thank to Ms Sarah Saunders and all other coordinators in the University of Kent who have provided me help and support during my study and work in Kent.

To all the friends I have made in Canterbury and Galway, especially Kaiyaw Yong and Inge Harcourt for their company, friendship, support and consistent encouragement.

Finally, to both my parents and my dear wife, maomao, without whose support, patience, understanding and love, I won't be who I am.

# CONTENTS

ABSTRACT .....	ii
ACKNOWLEDGMENT .....	iii
CONTENTS.....	iv
LIST OF FIGURES.....	viii
LIST OF TABLES.....	xi
Chapter 1      Introduction .....	1
Chapter 2      Principles of OCT .....	3
2.1    Background .....	3
2.1.1    Michelson Interferometer .....	3
2.1.2    Coherence .....	6
2.1.3    Low Coherence Interferometry .....	8
2.1.4    From LCI to OCT .....	10
2.2    Time-domain OCT .....	12
2.2.1    Light Sources .....	12
2.2.2    Axial Resolution.....	13
2.2.3    Transverse Resolution.....	13
2.2.4    Scanning .....	15
2.2.5    Photo-detector.....	16
2.2.6    Noises of TD-OCT .....	17
2.2.7    Numerical Processing.....	18
2.2.8    Sensitivity .....	18
2.2.9    Dispersion.....	19
2.3    Spectral domain OCT.....	21
2.3.1    Fourier-domain OCT.....	21
2.3.2    Swept-source OCT.....	31
2.4    Other OCT Developments .....	33

2.5	Summary .....	34
Chapter 3	Parallel-detection OCT .....	35
3.1	Parallel-detection OCT .....	35
3.2	2-D Detector Array .....	36
3.2.1	CCD .....	37
3.2.2	Photo gate .....	37
3.2.3	Charge Transfer .....	39
3.2.4	Frame Transfer .....	39
3.2.5	Signals of the CCD Array.....	42
3.2.6	Noises and Sensitivity .....	44
3.2.7	Dynamic Range.....	47
3.2.8	Specialised CCD Techniques.....	47
3.2.9	CMOS Devices .....	50
3.3	Full-field OCT.....	51
3.3.1	Coherence Radar .....	52
3.3.2	Full-field OCT .....	53
3.3.3	Phase Shifting Interferometry.....	55
3.3.4	Resolutions.....	61
3.3.5	Sensitivity .....	62
3.3.6	Crosstalk .....	63
3.4	Full-field Swept-source OCT .....	64
3.5	Line-field FD-OCT .....	66
3.6	Summary .....	67
Chapter 4	Full-field OCT .....	69
4.1	Time-domain Full-field Low Coherence Interferometry.....	69
4.1.1	Coherence Radar .....	69
4.1.2	Phase Stepping Interferometry.....	72
4.1.3	Topography Measurements.....	73

4.1.4	Multiple Delay Line FF-OCT .....	75
4.1.5	Time-domain Full-field OCT .....	83
4.2	Full-field Swept-source OCT .....	86
4.2.1	Optical Set-up.....	86
4.2.2	Theoretical analysis.....	88
4.2.3	Acquisitions .....	91
4.2.4	Spectrum Resampling .....	93
4.2.5	Results .....	94
4.3	Summary .....	96
Chapter 5	Line-field Fourier-domain OCT .....	97
5.1	Line-field Fourier-domain OCT .....	97
5.1.1	Optical Set-up.....	97
5.1.2	Resampling.....	100
5.1.3	Spatial Filter .....	100
5.1.4	Measurements with Andor DV877 camera .....	101
5.1.5	Using Mikrotrotron EoSens MC1362 CMOS camera .....	104
5.1.6	Comparison .....	107
5.1.7	Examples of B-scans images.....	108
5.2	Using Extended Light Sources in LF-FD-OCT .....	109
5.2.1	Extended Light Sources for OCT.....	109
5.2.2	Linear Light Sources .....	110
5.2.3	Visibility of Channelled Spectrum .....	111
5.2.4	Extended Light LF-FD-OCT Set-up .....	112
5.2.5	Incandescent lamp .....	114
5.2.6	LED.....	115
5.2.7	Xenon Flash lamp .....	116
5.3	Using Consumer-grade Digital Cameras in LF-FD-OCT.....	117
5.3.1	Challenges .....	118

5.3.2	Experiments .....	119
5.4	Summaries and Perspectives .....	123
Chapter 6	Coherence-gated Wavefront Sensing .....	125
6.1	Background .....	125
6.1.1	Adaptive optics.....	125
6.1.2	Shack-Hartmann Wavefront Sensor .....	126
6.1.3	Limitation of SH-WFSs.....	134
6.1.4	Coherence Gated SH-WFS.....	136
6.2	Mach-Zehnder Interferometer based CG/SH-WFS.....	139
6.2.1	Time Domain CG/SH-WFS .....	139
6.2.2	Swept-source Coherence Gated SH-WFS.....	142
6.2.3	Centroiding.....	144
6.3	Results .....	145
6.3.1	Single Reflector Object.....	145
6.3.2	Multi-layer Targets.....	154
6.3.3	Scattering Sample .....	159
6.3.4	Signal Strength .....	162
6.3.5	Challenges .....	163
6.4	Conclusions .....	165
Chapter 7	Conclusions .....	166
Reference	.....	169

# LIST OF FIGURES

Figure 2.1. Schematic of a Michelson interferometer.....	4
Figure 2.2. Terminology of imaging planes in OCT.....	16
Figure 2.3. A schematic of a standard FD-OCT .....	23
Figure 2.4. Schematic of a simple tuneable laser source .....	33
Figure 3.1. A simplified p-type silicon MOS gate of a 2D CCD array .....	38
Figure 3.2. A schematic of charge transfer on a full-frame CCD array.....	40
Figure 3.3. Different CCD arrays according to the transfer modes .....	41
Figure 3.4. Schematic of signal generation on a standard CCD array. ....	42
Figure 3.5. Schematics of a 'coherence radar' set-up .....	53
Figure 3.6. The focal plane and the coherence plane in an interferometer .....	62
Figure 3.7. Left: Schematics of LF-FD-OCT set-up. ....	67
Figure 4.1. Schematic diagram of a coherence radar set-up.....	71
Figure 4.2. Schematic of the synchronization of FF-OCT.....	73
Figure 4.3. Coherence images obtained with 3- step PSI and 4-step PSI.....	73
Figure 4.4. Axial LCI PSF and (b) Image of USAF 1951 test chart.....	74
Figure 4.5. Coherence images of a coin of 5 pence sterling.....	75
Figure 4.6. Variation of the wavefront delay due to an inserted optical delay. ....	77
Figure 4.7. Geometry of contour circles sampled by the coherence gate .....	78
Figure 4.8. Schematic diagrams of the coherence radar set-up with MDE.....	79
Figure 4.9 En-face coherence image obtained with the MDE in the reference.....	80
Figure 4.10. MDE inserted in the source path of the interferometer .....	80
Figure 4.11. En-face LCI image obtained using a MDE in the optical source path.....	82
Figure 4.12. En-face image obtained with MDE in the optical source path.....	83
Figure 4.13. En-face OCT images of human finger skin .....	84
Figure 4.14. In-vivo FF-OCT images of larvae of fruit fly <i>Drosophila Melanogaster</i> ..	85
Figure 4.15. Configuration of the FF-SS-OCT set-up.....	87
Figure 4.16. Measured tuning spectrum of the swept source BS-840.....	91
Figure 4.17. SS-OCT imaging sequence synchronised with the driving voltages. ....	92
Figure 4.18. B-scan OCT images of an air-glass interface as object .....	93

Figure 4.19 Improvement of SS-OCT signal by phase linearization.....	95
Figure 4.20. OCT images of paper collected by the FF-OCT system.....	95
Figure 5.1. Schematic diagram of LF-CS-OCT system .....	99
Figure 5.2. CS phase measured using a glass-air interface.....	100
Figure 5.3. The amplitude of A-scan peak versus the width of the slit. ....	101
Figure 5.4. A-scan peak values versus a depth range of 4.5 mm.. ....	102
Figure 5.5. A-scans measured with different exposure times of the camera.. ....	103
Figure 5.6. PSF roll-off with three different exposure times.....	103
Figure 5.7. A-scans signal measured with 7 different reference powers.....	104
Figure 5.8. A-scans measured from a glass-air interface using a CMOS camera .....	105
Figure 5.9. Signal peak roll-off curves versus axial position.....	105
Figure 5.10. Depth profile of A-scan peaks with different reference power .....	107
Figure 5.11. OCT B-scan images collected from fingers of the author.....	108
Figure 5.12. In-vitro B-scan images from different parts of human teeth.....	108
Figure 5.13. In-vivo B-scan images from a fruit fly larva. ....	109
Figure 5.14. Channelled spectra array.....	112
Figure 5.15. Schematic of the LF-FD-OCT with extended sources. ....	113
Figure 5.16. A channelled spectrum obtained using the SLD675 light source.....	114
Figure 5.17 Spectrum (right) emitted by a straight filament (left).....	114
Figure 5.18. Channelled spectrum using a linear tungsten filament light source....	115
Figure 5.19 Channelled spectrum and A-scan using a LED light source.....	116
Figure 5.20. Measured spectra of two xenon flashtubes.....	117
Figure 5.21. Xenon flashtube and recorded channelled spectrum. ....	117
Figure 5.22. A-scan peak decays measured with Andor and Retiga CCD.....	121
Figure 5.23 Channelled spectrum obtained using Nikon D80 and Andor .....	122
Figure 5.24. Spectrum acquired using Xenon flashlamp and the Canon 50D. ....	122
Figure 5.25. A-scan and B-scan using Canon 50D and Xenon flash.....	123
Figure 6.1 Schematic of the principle of SH-WFS .....	127
Figure 6.2. Procedures of numeric processing for SH-WFS measurements.....	128
Figure 6.3. First 10th Zernike polynomials in circular unit aperture.....	133
Figure 6.4. Schematic of the first physical CG/SH-WFS set-up.....	139
Figure 6.5. Schematic of CG/SH-WFS set-up .....	140

Figure 6.6. User interface of the control software for TD-CG/SH-WFS.....	141
Figure 6.7 TD-CG/SH-WFS images acquired from a single reflector. ....	142
Figure 6.8. Schematic of SS-CG/SH-WFS.....	143
Figure 6.9. Precision of standard SH-WFS spots centroiding .....	145
Figure 6.10. TD-CG/SH-WFS images obtained at near-zero OPD.....	146
Figure 6.11. Effect of straylight rejection in TD-CG/SH-WFS.....	147
Figure 6.12. Errors of TD-CG/SH-WFS.....	149
Figure 6.13. Zernike coefficients and reconstructed wavefront of TD-CG/SH-WFS	149
Figure 6.14. A-scan acquired with SS-CG/SH-WFS. ....	150
Figure 6.15. Three en-face images from a 3D volume by the SS-CG/SH-WFS .....	151
Figure 6.16. SH images obtained by SH-WFS, TD-CG/SHWFS and SS-CG/SH-WFS ..	151
Figure 6.17. Error of SS-CG/SH-WFS .....	152
Figure 6.18 Zernike coefficients and reconstructed wavefront of SS-CG/SH-WFS ..	153
Figure 6.19. Errors of TD-CG/SH-WFS, SS-CG/SH-WFS and standard SH-WFS.....	154
Figure 6.20. A 5 layer target made of two non-parallel microscope slides.....	154
Figure 6.21. SH-WFS image from the object .....	156
Figure 6.22. SH and CG-SH images collected from 5 layers.....	157
Figure 6.23. Reconstructed wavefronts from all 5 layers.....	159
Figure 6.24. Slopes, Zernike coefficients and reconstructed wavefront.....	159
Figure 6.25. SH images obtained with TD-CG/SH-WFS from paper .....	160
Figure 6.26. SH images obtained with SS-CG/SH-WFS from paper .....	160
Figure 6.27. Zernike coefficients and reconstructed wavefront in 50 $\mu\text{m}$ deep.....	161
Figure 6.28. Signal strength of SH-WFS, TD-CG/SH-WFS and SS-CG/SH-WFS.....	163
Figure 6.29. CG/SH-WFS spots without and with chrome apertures.....	163
Figure 6.30. SH spots acquired by TD-CG/SH-WFS at two OPDs.....	164

# LIST OF TABLES

Table 4.1 Main parameters of the EMCCD Camera, Andor DV887AC-UV .....	71
Table 4.2. Results obtained from the first MDE configuration .....	80
Table 4.3. Specifications of the swept source 'BroadSweeper-840' .....	91
Table 5.1. Overview of LD-FD-OCT technical performance.....	107
Table 5.2. Parameters of the three cameras we used in the experiments .....	120
Table 6.1. First 14 Zernike polynomials .....	132
Table 6.2. Errors of centroid coordinates obtained by TD-CG/SH-WFS.....	148
Table 6.3. Comparison of the accuracy of TD-CG/SH-WFS and SS-CG/SH-WFS.....	154
Table 6.4. Parameters of Lenslet arrays used in experiments .....	164

# Chapter 1 Introduction

Optical coherence tomography (OCT) is a non-invasive, non-contact imaging technique that allows cross-sectional imaging of scattering targets with high spatial resolution, high sensitivity and high dynamic range. OCT detects back-reflected light or back-scattered light, which can be considered as an optical analogue to ultrasound imaging. Because electro-magnetic radiation travels much faster than ultrasound wave does, the time resolution for OCT is too small to be detected directly by electronic detector. Instead, interferometric methods is used by introducing a reference light with a known optical path length. Unlike other optical tomography imaging techniques, such as optical diffraction tomography (ODT) [1, 2] and diffuse optical tomography (DOT) [3], OCT detects ballistic photons in order to measure optical properties of structured tissues [1].

Since its appearance, OCT has advanced dramatically in various fields of fundamental researches and clinical applications. Ophthalmology is the main field of OCT applications due to the transparent ocular structures of eyes. OCT has been combined with scanning laser ophthalmoscopy [2] to obtain high resolution imaging of the retinal [4-7] and anterior chamber [8-10]. Various OCT techniques have also been derived for different applications, e.g. polarisation-sensitive OCT is particularly useful in dermatology [11-14] and dentistry [15-17]. Doppler OCT [18-20] provides a non-invasive localised diagnostics of particle flow velocity in scattering media, e.g. blood flow in capillaries. Integrating with optical probes, such as endoscopes [21, 22], catheters [23], laparoscopes [24] and needles [25], OCT allow imaging internal body *in-situ*. OCT has also been used in biology researches [26-28], material analysis [29] and many other fields.

Parallel detection OCT, an alternative OCT technique is a combination of the OCT principle and full-field or line-field imaging. Two-dimensional (2D) detector arrays, such as CCD or CMOS cameras have been used as sensors in paralleled detection OCTs. This thesis focuses on various types of parallel detection OCT techniques that employ 2D detector arrays. It is easier to understand the parallel

detection OCT techniques by examining the principle of point-scanning OCT firstly; therefore, in Chapter 2, the principles and system designs of standard scanning OCTs are introduced. Technical descriptions and the performance of main OCT imaging schemes, including time-domain OCT, Fourier-domain OCT and swept-source OCT are presented. In Chapter 3, the principle of parallel detection OCT is given. A short review of 2D detector array technology is also presented, followed by descriptions of three types of parallel OCT approaches: full-field OCT, full-field swept-source OCT and line-field Fourier-domain OCT.

In Chapter 4 and Chapter 5, experiments with Full-field OCT and line-field OCT are described in detail. The possibility of using low-cost extended light sources and commercial digital cameras in line-field OCT is also investigated in Chapter 5. Extending the concept of coherence gating to adaptive optics [30-32], a novel coherence-gated wavefront sensing technique that combines the principle of LCI and a Shack-Hartman wavefront sensor is described in Chapter 6. The technique used in this work is similar to that performed in full-field OCT. Summaries of all parallel detection OCT techniques based on 2D detector arrays are given in the last Chapter, where advantages, limitations and an outlook of parallel detection OCT techniques including coherence-gated wavefront sensing are discussed.

# Chapter 2 Principles of OCT

Optical coherence tomography (OCT) is a non-invasive biomedical imaging technique that allow cross-sectional imaging of highly scattering tissue with high spatial resolution. It is an interferometric technique based on detection of interference between optical fields that contains depth-resolved information. In this chapter, the principles of OCTs are introduced, including three main OCT approaches: time-domain OCT, Fourier-domain OCT and swept-source OCT.

## **2.1 Background**

OCT is based on the concept of 'coherence gating' that is used by low coherence interferometry (LCI) or white light interferometry (WLI) [33, 34]. A brief mathematical description of the principle of a simple Michelson interferometer [35] is helpful to understand the principles of OCT.

### **2.1.1 Michelson Interferometer**

A simplified Michelson interferometer is illustrated in Figure 2.1, electromagnetic radiation is launched by a light source and propagates to a beam-splitter that divides the light beam into two paths that are referred as object path (arm) and reference path (arm) of the interferometer. Considering the light beam is reflected by a mirror in the reference path and return to the beam-splitter, while the object beam is returned from a reflective object, the two beams are recombined at the beam-splitter and follow a common path to a detector. Providing that the light source is both spatially coherent and monochromatic, if the lengths of two optical paths are equal, constructive interference occurs; if the lengths of two paths are half-wavelength different, destructive interference occurs and a weak signal is observed. Generally, the constructive interference occur when the optical path differences (OPD) are integer multiples of the wavelength of the light, while destructive interference appears when the OPDs are multiples plus half of the wavelength. An interference pattern of bright and dark fringes can therefore be recorded by scanning the OPD in a large axial range, compared to the wavelength.

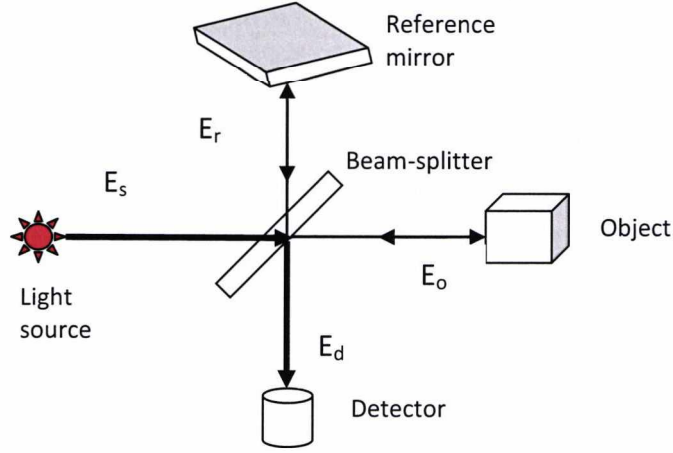


Figure 2.1. Schematic of a Michelson interferometer: light beam from a monochromatic point source is divided by a beam-splitter; two separate beams are reflected back and are recombined at the beam-splitter, which is later recorded by a photon-detector.

The mathematics treatment of the phenomenon is started from the expression of the electrical field of the source beam,  $E_s$  by the solution to Maxwell's equation. Given the light has a wavelength  $\lambda$ , the propagation field of  $E_s$  is given by

$$E_s(x, t) = A_s \exp[-i(\omega t - kx)] \quad (2.1)$$

where  $A_s$  is the amplitude of the optical field,  $k$  is the wave number ( $k = 2\pi / \lambda$ ),  $\omega$  is the angular frequency,  $x$  and  $t$  are distance and time of the field propagation; thus the field of the incoming (before reaching the target) object beam,  $E_o(x, t)$  and the corresponding reference beam,  $E_r(x, t)$  are expressed by

$$\begin{aligned} E_o(x, t) &= \sqrt{T} A_s \exp[-i(\omega t - kx_o)] E_s(x, t) \\ E_r(x, t) &= \sqrt{R} A_s \exp[-i(\omega t - kx_r)] E_s(x, t) \end{aligned} \quad (2.2)$$

respectively, where  $T$  and  $R$  are the transmission and reflection ratio of the separation of the light intensity at the beam-splitter;  $x_o$  and  $x_r$  are the corresponding propagation distances in two arms. Denoting the reflectivity of the

object and the reference mirror using  $R_o$  and  $R_r$ , after the two beams are recombined, the field at a photo-detector  $E_d$  is given by:

$$E_d(x_o, x_r, t) = \sqrt{T}\sqrt{R}\sqrt{R_o}A_s \exp[-i(\omega t - kx_o)] + \sqrt{R}\sqrt{T}\sqrt{R_r}A_s \exp[-i(\omega t - kx_r)]. \quad (2.3)$$

The contribution of the object arm and the reference arm to  $E_d$ , are

$$A_o = \sqrt{T}\sqrt{R}\sqrt{R_o}A_s \exp[-i(\omega t - kx_o)] \\ A_r = \sqrt{R}\sqrt{T}\sqrt{R_r}A_s \exp[-i(\omega t - kx_r)] \quad (2.4)$$

respectively. The photo-detector measures the intensity of incoming light by square law, since the integration time,  $T$  is much larger than  $1/\omega$ , the resultant photocurrent  $I_d$  is proportional to the time-average of the square of the electric field, which is expressed as

$$I_d(x, t) = \eta \langle E_d(x, t)E_d^*(x, t) \rangle_T = \eta \langle E_d^2(x, t) \rangle_T \quad (2.5)$$

where  $\eta$  is the detector response, which is assumed as perfect as 100% in following deductions. Substituting Eq. (2.3) and Eq. (2.4) into Eq. (2.5), we have:

$$I_d(x_o, x_r) = A_o^2 + A_r^2 + 2 \operatorname{Re}\{A_o(x_o)A_r^*(x_r)\} \\ = A_o^2 + A_r^2 + 2|A_o||A_r|\cos[k(x_o - x_r)] \quad (2.6)$$

where the first two terms are two auto-correlation terms of two interferometric arms, which contribute to an constant background in the output signal; the third term, a cross-correlation term, is responsible for interference fringes with a period of  $2\pi/k$ . Eq. (2.6) can be rewritten with only one variable, the optical path difference (*OPD*) as

$$I_d(\Delta z) = A_o^2 + A_r^2 + 2|A_o||A_r|\cos(kOPD) \quad (2.7)$$

*OPD* is an important parameter in describing interference phenomenon and is the basic of all interferometry method.

## 2.1.2 Coherence

Interference occurs in different ways, which is determined by another important concept in interferometry, coherence. There are two types of first order coherence in laser optics: temporal coherence and spatial coherence.

### 2.1.2.1 Temporal Coherence

Temporal coherence is a measure of the average correlation between the phases of an electromagnetic wave at a pair of times separated by a time delay  $\tau$  [36] at a given location. If the phase difference between  $t$  and  $t + \tau$  remains the same for  $\tau$  that has  $0 < \tau < t_c$ ,  $t_c$  is defined as the coherence time of the light. Because the light speed is constant in a certain medium, the distance that the light travel over  $t_c$  can also be used to describe the temporal coherence, which is known as coherence length  $l_c$ . Using  $V_g$  to denote the group velocity, we have  $l_c = V_g t_c$ . Interference occurs in the interferometer when the two optical paths coincide within a coherence length. The coherence length of an optical beam can also be quantified by the full-width-half-maximum (FWHM) of the autocorrelation function of the optical source,  $\Gamma(\tau)$ , which can be expressed as [37]

$$\Gamma(\tau) = \lim_{T \rightarrow \infty} \frac{1}{2T} \int_{-T}^T E_s(t) E_s(t - \tau) dt \quad (2.8)$$

The spectrum density function of the light source,  $S(k)$  is related to  $\Gamma(\tau)$  by the Wiener-Khinchin theorem [37]:

$$S(k) = \frac{1}{2\pi} \int_{-\infty}^{+\infty} \Gamma(\tau) \exp(ik\tau) d\tau \quad (2.9)$$

$S(k)$  is a Dirac delta function for a mono-chromatic source because  $\Gamma(\tau)$  is a constant. For a broadband light source,  $\Gamma(\tau)$  has a finite bandwidth, determined by the spectrum of the light.

### 2.1.2.2 Spatial coherence

Spatial coherence is defined as the degree to which the light at two spatial points have the same phase [36] at a certain moment. A high degree of spatial coherence is a requirement for a well-resolved fringe pattern recorded by a single detector in a standard OCT, since incoherent light would wash out the interference fringe pattern and reduce the fringe contrast. To evaluate the degree of the spatial coherence of a light source, the classical method is based on the Young's double slit experiment [38]. For a partial coherence beam of diameter  $D$ , coherence is only retained within an area,  $S_c$ , which is small than area  $\pi D^2 / 4$ . In the mathematical treatment of Michelson interferometer, spatial coherence between two point  $\mathbf{r}_1$  and  $\mathbf{r}_2$  is evaluated by the complex degree of spatial coherence,  $\gamma^{(1)}$  whose magnitude is expressed by

$$\gamma^{(1)} = \frac{\langle E(\mathbf{r}_1, t) E^*(\mathbf{r}_2, t) \rangle}{\sqrt{\langle E(\mathbf{r}_1, t) E^*(\mathbf{r}_1, t) \rangle} \sqrt{\langle E(\mathbf{r}_2, t) E^*(\mathbf{r}_2, t) \rangle}} \quad (2.10)$$

where  $E$  is electrical fields at the two points and the angular brackets denote time averaging over a time interval long enough when compared to the period of the light oscillations. Perfect coherence is obtained when  $|\gamma^{(1)}| = 1$  and for partial coherence light,  $|\gamma^{(1)}| < 1$ . For a partial coherent light beam, the value of  $|\gamma^{(1)}|$  usually decreases as  $|\mathbf{r}_1 - \mathbf{r}_2|$  increases. The coherence area is defined by the area that  $|\gamma^{(1)}| \geq 0.5$ . The concept of temporal and spatial coherence can be combined by mutual coherence function [36], defined as

$$\Gamma^{(1)}(\mathbf{r}_1, \mathbf{r}_2, \tau) = \langle E(\mathbf{r}_1, t) E^*(\mathbf{r}_2, t - \tau) \rangle \quad (2.11)$$

The function can be normalised as

$$\gamma^{(1)} = \frac{\langle E(\mathbf{r}_1, t) E^*(\mathbf{r}_2, t - \tau) \rangle}{\sqrt{\langle E(\mathbf{r}_1, t) E^*(\mathbf{r}_1, t) \rangle} \sqrt{\langle E(\mathbf{r}_2, t) E^*(\mathbf{r}_2, t) \rangle}} \quad (2.12)$$

which is referred as the complex degree of coherence. When the two fields interfere with each other, the resulting intensity which can be measured from the recorded fringe patterns. The values of brightest and darkest fringes are expressed as:

$$\begin{aligned}
I_{max} &= \langle E(\mathbf{r}_1, t)E^*(\mathbf{r}_1, t) \rangle + \langle E(\mathbf{r}_2, t)E^*(\mathbf{r}_2, t) \rangle \dots \\
&\quad + 2\sqrt{\langle E(\mathbf{r}_1, t)E^*(\mathbf{r}_1, t) \rangle} \sqrt{\langle E(\mathbf{r}_2, t)E^*(\mathbf{r}_2, t) \rangle} |\gamma^{(1)}| \\
I_{min} &= \langle E(\mathbf{r}_1, t)E^*(\mathbf{r}_1, t) \rangle + \langle E(\mathbf{r}_2, t)E^*(\mathbf{r}_2, t) \rangle \dots \\
&\quad - 2\sqrt{\langle E(\mathbf{r}_1, t)E^*(\mathbf{r}_1, t) \rangle} \sqrt{\langle E(\mathbf{r}_2, t)E^*(\mathbf{r}_2, t) \rangle} |\gamma^{(1)}|
\end{aligned} \tag{2.13}$$

Since the fringe visibility  $V_p$  can be calculated as:

$$V_p = \frac{I_{max} - I_{min}}{I_{max} + I_{min}}, \tag{2.14}$$

therefore the modulus of the complex degree of coherence and the visibility of the fringes have the relationship:

$$V_p = \frac{2\sqrt{\langle E(\mathbf{r}_1, t)E^*(\mathbf{r}_1, t) \rangle} \sqrt{\langle E(\mathbf{r}_2, t)E^*(\mathbf{r}_2, t) \rangle}}{\langle E(\mathbf{r}_1, t)E^*(\mathbf{r}_1, t) \rangle + \langle E(\mathbf{r}_2, t)E^*(\mathbf{r}_2, t) \rangle} |\gamma^{(1)}| \tag{2.15}$$

When  $|E(\mathbf{r}_1, t)| = |E(\mathbf{r}_2, t)|$ ,  $V_p = |\gamma^{(1)}(\mathbf{r}_1, \mathbf{r}_2)|$ . Eq. (2.15) indicates that the spatial coherence is proportional to the visibility of the interferograms at OPD=0.

### 2.1.3 Low Coherence Interferometry

OCT was developed from an optical interferometry technique, low coherence interferometry (LCI), which uses a light source with low temporal coherence to measure distances. By detecting interference fringes that occur when the optical path lengths of the reference and the object beam coincide within a coherence length, surface metrology with accuracy in the micron meter range can be obtained thank to its short coherence length. Compared with techniques using narrow-

linewidth lasers, the  $2\pi$  ambiguity [39] are avoided for surface topography measurement and thus no phase-unwrapping procedure is required.

The relationship between coherence length and the spatial resolution of LCI can be understood by expanding the output of the mono-chromatic model of Michelson interferometer to a low coherence model. Assume a continuous wave low coherence light source with negligible longitudinal modal structure, equation (2.7) can be expanded to

$$I_d(OPD) = \int_0^{\infty} S(k) \left[ A_o^2 + A_r^2 + 2|A_o||A_r| \cos(kOPD) \right] dk \quad (2.16)$$

where  $S(k)$  is now denoting a spectrum with a limited bandwidth. Similar to Eq. (2.9), Eq. (2.16) is a statement of a generalised Wiener-Khintchin theorem that is used for low coherence light source. As the Michelson interferometer described above, the power spectral density function of a stationary random process is the inverse Fourier transform of the cross-correlation function between the optical fields of the object beam and the reference beam. In this case, the cross-correlation function  $\Gamma_{or}$ , which is an analytic function, and its real part,  $A_{or}$  are given by

$$\begin{aligned} \Gamma_{or}(OPD) &= \langle A_o(z+OPD)A_r(z) \rangle = \frac{1}{2} A_{or}(OPD) + \frac{i}{2} HT\{A_{or}(OPD)\} \\ A_{or}(OPD) &= 2 \operatorname{Re} \left\{ A_o(z+OPD)A_r^*(z) \right\} \end{aligned} \quad (2.17)$$

where HT indicates Hilbert transform. In an ideal situation that the interferometer has zero OPD with no dispersion between the two arms, the cross-power spectral density equal to the power spectral density of the source [40]. If the spectrum of the light source has a Gaussian shape:

$$S(k) = \sqrt{\frac{2\pi}{\sigma_k^2}} \exp \left[ -\frac{(k-k_0)^2}{2\sigma_k^2} \right] \quad (2.18)$$

where  $k_0$  is the central (mean) wavelength and  $\sigma_k$  is the standard deviation of the spectrum, then Eq. (2.16) can be rewritten to

$$I_d(OPD) = A_o^2 + A_r^2 + 2|A_o||A_r|\gamma(OPD)\cos(kOPD) \quad (2.19)$$

where  $\gamma(OPD) = \exp(-\sigma_k^2 OPD^2)$  is the fringe visibility function of the interferogram. Defining the coherence length,  $l_c$  as the FWHM of the auto-correlation function of the spectral density function of the light source,  $l_c$  and  $\sigma_k$  are related by  $l_c = 2\sqrt{2 \ln 2} \sigma_k$ , therefore

$$\gamma(OPD) = \exp\left(-\ln 2 \cdot \frac{OPD^2}{l_c^2}\right) \quad (2.20)$$

and  $l_c$  is given by

$$l_c = \frac{4 \ln 2}{\pi} \frac{\lambda_0^2}{\Delta \lambda_{FWHM}} \quad (2.21)$$

where  $\lambda_0 = 2\pi / k_0$  is the central wavelength and  $\Delta \lambda_{FWHM}$  is the FWHM spectral bandwidth. Eq. (2.19) and Eq. (2.20) show that when the OPD become larger than the  $l_c$ , the value of signal  $I_d$  drop rapidly. This effect is referred as 'coherence gating', which is the fundamental of LCI and OCT techniques. The signal within  $OPD < l_c$  remains while the signal decay quickly as  $OPD$  moves out of this range. Therefore, by scanning a reference path delay, the longitudinal positions of reflection can be recorded with a resolution on the order of a coherence length. The coherence gate, in a reflective mode interferometer (e.g. Michelson interferometer), is of the size of the round-trip coherence length (half of  $l_c$ ), because the light travels forwards and return in the interferometric arms.

#### 2.1.4 From LCI to OCT

The idea of using optical gating to perform imaging in scattering tissue was first reported by M. Duguay in 1968 [41]. By using an high-intensity ultra-shot light pulse to induce birefringence in an media polariser, he demonstrate an ultrafast Kerr shutter to photograph light in flight and realise that the shutter can be used to

reject scattering light which is unwanted in the process of measuring the light echoes from inside of tissue. LCI method using broadband source to do axial measurement of human eyes *in-vivo* has been reported in 1988 [42]. OCT was firstly demonstrated in cross-section imaging of the human retina *in-vitro* in 1991 [5] and the first *in-vivo* images of OCT image of human retina were acquired in 1993 [4, 43]. Since then, OCT has been rapidly developing and being used in a wide variety of biomedical applications due to its advantages including high spatial resolution, contact-free and non-invasive operation.

OCT works under the same principle as LCI does except scattering samples are used as the object under investigation. Similar to LCI, early OCTs are based on scanning coherence gating axially; however, OCT measures amplitude of returning signal rather than the distance information as LCI does. With the focus of the object beam place under the top layer of the sample, part of the illumination light penetrate under the top of the sample into some distance that is not totally opaque. The penetrating light undergoes scattering and reflection inside the sample and part of the light returns to the interferometer. On the optical axis of the interrogating beam, the sample can be modelled as a number,  $N$  of discrete scatters, each at a depth of  $z_n$ . The returning light including scattering and reflection from each scatter to the detector is  $A_{o,n}$ ; thus the detected signal can be written by

$$I_d = A_r^2 + \sum_{n=1}^N \left[ A_{o,n}^2 + 2|A_o||A_r|\gamma(z_n)\cos(2kOPD_n) \right] \quad (2.22)$$

where  $OPD_n$  is the corresponding OPD for each  $z_n$ . The coherence gating introduced by  $\gamma(z_n)$  retains the signal at a certain depth determined by the optical length of the reference path. By displacing the reference mirror, the length of the reference path can be tuned, thus the 'coherence gate' can be scanned along the axial direction inside the sample. This allows selecting the return light from scatters and reflectors in each layer. The signal is detected by a photo-detector in terms of alternating current (AC) signal. A complete axial scan in depth which measure each

point in the axial line produced a signal sequence, referred as an A-scan, which represents a depth profile of back-scattered light intensity in depth. This depth profile does not present an absolute quantitative measurement of the back-scattering and reflection because the reflection, scattering and absorption in upper layers will affect the quantities of the measurement in lower layers; however, it can be used for imaging purpose. This is because OCT are sensitive to discontinuities of scattering potential, e.g. discontinuities of the refractive index or attenuation coefficient [1]. In fact, OCT can be considered as a band-pass measurement that detects high frequency Fourier components of the scattering potential [44], which are functions of derivatives of the scattering potential according to the Fourier derivative theorem.

In terms of scanning techniques, there are three type of OCTs working in two regimes, time-domain OCT needs scanning a probing beam in axial direction to obtained A-scan data; whereas Fourier-domain OCT and swept-source OCT, both working in spectral domain, acquire the depth-related information via applying Fourier transformation on spectral data, which eliminates the need for axial scanning.

## **2.2 *Time-domain OCT***

Time-domain OCT (TD-OCT) is the earliest and most straightforward OCT technique. As described above, during a TD-OCT acquisition, mechanical scanning is performed axially on the reference beam to applied coherence gating effect on continuous depths in the target. In order to collect lateral information, lateral scanning of the probing beam is required.

### **2.2.1 Light Sources**

Broadband light source are desirable for high axial resolution OCT, since the coherence length is inversely proportional to the spectrum bandwidth according to the dependence of the axial point spread function (PSF) on the spectrum of the light source. Near infrared (NIR) wavelength (e.g. typically between 700 nm and 900 nm for ophthalmology) are used to minimise scattering in tissue and achieve high penetration depth because light in this region presents a low absorption in water.

The most widely used optical sources for TD-OCT is the super-luminescent diode (SLD) [45], which combines a broadband spectrum (a few tens of nm to over a hundred nm) with high optical power (e.g. a few mW). An alternative is a mode-locked laser with femto-second pulses which produce a broadband spectrum as a result of the uncertainty principle [46]. In order to shorten the coherence length, it is possible to enlarge the bandwidth of the light source by combining multiple semiconductors [46]. However, this may also introduce a distortion of the auto-correlation function due to the side-lobes, which can be removed by spectral shaping of the source with a reduced sensitivity [47].

### 2.2.2 Axial Resolution

OCT decouples the spatial resolution of imaging into two categories: axial resolution and transverse resolution. The axial resolution  $\delta z$  is a measure of the axial point spread function (PSF). For TD-OCT, it is determined by the spectrum of the optical source, according to the generalised Fourier theory.  $\Delta z$  is generally independent of the interface optics (with some exceptions that are mentioned in the following sections). The axial resolution  $\delta z$  is quantified as half of the coherence length of the light source. Due to the double-pass configuration, it can be estimated from Eq. (2.21) by

$$\delta z = \frac{l_c}{2} = \frac{2 \ln 2}{\pi} \frac{\lambda_0^2}{\Delta \lambda_{FWHM}} \quad (2.23)$$

For example, for a broadband light source with 840 nm central wavelength and FWHM bandwidth of 20 nm, which is used in experiments described in this thesis, the theoretical FWHM depth resolution is around 16  $\mu\text{m}$ .

### 2.2.3 Transverse Resolution

The transverse resolution of OCT,  $\delta x$  is the same as in optical microscopy and is determined by the minimum beam waist of the optical beam in the object path; it is therefore directly inversely related to the numerical aperture (NA) of the interface optics [48]. Assuming Gaussian optics,  $\delta x$  can be estimated using first order

approximation of the diffraction limited spot size of the focused optical beam which is given by

$$\delta x = \frac{4}{\pi} \frac{f \lambda}{d} = 1.22 \frac{\lambda}{N.A.} \quad (2.24)$$

where  $f$  is the focal length of the objective lens and  $d$  is the diameter of the lens aperture. The transverse resolution can be enhanced by increasing the NA of the lens and it decays as the imaging plane is moving away from the focal plane of the objective lens.

Since the confocal effect rejects out-of-focus light, a limited depth range of detection is allowed. If the pinhole used is infinitely small, the FWHM of this axial range,  $\Delta z_{FWHM}$ , known as the depth of focus (DOF) or depth of field when refers to imaging plane is given by

$$\Delta z_{FWHM} = \frac{n \lambda_0}{NA^2} \quad (2.25)$$

where  $n$  is the refractive index of the medium. The coherence gate of OCT is generally at least an order of magnitude smaller than the DOF because standard OCT operates in cross-section imaging plane and large DOF is required; therefore the confocal gate has little effect in standard OCT depth resolution. However, due to the requirement of axial scanning of reference path length in TD-OCT, the confocal gate and coherence gate become departed as the OPD changes, which may result in reduction in transverse resolution and a drop in signal intensity from the coherence gate due to the confocal rejection. The DOF therefore defines the maximum effective depth range of OCT imaging, which is inversely related to the lateral resolution. For the applications that require large depth range, dynamic focus [50] may be employed to extend the depth range. DOF will become very small when large NA optics is used, for example, in novel OCT techniques, such as optical coherence microscopy (OCM) [51, 52]; the effect of DOF should be considered in those cases, which will be discussed in Chapter 3.

#### 2.2.4 Scanning

Scanning optical delay in the reference path is required in order to select depth information. The simplest way is to mount the reference mirror onto a motorised translation stage. This method has large depth range and little optical power loss but may result in slow scanning speed and suffer from vibration noise from mechanical movements [53]. Other methods, including multiple reflection [53], spinning cube [54], may be used to increase the scanning speed but suffer from large optical power loss. Diffraction grating was also used as an high speed delay element [55, 56] to introduce optical delay lines; however the complexity is relatively high and optical loss is also considerable.

Other than axial scanning, transverse scanning of the probing beam is required in a standard OCT system to synthesize cross-sectional images (B-scan) (illustrated in Figure 2.2) from a series of adjacent A-scans. The most popular approach is employing a galvanometric scanner [57]. Some novel scanning schemes, such as using rotating probe heads [58] and free-hand probes [59] have also been used in specialised OCT applications, such as endoscopy OCT. In order to present cross-section images, axial scanning and transverse scanning have to be combined. The most common scanning scheme is axial priority [5] where rapid axial scanning and slow lateral scanning are synchronised to weave the complete B-scan images. Alternative lateral priority method is also possible [60] to scan the beam rapidly in lateral direction and slowly in axial direction. In some applications, *En-face* or C-scan images are preferred in representing the OCT data in the plane that is comparable to conventional microscopy images [60, 61]. *En-face* imaging is useful for image alignment and especially useful for applications that established features can be easily recognised, such as retinal imaging. This can be obtained by scanning the probing beam in *en-face* plane. En-face images can also be obtained by a parallel detection OCT technique, known as full-field OCT [62], which is a main topic in Chapter 3.

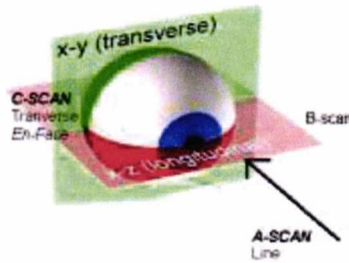


Figure 2.2. Terminology of imaging planes in OCT.

### 2.2.5 Photo-detector

There are a number of types of photodiode, including PIN photo detector, avalanche photo detector (APD) and the optically preamplifier PIN photo detector. The simplest example PIN photodiode is used as an example to give the mathematical treatment to the signal and noises analysis. A PIN photodiode is constructed based on a 'sandwich' structure where a PN junction is separated by a layer of intrinsic semiconductor layer (i-layer). The incident photons absorbed by the i-layer create electron-hole pairs that are separated by the electric drift field, which creates photocurrent to be measured. The photon has energy  $hc/\lambda$ , where  $h$  is Planck constant,  $\lambda$  denotes the wavelength and  $c$  is the light speed. Given a quantum efficiency  $\eta$ , defined as the percentage of the photons that create electron hole pairs of all, and the input optical power  $P_s$ , the generated electrical current,  $I_d$  is given by

$$I_d = \eta \frac{\lambda e}{hc} P_s \quad (2.26)$$

where  $e$  is fundamental charge. The ratio of  $I_d$  and  $P_s$  is defined as the response of the photodiode and denoted by  $R$ . The detection system has an electrical response bandwidth of  $\Delta f = B$  and is able to sample the optical signal within a time interval of  $T = 1/2B$ , the total number of photons received by the photodiode within this time interval is

$$N = \frac{\lambda P_s}{hc} T = \frac{\lambda P_s}{2Bhc} \quad (2.27)$$

Analog-to-digital (AD) conversion is required for digital representation of OCT signal. A standard  $n$  bit AD convertor on a frame grabber provide a dynamic range up to  $10\log(2^n)$  or  $20\log(2^n)$  depending on whether the signal is referred in the optical domain or the electrical domain. Common noise sources in the AD converters include offset error, scale error, nonlinearity and non-monotonicity. By Nyquist theorem, the frequency should be at least twice the highest sampled frequency that is required.

### 2.2.6 Noises of TD-OCT

The main sources of noises in TD-OCT are thermal noise, shot noise and relative intensity noise (RIN) [40]. Thermal noise arises through random particle motions in the detector electronics due to the non-zero thermal energy. Shot noise occurs due to the quantization of the light to charge.

The shot noise,  $S_i$  is generated by a photocurrent with mean amplitude  $\langle i \rangle$  is given by Poisson distribution:

$$S_i = e \langle i \rangle \quad (2.28)$$

With an assumption of Dirac pulses of the shot noise distribution, the shot-noise spectrum is white and its mean-square value can be expressed by

$$\langle i^2 \rangle = 2eI_d B \quad (2.29)$$

from which we know that the shot noise is signal dependent, that the root-mean-square (RMS) shot noise grows with the square root of the signal amplitude  $\sqrt{N}$ . Using  $20\log$  decibel, if the optical power is doubled, the signal grows 6 dB and the shot noise grows 3 dB; therefore the SNR grows 3 dB.

$RIN$  is a collection of noises that scale linearly with the power of the photocurrent,  $\langle i \rangle^2$ , including fluctuations of the source power and amplified spontaneous emission (ASE).  $RIN$  is related to the photocurrent by

$$RIN = \gamma \langle i \rangle^2 \quad (2.30)$$

where  $\gamma$  is the coefficient that is determined experimentally.

### 2.2.7 Numerical Processing

The electronic signal encodes the signal of interference inside a carrier and the detection process in TD-OCT is heterodyned. In order to obtain the cross-correlation signal from the output of the detector, modulation of the OPD phase is required to get rid of auto-correlation terms. High-pass filter is usually used to remove the direct current (DC) components in the signal, which is not depth dependent. The phase modulation is performed by introducing scanning of delay lines. If the OPD is scanning at a velocity  $v$  then the phase is modulated at a frequency,  $f$ , which has a relation:

$$f = \frac{v}{\lambda_0} \quad (2.31)$$

where  $\lambda_0$  is the central wavelength. It is necessary to apply a band-pass filter around the frequency  $f$ . The band-passed signal is then demodulated to extract the envelope of the signal [63]. This procedure is done by analogue electronics before the AD conversion, which can be performed with non-linear scaling to enlarge the dynamic range of the measurement.

### 2.2.8 Sensitivity

The sensitivity of TD-OCT, which is defined by the signal-to-noise ratio (SNR) under shot-noise limited imaging with a perfect reflector [1]. The shot noise can be made to dominate all noise sources by selecting sufficient large reference power. The SNR is the ratio of the signal power to the variance of the noise  $\sigma^2$ , which is given by the expression:

$$SNR_{TD} = \frac{\langle I_d \rangle^2}{\sigma^2} = \frac{R P_s}{2eB} \quad (2.32)$$

where  $R$  is the response of the detector,  $P_s$  is the optical power returned from the sample and  $B$  is the noise equivalent bandwidth of the electronic detection band-pass filter. In a shot noises limited case, SNR is independent of the reference arm power except the fact that the  $B$  is related to the reference scanning velocity [63] by

$$B = 2\Delta f = \ln 4 \frac{2}{\pi} \frac{v}{l_c} \quad (2.33)$$

The DC term of the detected signal can be cancelled by employing balance-detection scheme that two detectors were used with a  $\pi$  phase shift; thereby the amplitude of the AC signal is doubled and the  $RIN$  and negative effects of mechanical vibration of the optical system are reduced to minimal [64].

## 2.2.9 Dispersion

Group velocity dispersion (GVD) or second order dispersion (short as dispersion in following discussions) can degrade the axial resolution of an OCT system. We have assumed that both interferometric arms are linear and dispersion free in above description, thus the cross-correlation function equal to the auto-correlation function. However, in reality, GVD causes different wavelength to propagate with nonlinearly related velocity. The cross-correlation function will broaden if GVD mismatch is present between the two arms. This problem is similar to that of pulse broadening and chirping in a dispersive medium [65].

The propagation constant for the object path,  $\beta_o(\omega)$  and the reference path,  $\beta_r(\omega)$  are functions of angular frequency  $\omega$ , whose second order Taylor expansion around central frequency  $\omega_0$  are given by

$$\begin{aligned} \beta_o(\omega) &= \beta_o(\omega_0) + \beta_o'(\omega_0)(\omega - \omega_0) + \beta_o''(\omega_0)(\omega - \omega_0)^2 \\ \beta_r(\omega) &= \beta_r(\omega_0) + \beta_r'(\omega_0)(\omega - \omega_0) + \beta_r''(\omega_0)(\omega - \omega_0)^2 \end{aligned} \quad (2.34)$$

Assuming the GVD mismatch exists in length  $L$  between two arms, the wavelength-dependent phase mismatch  $\Delta\phi$  is thus given by [40]

$$\begin{aligned}\Delta\phi(\omega) &= 2\beta_o(\omega)l_r - 2\beta_r(\omega)l_r \\ &= \beta(\omega_0)OPD + \beta'(\omega_0)(\omega - \omega_0)OPD + \frac{1}{2}\Delta\beta''(\omega_0)(\omega - \omega_0)^2(2L)\end{aligned}\quad (2.35)$$

where  $OPD = 2(l_o - l_r)$ .  $\Delta\beta''(\omega_0) = \beta_o''(\omega_0) - \beta_r''(\omega_0)$  is the GVD mismatch. Only the difference in GVD between two arms exists in Eq. (2.35). The effect of dispersion can be decreased by equalising the GVD in the two interferometric arms. Since the group refractive index  $n_g$  is given by refractive index  $n$  by

$$n_g = n - \lambda \frac{dn}{d\lambda}, \quad (2.36)$$

and the GVD is given by the derivative of  $n_g$  :

$$GVD = \frac{dn_g}{d\lambda} = \lambda \frac{d^2n_g}{d\lambda^2} \quad (2.37)$$

The coherence length is therefore broadened [66] from Eq. (2.23) to

$$l_{c,disp} = \sqrt{l_c^2 + (GVD \cdot L\Delta\lambda)^2} \quad (2.38)$$

Due to the effect of dispersion mismatch, the axial resolution deteriorates. High orders of dispersion cause asymmetrical distortion and peak splitting [66]; therefore it is highly desirable to minimise the dispersion mismatch between the two interferometric arms. Dispersion is especially important in a fiber-based system, where there could be a large dispersion mismatch if the fibre lengths are not closely matched. Since the object may be dispersive itself and the propagation constant may vary with depth [67, 68], the dispersion compensation on the reference may not be straightforward; however the basic requirement is to ensure that components and fibre length in the two arms are matched [69]. For highly dispersive objects, inserting a similar medium as in the object arm into the

reference path is preferred to balance the object-induced dispersion. Further methods for compensating dispersion mismatch including using optical scanning delay lines [70, 71], phase modulator [72] and post-processing method [68] are all possible.

### **2.3 Spectral domain OCT**

According to Wiener-Khintchin theorem, the depth-dependent signal is related to the spectral power density of light source by a Fourier transformation (FT), therefore the depth information scan can also be obtained by applying a FT to the acquired spectrum data, which eliminates the need of scanning the OPD. This OCT approach is referred as spectral-domain OCT (SD-OCT). Based on this idea, dramatic improvements of OCT techniques in both speed and sensitivity [73, 74] have been realised. The direct access to spectral fringes pattern also allow numerical dispersion compensation [75] and spectroscopic analysis [76]. Improved phase stability helps the development of phase microscopy [77] and Doppler OCT [78].

Limitations of SD-OCT include limited depth range due to parallel detection at multiple wavelengths and sensitivity roll-off in depth [56], auto-correlation artefacts [79] and the incompatibility with dynamic focus, which will be introduced in following sections.

SD-OCT requires the spectrally separated interference signal, which can be implemented in two ways: by encoding the spectral information spatially from a broadband light and decoding the signal using a spectrometer; or by encoding the optical frequency in time and decoding the signal with fast single detector. These two methods are termed as Fourier-domain OCT (FD-OCT) and swept-source OCT (SS-OCT) respectively.

#### **2.3.1 Fourier-domain OCT**

Fourier-domain OCT (FD-OCT) [80, 81], also known as channelled-spectrum OCT (CS-OCT) uses the same broadband light source as the TD-OCT does and extracts spectral information by distributing different optical frequencies onto a linear detector array via a diffraction grating. The interference signal is recorded by the

spectrometer as a spectrum with peaks and troughs, known as channelled spectrum. A linear detector array is used to record the channelled spectrum that related to the depth-dependent information by a Fourier transformation. Lateral scanning is still required to acquire transversal information to generate a B-scan or a 3D volume. FD-OCT was developed based on spectral radar [80, 82, 83], whose initial development was limited by the lack of detector arrays with sufficiently high dynamic range and high speed. With the appearance and advance of semiconductor detector arrays, rapid developments of FD-OCT techniques have been promoted in the last decade. Using modern linear CCD detector arrays allow operating FD-OCT imaging with a line-rate up to hundreds of kilohertz, which allow fast B-scan imaging in video rate [84].

### 2.3.1.1 Principles of FD-OCT

FD-OCT employs a spectrometer to acquire spectral data. The set-up is illustrated in Figure 2.3, where a transmissive diffraction grating is used as an example; reflective diffraction grating can be employed with a similar configuration. Since spectral data are recorded individually, Eq. (2.16) can be rewritten as

$$E_O(k, \omega) = \sum_{n=1}^N A_{o,n} \cos(kx_{o,n} - \omega t) \quad (2.39)$$

where  $k$  is the wave number,  $x_{o,n}$  is the optical path corresponding to a reflector  $n$ , and  $A_{o,n}$  is the field amplitude recorded at the detector. The reference field remains as  $E_r(k, \omega) = A_r \cos(kx_r - \omega t)$ . The intensity recorded on the detector,  $I_{FD}(k)$  is the time average of the amplitude of the cross-correlation function between the object field and reference field, which is expressed by

$$I_{FD}(k) = \text{Re} \left\langle \left[ A_r \cos(kx_r - \omega t) + \sum_{n=1}^N A_{o,n} \cos(kx_{o,n} - \omega t) \right]^2 \right\rangle, \quad (2.40)$$

and thus,

$$I_{FD}(k) = A_r^2 + \sum_{n=1}^N A_{o,n}^2 + \sum_{n \neq m=1}^N A_{o,n} A_{o,m} \cos(2kz_{n,m}) + \sum_{n=1}^N A_r A_{o,n} \cos(2kz_n) \quad (2.41)$$

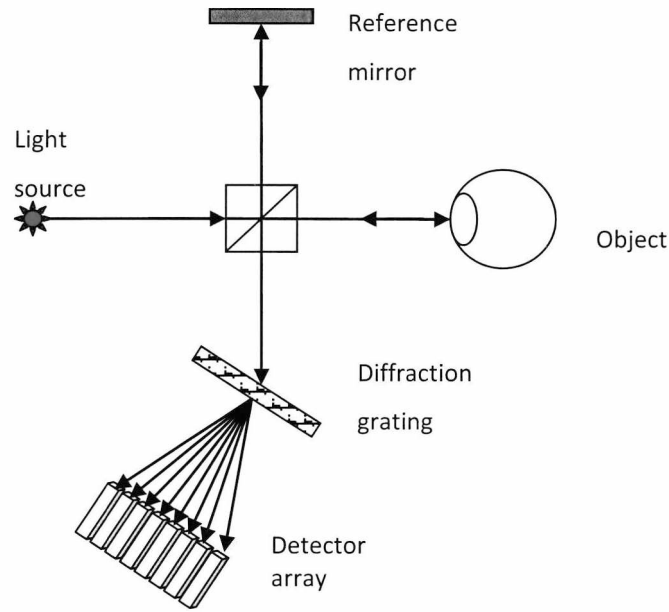


Figure 2.3. A schematic of a standard FD-OCT. A spectrometer is employed in the measurement path of the interferometer where a linear detector array is used to record the spectral data.

The first two DC terms in Eq.(2.41) produce a large peak at low frequency (around zero depth) after the FT. The third term is an cross-correlation function between signal from two different depths in the object, which produces modulations with arbitrary frequencies and thus may present output at any depth in the result of FT. The last term in Eq. (2.41) is a modulation of the reflection at depth  $z_n$  with a period  $k = \pi / z_n$ , which is of interest. The A-scan can therefore be retrieved by applying FT to the recorded spectrum. Since  $I_{FD}$  is a real function, the result of FT have symmetric values in both positive and negative frequencies, which cannot be distinguished directly. The techniques of retrieving complex expression from  $I_{FD}$  will be discussed later.

### 2.3.1.2 Axial Resolution of FD-OCT

Considering the power spectral density of the source, Eq. (2.41) can be expanded to

$$\begin{aligned}
I_{FD}(k) &= A + B + C + D, \quad \text{where} \\
A &= \gamma(0)A_r^2; \\
B &= \gamma(2z_n) \sum_{n=1}^N A_{r,n}^2; \\
C &= \sum_{n \neq m=1}^N A_{o,n} A_{o,m} [\gamma(2z_{n,m}) + \gamma(-2z_{n,m})]; \\
D &= \sum_{n=1}^N A_R A_{O,n} [\gamma(2z_n) + \gamma(-2z_n)].
\end{aligned} \tag{2.42}$$

where  $\gamma$  is the auto-correlation function, or the inverse FT of the source power spectral density that was defined in Eq. (2.20).  $I_{FD}$  presents the spectral data with finite discrete values of  $k$ ; the sampling number,  $N$  determines the number of data in an A-scan. From Eq. (2.42), the best possible axial resolution of FD-OCT,  $\delta z_{FD}$  depends on the FWHM of the auto-correlation function  $\gamma$ ; the axial resolution is therefore identical to that of the time-domain OCT, given by Eq. (2.23). The relationship between the depth range,  $\Delta z$  and the spectral resolution  $\delta k$ , according to the Fourier theory, is given by

$$\Delta z = \frac{\pi}{\delta k} = \frac{1}{4} \frac{\lambda_0^2}{\delta \lambda_s} \tag{2.43}$$

where  $\delta k = 2\pi \delta \lambda / \lambda_0^2$ , and  $\delta \lambda_s$  is the wavelength sampling resolution that is resolved by  $N$  number of detectors.

Although the best axial resolution is governed by Eq.(2.23), due to the limited spectral resolution, the real depth resolution or systematic depth resolution is the larger value in  $2\Delta z / N$  and  $\delta z_{FD}$ .  $2\Delta z / N$  can be reduced by using larger number of detectors to resolve the same optical bandwidth. According to Nyquist theorem, the sampling frequency should be at least twice the highest sampled frequency that is required; therefore the relationship  $2\Delta z / N \leq \delta z_{FD} / 2$  should be achieved.

### 2.3.1.3 Sensitivity Roll-off

Compared to TD-OCT, FD-OCT present higher sensitivity and greater measurement speed [85]. However, FD-OCT imaging exhibits a roll-off in sensitivity at depths away from the zero OPD position [56, 74]. In general, even diffraction-limited optical

imaging system presents a decaying contrast for high spatial frequency known as optical transfer function (OTF) [86]. In spectrometer, decaying visibility of the recorded channelled spectrum can be observed with higher fringe frequencies. Reasons of sensitivity roll-off of FD-OCT include limited optical resolution of the spectrometer [87], finite detector size [88], aliasing at high spatial frequency[85] and inter-pixel cross-talk [89].

Assuming the two beams are both Gaussian and superposed perfectly, the beam profile and the rectangular shape of the detector pixels are convolved with the interference signal [89, 90], the 'roll-off' can be modelled by considering the spectral resolution of the spectrometer. Each wavelength components  $I(k)$  is focused to a spot on the detector array with a PSF, whose FWHM is  $a$ . For a Gaussian PSF, the output of each detector,  $I_d(i)$  is related to the distribution function  $h(x, y, x_i)$  by [88]

$$I_d(i) \propto \int_{x_i - \Delta x/2}^{x_i + \Delta x/2} \int_{- \Delta y/2}^{\Delta y/2} h(x, y, x_i) dx dy \quad (2.44)$$

$$h(x, y, x_i) = \frac{4 \ln 2}{a^2} \exp \left\{ - \left( \frac{4 \ln 2}{a^2} \right) [(x - x_i)^2 + y^2] \right\} dy dx$$

where  $x_i$  is the horizontal position of detector  $i$  of the linear detector array,  $\Delta x$  and  $\Delta y$  are the pixel dimensions in horizontal and vertical direction. The depth related A-scan sensitivity can be obtained by Fourier transform of  $I_d(i)$ , which is evaluated as:

$$A(z) \propto (R_{id} \cdot \Delta x) \exp \left( - \frac{a^2 R_{id}^2 z^2}{4 \ln 2} \right) \frac{\sin(\Delta x R_{id} z)}{\Delta x R_{id} z} \quad (2.45)$$

where  $z$  is the depth and  $R_{id} = \Delta k / \Delta x$  is the reciprocal linear dispersion which is measured by the width of spectrum spread of  $1 \mu\text{m}$  at the focal plane. Eq. (2.45) shows that the roll-off of the sensitivity is mainly related to the depth  $z$  by a Sinc function and an exponential function. Other factors affecting the decay include the

pixel size and the dispersion mismatch. Limited detector linewidth  $\Delta x$  records a quasi-rectangular portion of a spectrum,  $\Delta k$ , instead of a single frequency, after the FT, presents a profile of a Sinc function. Sensitivity roll-off is worse with larger dispersion mismatch. With a given  $R_{fd}$ , the roll-off is mainly related to the spectral resolution of spectrometer. With a high spectral resolution, not only large depth range, but also high sensitivity and small roll-off are obtained in depth; therefore large detector number  $N$  is required. With the assumption of dispersion-free interferometer, Eq. (2.45) can be used to calculate the theoretical roll-off value at a certain depth. For all these reasons, the detector array of the spectrometer and dispersion compensation in the interferometer are critical to the sensitivity 'roll-off'.

#### 2.3.1.4 Extraction of Cross-correlation Terms

Auto-correlation terms are present in Eq. (2.42) produce noise after Fourier transform. The DC term  $B$  is an autocorrelation terms due to the reference power, which produce a large peak with its FWHM of a coherence length around zero OPD position. When imaging low-reflectivity sample, the magnitude of this peak is sufficiently large that its shoulders could obscure faint signals at OPDs up to many times [91]. The peak also reduces the depth range [79] and disable the most sensitive part of the measurement depth range; therefore removal of these terms from the recorded signal is required to achieve maximum imaging quality. The auto-correlation term  $C$  is from the object and is due to interference between scatters. This may produce artefacts in depths, especially when strongly reflective layers are present in the depth range of the measurement. However, because the object beam has less power than the reference beam and the term  $B$  dominates over the term  $C$ , the main task is to remove the term  $B$ . Term  $C$  is minimised by using high reference power to enlarge the cross-correlation signal.

The most straightforward method to remove the DC term is to subtract a pre-record frame that is obtained from the reference arm alone (with object arm blocked) [75]. This method however is dependent on the stability of reference signal. A more complex method [79] is to average the spectrum obtained for a large number of A-scans from each B-scan, which presents a dynamic reference power measurement during image acquisition. Averaging of A-scans from different lateral

positions, washes out the cross-correlation term due to the fact that all spectrum are modulated at different frequencies, leaving only the DC terms which is to be subtracted from the recorded data. This method not only removes auto-correlation terms, but also effectively removes pattern noises of the linear detector array.

### 2.3.1.5 Spectrum Resampling

The Fourier transformation should be carried out on spectral data that is linear to optical frequency, or wave-number  $k$ ; however the spectrometer of FD-OCT setup does not automatically meet this requirement. In Figure 2.3, the recorded signal of the spectrometer is the first order diffraction of the diffraction grating transmission. The disperse light of frequency  $k$  at an incident angle  $\phi$  are related by the grating equation:

$$d \sin \phi = \lambda = \frac{2\pi}{k} \quad (2.46)$$

where  $d$  is the pitch distance of the grating. The lateral position of frequency resolved light,  $x(k)$  recorded by the detector array is therefore related to  $k$  by

$$x(k) = L \tan \left[ \sin \left( \frac{2\pi}{kd} \right) \right] \quad (2.47)$$

where  $L$  is the distance between the grating and the detector. Eq. (2.47) shows that the  $k$ -dependent light is not distributed linearly on the detector. Applying FT without linearising  $k$ -dependent spectrum will result in a depth-dependent broadening of the axial PSF, which lead to a loss of axial resolution and a reduction of the PSF peak amplitude [81]. The broadening of PSF at the depths close to zero OPD is small but will deteriorate with depth increasing. A linearisation of the spectrometer is therefore required to maintain high sensitivity and constant depth resolution in the depth range of measurement.

The linearisation can be performed by optical methods and software approaches. Optical methods mainly use prism to compensate the non-linearity of the spectrum [92]; while the software methods involve determining the  $k$ -to-pixel

function,  $k_p$  and using this to resample the spectrum in linear  $k$  [93]. It requires either *a priori* knowledge or experimental measurement of the mapping function,  $k_p$ . These parametric methods seek to directly measure  $k_p$  for discrete values of the pixel index and then hypothesis a relationship in order to interpolate a continuous profile. A simple approach may make the approximation for the sine term in Eq. (2.46); therefore  $p$  is assumed linear to wavelength and  $k_p$  is reversely related to  $p$ . A more precise version of this method makes an additional trigonometric correction. Non-parametric approaches seek to determine  $k_p$  directly from a recorded channelled spectrum,  $I(p)$  which is given by

$$I(p) \propto A_o^2 + A_r^2 + 2A_oA_r \cos \left[ OPDk_p(p) + \theta_D(k_p) \right] \quad (2.48)$$

where  $A_o^2, A_r^2$  is the auto-correlation optical power from the object and the reference respectively;  $\theta_D$  is the phase difference due to chromatic dispersion. Assuming the system is free of higher order dispersion, thus  $\theta_D \propto k_p$ ; the phase term,  $\left[ OPDk_p(p) + \theta_D \right]$  in the cosine is therefore proportional to  $k$ . The phase term at each pixel,  $\theta_p$  can be calculated from the recorded spectral data. By linearising  $\theta_p$ , a linear  $k_p$  map,  $k_p'$  can be obtained. This method is based on the assumption of dispersion offset free; if large dispersion mismatch is present, the wavelength-dependent phase offset in the spectral fringe will make this method inaccurate [94]. One solution is to generate a channelled spectrum entirely in the source where there is no dispersion and the channelled spectrum is completely periodic in  $k$  [95]. An alternative solution is to measure at a second depth position where another phase array is present [94]. Assuming  $\theta_D$  does not change significantly over the small change in depth, the difference between two set of phase data,  $\Delta\theta$  is linear to calculate  $k_p$ , which can be used to calculate  $k_p'$ .

Using the method described in [94], the phase of the channelled spectrum can be obtained by applying FT twice. The recorded data is firstly Fourier transformed to depth domain; a digital windows is then applied to the result to remove the

symmetric component; an inverse FT was then applied to the single-side depth-related data, which produce an analytic form of the signal,  $I'(p)$ . The phase  $\theta_p$  can be thereby calculated as

$$\theta_p = \arg[I'(p)] = \tan^{-1} \frac{\text{Im}[I'(p)]}{\text{Re}[I'(p)]} \quad (2.49)$$

To remove  $2\pi$  ambiguity,  $\theta_p$  is unwrapped and thus the mapping function  $k_p$  is obtained. A polynomial is fitted to the  $k_p$ , based on which, the spectrum data can be resampled and converted to  $I(k)$ . The interpolation algorithm, such as linear interpolation and spline interpolation, are selected according to the requirements of precision and processing speed. Data resampling may lead to loss of the pixel-wise bandwidth, which may result in a reduction of the signal in large depth positions.

### 2.3.1.6 Dispersion Compensation

From the above discussions, we know that dispersion mismatch affect most fundamental properties of FD-OCT imaging. When it is present in the interferometer, a frequency dependent phase shift  $\theta_D(k)$  is imparted into the channelled spectrum [68, 96]:

$$I(k) \propto A_o^2 + A_r^2 + 2A_{or} \sum_{OPD=0}^{\infty} \cos[OPDk + \theta_D(k)] \quad (2.50)$$

which broadens the axial PSF and thus reduces the axial resolution. In this case, in order to conserve the axial resolution, dispersion mismatches have to be compensated. Due to the access to spectral information, it is possible to be done by numeric methods, for example by acquiring the complex channelled spectrum using Hilbert transformation. Phase correction up to third order is given by [96]

$$\varphi(k) = -c_2(k - k_0)^2 - c_3(k - k_0)^3 \quad (2.51)$$

where experiment-determined coefficients  $c_2$  and  $c_3$  represent the correction for GVD and third order dispersion respectively. With a single reflector, these coefficients can be retrieved from the phase of the channelled spectrum and used for the correcting the systematic dispersion mismatch. If object-induced dispersion is to be correct, more general method based on iterative imaging sharpness metric methods [96] should be considered.

### 2.3.1.7 Signal-to-Noise-Ratio

FD-OCT has a sensitivity advantage over TD-OCT [73] because FD-OCT acquires light from coherence gates in different depth simultaneously. The enhancement of sensitivity is related to the number of pixels in the linear detector array. For a reflector returning an optical power  $p_s$  dispersed across  $N_{FD}$  pixels, if the reference power contribution is  $p_r$ , the mean-square peak signal power in the A-scan is given by[91]:

$$\langle I_D \rangle_{FD}^2 = R^2 p_o p_r \frac{N_{FD}^2}{4} \quad (2.52)$$

where  $R$  is the detector response. Similar to the TD-OCT analysis, assuming shot noise limit acquisition, the noise on each pixel is:

$$\sigma_k^2 = e R p_r B_{FD} \quad (2.53)$$

where  $B_{FD}$  is the detection bandwidth which is equal to the bandwidth for TD-OCT if the detector array covers a domain equal to twice the FWHM of the source [74]. Given that no correlation occurs between the noises cross different pixels, the noise adds incoherently after FT. Assuming the source has equal power in all pixels of the spectrometer, the noise expression is given by

$$\sigma_N^2 = e R P_r B_{FD} N_{FD}. \quad (2.54)$$

The SNR is therefore

$$SNR_{FD-OCT} = \frac{RP_o}{2eB_{FD}} \frac{N_{FD}}{2}; \quad (2.55)$$

thus the sensitivity improvement factor, compared to the TD-OCT method, is in the scale of half the number of pixels for a Gaussian source [91].

Unlike in TD-OCT, where the signal can be AC filtered and *log* scaled before digitisation, FD-OCT records and digitises the signal including the DC terms from the linear detector array output. Most detector arrays integrate the digitisation into the read-out process. In this case, part of the dynamic range is allocated to the DC terms; therefore the dynamic range of FD-OCT imaging is limited by the portion of the dynamic range of the detector array that is allocated for measuring the cross-correlation term in the channelled spectrum. This limitation might not be severe in retinal imaging, but may lead to saturation artefacts when imaging objects with a large dynamic range [97, 98].

### 2.3.2 Swept-source OCT

Swept-source OCT (SS-OCT) [99] uses another approach to implement spectral-domain OCT. Under the same principle as FD-OCT, the A-scan is obtained from the spectral interferogram via FT; however, SS-OCT encodes the spectral information temporally by employing a wavelength tuneable light source that swept through a range of wavelengths rapidly (usually above 100 kHz) and recording the spectrum-resolved data by a high-speed photo-detector. The schematic of a standard swept source OCT is the same as the TD-OCT except that no axial scanning of the reference path is needed. Due to the required high speed of frequency sweeping, the photo-detector need to work at an increased bandwidth. All wavelength components are detected sequentially by the photo-detector that can work at up to gigahertz. Balanced detection configurations are possible for SS-OCT [100] as for TD-OCT. Swept sources can operate at 1300 nm region, compared to FD-OCT systems that generally operate at 800 nm region due to the relatively high cost of InGaAs detector array which is sensitive to light of wavelength above 1  $\mu\text{m}$ .

The sampling rate of the photo-detector, the linewidth and the tuning range of the tuneable source in SS-OCT, are analogous to the pixel size, the spectral

resolution and the spectrum bandwidth covered on the detector array in FD-OCT. After the interferogram being digitized, the numeric processing is therefore the same as that of FD-OCT. Accordingly, SS-OCT suffers from sensitivity roll-over similarly to FD-OCT. The main difference between SS-OCT and FD-OCT is the light source and the detector.

### **2.3.2.1 Tuneable Optical Sources**

Tuneable sources are used for SS-OCT. The instantaneous linewidth determines the OCT depth range, whereas the wavelength tuning range determines the OCT axial resolution. Various designs of tuneable sources have been used, though most of them are based on the simple schematic shown in Figure 2.4. The light source consists of a gain medium, a wavelength tuning element and an output coupler. Several options exist for the gain medium, although semiconductor optical amplifiers (SOAs) are the most commonly used, due to their large bandwidth and rapid gain response time. There are also different options for performing the wavelength selection. The first tuneable filters for OCT used a diffraction grating and a polygon mirror to scan the wavelength, which produce an A-scan rates of 15.7 kHz over a 70 nm sweep range, with a linewidth of less than 0.1 nm [101]. The scan rate was later improve to 115 kHz [102]. Fabry-Perot tuneable etalons was also used in SS-OCT, achieving A-scan rates of up to 60 kHz when both directions of the sweep were used [103]. The maximum scan rate of the tuneable filters is ultimately determined by the gain response time of the gain medium because after each tuning period, there is a delay while the stimulated emission builds up for the new wavelength [103]. The technique of Fourier-Domain Mode Locking (FDML) [104] was introduced in 2006, which produces a sweep rate equal to the cavity or loop round trip time. Because the design allows all wavelengths buffered in the cavity in a 'quasi-stationary' state, the gain medium can operate on all wavelengths and the gain response time is no longer a limitation. Using this method, the A-scan rates of 1.37MHz has been achieved [105].

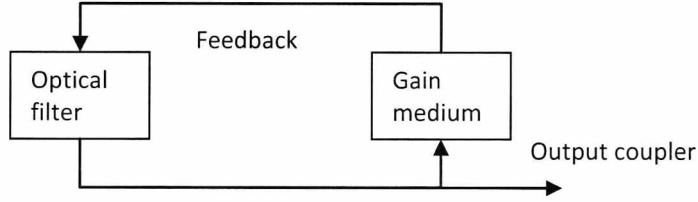


Figure 2.4. Schematic of a simple tuneable laser source. Light of narrow bandwidth is sequentially selected by an optical band-pass filter, whilst the gain medium compensates for the losses and feedback to the loop.

### 2.3.2.2 SNR of SS-OCT

A similar SNR enhancement of SS-OCT over TD-OCT was recognised [74] similarly to FD-OCT. Compared to TD-OCT, the total power illuminating the sample increases by a factor  $N_{SS}$ , which is the number of sampling point in each recorded wavelength tuning [91]. This is because the sample is only illuminated by one wavelength at a time, each wavelength component can thus have a power equal to that obtained by integrating the power of a broad bandwidth source used in TD-OCT over its full bandwidth. With assumptions of shot-noise limited detection and Gaussian shape spectrum, the SNR is similar to that given by Equation (2.55):

$$SNR_{SS} = \frac{\rho P_o}{2eB_{SS}} \frac{N_{SS}}{2} \quad (2.56)$$

where  $B_{SS}$  is the electronic bandwidth of the high speed detector. If the total wavelength tuning range is twice the FWHM spectrum of the light source, the detection bandwidth is then equal to that for TD-OCT [91] and the SNR therefore improves over that in TD-OCT by a factor of  $N_{SS}/2$ , similar to that of FD-OCT [73, 74].

## 2.4 Other OCT Developments

Apart from the three main approaches of OCT, other OCT modalities based on similar principles have also been investigated. For example, linear OCT [106] achieve the depth selection by detecting the time-domain interference signal on a linear detector array. Another time-domain method using spatial coherence of the light source as the coherence gate for depth selecting has also been

demonstrated [107] by illuminating the target with varied spatial mask. Functional techniques based on the principle of OCT have been developed for specialised biomedical imaging. Polarisation-sensitive OCT [108-110] generates maps of the depth-resolved changes in the polarisation state of light induced by anisotropic tissue properties, which allows detecting structural information and changes in birefringence tissue. Doppler OCT or Optical Doppler tomography [18-20] is developed as a phase-sensitive OCT method that combines Doppler velocimetry and OCT to provide a non-invasive localised diagnostics of particle flow velocity in scattering flowing media.

OCT technology is still being rapidly developed mainly in two directions. On one end, high speed, broadband or wide tuning range, high power light source are needed. Advances in developing fast swept sources has been continuously pushing the acquisition rate of OCT to new records. On the other end, high-speed detectors are mostly required for fast FD-OCT acquisitions. Low cost InGaAs camera sensitive to light of longer wavelength may pave the way for FD-OCT to be applied in new domains. High dynamic range detectors are also needed for OCT practices that required high sensitivity.

## **2.5 Summary**

In this chapter, the theoretical basic of OCT is discussed; mathematic treatment, optical configurations and data processing schemes were reviewed for the three OCT modalities: TD-OCT, FD-OCT and SS-OCT. FD-OCT and SS-OCT offer superior sensitivity, faster data rates and access to spectral information. TD-OCT still has an edge on penetration depth when equipped with dynamic focus; whereas in FD-OCT and SS-OCT, because the acquisition in axial direction is instantaneous, dynamic focus is difficult to be applied. TD-OCT is also useful in producing real-time *en-face* images.

# Chapter 3 Parallel-detection OCT

All OCT techniques discussed in the Chapter 2 are based on measurement of depth-dependent information (A-scan) at a point in the *en-face* plane. To acquire transverse information, lateral scanning of the probing beam or moving the target is required. These techniques are referred as point-scanning OCTs or 'flying-spot' OCTs comparing to alternative OCT methods that employ multiple detection channels to work simultaneously in parallel. These methods, known as parallel-detection OCTs, have been implemented in all three regimes; these are time-domain full-field OCT, full-field swept-source OCT and line-field Fourier-domain OCT. Two-dimensional detector arrays (2D DA) are used as sensors in all these methods; thus structures and operating principles of 2D DAs are also briefly reviewed.

## 3.1 *Parallel-detection OCT*

In order to acquire transverse information in scanning OCTs, lateral scanning of the imaging point is required by either moving the sample [1] or scanning the object beam [5, 111-113] in transverse plane, similar to that is used in scanning laser ophthalmology (SLO) [2, 114-116]. At any instant, only one point is illuminated, high density of optical energy is provided. The single mode illumination and single detector also produce a confocal benefit that rejects stray lights, which lead to high signal-to-noise-ratio. However, the electro-mechanical scanning has its limitations in scanning rate, usually up to a few tens of kHz. Because extra components are required for scanning the beam, the set-up is usually rather complex [117]. The scanning components may also be vulnerable to mechanical vibrations.

An alternative way to acquire transverse information is applying OCT acquisitions in parallel by using flood illumination and photo detector arrays. This method, known as parallel-detection OCT reduces or even eliminates the necessity of lateral scanning. Parallel OCT has been implemented in all three OCT regimes. In time domain, by using 2D flood illumination [62] of broadband light, *en-face* tomographic images can be acquired from a certain depth directly using a few phase-shifted frames that are sequentially recorded by a 2D DA. The surface of the

sensor is conjugated to the imaging plane on the target, which allows each pixels of the 2D DA to work as a single photodetector; together, a 2D en-face image is acquired without any transverse scanning of the probing beam. This method is known as Full-field OCT (FF-OCT) or wide-field OCT [118].

Adopting the principle of spectral-domain OCT, parallel swept-source OCT can be implemented based on a similar configuration to FF-OCT, with the broadband light source replaced by a frequency tunable source. A 3D OCT data volume can be obtained without any mechanical movement from a sequence of frequency-resolved frames. This is known as Full-field swept-source OCT (FF-SS-OCT) [119].

Parallel detection can also be applied in a spectrometer-based Fourier-domain OCT (FD-OCT). Using line-field illumination and together with a 2D sensor, an array of channelled spectra (CS) can be acquired from a single frame recorded by the camera, which finally leads to a B-scan OCT image. This method is known as line-field FD-OCT (LF-FD-OCT). Parallel FD-OCT can be also implemented by using demultiplexers to have a large number of FD-OCT channels working simultaneously. The imaging speed is not limited by the detector readout speed, ultra-high imaging speed up to 60,000,000 A-scans per second [120] can therefore be achieved.

Since all these parallel OCT techniques employ 2D DAs, a brief review of common 2D DAs is given below.

### **3.2 2-D Detector Array**

2D detector array is a general term that is referred to the two-dimensional solid state detector array (SSA) that provides conversion of light intensity into measurable voltage signals. These arrays are designed based on photodetection phenomenon that photons are absorbed by a solid semiconductor substrate and create electron holes which can be measured electronically. The solid semiconductor material used by SSA include silicon, Indium gallium arsenide (InGaAs), active-pixel sensor Indium, Cadmium zinc telluride (CdZnTe) and etc. In the region of visible light and near-infrared (NIR) wavelength (below one micron), two types of polysilicon-based SSAs are especially widely used: charge-coupled device (CCD) sensors and complementary metal-oxide-semiconductor (CMOS)

sensors. InGaAs sensor are more sensitive to the NIR light with wavelength between 1  $\mu\text{m}$  and 1.6  $\mu\text{m}$  than the silicon-based SSA . Other types of SSAs have been used in different wavelength region such as IR sensing, X-ray detection and Gamma ray detection, which are not compatible with OCT. Since the experiments described in this thesis are mainly in the region of 800 nm, a review of CCD and CMOS technology is given below. Both of these two type of SSAs are known as digital cameras when they are used as imaging sensors.

### 3.2.1 CCD

CCD was invented by W. Boyle and G. Smith in 1970 [121]. Since its emergence, CCD had become a granted choice for sensors in most imaging and spectroscopic instruments due to its high sensitivity, high quantum efficiency and large format. CCDs are silicon-based integrated circuits consisting of a dense matrix of photodiodes that operate by converting light energy in the form of photons into electronic charges. Electrons generated by the interaction of photons with silicon atoms are stored in a potential well and can be subsequently transferred across the chip through registers, output sense nodes. The signal is amplified by an amplifier on the chip, an analogue-to-digital-converter (ADC) converts the output voltage signal into digital unit.

### 3.2.2 Photo gate

2D CCD is a 2D array of metal-oxide-semiconductor (MOS) photo gate, e.g. a p-type silicon photogate (Figure 3.1). By applying a positive voltage  $V_{gate}$  to the photo gate electrode, the mobile positive holes in the p-type silicon migrate toward the ground electrode. This produces a void of positive charge in the left region, known as depletion region. Under the exposure to the incident photons, if a photon's energy is greater than the energy gap, the photon will be absorbed in the depletion region and an electron-hole pair (photogenerated carrier) is produced and is then stored at a storage capacitor until it is transferred out. The capacity of the storage capacitor, or well potential, depends on the substrate doping, gate voltage and the oxide thickness underneath the gate [122].

As absorbing the photons, the stored photogenerated carrier,  $V_{gate}$  drop by an amount

$$\Delta V = \frac{n_e e}{C} \quad (3.1)$$

where  $n_e$  is the number of electrons,  $e$  is the elementary charge and  $C$  is the sense node capacitor.

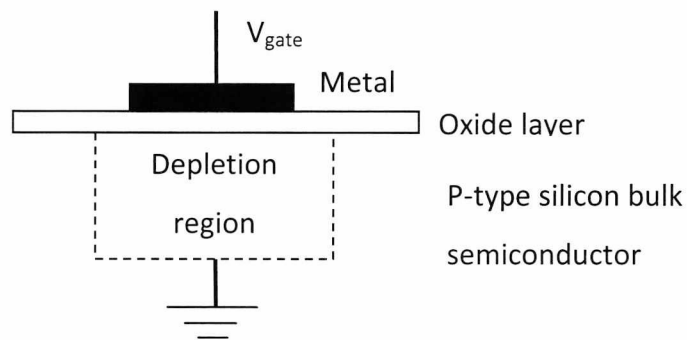


Figure 3.1. A simplified p-type silicon MOS gate of a 2D CCD array

The percentage of each pixel that is sensitive to light is defined as fill factor, which is a parameter that directly related to the sensitivity of the sensor. The ideal sensor has 100% fill factor, while in practice, it is a fraction of this value due to various of factors, including the architecture of the sensor (e.g. an interlaced sensor has a reduced fill factor), the structures for anti-blooming function, the requirements for additional control registers between active pixels and the illumination directions.

CCD arrays can be illuminated from the front side (through the gate structures) or from the back side. In a standard front-illuminated (FI) CCD, incident photons pass through the gate structures that absorb part of the incident photons and this reduces the fill factor and the sensitivity. This unwanted absorption is wavelength dependent that more short wavelength photons are absorbed than the long wavelength photons are; therefore the spectral response of FI-CCD to blue and UV light suffers from this absorption more intensively than the red or the NIR light does. For back-illumination (BI) CCD, light enters the gate from the other side to the

gate structures; therefore photons are free from the absorption; however, an 'etalon' effect (see Section 3.2.8.4) may be induced in this case.

### **3.2.3 Charge Transfer**

In CCD arrays, the photo-gates are usually overlapped to transfer the accumulated charges during readout. Each gate has a control voltage which is varied in time; therefore the voltage function is termed as clocking signal. When the integration time finishes, by manipulating the voltages on the gates, the charge will be transferred from one capacitor to the next one, and repeating this process will transfer the charge to the readout registers ultimately.

The ratio of the electrons transferred from one potential well to the next is defined as Charge transfer efficiency (CTE). In practice, CTE is always smaller than 100% due to transfer loss [123] which is the fraction of charge that is left behind during each transfer. The charge will be transferred for many (a few thousand) times before read-out, therefore CTE is important for low-noise readout especially in those array with large pixel number.

### **3.2.4 Frame Transfer**

According to the ways of charge transfer process, there are three type of CCD arrays with different architectures, include full-frame sensor, frame-transfer sensor and interline-transfer sensor.

In a standard full-frame sensor (Figure 3.3. a), a read-out register locates at the bottom of each column of the array. These registers, altogether receive a row each time and then transfers the charge packets in a serial way to the sense node. The entire horizontal serial register must be clocked out to the sense node before the next line enters the registers. Image data are transferred from the imaging region to the read-out register row by row. A 2D image is acquired after the whole 2D array of charges are transferred out of the array. Each image pixel may be composed by a number (two to four) of gates (Figure 3.2. a).

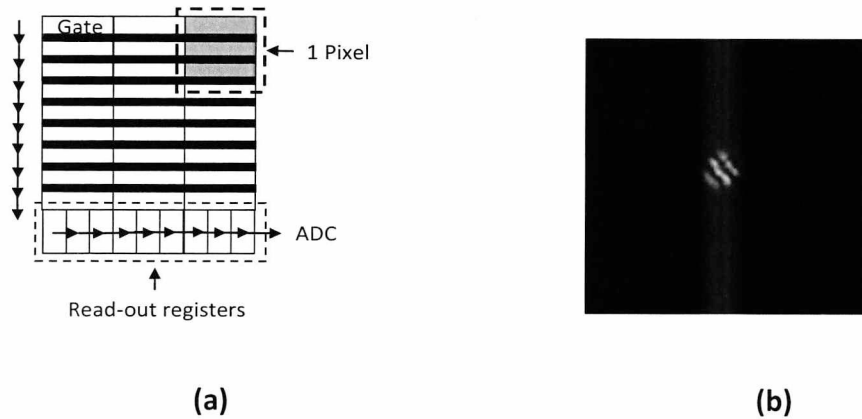


Figure 3.2. (a) A schematic of charge transfer on a full-frame CCD array; (b) an example of the 'smear' effect on the full-frame CCD that transfer the charge while open to exposure. This example image was acquired by Andor EMCCD DV887, with a exposure time of 100  $\mu$ s, much smaller than the charge transfer time, 59 ms.

With continuous illumination and absence of a shutter, only one row can be transferred to the read-out register each time and the rest of the imaging area is still exposure to the incident light. This may 'smear' the accumulated charges that are in the process of transferring. The smearing effect is normally observed in the vertical direction that the rows are transferred along, especially when preset exposure time is small compared to the read-out time, in which case, an external shutter is usually required.

A frame transfer sensor (Figure 3.3. b) separates the whole array into two regions: imaging region that is exposed to the incident light and storage region that is shielded. After integration time, the whole array of accumulated charges is transferred from the imaging region to the storage region via a number of transfers that equals to the row number of the storage region. Because the storage region is shielded, smearing effect is reduced or eliminated. A split frame transfer array (Figure 3.3. c) splits the storage section into two half, which locate at two ends of the imaging area. This configuration allows the image transferring time be halved compared to the frame transfer array.

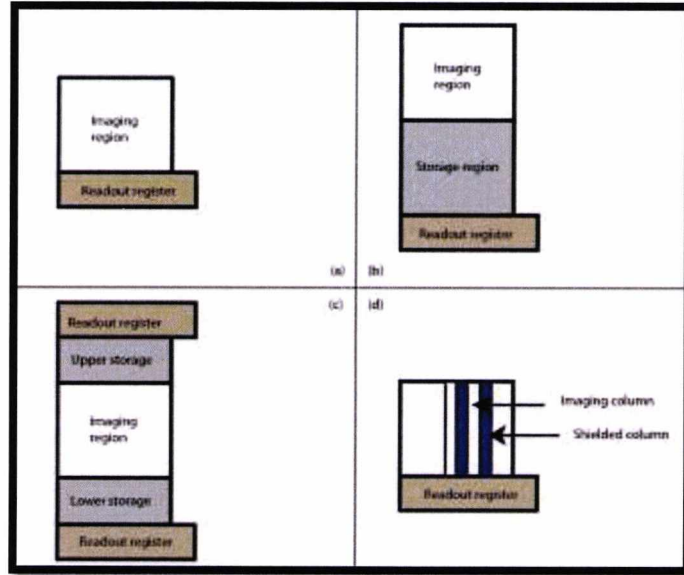


Figure 3.3. Different CCD arrays according to the transfer modes: (a) full frame, (b) frame transfer, (c) split frame transfer and (d) interline transfer.

Another type of array is interline transfer sensors, columns of photo-sensitive elements have been separated by columns of shielded registers. After the integration time, all imaging pixels (in column) transfer the accumulated charges to the adjacent storage registers by only one transfer event. Then the charges stored on the shielded registers will be simultaneously transferred to the readout registers while the charge for the next scene is being accumulated on the exposed pixels; thereby the high frame rate is possible without smearing. The shortcoming of this strategy is that the fill-factor is low because 50% of imaging cells are not sensitive to light. Micro-lens arrays are usually equipped to maximise the fill-factor in this type of sensors.

The frame rate of CCD camera is inversely related to the read-out time of a data frame. For a fixed output clock rate  $f_{clock}$ , the time to read a 2D image is directly dependent on the array dimensions. Given a detector array of  $m \times n$  pixels, ignoring additional pixel read, the frame read-out period is given by

$$t_{read} \approx \frac{mn}{f_{clock}} \quad (3.2)$$

and the frame rate of the array  $f_{frame}$  is therefore given by

$$f_{frame} = \frac{1}{t_{INT} + t_{read}} \quad (3.3)$$

where  $t_{INT}$  is the integration time of each frame. The maximum frame rate is thus  $1/t_{read}$ .

### 3.2.5 Signals of the CCD Array

The signal of the CCD array depends on many parameters including quantum efficiency (QE), charge well capacity,  $n_{well}$ , charge transfer efficiency (CTE), readout noise,  $N_{read}$ , response linearisation, pixel nonuniformity and etc. The process of signal generation is illustrated in Figure 3.4

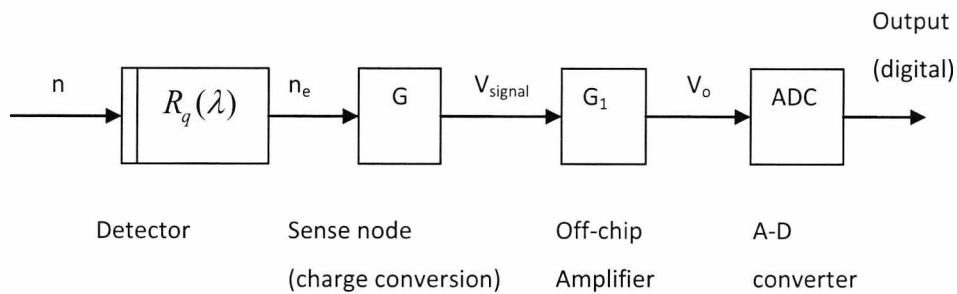


Figure 3.4. Schematic of signal generation on a standard CCD array.

Spectral response or quantum efficiency (QE) of the CCD array is a spectral function of the ratio of the incident photons that are absorbed and produce electron-hole pair to the whole incident photons. Absorption Coefficient in silicon is wavelength dependent. Long wavelength photons are absorbed deeper in the substrate than those with short wavelength. If the wavelength is too long so that the photon energy (inversely dependent on wavelength) is less than the band gap energy, the photon may pass through the substrate with no absorption. As a silicon based SSA, CCD is generally transparent for light beyond  $1.1 \mu\text{m}$  [122]. QE is also related to the gate voltage, the fill factor and the thickness of the depletion region. Techniques that improve the QE of CCD include increasing the thickness of the sensor substrate and using back-illumination sensor; however, increasing the substrate thickness will lead to increasing dark noise.

Transferred charges is converted to a voltage signal,  $V_{signal}$  at the output of the sense node.  $V_{signal}$  is proportional to the total number of electrons in the charge packet,  $n_e$ , including the photoelectron  $n_{pe}$  and dark electron  $n_{dark}$ . The photoelectron number  $n_{pe}$  is given by

$$n_{pe} = \frac{A_D}{q} \int_{\lambda_1}^{\lambda_2} \frac{E_e(\lambda)}{\pi} R_e(\lambda) t_{INT} d\lambda \quad (3.4)$$

where  $A_D$  is the detector area,  $E_e(\lambda)$  is the detector incidence and  $R_e(\lambda)$  is the spectral response. Assuming a perfect detector that produces zero dark photon, the array output voltage after the source follow amplifier can be expressed by

$$V_{signal} = \frac{G}{C} A_D \int_{\lambda_1}^{\lambda_2} \frac{E_e(\lambda)}{\pi} R_e(\lambda) t_{INT} d\lambda \quad (3.5)$$

The maximum output signal value or the saturation equivalent exposure (SEE) is obtained when the charge potential well is full, which is expressed by

$$V_{max} = G \frac{Gq}{C} (n_{well} - n_{dark}) \quad (3.6)$$

After digitisation, the output of the digital camera is the number of digital number,  $DN$  which is given by

$$DN = \text{int} \left[ V_{camera} \frac{2^N}{V_{max}} \right] \quad (3.7)$$

where 'int' denotes nearest integer function,  $V_{camera}$  is the output of the camera, including  $V_{signal}$  and the equivalent noise voltage  $V_{noise}$ . For an 8-bit CCD detector array, DN ranges from zero to 255.

### 3.2.6 Noises and Sensitivity

The sensitivity of CCD is defined as the lowest detectable light level above the noise floor, quantitatively, the input signal that produces a signal-to-noise-ratio (SNR) of one. This exposure is known as noise equivalent exposure (NEE). Three main sources of the noises of the CCD include photon noise, dark noise and readout noise. These noise sources contribute to the total noises by the 'root of sum of square' law as

$$\langle N_{total} \rangle = \sqrt{\langle N_{photon}^2 \rangle + \langle N_{read}^2 \rangle + \langle N_{dark}^2 \rangle} \quad (3.8)$$

where  $\langle N_i^2 \rangle$ , denotes the noise variance for source  $i$  and  $\langle N_i \rangle = \sqrt{\langle N_i^2 \rangle}$  is the noise equivalent electron RMS. Photon noise,  $N_{photon}$ , is a measure of the intensity variation in the signal itself. The detection limit is determined by the read noise and dark current noise.

#### 3.2.6.1 Photon Noise

Photon noise is inherent to the 'particle' nature of photons, which is a result of the variation in number of received photons for each pixel in a certain time. Photon noise is evaluated which can be expressed according to Poisson statistics by

$$\langle N_{photon} \rangle = \sqrt{n_{pe}} = \sqrt{\eta n} \quad (3.9)$$

where  $\eta$  is the quantum efficiency and  $n$  is the total number of the incident photons.

#### 3.2.6.2 Dark Current Noise

Dark current is the electric current that flows through photosensitive devices even when there is no incident photon. Physically, dark current is due to the random generation of electrons and holes within the depletion region that are swept by the high electric field. Dark current generates in many parts of the sensor including the neutral bulk material, the depletion regions and the surface states [122].

In practice, the dark current photon is constant under certain conditions, e.g. temperature, clocking speed, and it contributes to the output by a value called dark current noise  $N_{dark}$  that is described by Poisson statistics as the square root of the number of thermally generated dark current electrons,  $n_{dark}$  :

$$\begin{aligned} N_{dark} &= \sqrt{n_{dark}} \\ n_{dark} &= \frac{J_D A_D t_{INT}}{q} \end{aligned} \quad (3.10)$$

where  $J_D$  is the dark current density and

$$J_D \propto T^2 \exp\left(-\frac{E_g - E_T}{kT}\right) \quad (3.11)$$

where  $E_g$  and  $E_T$  are detector band gap and impurity band gap respectively;  $k$  is the Boltzmann's constant and  $T$  is the absolute temperature. Formula (3.10) and (3.11) show that the extent of dark noise contribution is dependent upon exposure time and the working temperature. Dark noise can be suppressed by lowering the working temperature. Cooling is selected according to the integration time and the acceptable noise level. For applications that low light are available, i.e. astrophotography, fluorescent microscopy, the dark current is the main source of noises and thus deep cooling are required to reduce the dark signal and to permit long integration time. However; cooling may reduce the QE [124] of the sensor. Modern CCD designs have greatly diminished dark noise to a few electrons per pixel even at room temperature [125]. For a CCD array with large number of pixels, binning can also be used to reduce dark noise.

The generation of dark current noise may vary spatially over the sensor area that lead to a fixed noise pattern (FPN), also known as scene noise, pixel noise and pixel nonuniformity. It is a result of differences in detector size, doping density, foreign matter trapped during fabrication and even thickness of coating. FPN does not change significantly from frame to frame, but vary from pixel to pixel. FPN can

be removed by performing a dark frame subtraction of an estimated mean FPN from the acquisitions.

### 3.2.6.3 Readout Noise

Readout noise is a combination of various on-chip noises that originate from the process of transferring and amplifying the photoelectrons and ultimately converting to voltages. This includes reset noise, 1/f noise, quantisation noise, amplifier noise and ADC noise [126]. Read-out noise, can be considered the CCD detection limit when fast frame rate is applied because of two reasons: first, short exposures combined with low dark current make the dark current noise contribution negligible; second, fast readout rate requires high amplifier bandwidth and results in high read-out noise. For long exposure or slow readout acquisition, dark noise become more prominent than the read noise, however, this is rare in interferometry applications, such as OCT imaging, because long exposure time will easily washout the interferogram which is very sensitive to object motions or system vibration.

### 3.2.6.4 SNR

The signal-to-noise ratio (SNR) of a CCD camera can be interpreted by

$$SNR = \frac{n_{pe}}{\sqrt{\langle N_{photon}^2 \rangle + \langle N_{dark}^2 \rangle + \langle N_{read}^2 \rangle}} \quad (3.12)$$

When the incident light power is high, the photon noise dominates ( $\langle N_{photon}^2 \rangle \gg \langle N_{dark}^2 \rangle + \langle N_{read}^2 \rangle$ ), the dark noise and read out noise can be neglected, the SNR can be approximated by

$$SNR \approx \frac{n_{pe}}{\sqrt{\langle N_{photon}^2 \rangle}} = \sqrt{n_{pe}} \quad (3.13)$$

If the incident optical power is very low that  $(\langle N_{photon}^2 \rangle \ll \langle N_{dark}^2 \rangle + \langle N_{read}^2 \rangle)$ , the dark noise and read out noise are dominant, with the expression of  $n_{pe}$  in Equation (3.4), the SNR can be approximated by

$$SNR \approx \frac{n_{pe}}{\sqrt{N_{dark}^2 + N_{read}^2}} = \frac{A_D \int_{\lambda_1}^{\lambda_2} E_e(\lambda) R_e(\lambda) t_{INT} d\lambda}{q\pi \sqrt{N_{dark}^2 + N_{read}^2}} \quad (3.14)$$

Eq. (3.14) indicates that with given dark noise and read-out noise, the SNR in low light condition depends on the QE and the pixel area of the sensor, which are the two main factors affecting the sensitivity of the CCD.

### 3.2.7 Dynamic Range

Dynamic range (DR) is the ratio between the largest non-saturating input, which can be approximated by SEE, to the smallest detectable signal, NEE:

$$DR = \frac{V_{max}}{V_{noise}} = \frac{SEE}{NEE} = \frac{N_{well} - n_{dark}}{\langle n_{total} \rangle} \approx \sqrt{N_{well}} \quad (3.15)$$

or in  $20\log$  decibels:

$$DR = 20 \log\left(\frac{SEE}{NEE}\right) \approx 10 \log(N_{well}) \quad (3.16)$$

Eq. (3.15) indicates that DR can be enlarged by using larger full well depth or reducing the noise.

### 3.2.8 Specialised CCD Techniques

Some specialised CCD technologies improve the CCD sensitivity significantly to enable single-photon detection. Developments have also been made in DR enhancement, anti-blooming and other aspects.

#### 3.2.8.1 ICCD

Intensified CCD (ICCD) is a variant of CCD that increases the sensitivity by optically connecting an image intensifier to the CCD sensor. The image intensifier is composed by a photocathode, a micro-channel plate (MCP) and a phosphor screen. The incident photons firstly fall onto the photocathode and generate photoelectrons that are accelerated towards the MCP and hit the phosphor screen with a large speed. The screen convert the multiplied electrons back to photons that are then guided to the CCD via fibers or a lens. The image intensifier has an inherently shutter function. When the voltage between the photocathode and the MCP is reversed, the emitted photoelectrons will not accelerated towards the MCP but return to the photocathode; thereby no electrons are emitted by the MCP and no incident photons to the CCD sensor. This gating function performs like a shutter, which is a main advantage of ICCD techniques. The shutter time can be as short as a few tens of picoseconds. The intensifying effect makes ICCD highly sensitive that can be used to detect single photon. ICCD does not depend on the chip temperature, because the signal are intensified before readout, therefore cooling is not essential.

### **3.2.8.2 EMCCD**

Electron-multiplying CCD (EMCCD) [127] is a special designed CCD that insert gain registers between the shift (read-out) registers and the output amplifier to amplify the signal before the read out process. EMCCD enables the photon electrons multiplication by a series of internal gain registers before the electrons arrive at the output amplifier, thereby the signal are multiplied with the same readout noise. The on-chip charge multiplication was achieved by inserting an array of EM gain registers between the shift registers and the readout sense node; the EM gain registers employ an impact ionization phenomenon [128] in silicon material to multiply the photon electrons. Although the gain at each stage of the gain register is small, after a series of amplification, great value of overall gain can be applied to the signal. With minimised dark current noise via deep cooling, high sensitivity can be obtained by EMCCD.

The limit of EMCCD sensitivity is not the readout noise but the spurious charge clock induced charge (CIC), which a result of impact ionisation [129] during charge transfers between the Si/SiO<sub>2</sub> interface. All CCDs have CIC (image area CIC) whose

value depends on transfer rate, clock amplitude and clock timing; while in EMCCD, the electron-multiplying gain registers introduce extra electron-multiplying CIC (EMCIC). EMCIC can be minimised by low clock swing and high clock speed, in particular minimising the time a clock is held high. CIC is also temperature dependent. The higher temperature gives a smaller CIC. Under deep cooling (required by limiting dark noise), CIC sets the limit of EMCCD's sensitivity.

EMCCD should be employed only when low light is present. When large signal charge is multiplied, as it transfer through the EM registers, a small amount of the charge could be left behind in each transfer and leads to a low level horizontal streaking from any bright features in the image. This is referred as charge transfer efficiency [127]. CTE may limit the effective dynamic range of EMCCD acquisitions.

High EM gain is also subject to statistical fluctuations that appear as noise of  $\sqrt{n}$  electrons because the gain register is stochastic and the exact gain value is unknown. Together with shot noise, the combination of this excess noise factor results in a noise of  $\sqrt{2n}$ , i.e. the uncertainty reduce the SNR by a ratio of a half. If the incoming light has sufficient power allowing both normal CCD operation and EMCCD acquisition, using EM gain will produce increasing noise.

### **3.2.8.3 Blooming Effect**

Blooming occurs when the incident intensity is higher than the saturation level of the potential well at some pixels, in which case extra photoelectrons overflow to adjacent potential wells, creating an area of saturation that may not have received saturation equivalent input. The blooming may happened in a pattern dependent on the structure of the detector, for example, some manufacturer allow vertical shifting of the charge but create potential barriers to reduce flow into horizontal pixels, which lead to a characteristic vertical streak. Blooming reduces the DR of CCD because it is problematic to acquire data from a weak signal with the presence of a strong signal in other part of the image. Some sensors have anti-blooming structures such as lateral overflow drains [130] that allows draining away extra photon-electrons. However this will lead to a reduction of the fill-factors and the QE. Anti-blooming may also affect the linearity of the sensor's response.

Alternatively, accumulation mode acquisition can be used to avoid blooming by performing successive scans of short exposures (below saturation level) and summing the scans to achieve effectively an exposure which is longer than that is allowed. The dynamic range is thereby increased. However, this normally requires fast frame rate if the object or the imaging system is subject to movement.

#### **3.2.8.4 Etalons Effect**

Back-illuminated CCD is sometimes required for high quantum efficiency. However, there is a issue related to this type of sensor known as etalon-effect, especially for spectrometer applications. Back-illuminated CCD's are thin silicon devices (~10-20 microns thick) that become semi-transparent in the NIR. Reflections between the nearly parallel front and back surfaces of these devices cause them to act as etalons. This etalon-like behaviour increases the effective path length in the silicon and thus the QE, but also leads to unwanted interference fringes when used in spectrometers due to multi-reflection induced interference. The extent of modulation (contrast of fringes) can be significant (> 20%) and the spectral spacing of fringes, typically 5 nm, is troublesome for many spectrometric applications at NIR wavelength. Thickening the silicon substrate may reduce or avoid the etalon effect.

#### **3.2.9 CMOS Devices**

Besides CCD, another type of DA that is widely used as imaging sensor is CMOS array. Modern CMOS array is consisted of an integrated circuit containing an array of pixel sensors; each pixel is composed by a photodiode and a number of transistors. The pn-junction photodiode is reversed biased by a certain voltage prior to the exposure; during the integration time, the charge on the photodiode are drain away slowing with the rate of draining directly proportional to the intensity of the incident light. The transistors, for example in a 4T cell of an active pixel sensor (APS) [131], include sense node, transfer gates, reset gates, selection gates and source follower readout transistor. The accumulated photo-generated carriers are transferred to the sense node where the carriers are converted to a voltage signal. Since the pixels are not accumulating charges, they cannot 'overflow' and affect adjacent pixels; therefore CMOS is immune to blooming effect.

CMOS sensors employ different procedures of charges read-out according to the pixel types and structures. Generally each row of the pixel array is clocked and a switching transistor or charge amplifier for that row of pixels is activated; charge on each pixel is transferred to the column output where a read-out register transfers the column to an A-D converter that produces the output continuously. The read-out process can be operated on only a part of the sensor, which can increase the frame rate. CMOS is free from the problems related to the CTE in CCD, because the charge-to-voltage conversion takes place in each pixel and the image is transferred out of the array row by row rather than pixel-to-pixel in CCD.

The dynamic processing of CMOS allows high levels of integration, i.e. implementing timing logic, exposure control, A-D conversion and imaging compression on chip can be integrated on a single-chip integrated circuit. Because a single bias voltage and clock level are used, CMOS usually consumes less power than CCD of similar size does as CCD requires more than one voltage bias of higher values. The CMOS array is generally faster than a CCD counterpart with similar pixel number, because imaging functions are applied to pixels simultaneously and the accumulated charges can be transferred in parallel. These advanced features make CMOS a better option in portable devices than CCD.

CMOS has a smaller fill factor and lower QE than CCD does, because part of the components in each CMOS pixel is not photon-sensitive. Micro-lens arrays can be employed to increase the fill factor. Another disadvantage is that because each pixel has an output amplifier whose offset and gain may vary, non-uniformity over the array may be presented and contribute to pattern noise. Details of different CMOS structures and read-out process can be found at [131].

Both CCD and CMOS sensors have been used in various parallel OCT techniques. According to the principles and imaging regimes that scanning OCTs are based on, three types of parallel OCTs are introduced below.

### **3.3 Full-field OCT**

Time-domain Full-field OCT (FF-OCT) is a parallel OCT method that allows producing *en-face* OCT images without transversal scanning of the object beam on the target.

The appearance of FF-OCT was inspired by a low coherence reflectometry technique, known as 'coherence radar' [132, 133].

### 3.3.1 Coherence Radar

Coherence radar is a parallel detection technique based on low coherence interferometry (LCI). It allows obtaining 3D topography of sample surface with high axial resolution but without transverse scanning of object beam. The first parallel detection method using a collimated beam to illuminate the object in a 2D field of view (FOV) was reported in 1992 by Dreselet et. al.[132]. A typical coherence radar set-up is illustrated in Figure 3.5. A broadband light source is used to project a collimated beam to the entrance of a Michelson interferometer. The object is flood-illuminated in a small 2D area by the object beam. Reflection on each point in this area is collected by a lens, L1 and focused by a second lens L2 onto a pixel of a 2D DA. Light from the reference beam goes through a similar path. Interference will be generated at the surface of the detector array, if the lights from both interferometric arms coincide within the distance of a coherence length of the broadband light source. By aligning the detector surface on the imaging plane of the target, at a certain moment, the interference occurs only at the pixels that receive the reflection from the object that travels a similar optical length as the reference beam does. The interference signal recorded by the 2D DA is modulated by a carrier that has the frequency  $f$  of the light. A demodulation process is employed, usually using phase-shifting interferometry (PSI) methods (described in the following section). Eventually an *en-face* image that contains a contour at the height defined by the axial position of the reference mirror is obtained. By axially displacing the object or the reference mirror continuously, 3D topography can be obtained. Coherence radar records 3D topography with a high accuracy defined by the short coherence length. Compared to a scanning LCI method, coherence radar eliminates the need for transverse scanning that may slow the imaging process and give rise to motion artefacts due to mechanical jitter.

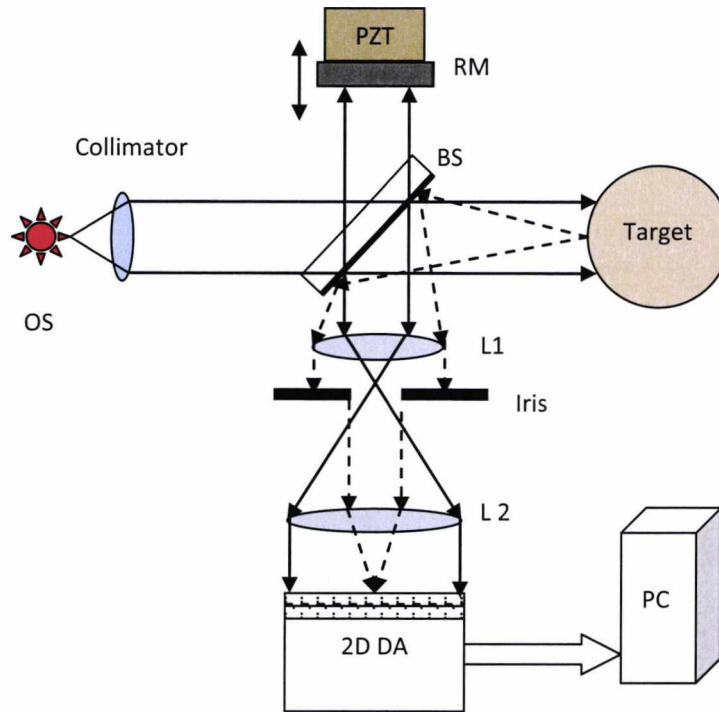


Figure 3.5. Schematics of a 'coherence radar' set-up. OS: broadband optical source; L1, L2, achromat doublets; BS: beam-splitter; RM: reference mirror; PZT: Piezo-electric actuator; DA, 2D detector array.

The idea was later implemented with Zernike polynomials analysis [134] and numerical filters [135] to improve the performance in terms of noise, optimal fringe evaluation and data-processing speed. Based on the same principle, a Nomarski microscope was combined with a differential polarization interferometer [133], which has demonstrated a precision of  $\sim 8$  pm rms. The author suggested using this technique on tomographic imaging of transparent or scattering samples, which later became known as Full-field OCT.

### 3.3.2 Full-field OCT

With a scattering medium used as the target, broadband NIR light can penetrate the medium for a depth of a few hundred microns and produce tomographic images based on the principle of OCT. Because of the full field of view, it is referred as Full-field OCT (FF-OCT) or Wide-field OCT [51, 62, 118, 136, 137]. FF-OCT uses a similar set-up to that the coherence radar does. Because back-scattering light is much weaker than the reflection light, high NA microscope objective lenses are usually used in the interferometers, which are referred as Linnik interferometers [51, 138].

The front focal plane of the objective lens is carefully placed to coincide with the coherence plane ( $OPD=0$ ). The backscattered light from each point in the field of view (FOV) is collected by the objective and is transferred onto the surface of the 2D DA. By placing the coherence plane and the imaging plane inside the target within the penetration depth, interference is generated and recorded by a 2D camera. Ideally (ignoring cross-talk), each pixel only receives the light from a single point in the imaging plane on the object; with all the pixels working in parallel simultaneously, the interference signal from all the points on an *en-face* plane ( $OPD=0$ ) can be recorded. To remove the DC signal due to incoherence light, fringes demodulation algorithm such as PSI method is performed onto several phase-shift images. Ultimately, an *en-face* OCT image is obtained directly from an axial position defined by the reference path length. By elevating the sample, the imaging plane translated axially, a 3D tomographic volume can be thereby obtained by repeating the imaging process in continuous layers. Like coherence radar, FF-OCT eliminates the need for transverse scanning of the beams that is essential for scanning OCTs.

Beaurepaire et. al. [62] reported the first FF-OCT system based on a Linnik polarisation microscope in 1998. An infrared LED was used to apply synchronous illumination with a 2D CCD camera. A diffraction limited transverse resolution of 2  $\mu\text{m}$  was obtained. In 2000, Bourquin et al. [139] developed a line-field OCT based on the same principle. The linear CMOS detector array allows heterodyne detection in parallel. The optical signals were detected at Doppler frequencies of 10 kHz up to 1 MHz, with a sensitivity of 65.7 dB. Later the same technique was extended to using a 'smart pixel' (CMOS) 2D DA [140].

By employing high NA optics, high transverse resolution up to conventional optical microscope resolution can be obtained by FF-OCT, which is sometimes referred as optical coherence microscopy (OCM). Ultra-high-resolution FF-OCT based on a Linnik interference microscope with high NA optics was reported by Dubois et. al. [138]. Transverse cross-section (*en-face*, or XY) images can be obtained in real time with a transverse resolution of  $\sim 0.5 \mu\text{m}$ .

The axial resolution can be controlled by shortening the coherence length of the light source. FF-OCT allows using partial coherent sources or incoherence optical

sources that emit light of large spectral bandwidth. Vabre et al. [118] reported a FF-OCT with high depth resolution ( $1.2\mu\text{m}$ ) which used a powerful halogen thermal lamp as the light source. Laude et. al. [136] used a 3W light bulb which presents 300 nm FWHM bandwidth in FF-OCT to produce high spatial resolution of  $1.1\mu\text{m}$  in free space ( $0.7\mu\text{m}$  in glass). A white-light FF-OCM allowing ultra-high-resolution sub-cellular-level en-face OCT imaging of biomedical tissues was presented by Dubois et. al. [137].  $1.8\mu\text{m} \times 0.9\mu\text{m}$  (transverse  $\times$  axial) spatial resolution has been achieved due to the extremely short coherence length of a tungsten halogen lamp.

As a parallel method, FF-OCT allow high data rate, a volumetric pixel rates of  $2.5 \times 10^6$  pixel per second has been reported by Ducros et. al. [141]. Video-rate three-dimensional OCT pictures have been acquired at a sensitivity of 76 dB using the 2D CMOS DA [142]. With InGaAs camera, FF-OCT has also been implemented at the wavelength range of  $0.9\mu\text{m} - 1.4\mu\text{m}$  [143, 144]. Dual band FF-OCT [145] allows the imaging using two broad band at both 800nm and 1200 nm which enlarge the penetration depth. With a 3D volume of FF-OCT images in continuous depths, the Power spectrum [113] and the phase retardation [146] of the sample can be obtained by Fourier relationship.

FF-OCT offers fast tissue imaging at the cellular level [147] which is comparable to histology results. Isotropic resolution of  $1\mu\text{m}$  has been achieved in *in-vivo* ocular imaging of rat eyes [148] using incoherence light source and high NA microscope objectives. It has also been used in *in-vivo* human retinal imaging [149]. Because transverse data are required simultaneously, high stability of the phase relationship across parallel channels is obtained in the *en-face* plane. FF-OCT operates at the en-face plane, which makes it compatible to be combined with other established optical imaging techniques, e.g. fluorescence microscopy [150], to perform multiple-modality imaging.

### 3.3.3 Phase Shifting Interferometry

Signal recorded by the 2D DAs in both coherence radar and FF-OCT is the integration of light intensity over a period of time; therefore no AC signal is available for demodulation. The recorded image from the DA is the fringe

interferogram that is modulated by the optical frequency, to obtain the interference signal, demodulation of the fringe data is needed. This is usually carried out by performing phase-shifting interferometry (PSI) method [151-154]. PSI is originally an optical phase measurement technique that was used to calculate the phase from interferograms [155-157]. It has been widely used in non-contact surface metrology due to its high measurement accuracy and rapid measurement. It is tolerant to low contrast fringes and easy to use with 2D detector array.

### **3.3.3.1 Phase-Modulation**

A typical PSI set-up uses a mechanical component to introduce discrete or continuous temporal phase shifts between the two interferometric beams. Many parts have been used including moving mirrors [137], photoelastic polarization modulators [62], diffraction gratings [115], acousto-optic Bragg cells [116] and half-wave plates [158, 159]. After a sequence of interferogram with shifted phases is recorded, by using a computer to analyse the intensity variations as a function of the phase shift, the original wavefront phase can be recovered.

With continuous phase modulation, images are integrated over a fraction of the period of the phase modulation, so that in each period of modulation,  $n$  phase shifted frames are acquired and are used to calculate the interference signal. This is known as  $n$ -bucket PSI method. Two-buckets PSI [160] and four-bucket PSI [138, 161] methods have been demonstrated for FF-OCT. An alternative way is to apply ' $n$ ' ( $n = 2, 3, 4$  [62] or  $5$  [162]) discrete phase shifts at certain phase values in the interferometer and the phase-shifted frames are recorded at each discrete phase steps. This is referred as  $n$ -step PSI in the following of the thesis.

Phase shifting can be performed instantaneously on a single camera by using spatially separated phase-stepped images with polarisation control [163] or holographic element with phase mask [114]. Heterodyne detection techniques based on the frequency-synchronous detection have been performed [164-166] to obtain FF-OCT images with a pair of cameras that acquiring images simultaneously with a  $\pi/2$  phase difference. Instantaneous phase shifting provides better phase

stability and is more tolerant to object movements, though the complexities of the optical set-up and the synchronisation are generally more demanding.

### 3.3.3.2 PSI Calculations

After acquiring the  $n$  images with phase shifts, the interference signal is to be extracted from the variance of the images. Assuming monochromatic illumination, the photo flux received on the camera at pixel  $(x, y)$  is given by

$$I(x, y) = \bar{I}(x, y) + A(x, y) \cos[\phi(x, y)], \quad (3.17)$$

where  $\bar{I}(x, y)$  denotes the average photo flux or the DC term,  $A$  is the amplitude of the interference fringes, and  $\phi$  is the optical phase.

### 3.3.3.3 Four-bucket PSI

Four-bucket PSI acquires images that are integrated during continuous sinusoidal phase modulation; therefore allow long exposure time on the camera. Given the phase modulation that has its amplitude  $\phi$  and its own phase  $\theta$  with a period  $T = 2\pi / \omega$  is introduced, the photon flux varies with time, expressed by

$$n(x, y, t) = \bar{n}(x, y) + A(x, y) \cos[\phi(x, y) + \phi \sin(\omega t + \theta)] \quad (3.18)$$

where  $\bar{n}(x, y)$  is the average photo flux at  $(x, y)$ . To simplify the derivation, the dependence on the location  $(x, y)$  is discarded and Eq. (3.18) can be rewritten as a sum of Fourier components by using the Bessel functions of the first kind  $J_n$  as

$$\begin{aligned} n(t) = & \bar{n} + AJ_0(\phi) \cos \phi \quad \dots \\ & + 2A \cos \phi \sum_{n=1}^{+\infty} J_{2n}(\phi) \cos[2n(\omega t + \theta)] \quad \dots \\ & - 2A \sin \phi \sum_{n=1}^{+\infty} J_{2n+1}(\phi) \sin[2(n+1)(\omega t + \theta)]. \end{aligned} \quad (3.19)$$

The integration is performed over each quarter period of the phase modulation, i.e. the integration time  $t_{INT} = T/4$ , four images are recorded in each period as the integration of the time-varying signal, given by

$$\begin{aligned}
I_j &= \int_{(j-1)\frac{T}{4}}^{j\frac{T}{4}} I(t) dt, \quad j = 1, 2, 3, 4 \\
&= \frac{T}{4} \left[ \bar{I} + AJ_0(\varphi) \cos \phi \right] + \\
&\quad \frac{T}{\pi} A \cos \phi \sum_{n=1}^{+\infty} \frac{J_{2n}(\varphi)}{2n} \left\{ \sin(jn\pi + 2n\theta) - \sin[(j-1)n\pi + 2n\theta] \right\} \\
&\quad - \frac{T}{\pi} A \sin \phi \sum_{n=1}^{+\infty} \frac{J_{2n+1}(\varphi)}{2n+1} \left\{ \begin{array}{l} \cos \left[ \frac{(2n+1)(j-1)}{2} \pi + (2n+1)\theta \right] \dots \\ -\cos \left[ \frac{(2n+1)j}{2} \pi + (2n+1)\theta \right] \end{array} \right\}
\end{aligned} \tag{3.20}$$

Linear combinations of the four frames give

$$\begin{aligned}
\sum_s &= -I_1 + I_2 + I_3 - I_4 = \frac{4T}{\pi} \Gamma_s A \sin \phi \\
\sum_c &= -I_1 + I_2 - I_3 + I_4 = \frac{4T}{\pi} \Gamma_c A \cos \phi
\end{aligned} \tag{3.21}$$

where

$$\begin{aligned}
\Gamma_s &= \sum_{n=0}^{+\infty} (-1)^n \frac{J_{2n+1}(\varphi)}{2n+1} \sin[(2n+1)\theta], \\
\Gamma_c &= \sum_{n=0}^{+\infty} \frac{J_{4n+2}(\varphi)}{2n+1} \sin[2(2n+1)\theta].
\end{aligned} \tag{3.22}$$

If  $\Gamma_c = \Gamma_s = \Gamma$ , the *en-face* images  $I_{4bucket}$  and phase map,  $\phi$  can be obtained by

$$\begin{aligned}
I_{4bucket} &= \sqrt{\sum_s^2 + \sum_c^2} = \frac{4T}{\pi} \Gamma \\
\tan \phi &= \frac{\sum_s}{\sum_c}
\end{aligned} \tag{3.23}$$

If  $\Gamma_c \neq \Gamma_s$ ,  $I_{4bucket}$  include a term that depends on  $\phi$ , which may present the residual fringe pattern in the calculated interference images.

### 3.3.3.4 Two-step PSI

Two-step methods [144, 148] employ minimal number of phase shifts to retrieve the interference signal. By introduce oscillating the reference mirror between two positions ( $\phi_1 = 0$ , and  $\phi_2 = \pi$  separated by a distance of a quarter of the average wavelength in a double pass configuration), the photo flux on each pixel (x,y) of the camera frame can be given by

$$\begin{aligned} I_1(x, y) &= \bar{I}(x, y) - \frac{I_0}{2} 2\sqrt{R_{obj}(x, y)R_{ref}} \cos \phi(x, y) \\ I_2(x, y) &= \bar{I}(x, y) + \frac{I_0}{2} 2\sqrt{R_{obj}(x, y)R_{ref}} \cos \phi(x, y) \end{aligned} \quad (3.24)$$

where  $I_0$  and  $\phi$  are the incident photon flux and the phase at the interferometer entrance;  $\bar{I}(x, y)$  is the average intensity of the photo flux received by the pixel;  $R_{obj}(x, y)$  and  $R_{ref}$  are the reflectivity of the object and the reference at (x,y). Assuming that the exposure time is very short and phase value are not changing during the exposure of the camera, the interference signal can therefore be retrieved by

$$R_{obj}(x, y) = \frac{[I_1(x, y) - I_2(x, y)]^2}{I_0^2 R_{ref} \cos^2 \phi(x, y)} t_{INT}^2 \quad (3.25)$$

The numerator of Eq.(3.25) can be used to represent the interference image of FF-OCT, because  $I_0$ ,  $R_{ref}$  and  $t_{INT}$  are all constant and do not change the visualisation of the imaging. The  $\cos \phi(x, y)$  is dropped, therefore parasite fringes will be present in the images.

### 3.3.3.5 3-step PSI and 4-step PSI

Phase stepping method, or n-step PSI method are selected when long integration time is not needed or cannot be obtained. Given the phase modulation has the

amplitude of  $\varphi = 2\pi$ , in each phase modulating period,  $n$  images are obtained, the image value at pixel  $(x, y)$  of recorded fringe images for the  $j^{\text{th}}$  phase step,  $I_j(x, y)$  can be expressed in general as

$$I_j(x, y) = \bar{I}(x, y) + A(x, y) \cos\left[\phi(x, y) + \frac{2j}{N}\pi\right], \quad (3.26)$$

$$\begin{cases} j = 0, 1, \text{ and } 2 & \text{when } N = 3 \\ j = 0, 1, 2 \text{ and } 3 & \text{when } N = 4 \end{cases}$$

where phase shift  $\varphi_j = 0, 2\pi/3$  and  $4\pi/3$  for 3-step PSI; whereas  $\varphi_j = 0, \pi/2, \pi$  and  $3\pi/2$  for 4-step PSI. The coherence image can then be computed using the formula:

$$I_{3sPSI}(x, y) = \sqrt{(I_0 - I_1)^2 + (I_1 - I_2)^2 + (I_2 - I_0)^2} \propto A(x, y) \quad (3.27)$$

$$I_{4sPSI}(x, y) = \sqrt{(I_0 - I_2)^2 + (I_1 - I_3)^2} \propto A(x, y) \quad (3.28)$$

respectively.

### 3.3.3.6 Phase Error

Assuming shot noise is the predominate noise source, the RMS phase error  $\sqrt{\langle \varepsilon^2 \rangle}$  can be estimated [161] by

$$\sqrt{\langle \varepsilon^2 \rangle} \approx \frac{1}{\gamma \sqrt{N}} \quad (3.29)$$

where  $\gamma = A/\bar{I}$  is the fringe contrast.

In practice, error sources include incorrect phase shifting, stray reflection, quantisation error, frequency stability and the non-linearity of the detector response. The phase error can be reduced by simply using frame-averaging. More complicated algorithm are available including using Carré Equation [151], Hariharan five measurement [154] and an error-compensating algorithm that used data-sampling windows [167]. Although the PSI is subject to various systematic [154, 168-171] and random error [167, 172-174], the main interest of FF-OCT is the envelope

intensity of the interference fringes rather than the phase value, therefore simple PSI methods, such as 3-step PSI or 4-step PSI, are usually sufficient to retrieve the OCT signal.

### 3.3.4 Resolutions

Low NA lenses are usually used to provide large depth of view in scanning OCTs. As a result, the lateral resolution is limited. Since FF-OCT is a combination of LCI and microscopy, both the coherence length of the light source and the NA of the optics affect the axial resolution. For a microscope set-up, with assumption of a Gaussian beam, the lateral resolution is given by

$$dx = \frac{2\lambda}{\pi} \frac{1}{NA} \quad (3.30)$$

where  $\lambda$  is the wavelength and  $NA = n \sin \theta$  is the numerical aperture of the objective lens and  $\theta$  is the divergence of the beam. The depth of focus is twice the Rayleigh range, given by

$$dz = \frac{\pi}{2\lambda} dx^2 = \frac{2\lambda}{\pi} \frac{1}{NA^2} \quad (3.31)$$

From Eq. (3.30) and Eq. (3.31), we can see that the lateral resolution and the depth of field of the microscope are both inversely related to the NA of the optics. High NA produces high spatial resolution, in both transversal and axial planes. With the coherence plane and the focal plane of the objective superposed, FF-OCT's transverse resolution is similar to that of the microscope that it uses. However, when high NA optics is used, the axial resolution of FF-OCT will be governed by not only the coherence length of the optical source (see Eq. (2.23)) but also the depth of focus of the objective.

Cares should be taken to compensate the departure of focal plane from the coherence plane when the sample is moving axially; otherwise, the contrast of the interferometric signal and the transversal resolution decay quickly [138]. Figure 3.6 illustrates this phenomenon. As the sample is elevating in the axial direction to

acquire deeper *en-face* FF-OCT images, the coherence plan and the focal plane move away from each other because the optical path in air is replaced by an optical path in the medium which has a refractive index,  $n$ , usually larger than 1 as in air. With a small depth of focus, the axial PSF of FF-OCT measurement degraded quickly when coherence plane is moving away from the focal plane because most of the light returning from the focus region does not contribute to the interference signal; whereas the light returning from the coherence gate is out-of-focus. The interference signal, in this occasion, is mainly due to multi-scattering light from the depths that are out of focus [138], thus the lateral resolution will also drop. To correct this focus departure, focus readjustment is required by elevating the objective for a distance  $\Delta Z$ , given by

$$\Delta Z = \left( \frac{n^2 - 1}{n^2} \right) e \quad (3.32)$$

where  $e$  is the elevating distance of the sample.

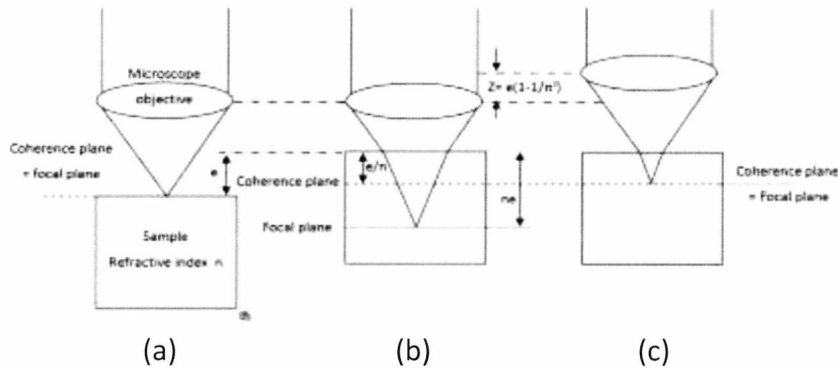


Figure 3.6. The focal plane and the coherence plane in an interferometer: (a) the focal plane and coherence plane coincide at the surface of the object; (b) the object is moving upward for a distance  $e$ , therefore the focal plane move down for a distance  $(n-1)e$  and the coherence plane move up for  $(1-1/n)e$ ; (c) the focal plane match the coherence plane again by elevating the objective for a distance  $Z=e(1-1/n^2)$

### 3.3.5 Sensitivity

The minimal detectable reflectivity can be written as [136, 175]:

$$R_{\min} = \frac{(R_{inc} + R_{ref})^2}{4MR_{ref}} \left( \frac{1}{n_{well}} + \frac{\langle N_{total}^2 \rangle}{n_{well}^2} \right) \quad (3.33)$$

where  $R_{inc}$  denotes the portion of the incoherent light in the total incident light, which is a limiting factor of the sensitivity;  $M$  is the image accumulation number for averaging. Calculating the derivative of Eq. (3.33) shows that the minimal value of  $R_{min}$  is achieved when  $R_{ref} = R_{inc}$ . The above equation also indicates that the sensitivity of FF-OCT can be improved by increasing  $n_{well}$  of the 2D DA if the optical power is not limited by the source, or by increasing the imaging accumulation if the sample is stable during the image acquisitions.

### 3.3.6 Crosstalk

A main challenge of FF-OCT is the high cross-talk across parallel channels. Ideally, each pixel on the DA should only receive the light from a point in the sample that is defined by the imaging paths. With the reference light, interference signal recorded by a single pixel should only related to that measuring point; and all parallel OCT channels operate independently from the others. However, in practice, the 2D FOV is flood illuminated and the 2D DA is fully opened at the same time. When a scattering medium is under interrogation, the multi-scattering light from a imaging point can go to any detector channel; each pixel receives multi-scattering light and stray light from many other points than the one it is supposed to record.

The interference signal recorded by a single pixel in the 2D DA not only include the OCT signal of interests, but also include unwanted interference of two sources: cross-correlation interference between the stray light from other points in the object and the reference beam; and auto-correlation (self-interference) between different points in the object as long as the optical length variations are within a coherence length. Both cross-correlation and self-interference will contribute to seemingly random variations in images, known as speckles. The scale of the speckle pattern causes a reduction in the effective resolution since thin boundaries become obscured [1]. Speckle is therefore an obstacle in observing specific features that are close to the diffraction limits. Details about multi-scattering events in FF-OCT in both theoretical modelling and experimental investigation are described in [176, 177].

The crosstalk may produce a strong speckle noise in the FF-OCT images, especially for those FF-OCT systems that use spatially coherent illumination [46,

178, 179]. This is in contrast to the situation in scanning OCT, where the point illumination and the confocal aperture of the single mode source limit the crosstalk. However, in FF-OCT, cross-talks can be reduced by using partial spatially coherent light sources or incoherence light sources [118, 180]. Use of partially spatially coherent light was recognised to improve the lateral resolution by decreasing speckle in non-OCT imaging [181, 182]. Because of the low spatial coherence, the light propagates in each channel have little or no coherence relationship with the adjacent channels; therefore the self-interference cross-talk can be reduce. However, using spatially incoherent illumination from an extended light source may suffer from reduced SNR due to the low photon number per spatial mode [180]. Alternative methods that use multi-mode fibre [183] and fibre bundles [184] to create multi-mode illumination in FF-OCT have been reported. Reduction of Speckle is also possible by averaging *en-face* slices in axial direction [185].

### **3.4 Full-field Swept-source OCT**

FF-OCT can be performed in spectral domain, known as Full-field Swept-source OCT (FF-SS-OCT). It is a relative new form of parallel detection OCT technique that combines the optical set-up of FF-OCT and the principle of swept-source OCT. By employing a wavelength tuneable light source, 2D interferograms are recorded by a 2D DA as a function of varying wavelength. After collecting a stack of spectrum-encoded interferogram images, the channelled spectrum, which relates to the depth information via a Fourier transform, is retrieved on each pixel of the DA. By performing inverse-Fourier transform on each retrieved spectrum, the depth-related A-scan signal can be obtained at each point in the transverse plane. Swept-source OCT allows acquiring depth information without axial scanning; 2D full-field acquisitions are performed in parallel to acquire transversal information simultaneously. With the combination, a whole 3D volume is acquired without any mechanical movement of the set-up.

The transverse resolution of the FF-SS-OCT is determined by the optics. By using high NA microscopy optics, ultrahigh spatial resolution,  $\sim 3 \mu\text{m}$  axial and  $\sim 4 \mu\text{m}$  transverse [112] has been demonstrated. The microscope-based FF-SS-OCT set-up

can be easily adapted to perform conventional microscopy imaging and time-domain FF-OCT, which allows multi-modal imaging. However, the optimal transverse resolution cannot be achieved at all depths in the depth range of SS-OCT due to the shallow depth of view induced by the high NA optics. Since the 3D volume is obtained without moving the optical system or the sample, with high NA optics, the lateral resolution degrades quickly as the depth is away from the focus plane. Methods that solving Inverse scattering problems [186] have been proposed to correct this problem in FF-SS-OCT [187].

With the acquired volume data, phase information can be calculated from the A-scan lines and a 3D phase volume [188] can be thereby obtained. Because phase map in all *en-face* planes are obtained simultaneously, FF-SS-OCT present high phase stability. Phase measurements of targets including finger print [189, 190], integrated circuits[182], composite materials[166] and onion skins [188] using FF-SS-OCT have been evaluated recently.

The most critical limitation of FF-SS-OCT is the sensitivity to object movement due to relatively large acquisition time for acquiring stacks of images. Sample motion during the wavelength sweeping may lead to image blurring and additional artefacts. The effect of axial motion on the measured spectra is similar to the effect of non-balanced group velocity dispersion (GVD) in the interferometer. It causes the optical path lengths in the sample arm to vary with the wave number. An axial motion cross-correlation of sub-bandwidth reconstructions (CCSBR) algorithm [191] is capable of detecting and correcting the artefacts induced by axial motion in FF-SS-OCT as well as the GVD mismatch. By cross-correlating images that were reconstructed from a limited spectral range of the interference signal, a phase error is determined which is used to correct the spectral modulation prior to the calculation of the A-scans. However, this algorithm can only deal with the axial movement, which is usually combined with lateral movement and rotation in real life measurements. Although advanced A-scan based [38] and 3D based transverse motion compensation methods [82] are possible, fast camera is still mostly preferred to enhance FF-SS-OCT imaging quality.

A comparison between the signal noise ratio of FF-SS-OCT and time domain FF-OCT is given in the next chapter, including both mathematic treatments and experiments results.

### **3.5 Line-field FD-OCT**

Parallel detection can be combined with FD-OCT to allow simultaneous B-scan OCT imaging. Standard FD-OCT employs a spectrometer to acquire a channelled spectrum that is encoded by depth-dependent interference signal. Parallel FD-OCT uses a 2D detector array to acquire an array of channelled spectrum from the object that is illuminated in a line field. This method is called Line-field Fourier-domain-OCT (LF-FD-OCT) [192]. The schematic of the optical setup is illustrated in Figure 3.7, top.

The principle of LF-FD-OCT was firstly demonstrated by Zuluaga et. al. [111]. With the object illuminated in full-field (2D), by simply using a vertical slit at the entrance of the spectrometer that equipped with a 2D camera; a column of spectra were recorded in parallel that allow producing a B-scan OCT image along the direction of the slit. The idea was later improved by Yasuno [181, 192-194] and Leitgeb [183] by employing a cylindrical lens to separate the functions of the optical paths in two planes: in horizontal direction, the optical path is similar to a standard scanning FD-OCT. Broadband light with interference signal enter the spectrometer and present a channelled spectrum (CS) on a row of the 2D DA; in vertical direction, the optical path is similar to FF-OCT except for the fact that the target is illuminated in a line field. Each point on this line-field is imaged onto a row of the 2D DA; altogether a column of CS is obtained from the line field. A B-scan OCT image is thereby obtained from a single shot of the 2D DA. The schematic of the optical path in vertical and horizontal planes is illustrated in Figure 3.7.

With sufficiently fast 2D DA, LF-FD-OCT may present a improvement of A-scan rate compared with conventional scanning FD-OCT. In-vivo imaging of human anterior chamber [183] and retina [193] have been reported. Like other parallel OCT techniques, parallel channels of LF-FD-OCT are acquired simultaneously, which presents good phase stability in the line field; therefore it has been used in

quantitative phase mapping [195]. In Chapter 5, a LF-FD-OCT setup is demonstrated to test the possibility of integrating commercial photographic equipments, such as flash light and imaging sensors, in LF-FD-OCT.

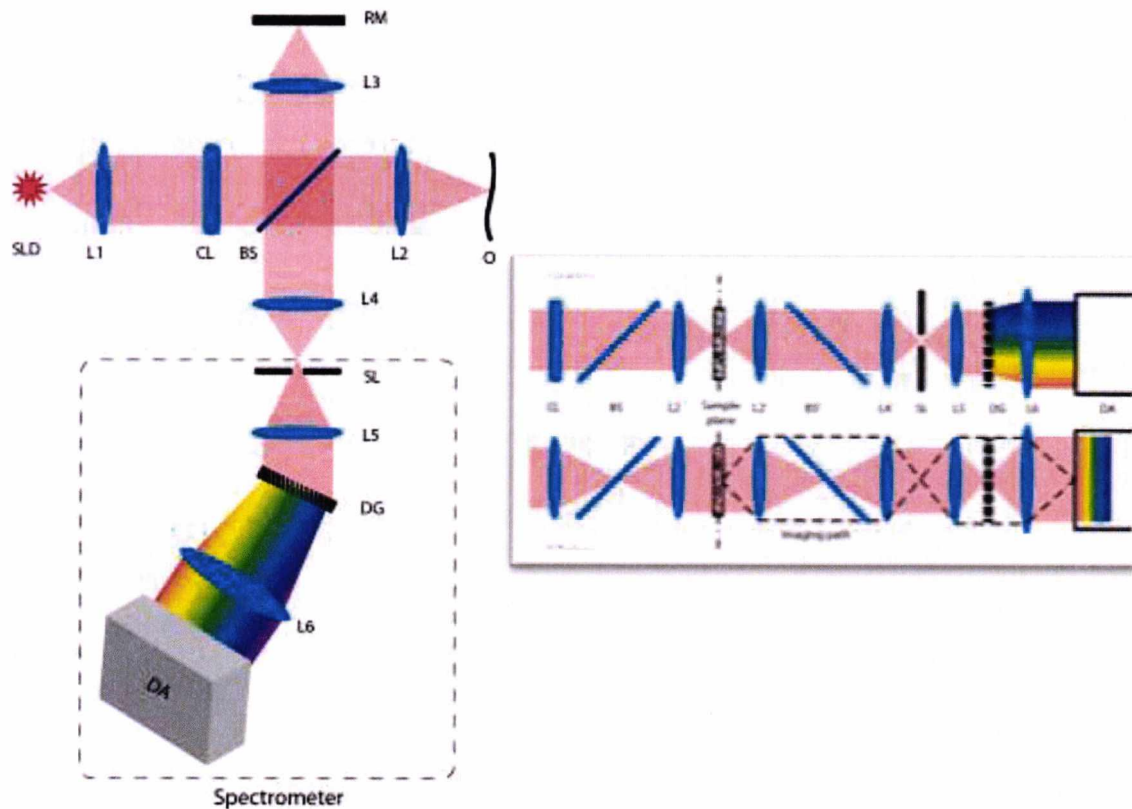


Figure 3.7. Left: Schematics of LF-FD-OCT set-up: SLD, broadband light source; L1, collimating lens; CL, cylindrical lens; BS, beam splitter; L1,L2,L3,L4,L5,L6, achromatic doublets; RM, reference mirror; OBJ, object; SL, vertical slit; DG, transmission diffraction grating; DA, 2D detector array; right: optical paths in horizontal plane (X-Z) and vertical plane (Y-Z) respectively.

### 3.6 Summary

The main advantage of the parallel OCT over the scanning OCT is that parallel detection reduces or avoids the necessity of transverse scanning of the object beam, thereby enables simultaneous acquisitions at multiple positions on the *en-face* plane. Parallel detection OCTs allow using incoherent or partial coherent light sources, which may improve the axial resolution and leave less speckles. This may also allow high illuminating power at reduced costs. Given fast camera is used, parallel detection OCT may produce a higher imaging rate than a standard scanning

OCT. Parallel OCTs allow phase-stable cross-sectional acquisitions [119, 195-198] due to its high phase stability across scanning-free parallel channels.

However a few limitations of this method should be considered. The main limitation of parallel OCT using 2D DA is the lack of AC techniques, such as analogue signal mixing. As a result, the SNR of parallel OCT suffers from various  $1/f$  noises; the lack of narrow-band heterodyne demodulation techniques make the parallel OCT vulnerable to bandwidth-dependent noises, such as shot noise and excess noise. In FF-OCT, lock-in detection is usually performed by synchronising stroboscopic illumination [62] with the detector array to reduce extra noise sources.

2D DAs have a data depth bit up to 16 bits. Because the digitisation has to be carried out inside the camera unit before any signal processing, such as background subtraction, can be applied, the dynamic range of the 2D DA is limited because it is shared by DC terms and the AC terms. This is in contrast to the scanning OCT that use a single photo detector where analogue signal processing can be done before ADC and thus the dynamic range can be used on the AC term only. The sensitivity, SNR and penetration depth of parallel detection using DA are still inferior to that of scanning OCTs. This is not only because the light energy from the optical source is spread onto a line or 2D area instead of a point, but also because parallel OCTs suffer from cross-talk across parallel channels.

FF-OCT images are not produced instantaneously with a single acquisition. In order to perform PSI, several frames are usually required before the interference signal can be retrieved. Simultaneous phase shifting is possible to produce instantaneous imaging. Simultaneous FF-OCT [199] has been reported recording multiple phase-shifted frames on a single camera, which presented great phase shift stability. Similarly, Akiba et. al. [165] used two CCDs to produce images of different polarisation simultaneously, but these methods reduce the size of the *en-face* images and increase the complexity of the setup.

When high NA optics is used, dynamic focusing is required in FF-OCT systems [144] which may slow the imaging rate further. For FF-SS-OCT, the acquisition time is especially long because stacks of images are to be required before the numeric processing.

# Chapter 4 Full-field OCT

Full-field OCT (FF-OCT) is a parallel detection OCT method that employs full-field illumination to acquire transversal information. In this chapter, experiments based on FF-OCT configurations for different imaging and measurement purposes are described. A coherence radar set-up was initially built to allow topography measurement of object surfaces. The set-up was later modified to perform FF-OCT acquisitions to investigate tomographic structures inside biological mediums. By employing microscopic objectives with high numeric aperture (NA), a Linnik interferometer based FF-OCT was assembled to allow imaging of a biologic medium with high lateral resolutions. At the end of the chapter, a FF-OCT setup that employs swept source acquisition is described. Operating the same full-field set-up in both time-domain and spectral domain, a comparison of signal-to-noise ratio between time-domain and spectral domain OCT methods is performed.

## 4.1 Time-domain Full-field Low Coherence Interferometry

A coherence radar was assembled based on a Michelson interferometer to evaluate the performance of topography measurement of object surfaces. Based on this set-up, a novel method of curvature measurement using multiple-delay lines is demonstrated.

### 4.1.1 Coherence Radar

The coherence radar set-up is illustrated in Figure 4.1. A super luminescent diode (SLD), SLD-381, Superlum, is used as the light source that has a near-Gaussian spectrum with central wavelength at 850 nm and a FWHM wavelength bandwidth of  $\sim 20$  nm. Such a spectrum shape determines a coherence gate of  $\sim 16\mu\text{m}$  in air. The NIR light emitted from the SLD was collimated by a x5 microscope objective, L1. The beam that has a diameter of  $\sim 12$  mm is split 50:50 by an unpolarised plate beam splitter, BS1 (See Figure 4.1), which is sufficiently thick (8 mm) to avoid the second reflection from the second surface of BS1. The reflective surface of the beam splitter is oriented towards the reference path; therefore a second identical

beam splitter is inserted into the reference path to compensate for the dispersion mismatch. Half of the field are reflected by the BS and projected into the reference path and reach a mirror, RM, through a pair of lenses L2 and L3. The transmitted beam through BS follows the object path, travels through a pair of conjugated lenses, L4 and L5, and ultimately flood-illuminates the object, OBJ, in a 2D area. Both RM and OBJ are mounted on translation stages, TSR and TSO respectively, which produce axial displacements. Two neutral density filters, NDF1 and NDF2 in both interferometer arms were inserted to balance the light intensity in two paths. The reference mirror is attached to a Piezo-electric actuator, PZT that performs phase modulation. The light reflected by the OBJ and RM, follow return paths in the two arms and recombine in the measurement path. The recombined beams are delivered by a telescope, composed by lenses L6 and L7, to a 2D detector array, a CCD camera. The plane of the camera is carefully aligned to be conjugated with the front focal plane of lens L5, in other words, the camera images the front plane of L5, similar to a conventional microscope, though a background image is contributed by the RM. By movement, RM can reach the position where the optical path difference (OPD) becomes zero. The interference signal is retrieved by phase-shifting interferometry.

The CCD camera is an electron-multiplying CCD (EM-CCD), DV887 AC-UV from Andor technology. There are 255 EM registers, which can provide a signal amplification of 60 dB at the maximum. The number of EM registers can be selected or totally switched off according to the light level of the scene. The CCD chip is front-illuminated and a 14 bit AD converter (ADC) allows a maximum frame rate of 16 fps at full resolution. The main parameters of the camera are listed in Table 4.1.

For the phase modulation, the PZT and the CCD are synchronised via a function generator and a delay generator, to secure precise phase-shifted frames. Two programs were created in Visual C++ and LabVIEW are used to control the acquisition and to perform the calculation in real-time.

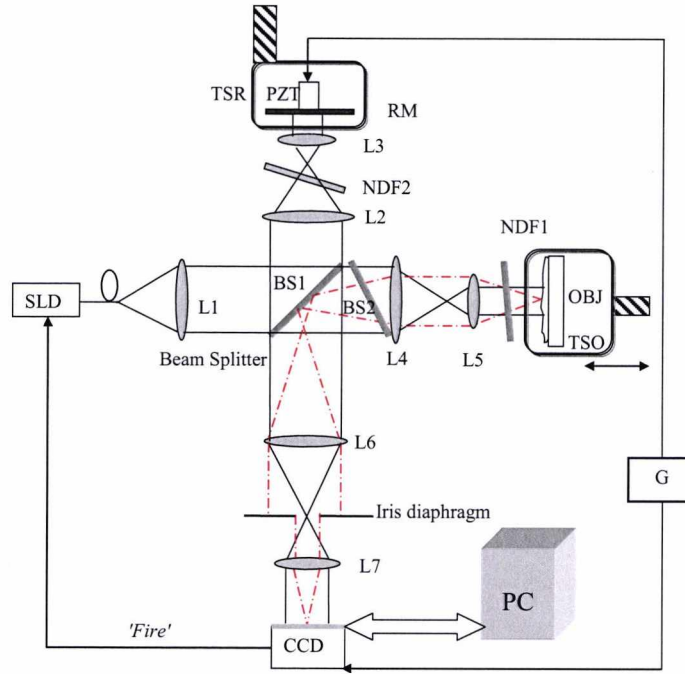


Figure 4.1. Schematic diagram of a coherence radar set-up. SLD: super luminescent diode; RM: Reference mirror; L1: x5 microscope objective; L2, L3, L4, L5, L6, L7: doublet lens of focal length 100 mm, 75 mm, 100 mm, 75 mm, 100 mm and 150 mm respectively; NDF1, NDF2, neutral density filters; BS1, BS2, identical beam splitters, 8 mm thick; PZT: Piezo-electric actuator; OBJ, target object; TSO and TSR, one-dimensional translation stages; ID: iris Diaphragm; CCD, 2D digital camera, Andor DV887 AC-UV; G, function generators and synchronising circuits.

Table 4.1 Main parameters of the EMCCD Camera, Andor DV887AC-UV.

Active Pixels	512 X 512	AD resolution	14 bits
Pixel Size	16 $\mu\text{m}^2$	Readout Speed	200 ns per pixel
Image Area	8.2 X 8.2 $\text{mm}^2$	Max Readout Rate	5 MHz
Pixel well depth	192,132 $e^-/\text{pixel}$	CCD Sensitivity	13.5 electrons per AD count
CCD type	Front illumination	Single Pixel Electrons	35.52
Coating	UV	Base Level	718

#### 4.1.1.1 Stroboscopic Illumination

The timing control of the camera acquisition in PSI is critical not only for the phase error which may lead to artefacts (residual fringe pattern) in the resulting image, but also for the image quality of each individual frame. Because the camera does not have a shutter, the sensor is open even after the exposure time while the charge is transferred from the detector array, which leads to 'smearing' effects (see

Chapter 3). A stroboscopic illumination is therefore required to reduce the 'smearing'. A pulse of duration equal to that of the pre-set exposure time, 'fire', is sent from the camera synchronisation output port to the driver of the SLD, which toggles the source on and off during exposure and read-out respectively. The stroboscopic illumination also reduces the 'washout' of the interference, due to movement of the object.

#### 4.1.2 Phase Stepping Interferometry

Three-bucket PSI and four-bucket PSI methods are adopted to resolve the interferometric signal. By modulating the reference path length using the PZT, a variation of the OPD is introduced; 3 or 4 phase-shifted frames are recorded and used in the calculation as a bundle. The displacement of the mirror is for fractions of the central wavelength,  $\lambda_o = 850 \text{ nm}$ ). To perform this, the PZT was calibrated by moving integer number of  $\lambda_o$  while varying the amplitude of the external voltage applied to the PZT driver. The axial displacement can be recorded by counting the fringe shifts in the image. The average voltage variation for each wavelength shifts gives the value  $V_{pv}$  which was used to produce the axial displacement of  $\lambda_o$ . For  $\lambda_o = 850 \text{ nm}$ ,  $V_{pv} = 1.2 \text{ V}$  is used. 3 or 4 acquisitions were performed within each modulation period, T. Each acquisition takes place with a phase shift of  $2\pi / N$  (N= 3 or 4) to the previous one. The camera is triggered by a period signal that consists of N pulse in each T, which is synchronised with the PZT modulation signal. The light source is switched on and off by a fire signal from the CCD to perform a stroboscopic illumination. The calculation of PSI is carried out by the PC program during the gap of image data transfers. In this way, the system frame rate is dictated by the frequency of phase modulation. The timing sequence of 4-step PSI is illustrated in Figure 4.2 as an example. The green bars only indicate the exposure time of the CCD, and their heights are not in phase value.

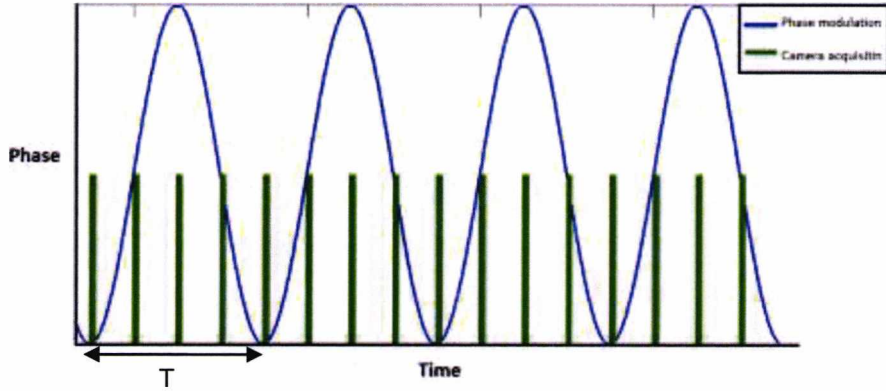


Figure 4.2. The sequence of timing for 4-step PSI phase modulation and the camera acquisitions. Four acquisitions take place within one period  $T$  of the phase modulation to the reference mirror. The start of the four acquisitions are synchronised at the phase value  $0, \pi/2, \pi$  and  $3\pi/2$  respectively. The pulses are not phase modulation amplitude but only for the purpose of indicating the timing of acquisitions,

The algorithms of 3-step PSI and 4-step PSIs were explained in the Chapter 3, therefore are not repeated here. Coherence images are calculated in real-time after each set of  $N$  acquisitions. Two coherence images acquired with 3-steps and 4-steps from a mirror are shown comparatively in Figure 4.3. Some residual fringes are observed in these images due to phase errors. The images show that the residual fringes in the 4-bucket PSI image is in smaller contrast than those in the 3-bucket PSI image.

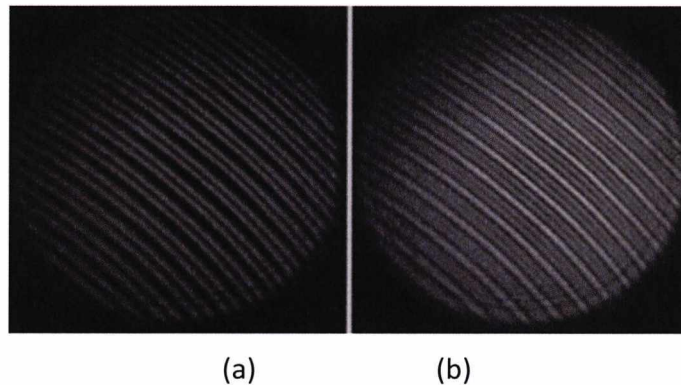


Figure 4.3. Interference images obtained with (a) 3- step PSI and (b) 4-step PSI algorithm.

### 4.1.3 Topography Measurements

The axial point-spread-function (PSF) is measured first by axially displacing an object mirror in small steps ( $5 \mu\text{m}$ ) along a large depth range ( $60 \mu\text{m}$ ) around zero OPD. The measured PSF and the fitted curve are shown in Figure 4.4 (a). The FWHM of

the fitted curve indicates a FWHM depth resolution of  $16\ \mu\text{m}$ . The pixel size of the camera is  $16 \times 16\ \mu\text{m}^2$  and the optical system has a x2 magnification; thus the best transverse resolution is  $16\ \mu\text{m}$ . Using a USAF test chart as the object, the result image in Figure 4.4 (b) shows that the bars of Group 5, Element 5 can be resolved, which leads to a transverse resolution of about  $10\ \mu\text{m}$ .

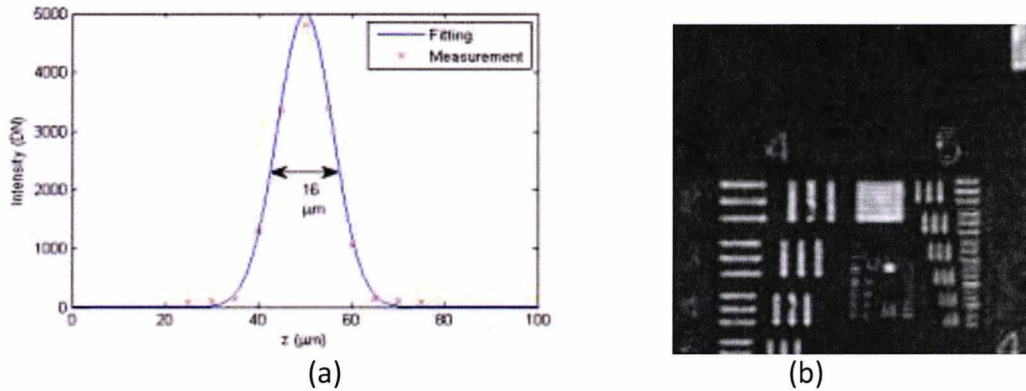


Figure 4.4. (a) Axial LCI PSF, fitting curve(blue) gives a FWHM =  $16\ \mu\text{m}$ ; (b) Image of USAF 1951 test chart.

Topography images have been acquired from a coin (5 pence sterling) in real-time at a frame rate of 3 fps. The direct image (a) and coherence images (b-e) are displayed in Figure 4.5. In the direct image from the camera (a), high background value is present to the reference beam. The coherence images (b)-(e) were obtained after the object coin was moved axially to three different depth positions with an increment of  $30\ \mu\text{m}$ . As the images show, contours at varied heights on the coin surface are selected by the coherence gate of  $16\ \mu\text{m}$  and the light from other height is rejected. (c) and (d) show different parts of the letter 'P' and the dots on the coins can be distinguished between different height. A zoomed coherence image is shown in (e) where the base of the coin is at  $\text{OPD} = 0$ . The scratches on the coin surface are observed. Because of the reflectivity of the metal surface is high, thus some residual fringes are visible in both (b) and (e) over the area that is flat and smooth.

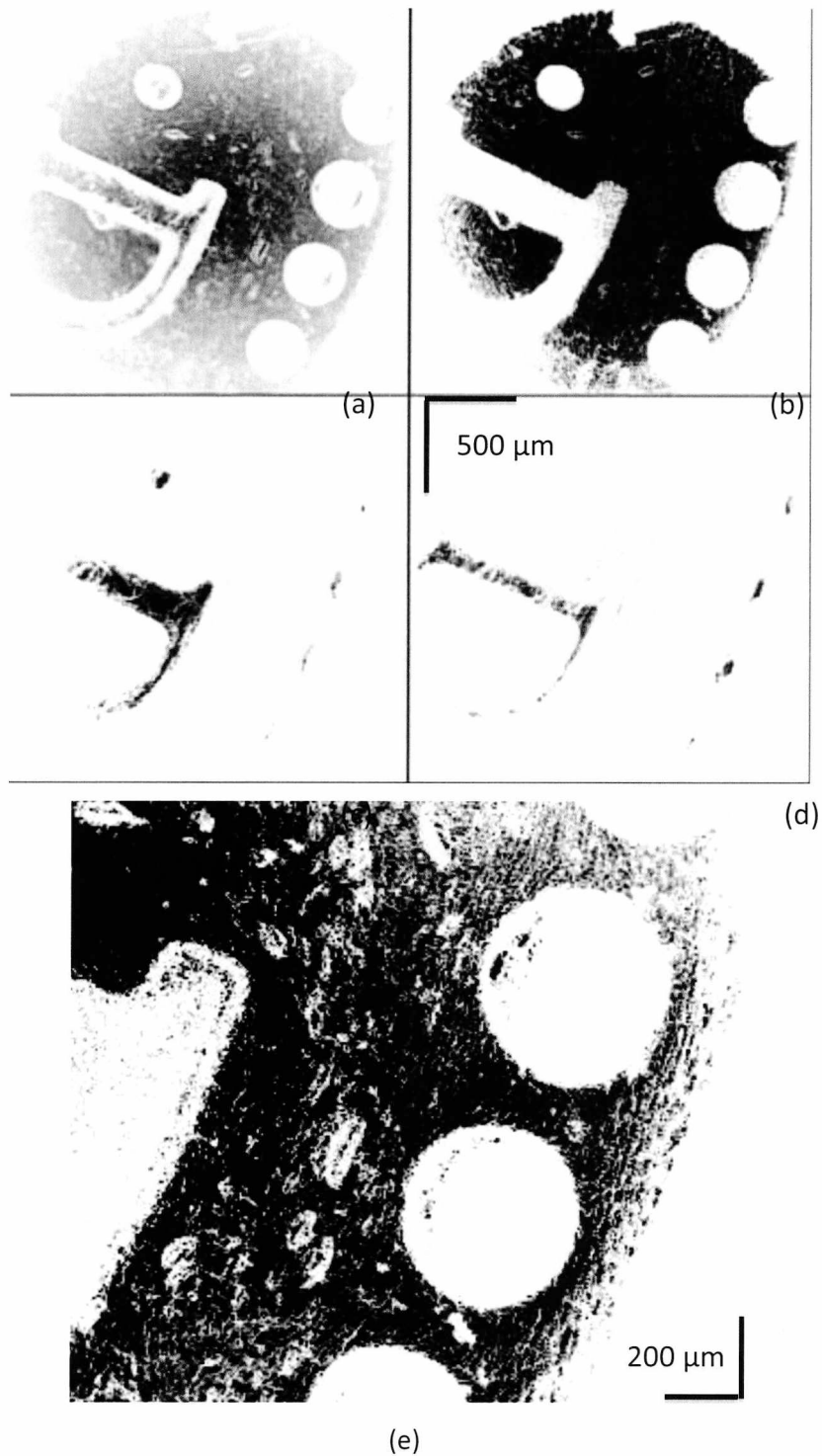


Figure 4.5. (a): A direct image of a coin of 5 pence sterling; (b), (c) and (d): coherence images of the same location on the coin at three different axial positions separated by  $30 \mu\text{m}$ ; (e): zoomed coherence image of the base of the coin.

#### 4.1.4 Multiple Delay Line FF-OCT

Coherence radar has been demonstrated capable of producing *en-face* depth-resolved topography images from a reflective surface. Based on this, a novel

technique to measure the curvature of a spherical single layer object is also demonstrated. The method consists in introducing multiple optical delays into the interferometer using a multiple optical delay elements (MDE). This leads to a compound *en-face* OCT image containing the *en-face* OCT images generated for each delay. Each *en-face* OCT image contains contours of the object surface corresponding to an OPD value determined by a given delay in the MDE. In this section, the optimal combination of the coherence radar set-up with MDEs is presented. Two possibilities are discussed and evaluated, using: MDE in the reference path and in the optical source path. This technique presents the potential to allow fast and precise curvature measurements of human cornea.

The curvature of a reflective object (such as human cornea) is traditionally measured by acquiring a number of either B-Scan [200] or C-Scan (*en-face*) OCT images [201]. With B-Scans, several images at different known polar angles are needed to infer the curvature of the object surface, while with C-Scans, a stack of images from different known depths are required. However, both methods require acquisition of multiple 2D images, which is time-consuming. Therefore this method is not compatible with *in vivo* imaging of moving targets, such as human eyes that are subject to involuntary motions. The method presented is a modification of the configuration presented by Plesea [202, 203]. This configuration was based on a flying spot configuration, using an *en-face* scanning LCI set-up, equipped with multiple known delay lines into the reference arm of the interferometer. Each delay created a contour in the C-Scan image, and together they formed a group of contours separated spatially. The axial position of any pixel in the transversal section of the cornea image can ultimately be inferred from the known delays in the MDE and the measured radius of curvature of the object. The variation of the wavefront in the reference beam due to an inserted optical delay element of two steps and the corresponding spatial variation of the coherence gate in the object due to the two optical delays and the resulting depth-encoded topographic image are illustrated in Figure 4.6.

The 2D transversal scanning was slow, 500 Hz line rate, therefore the imaging process allowed manifestation of motion artefacts due to mechanical jitter. Each *en-*

face acquisition required a 0.5 second, which is relatively long in comparison with the eye movement. Since coherence radar enables acquisition of depth-resolved topographic images without transverse scanning, imaging time can be less than 0.5 s.

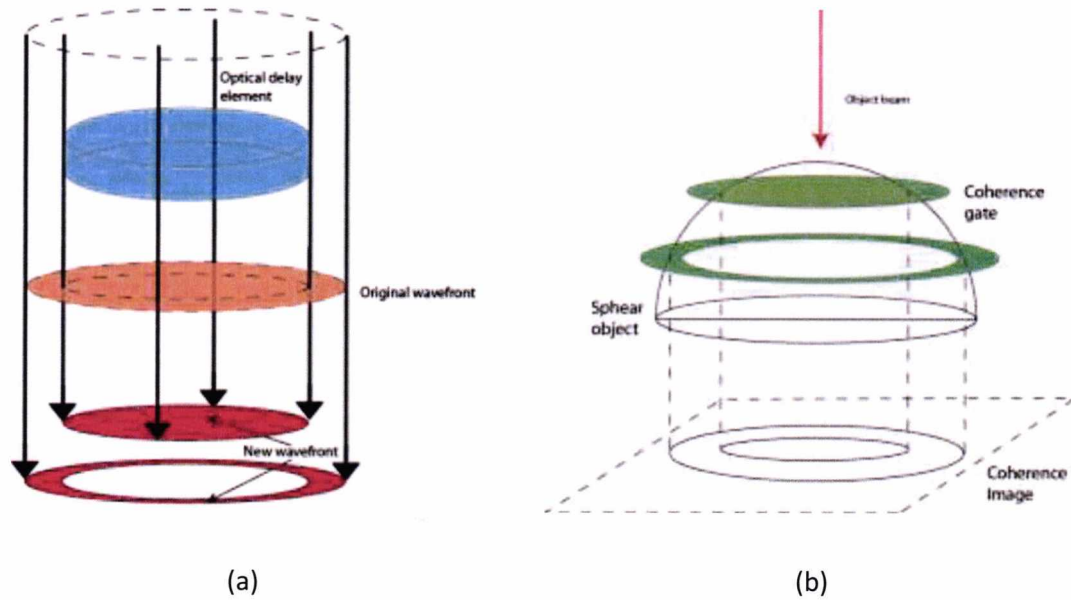


Figure 4.6. (a), Variation of the wavefront delay in the reference beam due to an inserted optical delay element of two steps and (b) the corresponding spatial variation of the coherence gate in the object due to the two optical delays and the resulting depth-encoded topographic image.

#### 4.1.4.1 Principle

The simplest method to introduce a delay in the MDE is by inserting a glass slide into the beam. Considering each such slide of thickness  $t$  inserted into the reference path, since the beam travels along the same optical path in double pass, the increase of the optical path length  $\delta$  can therefore be expressed by  $\delta = 2(n' - n)t$  where  $n$  and  $n'$  are the refractive indices of the air and the glass slide respectively. Correspondingly, the change of the optical path length in the object arm is  $\delta = 2nd$ ; therefore, the variation of imaging depth in the object arm can be calculated as  $d = t(n' - n)/n$ . Given  $n' = 1.5$  for the glass slides used in the experiments and  $n = 1$  for air, thus  $d = t/2$ . With a sphere object illustrated in a 2D area (Figure 4.7), the radius of the object,  $R$ , can be obtained by

$$R = \frac{1}{2kd} \sqrt{(X_{i+k}^2 - X_i^2 + k^2 d^2)^2 + 4k^2 d^2 X_i^2}$$

or

$$= \frac{1}{kt} \sqrt{\left(X_{i+k}^2 - X_i^2 + \frac{k^2 t^2}{4}\right)^2 + k^2 t^2 X_i^2}$$
(4.1)

where  $X_i$  and  $X_{i+k}$  are the radius of circular contours in the *en-face* image where  $i$  and  $k$  are the original number and the additional number of glass slides. The geometry of the OPD across the reference beam section is illustrated in Figure 4.7.

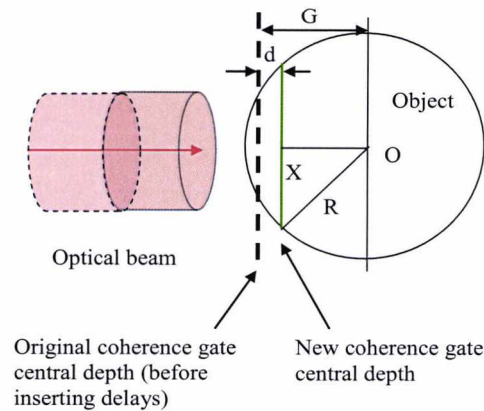


Figure 4.7. Geometry of contour circles (green) sampled by the coherence gate out of a sphere object.

#### 4.1.4.2 First Configuration

An MDE was fabricated by using four spatially separated windows, equipped with different number of glass slides (Figure 4.8, b). The microscope slides have uniform thickness of  $180 \mu\text{m}$  ( $\pm 20 \mu\text{m}$ ), given by the manufacturer. Two approaches to introduce MDE into the interferometer have been evaluated. The straightforward way to introduce delays is inserting the MDE into the reference beam in such a way as to be transmitted through equally by the four windows (Figure 4.8, c). Another possible location to introduce MDE is in the optical source path, before the light enters the interferometer. The two locations, A and B, where MDE can be inserted are illustrated in Figure 4.8 (a).

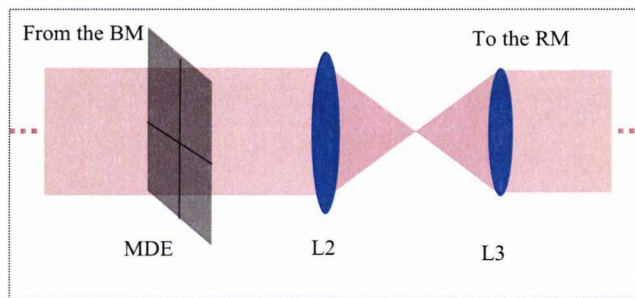
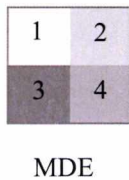
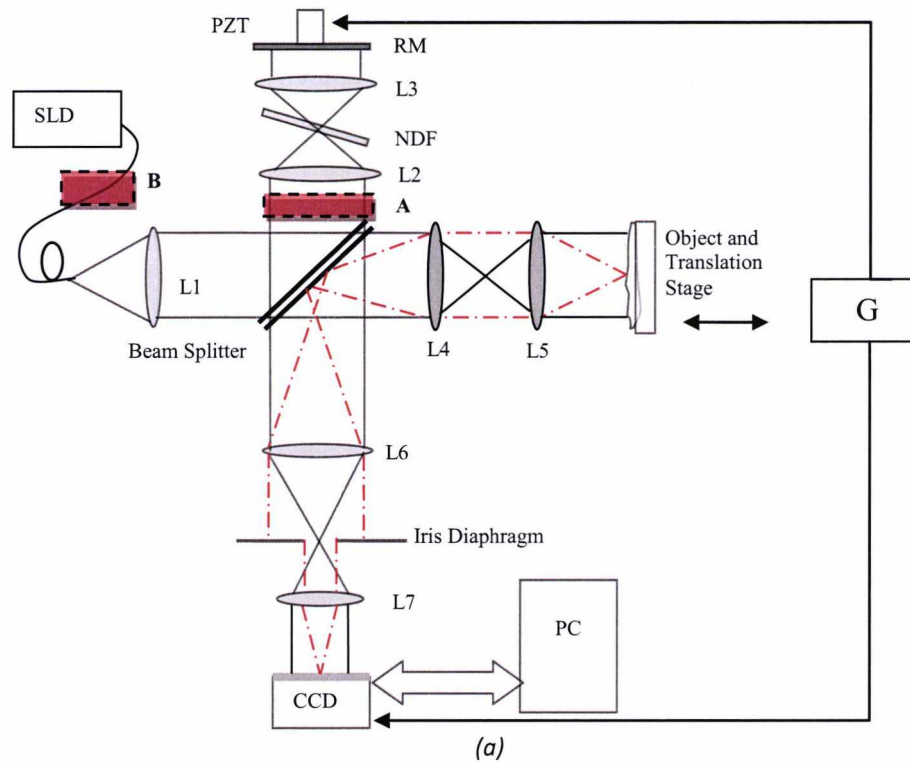


Figure 4.8. (a) Schematic diagrams of the coherence radar set-up with MDE that can be inserted into two locations: position A and position B. The optical set-up is identical to that illustrated in Figure 4.1; (b) The MDE, (the digit in each window indicates the number of glass slides in that specific window) was inserted between the BM and L2 in the reference path (c) of the interferometer in Fig. 4.8.

Let us consider first the MDE inserted into the reference path. Because the four windows sample the reference beam equally; each quarter of the reference beam that reaches the camera carries a certain delay, which enables detection of reflections from a different height on the object surface. With a metal ball of 7 mm diameter as object, four contours are recorded in a single *en-face* coherence image. Each contour corresponds to a certain height on the object, determined by the delay concerned. The image acquired with this configuration is displayed in Figure 4.9, wherefrom the four radii measured in each quarter circle contour are 0.905

mm, 1.221 mm, 1.453 mm and 1.606 mm respectively. Using Eq. (4.1), the diameter of the metal ball resulted from this experiment is calculated as 7.13 mm. The error of the measurement is a result of the error of the slides thickness, which is about than 10%. The size of the *en-face* image collected is  $4.2 \times 4.2 \text{ mm}^2$ .



Figure 4.9 *En-face* coherence image obtained with the MDE inserted in the reference path.

Table 4.2. Results obtained from the first MDE configuration.

Contour radius (mm)	Object radius (mm)
$r_1 = 0.905$	/
$r_2 = 1.221$	
$r_3 = 1.453$	$R_{23} = 3.651$
$r_4 = 1.606$	$R_{34} = 3.381$
Average	$\overline{R} = 3.567$

#### 4.1.4.3 Second Configuration

Previous solution presents two main disadvantages. Firstly, each delay line samples the curvature within a limited polar angle range only. Thus the method is applicable to curved objects with polar symmetry only, as the polar variation of curvature cannot be evaluated. In addition, due to the fact that the contours are incomplete, averages to improve the numerical results are not possible. These disadvantages are overcome by introducing the delay elements into the optical source path, delay position B (Figure 4.8). The alignment of MDE in position B is shown in Figure 4.10. The light from the source is collimated by lens A, the collimated beam transmits the MDE and was focused by lens B to be coupled to a single-mode fiber connecting to the entrance of the interferometer. The light at the entrance of the interferometer now has multi-axial-mode.

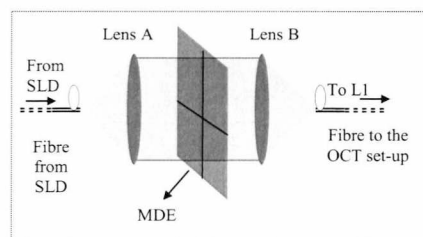


Figure 4.10. MDE inserted in the source path of the interferometer between a pair of microscope objectives where the optical beam is collimated.

Because light incurring all delays is split 50:50 and entered both the object and the reference path, both positive and negative OPDs are generated and as a result, the number of the contour circles in the image can be doubled if the axial range of the system is sufficiently large. In other words,  $n$  number of windows containing different number of slides result in ' $2n-1$ ' complete contour circles. With the same MDE, double of the contour number provides a larger set of data to be calculated and averaged, and thus may improve the precision of the measurement. For instance, with 4 windows, 7 complete circles can be generated in the single *en-face* image, so that the thickness error of the glass slides would influence the accuracy of results less.

The image obtained from the same object ball with this improved configuration is shown in Figure 4.11. In (a) and (b), two windows with a thickness difference of  $t=180\ \mu\text{m}$  were used to sample the collimated beam, thus 3 complete circles were obtained. The two images are acquired at different axial positions. By increasing the thickness difference of the two windows, 3 circles with larger separation were obtained as shown in (c).

Number of the windows was later increased to 3 and 4, and the result images are shown in (d) and (e), 5 and 7 circles are acquired in a single image respectively. The images with 5 circles (d) was selected to perform the measurement; which gave an average radius value as 7.11 mm, slightly improved from the result of the previous method. In the image (e), extra circles are visible, however it is difficult to label each circle to the specific thickness difference value.

One issue related to both approaches is that the light returned from different heights of the object surface exhibit different intensity. The light reflected from the outer part of the sphere is less intense due to the larger incidence angle. Most light from larger incident angles is reflected sideways off the imaging lens and as a result, the larger the radius of the contour, the less is its intensity in the image.

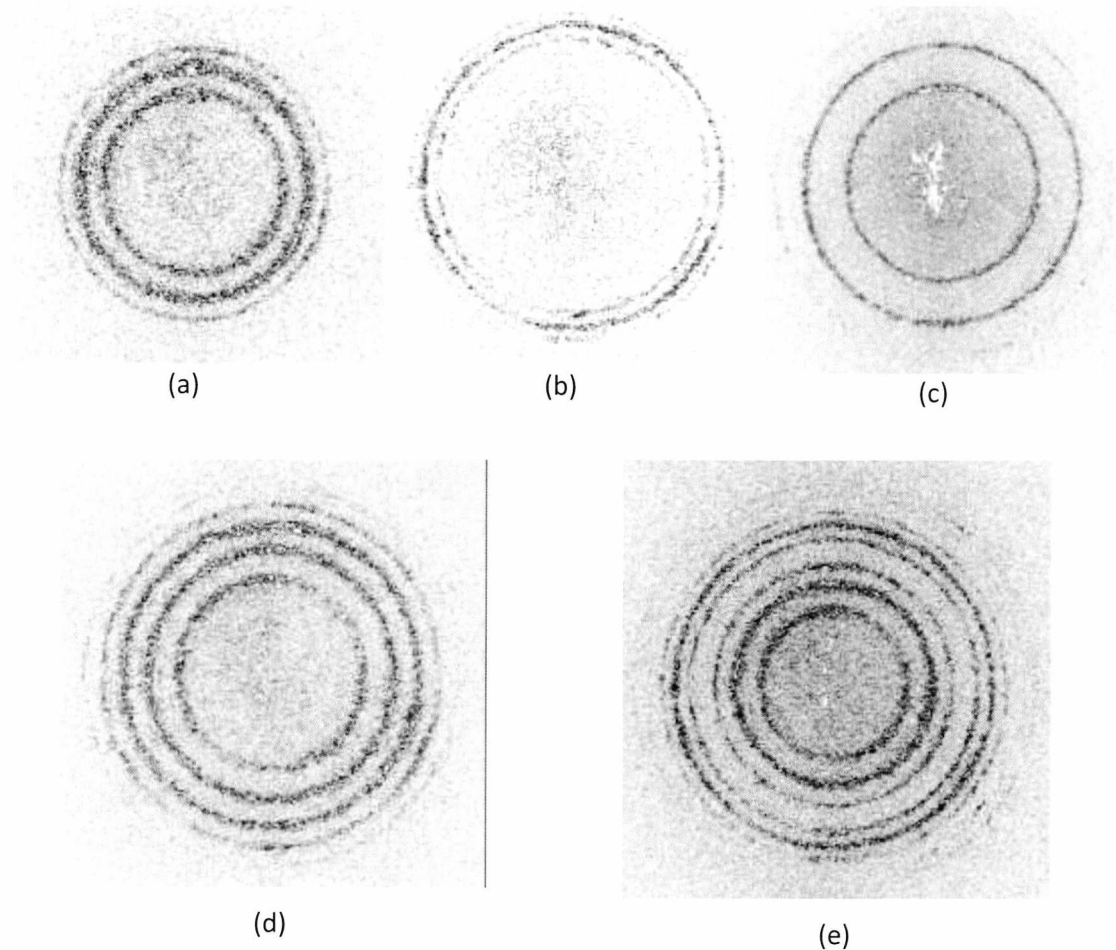


Figure 4.11. En-face LCI image obtained using a MDE introduced into the optical source path: (a), MDE made of 2 delays, introducing relative delays of '0' and 't', (b) same MDE as (a) but acquired at a longer reference path; (c), MDE made of 2 delays, introducing relative delays of '0' and '2t'; (d), MDE made of 3 delays, introducing relative delays of '0', 't', and '2t'; (e), MDE made of four windows with delays of '0', 't', '2t' and '3t'.

Another problem unique to the second configuration is that of non-uniform power distribution within each contour of the multiple contours. Light with all delays are split into two interferometer arms equally; after recombining all contributed to the middle circle as an auto-correlation. This effect means that the middle circle consumed half power of the interference signal, whereas the circles that represent cross-correlation exhibit less intensity. This effect is illustrated in Figure 4.12 (b). The average image value of the middle circle is similar to the inner one, though it is acquired from larger reflection angles than those produce the inner one. This is because the optical power contributes to  $OPD=0$  is double of the other two. This effect is in contrast to the results shown in Figure 4.9 where the circle

from the smaller reflection angle exhibits larger signal value. The more delays are used, less is the intensity in the image for these contours, which limit the number of the circles that can be introduced. As a result of the combination of these two issues, multiple circles bear all different image intensity, which makes the automatic radius measurement difficult and increase the error. Some expected circles are even not visible if too many delays are used, due to the limited dynamic range of the system.

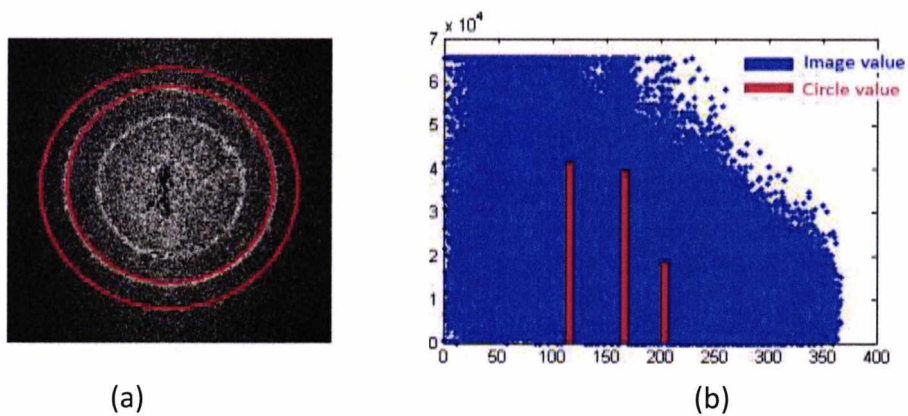


Figure 4.12. (a) En-face LCI image obtained using a MDE introduced into the optical source path, the MDE is composed by two optical delays, which produce three circles, one from  $OPD=0$  and the other two from positive negative value of the delay difference; (b) the blue background is the image pixel value plotted versus the polar distance to the centre of the circles, whose baseline can be considered as noises; the three red bars indicate the average pixel value along the three circles due to MDE.

#### 4.1.5 Time-domain Full-field OCT

By replacing the Lens, L3 and L5 (in Figure 4.1), with microscope objective lenses (X10, NA=0.25), the coherence radar set-up was modified to a FF-OCT set-up that can obtain *en-face* images from the inside of highly scattering media. FF-OCT images from my own finger were acquired, as shown in Figure 4.13. (a) shows some image artefacts due to involuntary movements of the finger. Axial movements reduce the resolution and lead to image blurring, while lateral movements produce some microscopy-like features and reduce the resolution if the movement is too fast. In Figure 4.13 (a) the finger is out of the coherence gate and subject to lateral movement. The transverse resolution is poor; the blurred edges of the fingerprint are actually microscopy image that come from the skin surface.

By pressing the finger on a glass plate support, this movement is reduced and a better image is obtained (Figure 4.13. b). The bright (low image values that is marked with the red lines; the greyscale is reversed in Figure 4.13.) and dark regions (high image values) exhibit similar structures; the dark region indicates where the coherence plane sections the target. Other than that area, the incoherent signal is suppressed by the PSI algorithm.

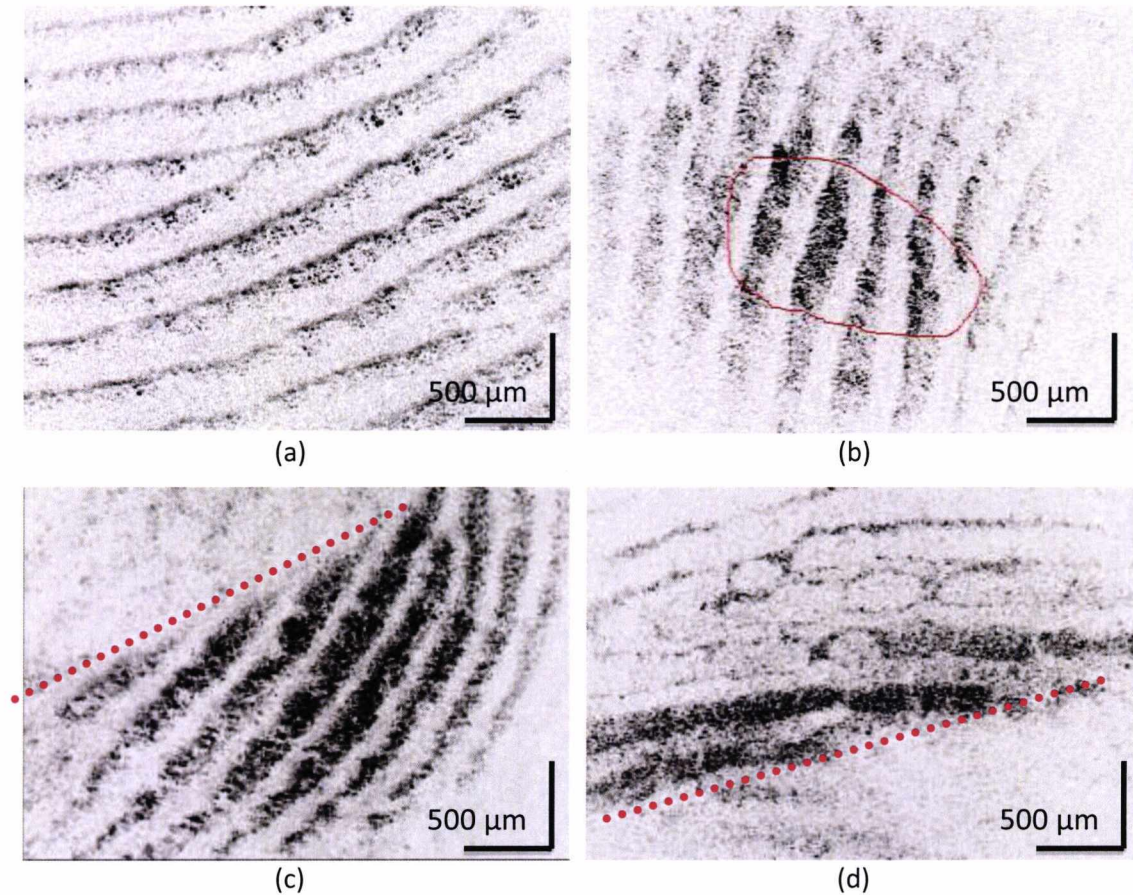


Figure 4.13. En-face OCT images of human finger skin obtained using FF-OCT in vivo. (a) and (b) low reference power, some microscope image seen; (c) and (d) higher reference power; (a) out of coherence gate; (b), (c) and (d): selected en-face views by PSI coherence gate.

The microscope image value can be further suppressed by increasing the power of the reference beam. By reducing the optical density (OD) of the NDF2 (in Figure 4.1, NDF1 was not used here) from 1.0 (used in acquiring Figure 4.13. a and b) to 0.6, the power of the reference was increased by 2.5 times, the incoherent microscopy signals are suppressed significantly that the boundary between coherence image and microscope image (red dotted line) become clear, as shown in (c) and (d).

A pair of x20 microscope objectives with higher NA (0.40) was used to acquire *en-face* FF-OCT images from larvae of fruit fly *Drosophila Melanogaster in-vivo*. The embryo suffered movements that affected the image. The heart beats, while body contractions occur in both axial and lateral direction irregularly, in a scale of once every 10-20 second. The FF-OCT worked at a comparatively low speed, about 3 fps; therefore suffering from movements of the sample and producing less contrast and high incoherent microscopy features. Some examples are shown in Figure 4.14 (a)-(f), where (a) is a FF-OCT image collected at the depth of the microscope base slide. Because the refractive index of the embryo body is higher than the air, the coherence plane inside the embryo is closer to the objective than the slide surface, where the focus was initially placed, therefore the resolution is poor. The imaging

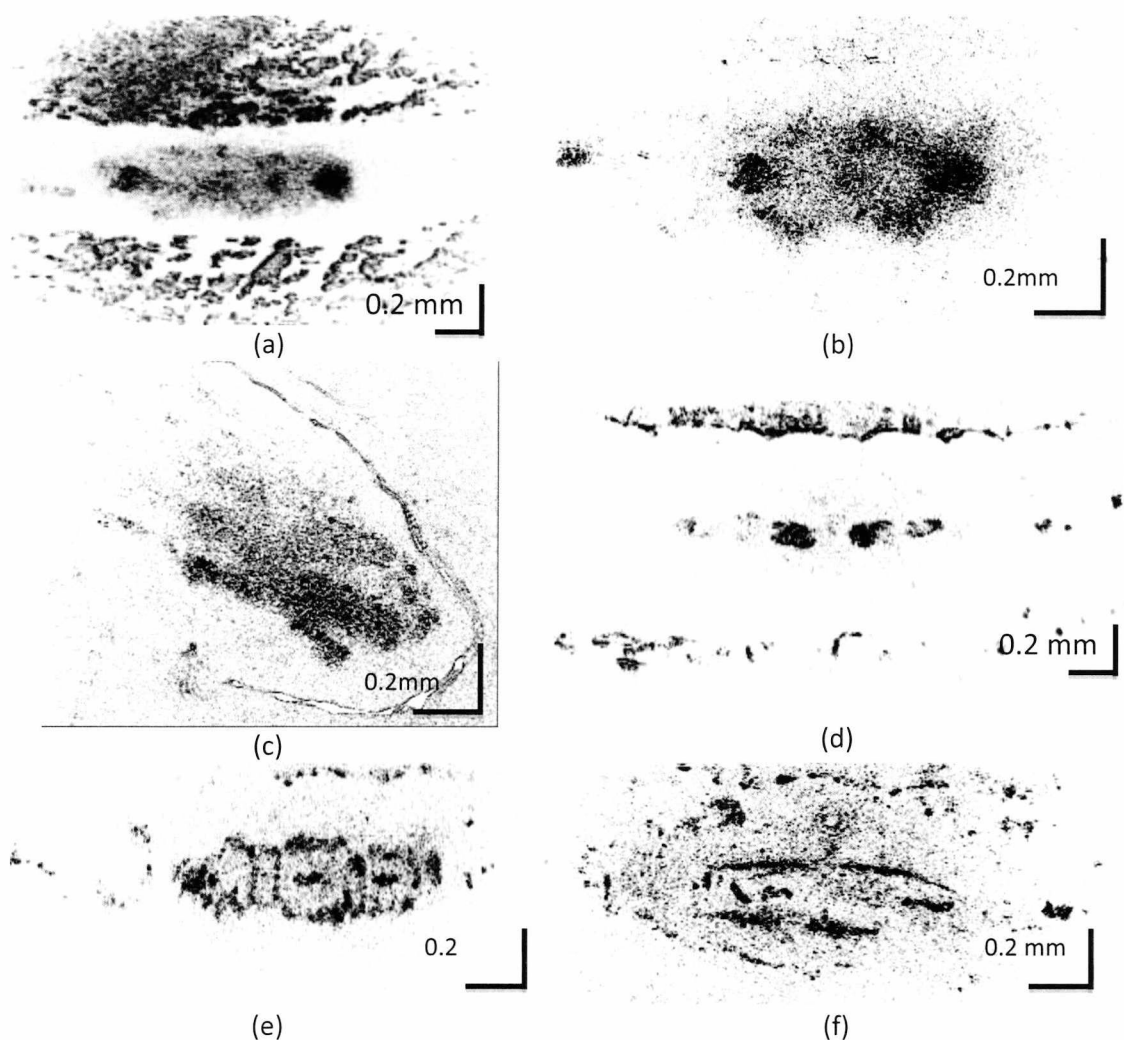


Figure 4.14. *In-vivo* FF-OCT images of larvae of fruit fly *Drosophila Melanogaster* : (a), (b) example of loss of contrast and resolution due to sample movement; *In-vivo* FF-OCT images from the end(c) and the middle of larva body from different depths (d),(e) and (f) acquired with shorter (0.5 ms) exposure time, where 200 EM gain was applied to compensate for the signal loss.

was selected higher up in Figure 4.14 (b), where better resolution is obtained in the middle of the embryo body. The structure of two chambers can be observed.

In order to reduce the effect of object movement, a shorter exposure time (0.5 ms) was used and EM gains were applied to the camera to compensate for the loss of signal, thereby both the contrast and the lateral resolution improved, so that different types of structures such as layers and chambers can be seen in various depths and positions in the sample. *En-face* images obtained from one end of the embryo body (Figure 4.14 c), and from the middle of the body (d, e and f) reveal some high contrast tomography features.

## **4.2 Full-field Swept-source OCT**

The FF-OCT set-up also allows swept-source OCT acquisitions by replacing the broadband SLD with a wavelength tuneable source.

### **4.2.1 Optical Set-up**

The Full-field OCT setup was modified, as shown in Figure 4.15. A tuneable semiconductor light source 'BroadSweeper-840', SUPERLUM, was used to illuminate the sample in full-field. It has a spectral tuning range width of 55 nm, at central wavelength of 847 nm. The spectral linewidth is approximately 40 pm. In our experiments, the spectrum is sampled in 1024 steps, which leads to an effective spectrum resolution of 53 pm, close to the spectral linewidth of the source output. According to the relation between the depth range of SS-OCT and the spectral resolution, the maximum depth  $\Delta Z$  is given by:

$$\Delta Z = \frac{\lambda_0^2}{4\delta\lambda}, \quad (4.2)$$

where  $\lambda_0$  denotes the central wavelength of the spectrum and  $\delta\lambda$  denotes the effective spectrum linewidth. The maximum axial range is calculated as 3.34 mm in air. The maximum sweep rate of the light source is 200 Hz. The wavelength is driven by external voltage, controlled by an I/O board, NI USB-6215, National Instruments. This I/O board is electrically isolated from the PC and the driving board of the

camera in order to avoid electronic interferences that may enlarge the peak profile of light emission, phenomenon that has been previously observed by me with a non-isolated board. Since SS-OCT acquires depth information without axial movement, two low NA (0.15) objectives (x5) were used as imaging optics to allow a sufficiently large depth of view. These lenses are placed on two one-dimensional translation stages providing platforms for sample and reference mirror moving axially without changing the focus. The same camera Andor DV887 was employed as the detector array, where a zoom lens (18-108 mm/ f2.5) was mounted on position L5. This configuration, being compatible with both time domain and spectral domain operation regimes, can be used to evaluate comparatively the signal-to-noise ratio (SNR) in the two regimes.

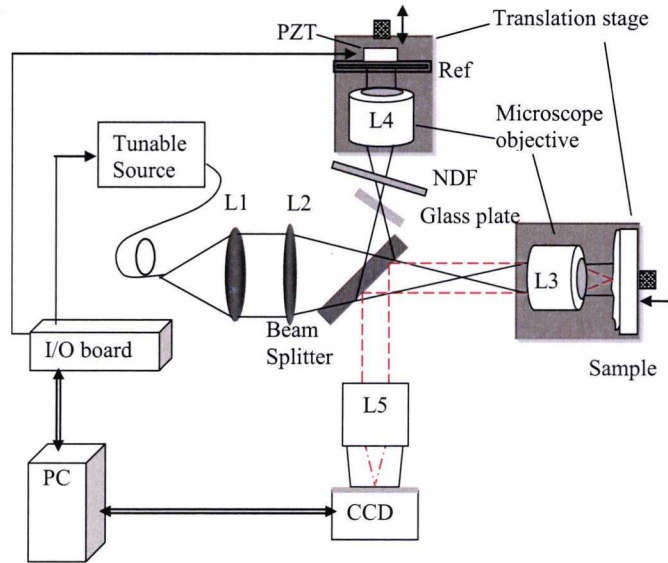


Figure 4.15. Configuration of the FF-OCT set-up that allows both time-domain and swept-source acquisitions. L1: x5 microscope objective; L2: 150 mm focal length doublet lens; L3, L4: identical microscope objectives, ZEISS EC PLAN NEOFLUAR® OBJ 5X; L5: zoom lens, 18-108 mm focal length, NA 2.5; Ref: reference mirror; PZT: Piezo-electro mechanic actuator; NDF: neutral density filter; CCD: Andor DV887.

The theoretical axial resolution of the SS-OCT determined by the FWHM bandwidth of the wavelength tuning range as:

$$\delta z = \frac{2 \ln 2}{\pi} \frac{\lambda_0^2}{\Delta \lambda} \quad (4.3)$$

from which,  $\delta z$  is calculated as  $6 \mu m$ . With the axial range of over 3.34 mm, in order to achieve this depth resolution, at least 512 depth layers should be obtained, with each *en-face* image is of  $6.5 \mu m$  ( $3.34 \text{ mm}/512$ ) thick; therefore, 1024 sampling points in wavelength sweeping are selected.

## 4.2.2 Theoretical analysis

As presented in the Chapter 3, the expression of the CCD array output [122] at a pixel  $(x,y)$  can be written as:

$$V_{idCCD}(x, y) = n_e \frac{Gq}{C} \quad (4.4)$$

where  $n_e$  is the electrons number in the charge packet, G is on-chip amplifier gain, q is electron charge and C is sensor node capacitance.

### 4.2.2.1 Time-domain FF-OCT

In time-domain FF-OCT acquisition, ignoring the effect of cross-talk between parallel channels, the phase-shifted image with the  $i^{\text{th}}$  phase shift,  $V_{idCCD}(x, y)$  can be expressed as:

$$V_{idCCD_i}(x, y) = \overline{V_{idCCD_i}}(x, y) + \frac{Q_e t G q}{2 E_v C} \sqrt{R_R R_S} P_{id}(x, y) \cos[\phi + \theta_i] \quad (4.5)$$

where  $\overline{V_{idCCD_i}}(x, y)$  is the average detector output,  $P_{id}(x, y)$  is the light source output power per unit of volume,  $Q_e$  represents the CCD quantum efficiency, t is the integration time and  $E_v$  is the photon energy,  $R_R$  and  $R_S$  are the reference and sample arms reflectivity respectively,  $\phi$  is the phase difference between the object and reference waves and  $\theta_i$  is the  $i^{\text{th}}$  phase shift value. For instance, in 3-step PSI, the increment in phase is  $2\pi/3$ . The OCT signal  $D_{oct}(x, y)$  can be calculated by:

$$D_{tdFFOCT}(x, y) = \frac{\sqrt{2\{(V_{tdCCD1} - V_{tdCCD2})^2 + (V_{tdCCD2} - V_{tdCCD3})^2 + (V_{tdCCD3} - V_{tdCCD1})^2\}}}{3} \quad (4.6)$$

$$= \frac{Q_e t G q}{2E_v C} \sqrt{R_R R_S} P_{td}(x, y)$$

The simplified model of on-chip noise [122] applied to the same detector given in the previous chapter can be expressed as:

$$N_{noise} = \sqrt{\langle N_{SHOT}^2 \rangle + \langle N_{Dark}^2 \rangle + \langle N_{Read}^2 \rangle} \quad (4.7)$$

where  $\langle n_{SHOT}^2 \rangle$  is the shot noise;  $\langle n_{DARK}^2 \rangle$  is the dark current noise and  $\langle n_{read}^2 \rangle$  is the readout noise. Let us consider that the dark current noise and read-out noise can be reduced to a negligible value by using high power illumination and cooling. The shot noise dominates over the rest of the total noise, and therefore

$$\langle N_{SHOT}^2 \rangle = \frac{Q_e t G q}{4E_v C} (R_R + R_S) P_{td}(x, y) \approx \frac{Q_e t G q}{2E_v C} R_R P_{td}(x, y) \quad (4.8)$$

where in the last approximation the similar value of  $R_R$  in comparison to  $R_S$  was used. The SNR of TD- FF-OCT is thus given by

$$SNR_{TDFFOCT}(x, y) = \frac{Q_e t G q}{2E_v C} R_S P_{td}(x, y) \quad (4.9)$$

#### 4.2.2.2 Swept-source FF-OCT

In SS-FF-OCT operation, the light wavelength is tuned in a large number of discrete steps. In this case, signal from a narrowband, rather than a broadband light is integrated on the CCD array. For an optical wave number  $k$ , each pixel  $(x, y)$  of the array has an output:

$$V_{ssCCD}(k_m) = \frac{Q_e t G q}{4E_v C} S_{ss}(k_m) [R_R + R_S + 2\sqrt{R_R R_S} \cos(2k_m \Delta z + \phi_i)] \quad (4.10)$$

where  $S_{ss}(k)$  is the source spectral density and  $\Delta z$  is the OPD. Ignoring the effect of cross-talk, the detector position  $(x,y)$  is universal in what follows, therefore this notation can be dropped in the following equations. Applying a DFT to the  $V_{ssCCD}(k)$  in [43], the A-scan represented from points  $D[z_n]$  [204] can be expressed as:

$$D[z_n] = DFT\{i_{ssCCD}\} = \sum_{m=1}^M i_{ssCCD}[k_m] \text{Exp}[-2jk_m z_n] \quad (4.11)$$

In case a single reflector is used as object, placed at an optical path difference =  $z_0$ , the peak value of  $D[z_0]$  is:

$$D[z_0] = \frac{Q_e t G q}{2E_v C} \sqrt{R_R R_S} \sum_{m=1}^M S_{ss}(k_m) \quad (4.12)$$

Similar to the reasoning in Eq. (4.8) , the shot noise transformed from the  $k$  domain to the  $z$  domain can be written [74] as:

$$N_{noise} = \sqrt{\sum_{m=1}^M \sigma^2[k_m]} \approx \sqrt{\frac{Q_e t G q}{2E_v C} R_R \sum_{m=1}^M S_{ss}(k_m)} \quad (4.13)$$

where  $\sigma[k_m] = \sqrt{V_{ssCCD}(k_m)}$  is the standard deviation of white noise from  $V_{ssCCD}(k_m)$  .

The SNR of SS-FF-OCT is thus

$$SNR_{SSFFOCT} = \frac{Q_e t G q}{2E_v C} R_S \sum_{m=1}^M S_{ss}(k_m) \quad (4.14)$$

When the integration time interval in TD-FF-OCT is equal to the summation of integration intervals required for the complete tuning of the spectrum in SS-FF-OCT, and assuming that the time domain broadband source has a similar spectrum profile as the spectrum covered by the tuning source,  $P_{td}(x,y)$  can be thought of as the coherent addition of  $M$  waves of amplitude  $S_{ss}(k_m)$  . This leads to:

$$\sum_{m=1}^M S_{ss}(k_m) = P_{td}(x,y) \quad (4.15)$$

Using Eq.(4.9), (4.14) and (4.15), the connecting relation between the SNRs in SS-FF-OCT and TD-FF-OCT can be obtained as:

$$SNR_{SSFFOCT} = M SNR_{TDFFOCT} \quad (4.16)$$

Experiments have been performed to evaluate this derivation.

### 4.2.3 Acquisitions

For SS-OCT acquisition, spectral-encoded images were performed by tuning the external driving voltage applied to the BS-840. The main parameters of BS-840 are given in Table 4.3. The tuning spectrum of the source in low-power mode was measured versus the driving voltage for calibrations, as shown in Figure 4.16. From these results, over the 50 nm sweeping range, an effective linewidth of ~45 pm can be achieved for acquisitions.

Table 4.3. Specifications of the swept source 'BroadSweeper-840'

Parameters	High-Power Mode	Low-Power Mode
PM fiber output power (mW)	5	1
Spectral tuning range (nm)	826 - 873	820 - 875
Tuning width (nm)	47	55
Spectral line width, nm	0.04	0.04
Side-mode suppression, dB	>50	>50
Polarization degree (slow axis, %)	>90	>90
Sweep rate range (Hz)	1 - 200	1 - 200
External driving voltage rang (V)	3.0 - 5.0	3.0 - 6.0
MAX driving voltage speed (V/S)	>200	>200

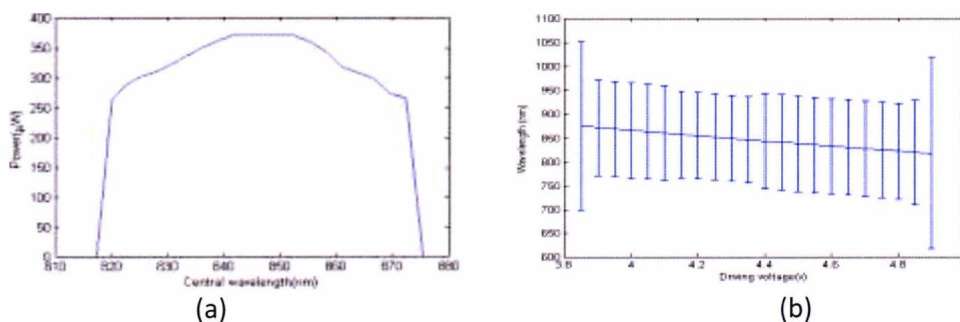


Figure 4.16. (a): Measured tuning spectrum of the swept source BS-840; (b): relationship between driving voltage and the emitted wavelength, the error bar indicates the spectral linewidth (scaled x 200).

The swept source was driven by discrete voltages, otherwise, if the source is sweeping continuously, the continuous exposure could wash out the interference signal during the CCD's transfer and readout time due to lack of shutter. The

wavelength was tuned in steps and the illumination was switched off during the CCD's readout time. This procedure slowed down the acquisition therefore the object had to be fixed during the acquisition.

To obtain the voltage values required for linear modulation of the frequency of the light emitted, the boundary of the wavelength tuning range,  $\lambda_0$  and  $\lambda_N$  was converted to the instantaneous light frequency range ( $k_0 = 2\pi / \lambda_0$  and  $k_N = 2\pi / \lambda_N$ ) first. Then the frequency was sampled equally to  $N = 1024$  values:

$$k_n = k_0 - n(k_0 - k_N) / N, \quad (n = 1, 2, 3, \dots, N); \quad (4.17)$$

the corresponding wavelength values were thereby obtained as  $\lambda_n = 2\pi / k_n$ . Further procedure to linearise the optical frequency of the data is discussed later. For each desired wavelength value, voltage  $v_n$  was sent to the SS and between two camera acquisitions, light source was switched off by the driving voltage to reduce the 'smearing' effect. The sequence of acquisition is illustrated in Figure 4.17.

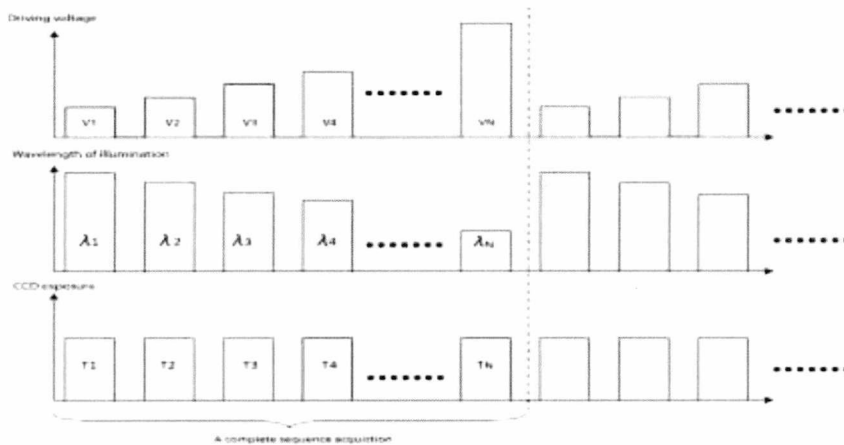


Figure 4.17. Imaging sequence synchronised with the driving voltages to the swept source.

The voltage signal controlled by the I/O board was synchronised with the camera acquisition via software. Because the camera frame rate,  $FR = 17$  fps is much lower than the sweeping rate of the source, the acquisition rate is limited by the frame rate of the camera. Each complete sequence of spectral-encoded images take  $N / FR$  seconds to finish; therefore a OCT volume of  $515 \times 512 \times 512$  voxels were acquired in 64 second, corresponding to 4,000 A-lines per second. A reference

frame was recorded beforehand with object arm blocked as the dark frame, which was later used to reduce the DC term in the acquired spectrum before the Fourier transforms. The numerical processing including digital Hamming windowing and Fourier transforms are performed after the acquisition using my programs written in C++.

#### 4.2.4 Spectrum Resampling

Our calculations are based on the assumption of ideal linearity between the driving voltage and the wavelength output. The experiments showed that the spectrum data collected with these calculated voltages were not linear to  $k$ . For increased OPD values, the point-spread function (PSF) in depth becomes broader. This phenomenon suggested that there is either optical dispersion mismatch in the set-up or imperfect linearity between the source frequency and the sampling data, or a combination of both; therefore, spectrum resampling is required. An example of this effect is shown Figure 4.18 (a), displaying a B-scan image of an air-glass interface without spectrum resampling. This was retrieved from the 3D data volume according to the procedure explained above.

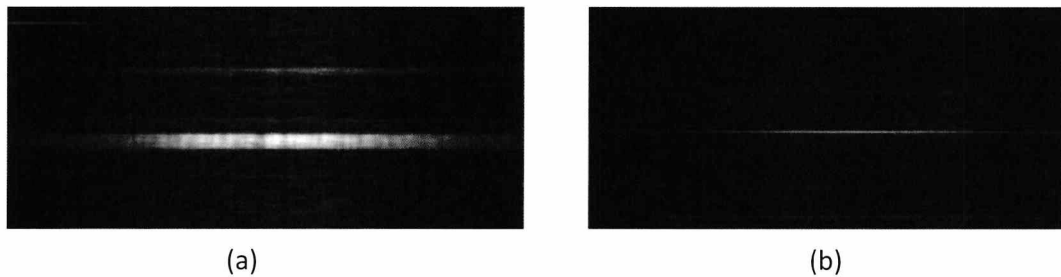


Figure 4.18. B-scan OCT images of an air-glass interface as object, without (a) and with (b) spectrum resampling.

In order to determine the proper voltage dependence on the wavelength of the source, a calibration method (described in Section 2.3.1.5) based on phase oriented fringe analysis technique [205] was applied and has been proved useful to optimise the axial PSF for spectral-domain OCT [204]. The core of this method is to retrieve the phase information from the spectrum acquired. To this goal, a Fourier transformation on the spectrum data was performed, and then a flat-top window was applied to select the positive term from the symmetric result. After that, applying an inverse FFT on the results enables the reconstruction of the spectrum with both amplitude and phase information. The phase of the spectral data  $\phi_j$

varies linearly to the source instantaneous optical frequency  $k_j$ , according to the relationship [204]

$$k_j = \frac{c}{4\pi OPD} \phi_j \quad j = 1, 2, 3, \dots, N \quad (4.18)$$

where  $c$  is the speed of light and  $OPD$  is the optical path difference. To obtain linear  $k_j$  from  $\phi_j$  that was obtained in previous step, a three-order-polynomial curve fitting for  $\phi_j$  versus  $k_j$  was performed. Resampling this curve using linear phase  $\phi'_j$  lead to a new array of  $k'_j$  and corresponding voltage values  $v'_j$ . The spectrum can be resampled based on  $k'_j$  or by applying these calibrated  $v'_j$  to the swept source; these two approaches provide similar improvements. With spectrum resampling, the spectrum data that produces Figure 4.18 (a) was resampled. Applying FT on the resampled spectrum gives an improved B-scan image, shown in Figure 4.18 (b).

The A-Scan signal intensity exhibits a 10 dB improvement over the uncalibrated result and the actual depth resolution is also improved. Figure 4.19 shows the improvement of signal intensity and pulse width after calibration. (a) is the A-scan data acquired from the air-glass interface with an OPD of  $\sim 1$  mm. (b) and (c) show two B-scan images of a printing paper sheet, without and with resampling.

In order to switch the system to the FF-OCT regime, the optical source should have been replaced with a large bandwidth source. Instead, we use the same tuning optical source and simulate the operation of a FF-OCT set-up by measurements over a large time scale range while the source is tuned continuously. We have therefore applied 250 kHz (maximum rate allowed by the I/O board) sampling rate to drive the swept source to make it work at the maximum sweep rate, 200 Hz, i.e. in each sweeping period (10 ms), the I/O board generated 2500 wavelength-sampled narrow-band pulses, and the camera was open for a 10 ms interval to acquire quasi-broadband light. As a result, the integration period is the same in both time-domain and spectral-domain approaches. 4-step PSI method was used to generate *en-face* OCT images.

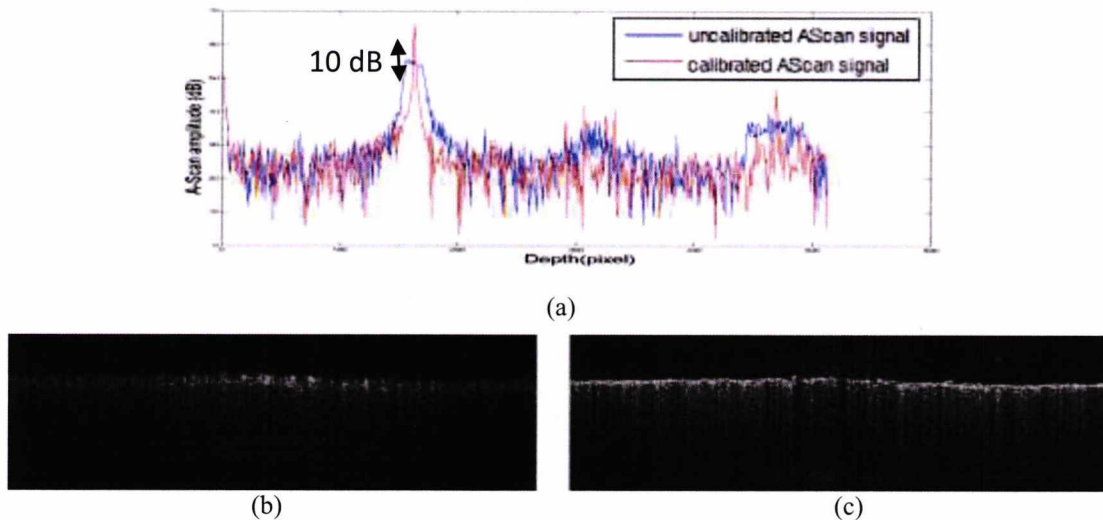


Figure 4.19 Improvement of SS-OCT signal by phase linearization. The top row: A-scan data profile for an air-glass interface at a depth of 1 mm before calibration (blue) and after calibration (red). Bottom row: B-scan OCT images of paper, vertical scale 750  $\mu\text{m}$  in depth measured in air, using data before calibration (b) and after calibration (c).

#### 4.2.5 Results

The SNR was measured using print paper as a sample, which is scattering and low reflective. The light source power was set just below the CCD saturation equivalent. The *en-face* time domain FF-OCT image and a B-scan OCT image retrieved from the 3D data volume obtained by SS-OCT are shown in

Figure 4.20. The paper was slightly tilted to create two regions in the *en-face* image for the convenience of distinguishing the coherence signal from the background. From these images, data from outside coherence was collected (dark areas in the images with even intensities), which determine the noise value and data from the brightest part of the images (which determine the signal values). The average results obtained lead to SNR values of 12.76 dB in TD-FF-OCT and 19.16 dB in the SS-FF-OCT. The SNR enhancement is 6.4 dB, smaller than 27.09 dB expected from Eq.(4.16).

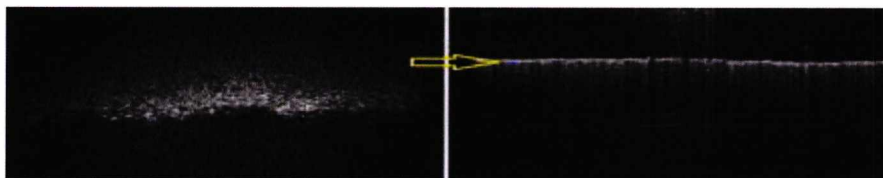


Figure 4.20. OCT images of paper collected by the FF-OCT system. Left: C-scan OCT image, obtained in the TD-FF-OCT regime; Right: B-scan OCT image obtained in the SS-OCT regime.

### 4.3 Summary

A coherence radar set-up was built, based on parallel detection and LCI principles, which allowed us to obtain *en-face* thin sections of objects. A novel method to measure the curvature of spherical objects was presented, based on the coherence radar set-up, which employs multiple optical delay lines to acquire multiple depth-resolved contours in a single *en-face* image. By placing the MDE with  $n$  different optical delays in the optical source path,  $2n-1$  contours at maximum can be generated. FF-OCT combined with multiple delays, provides an alternative way to the surface topography and surface curvature measurement. The method is especially useful for curvature assessment of moving targets. However, its use on ophthalmologic applications, such as cornea is limited for the moment by the frame rate of the camera. With a faster camera, improvement is possible in shortening the time between the phase-shifted frames, to tolerate motion artefacts. Unfortunately, no faster camera was available by the time these experiments were performed. Another concern with this method is the thickness error of the glass slides, which has to be very small. Because this MD method is highly sensitive to error of glass thickness, unwanted contours could be generated if errors exist. The glass plates used in the experiments have a thickness error of approximate 10%, which limited the measurement precision.

By using a high NA optics, FF-OCT acquisitions were performed from inside biological samples. FF-OCT provide *en-face* images with high spatial resolution. Images from my finger and from larvae of fruit fly have been acquired. The imaging regime was later extended from time domain to spectral domain. The same system was used to deliver a 3D volume of OCT images in the SS-OCT regime and *en-face* OCT images in the TD-OCT regime. Measurements in the two regimes of FF-OCT were performed to compare the achievable SNR in time domain and spectral domain. The results demonstrate, as expected, that the SNR of SS-OCT is better than that of TD-OCT, however not to the level predicted by theory. This deviation may be the result of the slow acquisition that may partially wash out the interference fringes and leads to loss of signal intensity.

# Chapter 5 Line-field

## Fourier-domain OCT

Fourier-domain OCT (FD-OCT) [83] is described in Chapter 2 and techniques of combining FD-OCT with parallel-detection are introduced briefly in Chapter 3. In this chapter, experiments of a parallel-detection FD-OCT set-up that uses a line-field illumination are described; the performance of the system is evaluated; images from human skin, teeth and fruit fly larva are shown. Base on this set-up, several extended light sources and imaging sensors were equipped and experimentally evaluated to identify procedures to integrate elements that normally equip commercial digital cameras, to perform line-field FD-OCT. Limitations and potentials are discussed by the end of the chapter.

### 5.1 *Line-field Fourier-domain OCT*

#### 5.1.1 **Optical Set-up**

Line-field Fourier-domain OCT (LF-FD-OCT) is a parallel-detection FD-OCT method that allow acquiring a B-scan FD-OCT image from a single shot of a 2D detector array. The optical set-up was built as illustrated in Figure 5.1. A SLD (SLD-381, Superlum) was employed as the light source. At 150 mA pumping current, the optical power is measured as 5.05 mW; the central wavelength is at 855 nm and the FWHM spectrum width is 24 nm. The optical system was composed of a Michelson interferometer and a multi-channel spectrometer that employs a 2D detector array, connected by a spatial filter. Light from the source was collimated by collimator, L1. The collimated beam has a diameter of 10 mm and is sent through a cylindrical lens, CL. On the back focal plane of CL, the beam is focused into a horizontal line that is relayed by a pair of lenses, L2 and L3 and reshaped into vertical lines in both the object and the reference arm. Two interferometric beams are separated by a 50-50 beam-splitter, BS. The reflection is projected onto the object, OBJ that is on the front focal plane of L2. A line-field is illuminated in the vertical direction. The lengths of the illuminated lines on the object is  $\sim 7$  mm. In the reference path, identical

optics to the object arm are aligned. The reference mirror, RM is mounted on translation stages. Light returning from the OBJ and the RM, recombine at BS. A piece of glass plate, BS2 was inserted into the reference path to compensate for dispersion mismatch created by the BS. A neutral density filter (NDF) was also placed in the reference path to balance the power in two arms. A slit, SL, is inserted into the measurement path at the imaging plane of OBJ. Recombined light travelled through a linear spatial filter to the spectrometer. The spatial filter is composed of a pair of lenses, L4 and L5 with a slit in between. The slit is placed in vertical direction and is conjugated to the line-field on the object. The spectrometer uses an AR-coated (central wavelength at 830 nm) transmission diffraction grating, DG that has 1200 grid lines per mm. After the light transmits the DG, the first order diffraction is captured by a lens, L6 (10 cm focal length) and recorded by a 2D camera, Andor Ixon DV887. When the optical path difference is within the axial range of FD-OCT, modulation of the spectrum will be produced along vertical direction and be recorded by the 2D detector array.

One distinctive property of this optical configuration is that convergence of the beams along the optical path in the two dimensions, 'x' and 'y', is different, due to the cylindrical lens. The two perspectives of the set-up are illustrated in the bottom of Figure 5.1. Each point of the vertical line that is illuminated on the object produces a spectrum that is recorded by a row of the 2D camera in the 'x' direction; in the 'y' direction, the illuminated line-field on the object is conjugated to the sensor surface of the camera; in other words, the camera is imaging the object in 'y' direction. Given the OPD is within the depth range, with all rows together, a column of channelled spectra (CS) is acquired simultaneously. Each row of the camera read-out produces an A-scan after Fourier transform (FT), thereby a B-scan FD-OCT image is obtained from a single camera frame.

Stroboscopic illumination scheme is applied by synchronising the light source with the CCD to avoid 'smearing' effect, similar to in Full-field OCT (see Chapter 4). Etalon-effect due to the glass cover in front of the camera sensor may produce unwanted fringes that modulate the spectrum (see Chapter 3). It is less problematic in scanning FD-OCT because the linear detector can be tilted to eliminate the multi-

reflections within the etalon; however this is not helpful in LF-FD-OCT that uses a 2D DA. Software has been used to eliminate the pattern of Etalon-effect by subtracting a pre-defined spectrum image, however, in doing so, part of the dynamic range is sacrificed.

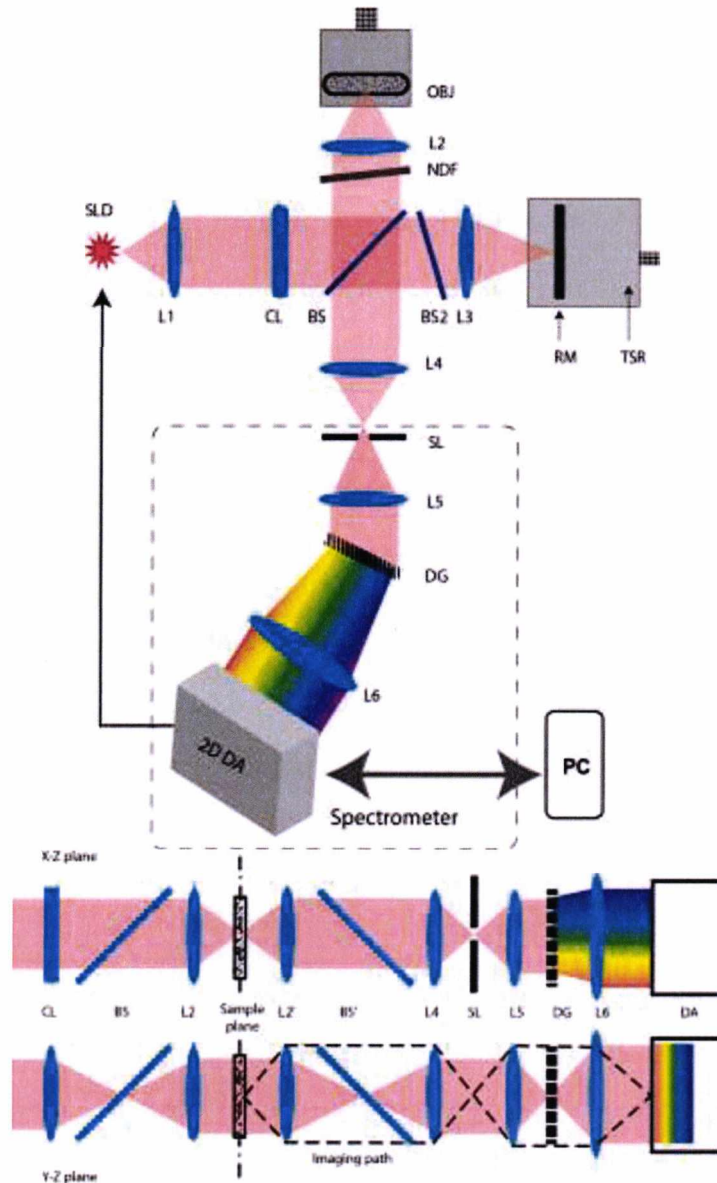


Figure 5.1. Top: schematic diagram of LF-CS-OCT system. SLD: superluminescent diode, SLD-381, L1: Achromatic lens, focal length: 32.9 mm, CL: cylindrical lens, focal length: 10 cm, BS: polarisation insensitive beam-splitter, L2, L3, L4, L5, L6: lenses with focal length of 30, 30, 100, 150 and 150 mm respectively, NDF: neutral density filter, DG: transmission diffraction grating, CCD: Andor Ixon DV877 EMCCD. Bottom: Perspective of optical paths in 'x-z' and 'y-z' planes. In the horizontal plane, the detection arm is configured as a spectrometer. A channelled spectrum is produced for each pixel within the line projected over the objet target. In the vertical direction, the system operates as an imaging system.

### 5.1.2 Resampling

Since the diffraction grating spectrometer does not disperse the spectrum linearly in wave number,  $k$ , a wavelength dependent data resampling [205] is implemented similarly to the procedure used in the full-field Swept-source OCT method (see Chapter 4). FT is applied to each resampled spectrum from the 2D camera. An original and a linearised phase graph are displayed in Figure 5.2 (a, b). Experiments show that resampled data present an average improvement of 7 dB in the peak value of the PSF over the results from original spectrum data. The spectrum resampling also ensures a consistent depth resolution across the entire depth range, which is confirmed by Figure 5.2 (d). A LabVIEW program was written by for the purpose of camera control and data processing.

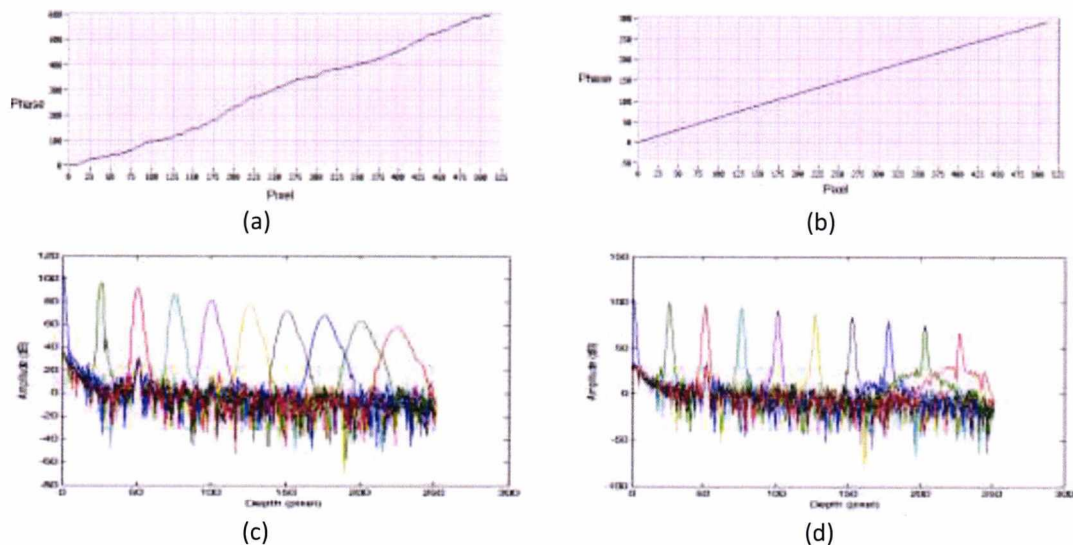


Figure 5.2. CS phase from a single spectrum measurement using a glass-air interface, before (a) and after (b) linearization; PSF versus depth obtained without (c) and with (d) spectrum resampling.

### 5.1.3 Spatial Filter

The spatial filter between the interferometer and the spectrometer (Fig. 5.1.) rejects the stray lights from regions outside the focus. The output beam of the interferometer was shaped as a vertical line, about 7 mm long. The mechanical slit used in the spatial filter is 15 mm long and its width is adjustable. The slit width plays an important role in refining the contrast of the CS; an evaluation of the effect the spatial filter was performed. The relationship between the A-scan peak values measured from a mirror at OPD of  $100 \mu\text{m}$  versus the width of the slit is shown in Figure 5.3. The CCD was saturated when the slit was wider than  $750 \mu\text{m}$ . From the

data collected from 50  $\mu\text{m}$  to 750  $\mu\text{m}$ , the maximum intensity was obtained at around 550  $\mu\text{m}$ . The peak of the A-scan is related to both the contrast of the CS and the incident light power. Larger opening make the intensity decrease due to washout of the channelled spectrum, while for smaller opening, the value is low due to low transmission and small irradiance. The experiment results show that increasing the width of the slit above 550  $\mu\text{m}$  does not change the peak value though increase the optical power, therefore 550  $\mu\text{m}$  is considered as the upper limit of the optimal slit width in the following measurements. For most measurements, the slit was opened between 200  $\mu\text{m}$  and 500  $\mu\text{m}$  to attain the CS with the maximum contrast with sufficient optical power.

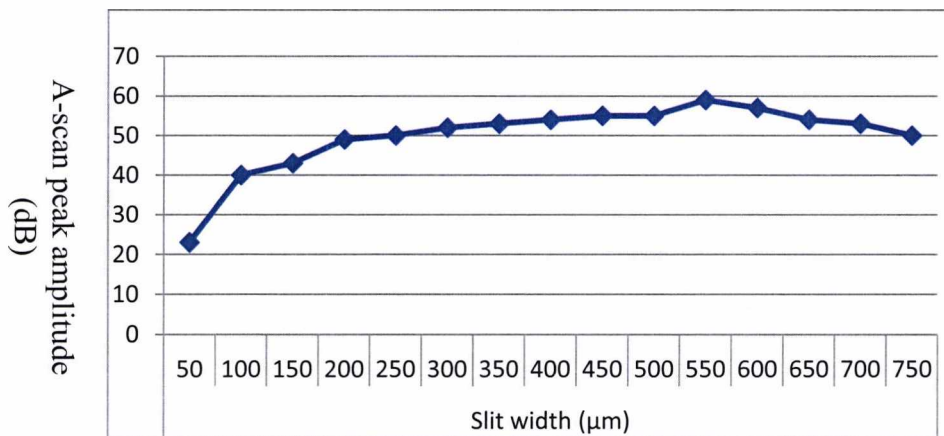


Figure 5.3. The amplitude of the A-scan peak when a mirror was used as a sample versus the width of the spatial filter slit.

#### 5.1.4 Measurements with Andor DV877 camera

##### 5.1.4.1 Sensitivity Roll-off

To evaluate the sensitivity roll-off of the LF-FD-OCT in depth, a microscope slide was firstly used as the object. The experiments were performed by fixing the object and moving the reference mirror axially to change the OPD value. Figure 5.4 shows the A-scans obtained by moving the reference mirror axially around the zero-OPD position towards the positive and negative depth value. Each CS is sampled by 512 pixels, which produces 256 point in depth after the FT. The single-side depth range is  $\sim 2.3$  mm. The measurement was performed over the double-side depth range

(~4.5 mm). Signal attenuation of 6 dB is achieved at 1.65 mm and 1.34 on the positive and the negative OPD side respectively.

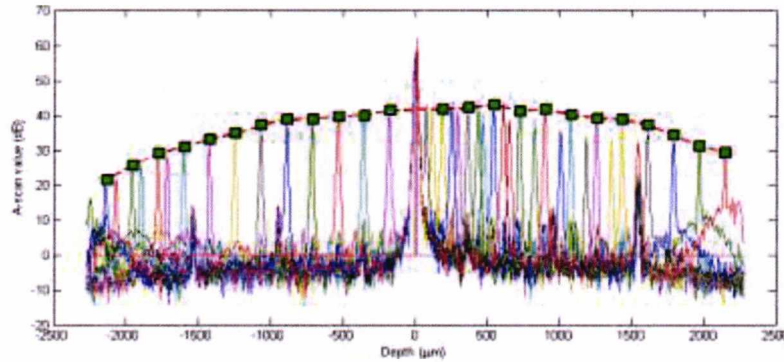


Figure 5.4. A-scan peak values measured from a glass-air interface versus a depth range of 4.5 mm. Note some peaks due to the second surface of the glass plate are visible on the positive OPD side.

#### 5.1.4.2 Exposure Time

With a certain NDF in the reference beam and a fixed slit opening in the spatial filters, the signal amplitude of LF-FD-OCT is dependent on the exposure time and the power of the optical source. For LF-FD-OCT, because the optical power is distributed to a line field, which reduce the optical density in each measuring point on the sample, maximum optical power is usually required from the source; therefore, the main parameter limits the signal amplitude is the exposure time. Ideally, the relation between signal amplitude and the integration time should be linear. However, in reality, long exposure time may suffer from mechanical shaking or object movement and washout the fringes in CS; when small exposure time is used, the detector readout noise may contribute to the total noise more than the shot noise does, which lead to an nonlinear relationship between the signal value and the integration time. In order to investigate this relationship, the dependence of the OCT signal on the exposure time was performed by measuring OCT A-scan signals from a microscope glass slide at a depth position, OPD = 500  $\mu\text{m}$  - 700  $\mu\text{m}$ . Assuming shot noise dominates over other noise sources, doubling the exposure time should lead to 6 dB enhancements and 3dB rise in the signal and noise respectively. Figure 5.5 illustrates the results of experiments with 5 different exposure times. The results show that for 16 times of exposure time (4 steps), a signal enhancement of 24 dB is obtained, corresponding to 6 dB per doubling; the

background (noise) level rises by 12 dB, 3 dB per doubling, which meet the expectations.

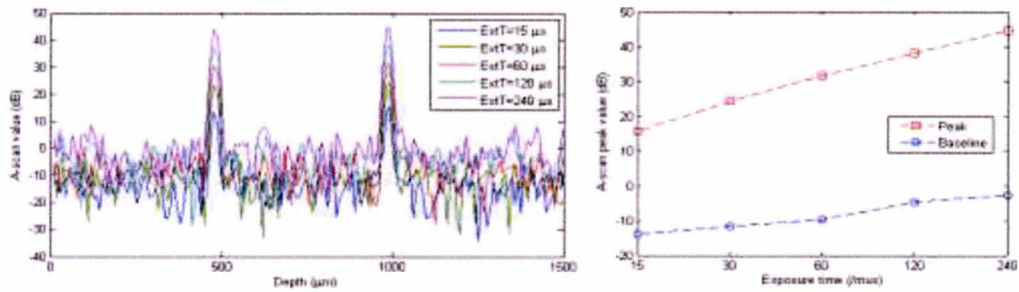


Figure 5.5. Left: A-scans of the microscope slide showing two peaks corresponding to the glass-air and air-glass interface for different exposure times of the CCD camera. Right: the peak value and background average value of the above A-Scan data. The background data is an average of the region between two peaks on the baseline.

The sensitivity roll-offs with different exposure times from a single reflective object are illustrated in Figure 5.6. Irrespective of the exposure time, the same decay slope was obtained, similar to the previous results. The signal/noise variations are rather constant over the depth range of 1.5 mm.

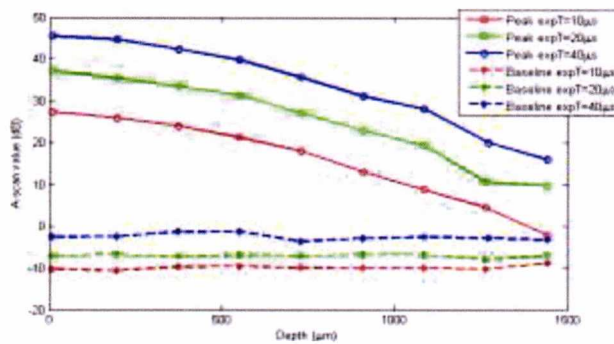


Figure 5.6. Peaks of PSF roll-off and baseline value versus object axial position with, acquired with three different exposure times: 10 μs, 20 μs and 40 μs.

### 5.1.4.3 Reference Power

NDFs were used to balance the light power between the two interferometric beams and make good use of the dynamic range of the camera. To evaluate the signal/noise value of the LF-FD-OCT versus the reference power, the interference signal was measured from a thicker microscopy glass slide at a depth position, OPD = 0.3 mm - 1.3 mm, with 7 different reference powers, introduced by using NDFs of different optical densities (ODs). Transmission through the filter is denoted as:

$T = T_0 10^{-n}$ . Figure 5.7 (left) demonstrates the relation between the A-scan peak amplitude of FD-OCT and the reference power. The drop of signal amplitude should be 5.2 dB from OD = 0.04 to OD = 0.3 and 6 dB for the rest intervals (OD changes for 0.3) according to the relation:  $\Delta S = 20 \log \Delta OD$ , where  $\Delta S$  and  $\Delta OD$  stand for the variation of the signal value and the OD value. Figure 5.7 (right) shows the two peaks of the A-scans and noise level obtained with these 7 NDFs.  $\overline{\Delta S}$  are measured as 5.1 dB, 5.3 dB, 5.1 dB, 5.0 dB, 4.3 dB and 3.8 dB respectively. The noise drops are 3.9 dB, 4.3 dB, 3.2 dB, 2.4 dB, 1.1 dB and 0.5 dB. The best SNR is obviously obtained with minimal OD; however the results show the noise drop is less linear than the signal drop. With large OD, the recorded image value on the 2D camera is low and therefore the read-out noise and the dark noise dominate the shot noise and present milder noise drops. As seen in Figure 5.7 (left), there is a slight horizontal shift of the peak positions due to the thickness variation of the NDFs.

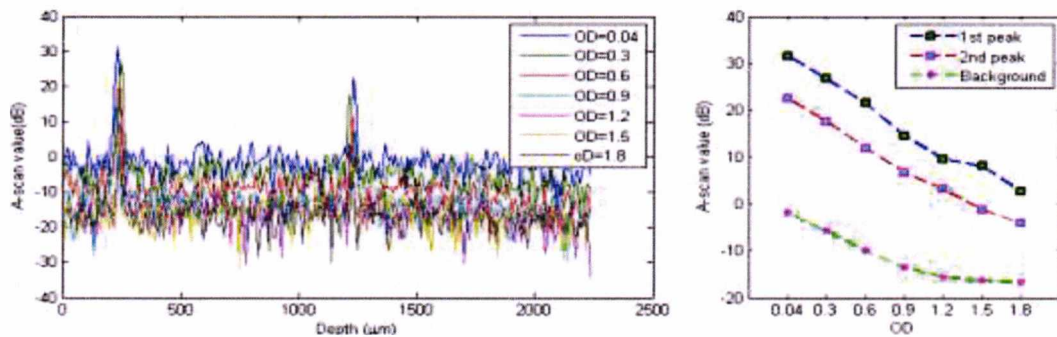


Figure 5.7. A-scans signal (left) with the peaks and background values (right) measured from a microscope glass slide with 7 different reference powers, controlled by changing the ODs of the NDF in the reference path.

## 5.1.5 Using Mikrotron EoSens MC1362 CMOS camera

### 5.1.5.1 Sensitivity Roll-off

The experiments were repeated on a different camera, Mikrotron EoSens MC1362, which has a CMOS sensor with a maximum frame rate of 500 fps. The results (Figure 5.8) show a similar profile shape to that acquired by the CCD. Because the CMOS sensor has smaller size pixels (and so a larger number of pixels within the same beam footprint) to resolve the spectrum, the depth range is improved in comparison to the CCD set-up. The 6 dB depth range extended to more than 2 mm

in both positive and negative OPD sides. The acquisitions integration time of the CMOS is 120  $\mu$ s.

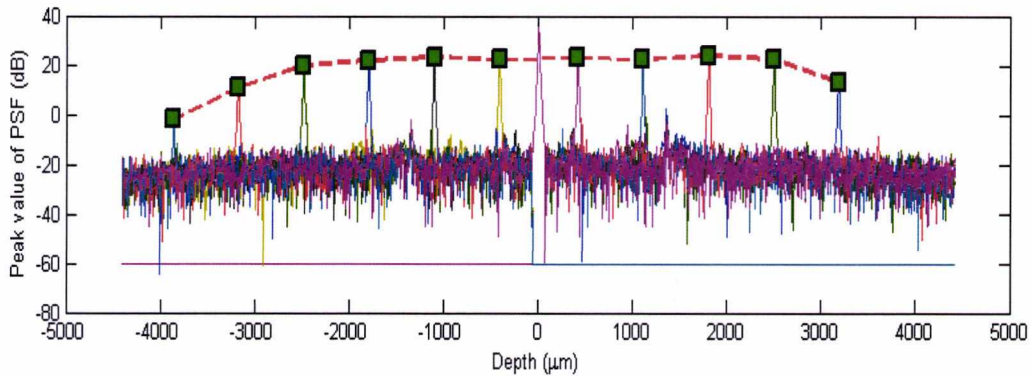


Figure 5.8. A-scans measured from a glass-air interface using a CMOS camera (Mikrotron EoSens MC1362) as the sensor in a depth range from OPD = -3.9 mm to OPD = 3.2 mm.

### 5.1.5.2 Exposure Time

With the Mikrotron MC1362, better performance in sensitivity 'roll-off' are obtained (Figure 5.8 and Figure 5.9) compared with that obtained by Andor DV887 (Figure 5.4 and Figure 5.6) due to larger number of pixels and finer spectrum resolution. Ideally, the increase of exposure time from 30  $\mu$ s to 60  $\mu$ s should expect 6dB signal enhancement to the signal and 3dB to the noise; further increasing to 90  $\mu$ s, the signal and noise level should rise for 3.5 dB and 1.8 dB respectively. The experiment results in Figure 5.9 meet the expectation sufficiently well.

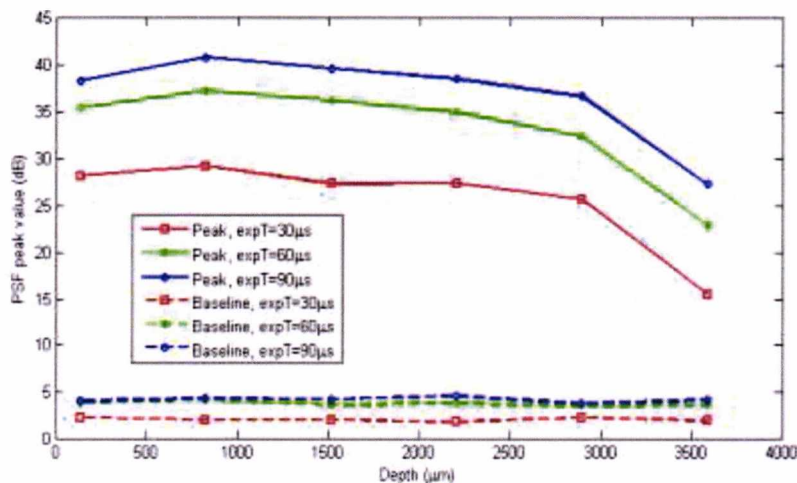


Figure 5.9. Signal peak roll-off curves and background values versus axial position of target, an air-glass interface, recorded by Mikrotron EoSens MC1362 with three different exposure time: 30, 60 and 90  $\mu$ s.

### 5.1.5.3 Reference Power

Measurements with different NDFs at increasing depths were repeated with the CMOS camera. Measurements of peak values of FD-OCT from the air-glass interface were performed as the object is moving axially away from  $OPD = 0$ , repeated with increasing OD in the NDFs used in the reference arm. The results are shown in Figure 5.10. The focus of object beam was placed at the farthest end of the depth range, therefore with the object moving axially towards to lens, the intensity of the total returning light from the object (measured with reference path blocked) improves. This arrangement of the object beam produces a rather flat profile of the A-scan peaks in depth, though the lateral resolution might be sacrificed. 6 NDFs were used to alter the ratio between the object and the reference power. As shown on Figure 5.10 (a), the depth profiles of the A-scan peak present two different shapes due to the ratio changing. From Figure 5.10(b), we can see the object power (area in blue) is similar to the reference power (lines) when  $OD = 0.6$ . When the power of the reference beam is much lower than that of the object, the signal intensity increases in depth due to the fact that the large power in object beam dominates the interference; however such a case is not applicable in real OCT imaging with scattering objects.

The average signal drop  $\overline{\Delta S} = 3.1$  dB, 6.9 dB, 9.2 dB, 4.8 dB and 7.5 dB with the OD increasing for  $OD = 0.3$  to  $OD = 1.8$  with an interval of 0.3. The variations of  $\Delta S$  due to reference power are quite large, which is possibly related to the non-linearity of the CMOS's response. Doubling the reference power by reducing the OD from 0.6 to 0.3 only presents 3.1 dB enhancement to the signal value; while halving the reference power ( $OD = 0.6$  to  $OD = 0.9$ ) leads to a signal drop of 6.9 dB; therefore  $OD = 0.6$  presents the optimal interference signal, which can be confirmed by Figure 5.10 (b). It is obvious that the reference power is similar to the object power when  $OD = 0.6$ . In practice, the selection of NDF should consider using the most of the dynamic range of the camera; however, balanced should be made with other factors including, exposure time, focus position and width of the spatial filter.

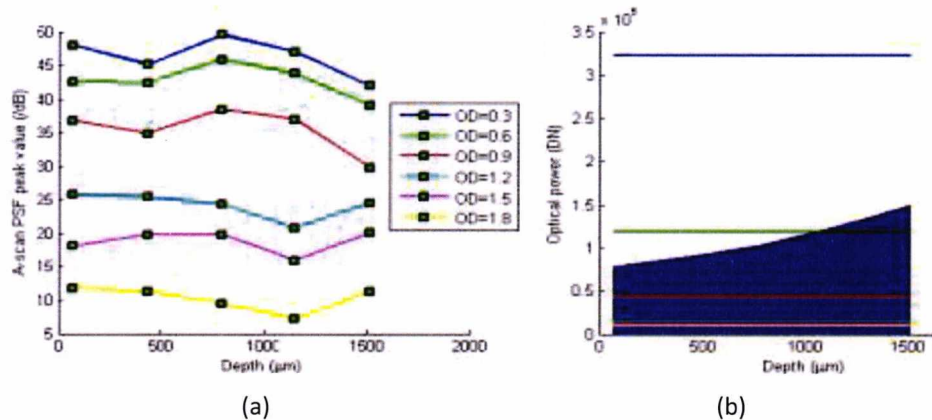


Figure 5.10. (a) The A-scan peak values of LF-FD-OCT versus depth with different reference power controlled by changing the OD of the NDF in the reference beam; (b), the power of reference beam (lines) with 6 different NDFs and object power (area) collected at different depth positions, these two group of data were acquired by the camera directly.

### 5.1.6 Comparison

A comparison of the system performance of the LF-FD-OCT using two cameras, Andor Ixon DV877 EMCCD and Mikrotron EoSens MC1362 CMOS is summarised in Table 5.1. The SLD output power is 5 mW. With a 50-50 beam-splitter, half of the light power is distributed into 512 channels for Andor, each channel uses less than 5 μW on average. With the CCD working at 17 fps, the equivalent A-Scan rate is 8.7 kHz. The sensitivity is measured by using a mirror as object and subtracted the average background (noise) value from the measured A-scan PSF.

Table 5.1. Overview of LD-FD-OCT technical performance using two cameras

Parameters	Andor DV887 (Exposure time = 300 μs)	EoSens CMOS MC1362 (Exposure time = 120 μs)
Spectral resolution	0.078 nm/pixel	0.043 nm/pixel
Max depth range	2.3 mm	4.2 mm
Depth resolution	17 μm	17 μm
B-scan width	7 mm	8.6 mm
Lateral resolution	36 μm	24 μm
Sensitivity	63 dB	60 dB
6dB depth range	~1.5 mm	>2.2 mm
Max frame rate	17 fps (8.7 k A-Scans /s)	500 fps (500 k A-Scans /s)

## 5.1.7 Examples of B-scans images

### 5.1.7.1 Skin

A number of biological tissues were imaged to test the performance of the LF-FD-OCT. The first *in-vivo* measurement was for finger skin that is scattering and the stratum corneum, at the top, shows higher reflectivity than the tissue inside. Figure 5.11 presents several *in-vivo* B-scan images collected from four of my fingers, the difference of epidermis thickness are noticeable. Sweat ducts can be observed in Figure 5.11 (c).

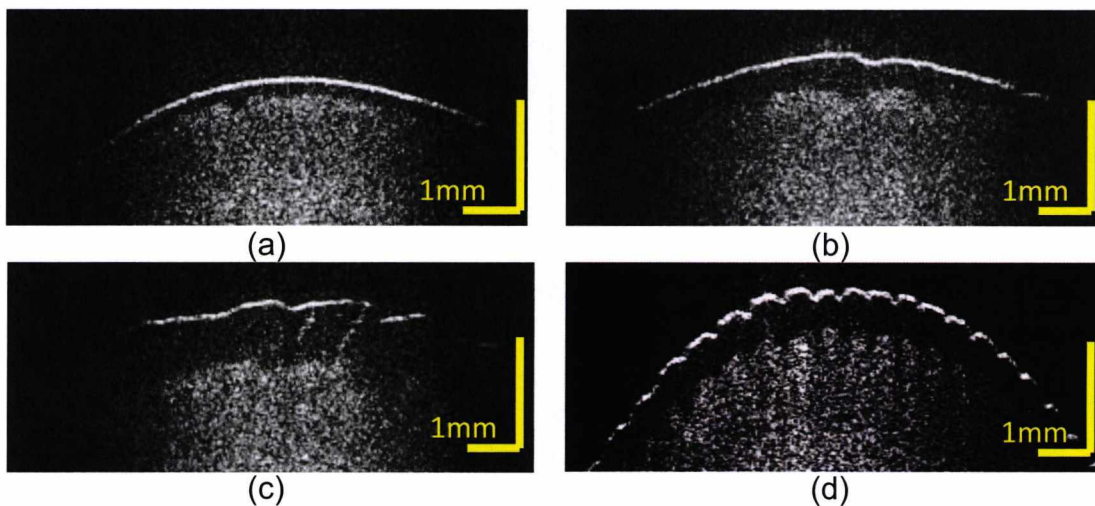


Figure 5.11. OCT B-scan images collected from fingers of the author: (a) little finger; (b) middle finger; (c) thumb and (d) index finger.

### 5.1.7.2 Teeth

B-scan images of a human tooth excised from a patient are shown in Figure 5.12. Metal fill-in material and its boundaries can be located in the left image. Internal inhomogeneities structures of a different part of the tooth are observed in the image on the right.

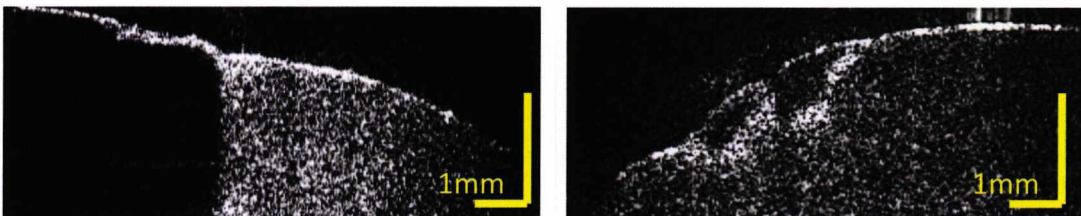


Figure 5.12. In-vitro B-scan images from different parts of human teeth, left: metallic fill-in; right: scattering features.

### 5.1.7.3 Fruit Fly Larva

*In-vivo* imaging on imaging fruit fly *Drosophila melanogaster* larvae was performed and some cavities and layer structures can be seen in the B-scans in Figure 5.13. The imaging quality is reduced due to the periodic movement of the live larva. In the developing stage, the larva executes a combination movement due to slow lateral peristaltic force and axial displacements of fast heartbeat.

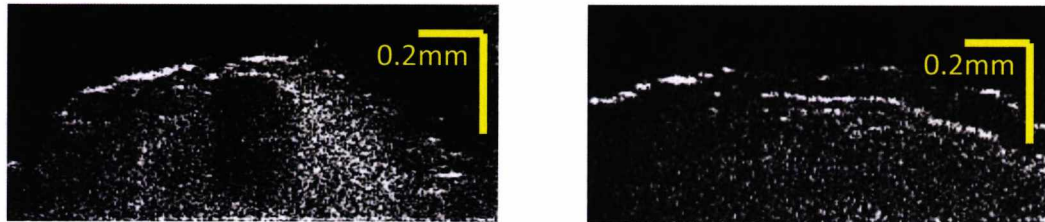


Figure 5.13. *In-vivo* B-scan images from a fruit fly *Drosophila melanogaster* larva, Left: a cavity structure can be observed in the middle of the image; right: layer structures observed in sagittal planes of the larva body.

## 5.2 Using Extended Light Sources in LF-FD-OCT

High spatial coherence is required for scanning OCT to attain good contrast of interference-modulated channelled spectrum; therefore, a single-mode light source, e.g. an SLD coupled to a single-mode fibre or a broadband femto-second laser [50] is required for illumination; thus, a SLD is used as the light source in our LF-FD-OCT setup. However, multi-mode or extended light sources have been used in parallel-detection OCT [118, 136, 144, 206-208]. In this section, trials of using multi-mode or extended light sources in the LF-FD-OCT set-up are described.

### 5.2.1 Extended Light Sources for OCT

The advantages of using multi-mode light in parallel OCT have been recognised, including improving resolution [118, 137, 209] and reducing speckles [180, 183, 210]; therefore thermal lamps and Xenon lamps [211-213] have been extensively used in FF-OCT [136, 137, 147, 206]. Using extended light in FD-OCT, have been reported recently in both scanning system [214] and in parallel set-up [207, 213]. An extended source is a type of multi-mode light source, whose angular size exceeds the resolution of the instrument being used to observe it [215]. All types of

extended sources, including surface emitting LED, incandescent light bulb, gas discharge lamp (e.g. a Xenon lamp) produce multi-mode light.

In our LF-FD-OCT system, the single-mode SLD exhibits spatial coherence in all directions. This is important for the dispersion direction (see the 'x-z plane' in the bottom of Figure 5.1), in our case, horizontally, because high spatial coherence is required to maximise the visibility of the CS. However, the spatial coherence is not required along the parallel direction (vertical), which leads to cross-talk between parallel channels. In the B-scan images this appears as speckle noise, which can be seen in Figure 5.11 - Figure 5.13. As discussed in Chapter 3, along the parallel direction, multi-mode radiation can be applied to reduce cross-talks. Therefore an ideal light source for LF-FD-OCT should have perfect spatial coherence along the dispersion direction (horizontal) and be incoherent in the parallel direction (vertical). A solution to approach these requests is given by using extended light sources that have line shapes.

### **5.2.2 Linear Light Sources**

An extended light source emits transversal multi-mode light in all directions, therefore, to obtain spatial coherence in the dispersion direction is challenging. Generally, that the smaller the emitting area of the light source, the better the spatial coherence and the better visibility of the interference fringes can be obtained in FD-OCT [206]. Therefore, a thin linear extended source, for example, a straight filament of a incandescent bulb or a straight electric arc from a gas discharge lamp, is possibly capable of providing multi-mode linear illumination.

In order to preserve the spatial coherence along the dispersion direction, the width of the linear sources should be keep at minimal; however, in reality, these sources cannot be very thin (compare to the dimension of a single-mode source), thus partially coherent light may lead to an increase in the DC terms and a reduced contrast of the CS obtained by the FD-OCT. The A-scan signal is thus lowered, depending on the degree of the spatial coherence. Improving spatial coherence from extended sources was demonstrated by Dennis Gabor [216], the inventor of holography, who passed monochromatic light from a mercury-vapour lamp through

a pinhole spatial filter and successfully produced light with improved spatial coherence. When a wave with finite coherence area is incident on a pinhole, the wave suffers diffraction on the pinhole. Far from the pinhole the emerging spherical wavefront is approximately flat. The coherence area is then increased while the coherence length is unchanged; however, the effective brightness of the source is significantly reduced.

### 5.2.3 Visibility of Channelled Spectrum

In order to improve the spatial coherence in dispersion direction using a linear light source in our LF-FD-OCT set-up, a slit is required as a spatial filter. Reducing the opening width of the slit in front of the light source will improve the spatial coherence in dispersion direction. An evaluation method of spatial coherence is demonstrated by using the Young's double slit experiment [38]. In my LF-FD-OCT with extended light sources, the visibility of the channelled spectrum will be a product of 3 factors: the temporal coherence factor (OPD), the spatial coherence factor and the polarisation. The two interfering terms in the self correlation term can be assumed as having exactly the same polarisation, as the two glass plates are inclined at the same angle to the incident beam direction (and so the same polarisation, apart from some  $\pi$  phase factor). Therefore, by fixing the object at a constant OPD, the spatial coherence of the light source in dispersion direction can be evaluated by examining the contrast of the CS from the spectrometer. The cross-talk is assumed as negligible when reflective objects are used as the target.

To evaluate the contrast of the channeled spectrum, the interference visibility is to be calculated using Eq. 2-14:

$$\gamma = \frac{I_{max} - I_{min}}{I_{max} + I_{min}} = \frac{A_{p-v}}{2\bar{I}} \quad (5.1)$$

where  $I_{max}$  and  $I_{min}$  denote the value of the local peaks and troughs of the CS respectively;  $A_{p-v}$  represent the peak-to-trough amplitude and  $\bar{I}$  denote the average value of the peaks and the troughs. The  $A_{p-v}$  and  $\bar{I}$  can be obtained by a

numeric algorithm, composed by noise reduction, signal decomposition and fringe envelope extraction. In the signal decomposition step, the DC trend of the CS is separated from the AC fringe waveform; thereby  $A_{p-v}$  can be obtained from the double of the AC waveform envelope; while  $\bar{I}$  is the DC trend of the spectrum. An example of 2D CS and the retrieved data, including the CS (blue), the decomposed DC (green) and AC waveform (red) with its envelope are shown in Figure 5.14. This example image was obtained from an air-glass interface using a Xenon flashtube as the light source of the LF-FD-OCT, which will be described in following section. The average visibility is  $\bar{\gamma} = 24.1\%$ . In the following examples, all visibility values are calculated with the same algorithm.

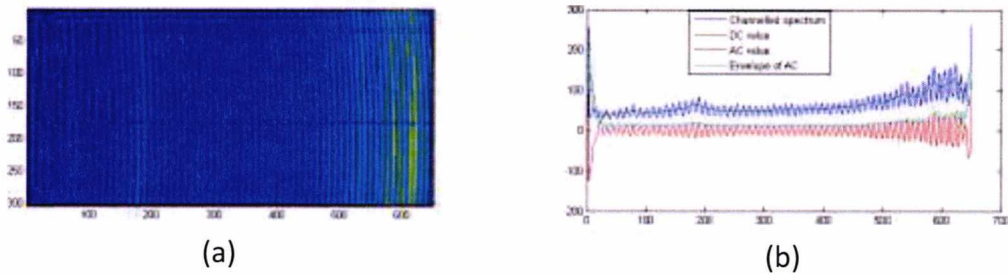


Figure 5.14. (a) A image of channelled spectra array recorded by the 2D camera in the LF-FD-OCT system from a single air-glass interface; (b) the data extracted from a row of the spectrum to evaluate the visibility of the channelled spectrum, including the original CS (blue), the low frequency component of CS (green) which can be obtained by  $(I_{max} + I_{min}) / 2$ , the high frequency component (fringe) of CS (red) and the envelope of the fringes (cyan), which is acquired by  $(I_{max} - I_{min}) / 2$ .

#### 5.2.4 Extended Light LF-FD-OCT Set-up

The original Line-field FD-OCT system was modified to accommodate light sources with transverse multimode radiation, including a tungsten incandescent lamp that has a linear filament, a red LED and a xenon flashtube, the latter two are both integrated on a commercial digital camera body. An SLD (SLD-675, Superlum) with a central wavelength of 675 nm and FWHM bandwidth of 8.8 nm was used to aid the alignment and present a reference to be compared with the results of the incoherent light sources.

A slit, SL1, was inserted into the light source arm of the LF-FD-OCT system in vertical direction, between two lenses L11 and L12, as shown in Figure 5.15. The

linear light sources were mounted vertically and were focused by L11 onto the SL1. Ideally, each entrance point on SL1 illuminate one channel of the LF-FD-OCT. When the LED (has a 2D area) or the SLD were used; a cylindrical lens with a focal length of 10 cm was used between L2 and the beam-splitter, BS, similar to the original LF-FD-OCT set-up (Figure 5.1). The camera, Retiga EXi-fast 1394, is a monochrome CCD camera with  $1392 \times 1040$  pixels, 10 frames per second at full resolution, 12 data bit and pixel size of  $6.45 \times 6.45 \mu\text{m}^2$ .

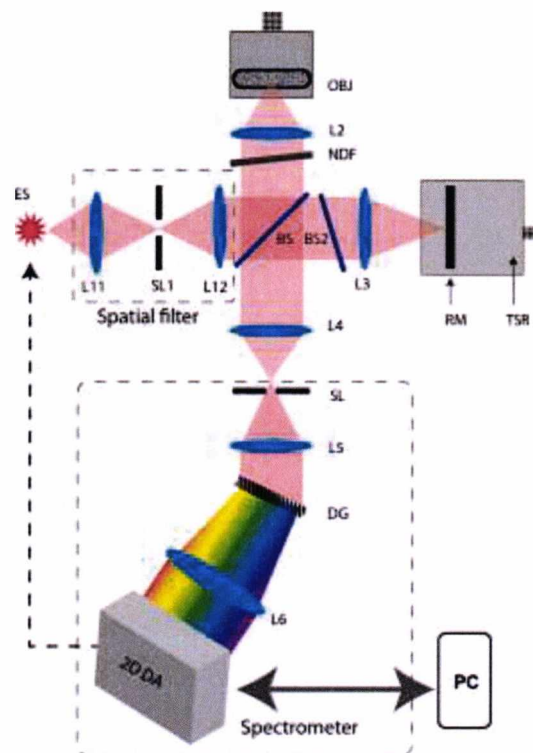


Figure 5.15. Schematic of the LF-FD-OCT. ES: an extended light source; a spatial filter is composed by two achromatic doublets, L11 ( $f=50$  mm) and L22 ( $f=100$  mm) with a slit, SL1, oriented vertically. 2D DA, CCD monochrome camera, Retiga EXi-fast 1394,  $1392 \times 1040$  pixels, 10 fps, 12 bit and pixel size  $6.45 \times 6.45 \mu\text{m}^2$ ; the rest parts are identical to that in Figure 5.1.

In the tests with different sources, we used an air-glass interface of a glass tube as the object. The surface of the tube was firstly illuminated by the SLD-675 as the light source. The visibility of the channelled spectrum was measured as  $\bar{\gamma} = 75.5\%$  from the spectrum. The CS obtained from the air-glass interface using the SLD is displayed in Figure 5.16. The OPD is about 0.1 mm.

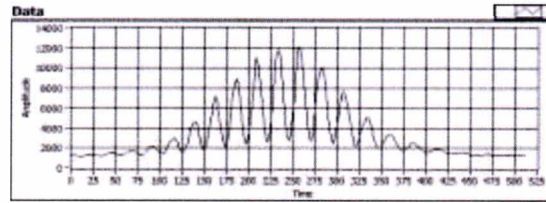


Figure 5.16. A channelled spectrum obtained from a glass-air interface using the SLD675 as the light source.

### 5.2.5 Incandescent lamp

The first extended source we tried was an incandescent light bulb with a linear filament. The tungsten filament incandescent lamp is a simple thermal source that exhibits a smooth, continuous spectrum from about 400 nm to over 1000 nm. The filament and the measured spectrum are displayed in Figure 5.17. The linear filament has a thickness smaller than 0.5 mm and is ~90 mm long.

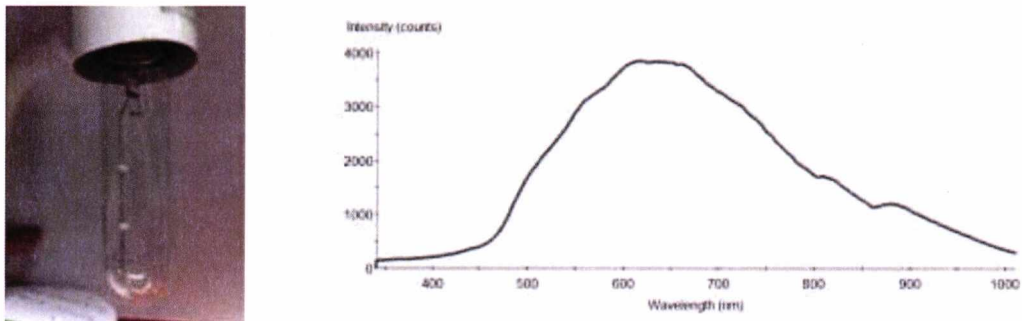


Figure 5.17 Spectrum (right) emitted by a straight filament (left) of an incandescent bulb (130 V, 30 W)

The linear filament of the incandescent lamp was inserted as the light source in Figure 5.15, oriented vertically. The width of the slit was set at 50  $\mu\text{m}$  in most experiments. The CS obtained using the linear filament as the light source and the glass-air interface as object can be observed in Figure 5.18. 15 peaks and 15 valleys are observed, which give an average fringe visibility of 2.8% using the algorithm described in Section 5.2.3. This value is low for any meaningful measurement. The filament is subject to vibrations at a frequency of a few hertz as it is operating. The vibrations handicaps further experiment because the slit is only open for 500 $\mu\text{m}$ ; the vibrations produce large instability to the measurements.

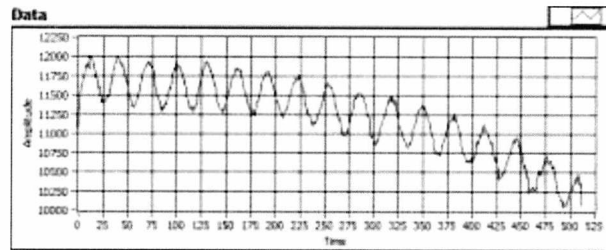


Figure 5.18. Channelled spectrum from a single air-glass interface using a linear tungsten filament as the light source, recorded by Retiga CCD.

## 5.2.6 LED

The second extended light source that was tested was a LED from a compact digital camera, Canon PowerShot S500 (or Canon Digital IXUS 500). The spectral characteristics of LED emissions are similar to that of the SLDs at similar wavelengths. The spatial coherence of LEDs depend on their micro-fabrication structure [217], for example, the edge-emitting LED (EELED) have a smaller area (diameter of tens of micron) and much improved spatial coherence than normal surface-emitting LED (SELED). In fact, SLD is a type of EELED that operates in the super-luminescence mode. SELED has a large emitting area, thus provides wide angle and multi-mode illumination. LEDs have a fast temporal response, less than one microsecond compared to milliseconds that is needed by Xenon lamp [218]; therefore allow stroboscopic illumination scheme.

The LED on Canon S500 body was used as the light source and CS is recorded by Retiga CCD. In fact, the imaging sensor of Canon S500 can be used as the detector array in the spectrometer at the same time by devising proper interface optics. The separate camera was used in the experiment for the convenience of alignment. A spectrum with a central wavelength of 610 nm and 45 nm FWHM bandwidth was measured. Because the LED has a 2D emission area, a cylindrical lens was inserted (similar to Figure 5.1) between a pin-hole (instead of the slit, SL1) and BS. The CS and the A-scan measured from the air-glass interface are shown in Figure 5.19. The average visibility of the CS is 27.3% from the central part (5 peaks) of the spectrum. This result is better than that of the incandescent lamp. The main limitation in using this LED in further experiments is its low brightness. In order to obtain good spatial

coherence from the relatively large square emission area, a large proportion of the emission was wasted by the spatial filter.

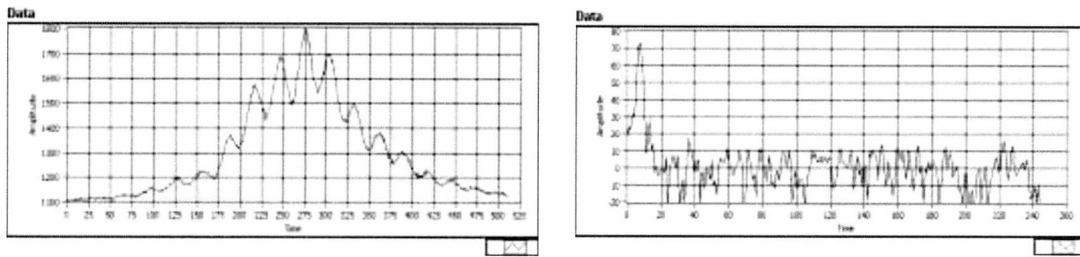


Figure 5.19 Channelled spectrum (left) and A-scan (right) obtained from the single air-glass interface using a 610 nm LED as the light source in the LF-FD-OCT.

## 5.2.7 Xenon Flash lamp

For OCT applications, short-arc continuous Xenon lamp has been tested and compared with a thermal tungsten halogen lamp in a time-domain LCI set-up [206] and the author concluded that a xenon lamp has higher radiation or energy flux than halogen lamp though the contrast of OCT images may be reduced due to the broadened baseline in the PSF which is a result of the spikes in the spectrum of the xenon lamp. For FD-OCT, the spectral spikes could have saturated some parts of the detector array, while the rest part of the spectrum remains low in value, which in fact reduce the dynamic range of the measurement.

Nowadays, most consumer-grade digital cameras have integrated a built-in xenon flash lamp. There are also independent flash units that could be used together with the camera that produce large optical power. Xenon flash lamp produces pulses of short duration, typically a few milliseconds [219]. Similar to thermal lamps, the Xenon flash lamps produce continuous-spectrum output from 250 nm to over 1  $\mu\text{m}$ . However, on top of the thermal-like spectrum, there are several peaks at 450 nm and between 650 nm and 1000 nm [220]. We selected two xenon flash lamps to compare the spectral shapes. Spectra of an integrated flash lamp on the body of the Canon S500 and a more powerful independent flash unit Vivitar 285HV were measured as shown in Figure 5.20. In the Vivitar's spectrum, the peaks between 800 nm and 900 nm saturate the camera before sufficient spectrum data are recorded; thus only little exposure level is allowed, which cancels the advantage of the powerful output. The Canon flash delivers a relatively smooth

spectrum, especially in the NIR region; therefore, FD-OCT data were acquired with the Canon flash.

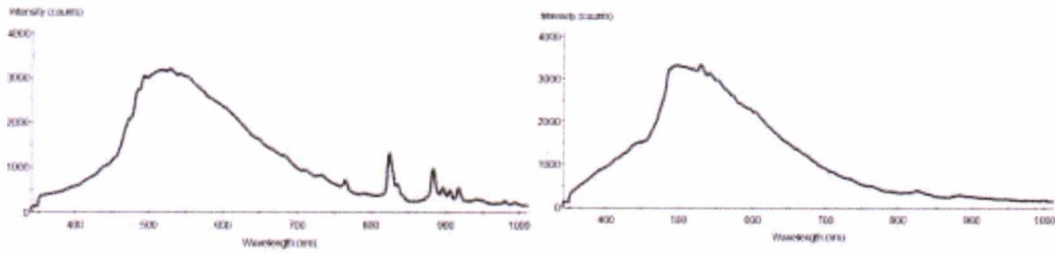


Figure 5.20. Measured spectra of two xenon flashtubes: Vivitar 285HV xenon flash (left) and Canon Ixus S500 integrated flashtube (right).

The lens and the diffuser in front of the Xenon tube were removed (see Figure 5.21. left) and the glass tube was used as the target. Sampling the bandwidth from about 500 nm to 700 nm, a CS with a visibility of 21.2% is obtained as shown in Figure 5.21. right.



Figure 5.21. Left, naked Xenon flashtube; right, recorded channelled spectrum due to the interference between the two surfaces of the microscope slide.

### 5.3 Using Consumer-grade Digital Cameras in LF-FD-OCT

Our goal is to evaluate the possibility of using the lights and the imaging sensor on a DSLR camera body as the light source and the detector in LF-FD-OCT. To do this, several low-cost cameras were evaluated with the extended sources.

OCT developers prefer scientific cameras that have high sensitivity, high dynamic range and low noise sensor. From Chapter 3, we know that a high dynamic range is important to obtain sufficiently large interference signal from the background. Technology of semiconductor imaging sensor has been developed rapidly in the last two decades. A large number of camera manufacturers are competing to promote new CCD and CMOS cameras with high-speed, low-noise, versatile functions in comparatively low cost, especially for the commercial digital

single-lens reflex camera (DSLR) and the machine vision camera markets. Most DSLRs, especially the mid-low grade devices have an LED and a flash-lamp integrated on the camera body; this has inspired us to attempt using a low-cost camera to replace the scientific cameras in LF-FD-OCT.

### 5.3.1 Challenges

Compared to the 2D cameras used in OCT research, consumer-grade DSLRs present higher noise values because the DSLRs are not hermetically sealed, when operating at ambient temperature, electrons in response to thermal excitation of the detector will be produced in addition to the captured photons. Additionally, the pixel size of DSLR is smaller than most scientific cameras. Most DSLR cameras use the sensor of a size ( $\sim 24 \text{ mm} \times 16 \text{ mm}$ ) similar to Advanced Photo System-Classic (APS-C) film. Because the camera manufactures are after pixel number more than pixel size, typical pixel size of modern DSLRs is a square with a length of  $4 \text{ }\mu\text{m}$  to  $6 \text{ }\mu\text{m}$ , whereas the majority of scientific cameras have pixel larger than  $10 \times 10 \text{ }\mu\text{m}^2$ . Large pixel area allows a larger quantum well thus better sensitivity and dynamic range. Commercial colour cameras have colour filter array (CFA) attached to the sensor, usually in the form of Bayer filters [221]. This element provides the capability to gather chromatic information by applying three optical band-pass filters onto each pixel. However, when these cameras are used in OCT, the QE of the sensor will be further reduced by about one third, which makes the camera less sensitive. Another feature of the commercial cameras is that they are equipped with 'anti-blooming' gates (see Chapter 3) to allow excess current to flow out of the pixel before the charges spills into adjacent image pixels. This feature reduces the fill factor of the sensor and leads to non-linearity response.

Modern DSLRs employ fast curtain mechanical shutter to enable very small exposure times. However, when it is synchronised with a flash unit, the shortest exposure time allowed by a DSLR becomes much larger, which is known as flash sync speed. For example, most DLSR have a minimal exposure time (shutter speed) of a fraction of a millisecond, however the flash sync speed is rarely shorter than  $1/500$  second. That means that when the flash is used together with the camera, the minimal exposure time is a few times of the minimal shutter speed. The reason

of this degradation is due to the shutter mechanism of the focal-plane shutters (in contrast to central shutter) used in DSLR. The focal-plane shutters have two blades moving in a settled sequence. When a very small exposure time was used, the second blade can start to move before the first one blocking the incident light beam. There is no problem when this fast movement is in the continuous illumination because there is a constant exposure duration on different regions of the sensor. However, the flash pulse is short, compared to the speed of the blade. When the flash is used, the pulse will generate a pattern of the moving blades at the instant of flash emission. To avoid this artefact, most DSLRs limit the minimal exposure time when synchronised with a flash unit. In some high-end DSLR, a leaf shutter is used instead, which allows the camera to be synchronised at a higher speed.

Commercial DSLRs have slow frame rate (normally a few fps at full speed) due to large number of pixels. The flash-lamp also needs a period of time to recharge its capacitor before the next emission. Thus LF-FD-OCT is more compatible because only a single frame is required to produce a B-scan OCT image.

### **5.3.2 Experiments**

The Andor EMCCD was replaced by three cameras in following experiments: a middle-grade industrial CCD camera, Retiga Exi-fast1394, an entry-level DSLR Nikon D80 and a middle-grade DSLR, Canon EOS 50D. Technical parameters of Andor, Retiga and Canon are listed in Table 5.2. Nikon D80 is a discontinued DSLR which is inferior to the Canon 50D.

#### **5.3.2.1 Retiga EXi-fast 1394**

Retiga Exi-fast 1394 is a CCD camera that offers 1.4 million pixels and integrates an internal electrical shutter that is helpful in the applications that require small exposure time. Generally, it is less sensitive than the Andor (without applying EM gain) and provides a relatively smaller dynamic range, 12 instead of 14 bits. The full well depth of Retiga is 18,000 e<sup>-</sup> in comparison to that of Andor, 192,000 e<sup>-</sup>, expected due to an area pixel smaller by a factor of more than 6. It is a useful intermediate step between the scientific cameras and commercial DSLRs. Due to

the larger number of pixels of Retiga, better spectrometer resolution and thus larger image depth is achievable.

Table 5.2. Parameters of the three cameras we used in the experiments

	Andor DV887	Retiga Exi-fast1394	Canon EOS 50D
Sensor type	E2V TECH CCD87	SonyICX285 CCD	Canon CMOS
Pixel number	512 × 512	1360 × 1040	4752 × 3168
Pixel size ( $\mu\text{m}^2$ )	16 × 16	6.5 × 6.5	4.7 × 4.7
Sensor size ( $\text{mm}^2$ )	8 × 8 $\text{mm}^2$	8.8 × 6.8	22.3 × 14.9
AD frequency (MHz)	5	20, 10, 5, 2.5	NG*
Max. frame rate (fps)	17	10	6.3
AD resolution (bits)	14	12	14
Full well capacity (e-)	192,132	18,000	NG
Read noise	35.52 e- @5MHz	8 e-	
Dark current	0.0058 15e-/pix/s (-92.9 °c)	0.15e-/pix/s (cooled)	
Linearity	< 1% over 14 bits	NG	
Response uniformity (%)	< 0.01	NG	
Minimal integration time	20 $\mu\text{s}$ in 1 $\mu\text{s}$ increment	10 $\mu\text{s}$ – 17.9 min in 1 $\mu\text{s}$ increment	1/8000-30 sec with 0.3/0.5 EV increment
Sensitivity	13.5 e- per AD count	NG	ISO 100-12800 with 0.3/(1 EV increment)
Single pixel	35.52 electrons		NG
Base level	718		
Binning	Any size	2×2, 4×4, 8×8	2(1.4×1.4), 2×2
(ROI) Region of interest	1×1 to full frame	1×1 to full frame	Full frame
Trigger mode	Internal/external/software	Internal/external/software	Software/wired/wireless/IR remote
Synchronisation output	TTL input and output	TTL input and output	PC sync flash terminal
Shutter	No	Integrated electronic shutter	Focal-plane mechanical shutter
Filter	UV coating	Removable IR cutting filter	Built-in low pass filter
Connection	Camera link	IEEE 1394 FireWire	USB 2.0
Extra	255 steps EM gain		Anti-dust coating

(\* 'NG' -- 'not given' by the manufacture)

We used all cameras in the original set-up (Figure 5.1) with a glass tube (air-glass interface) as the target to compare the decay with OPD in the A-scans (Figure 5.22). As expected, the system equipped with the Retiga camera offers a depth range double of that of the Andor. The signal is slightly lower than that of the Andor over the most of the depth range due to less data bits (12 compare to 14 in Andor) is available. Using the exposure time, 1ms, the sensitivity of the system equipped with the Andor is 7 dB higher than that of the Retiga. However, because of the high

spectral resolution, the value of A-scan peak obtained by Retiga surpasses that obtained with Andor over 750  $\mu\text{m}$  in depth. From this comparison, Retiga seems able to replace the sensitive Andor camera even for the same light source.

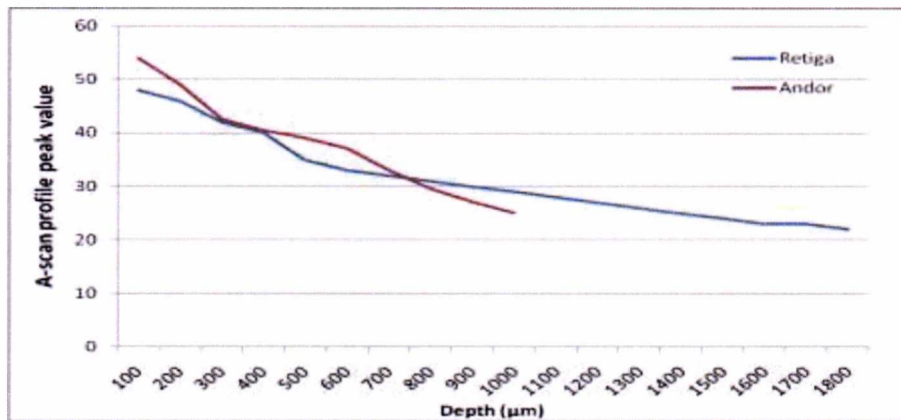


Figure 5.22. A-scan peak decays measured from an air-glass interface over the depth range of FD-OCT with two detector arrays: Andor DV887 and Retiga EXi-fast 1394.

### 5.3.2.2 Nikon D80

Nikon D80 is an entry-level DSLR model released in 2006. It has a Sony CCD sensor with 10 mega pixels. We used the LED from the Canon S500 as light source and the glass tube as the object to examine the visibility of the CS and to compare the results with the Andor. The recorded CS obtained with Nikon and Andor are shown in Figure 5.23. The average visibility of the central regions of the channelled spectrum obtained with Andor and Nikon are 27.3% and 18.3% respectively. This difference is possibly related to the alignment error, because Andor and Retiga have live view output to the PC that can help adjusting the alignment, whereas it is difficult to find the best focus position with Nikon D80 due to lack of live view. The alignment of Nikon was carried out by observing through the viewfinder on the camera body and by examining the recorded images repeatedly. Besides, random noise is seen in the channelled spectrum obtained by Nikon, which is expected due to a higher dark noise and the limited sensitivity. The preliminary result obtained using Nikon suggests that it is possible to employ commercial cameras in FD-OCT. To continue the test, we selected a more advanced DSLR with better sensitivity, the Canon 50D.

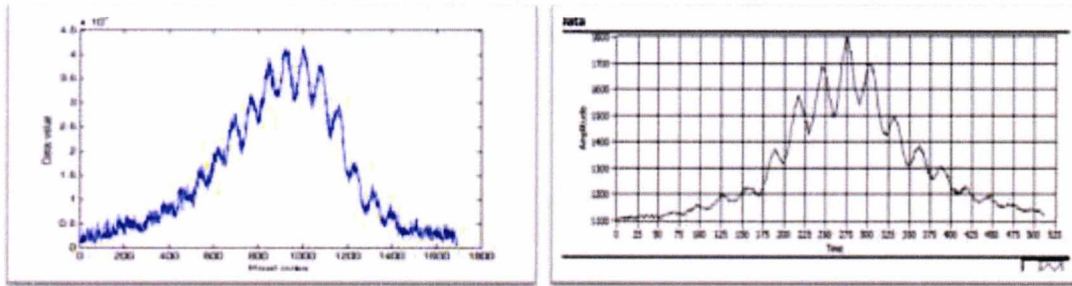


Figure 5.23 Channelled spectrum obtained using 2 cameras: Nikon D80 (ISO=800) (left) and Andor DV887 (right).

### 5.3.2.3 Canon EOS 50D

Canon EOS 50D is a middle-class DSLR that is equipped with a CMOS sensor. With this camera, we use the Canon S500's xenon flash lamp as the light source for LF-FD-OCT. The manufacture attaches an integrated IR filter to the top of the sensor to stop the NIR light (which reduces noise due to NIR in photography); thus the sensor is insensitive to NIR light. The effect of this filter can be seen in Figure 5.24, where a white (full-colour) spectrum from the Xenon light source was recorded by Canon 50D. We know from Figure 5.20 that there are a few spikes between 800 nm and 900 nm in NIR region of the spectrum of the Xenon flash-lamp; therefore the '800 nm - 900 nm' region is difficult to be used in FD-OCT anyway. Another region in the spectrum, between 500 and 700 nm (yellow-red) is thus selected for FD-OCT calculation.



Figure 5.24. Spectrum image acquired using the Xenon flash lamp as the light source and the Canon 50D DSLR as the detector array in LF-FD-OCT.

A 150 mm focal length doublet was used in front of the sensor to cover the wavelength bandwidth of more than 200 nm. Because Canon S50's flash is integrated to the camera body, there is no synchronisation output to connect to Canon 50D. Therefore, we operated the Canon 50D in 'bulb' mode (the release and reset of the shutter was controlled manually) to apply a long exposure time which is long enough to capture the pulse from the flash. The sensor was open for a few seconds and the ambient light was kept to the minimal. The measurements were

implemented at the sensitivity setting ISO=800. Two microscope slides were attached together as the object to examine the ability to resolve multiple layer structure. An A-scan data retrieved from a B-scan image acquired with Canon 50D are shown in Figure 5.25. The three layers of the object were resolved; however the signal is rather low.

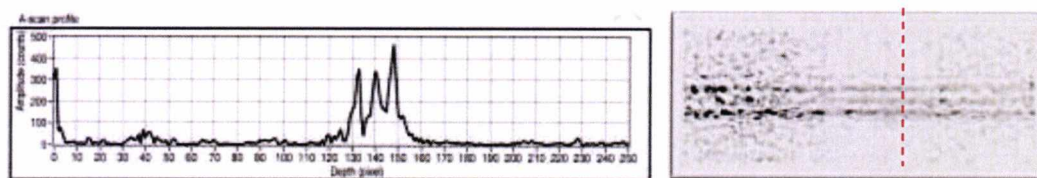


Figure 5.25. A-scan (left) extracted from a B-scan image (right) obtained from two microscope slides using Canon 50D as the detector array and the Xenon flash on a separated camera as the light source in LF-FD-OCT. The red dot line indicates the position of the A-scan.

#### 5.4 Summaries and Perspectives

In this chapter, a prototype of LF-FD-OCT setup is described, including its structure and acquisition method. The LF-FD-OCT set-up uses a 2D camera to perform parallel detection; the system structure is comparatively simple and compact. The setup were tested with different exposure times and attenuation values. The sensitivity roll-off curve is drawn and image examples obtained from biological samples are demonstrated. LF-FD-OCT setup is a simple optical device that is composed of a Michelson interferometer and a spectrometer, both of which could be built into highly integrated optical parts without any moving components. The system performance is mainly related to the light source and the detector array.

Experiments that employ different extended sources and 2D cameras in an effort to simplify and lower the cost of the LF-FD-OCT set-up have been presented. Extended sources were tested as light sources of LF-FD-OCT compared to the SLD; low-cost DSLRs have been tested.

There is a trade-off of spatial coherence, which has to be put right when using incoherent light sources for LF-FD-OCT. We require them being incoherent along the lateral object direction; while at the same time, a good spatial coherence should be preserved to provide good visibility in the channelled spectrum. The linear filament has an ideal physical shape though exhibits a small vibration which deteriorates the

signal quality. The LED has a very good spectral shape and enables high spatial coherence; however its limited emission brightness leads to a signal too low to be used on scattering tissue imaging. The xenon flash-lamps have spikes in the NIR region while the arc shape is not perfectly linear and not stable. The optical power per mode in all extended sources is still low to meet the requirement of high sensitivity OCT acquisition. To make full use of the improved depth resolution, the light power has to be increased. The results from the experiment using extended sources have shown small depth resolution, but also lower sensitivity, which direct such FD-OCT systems towards a limited range of applications, such as measurement of paper thickness or layers of translucent objects.

The ability of the DSLR cameras to resolve the channelled spectrum from the spectrometer is also presented. A DSLR was demonstrated capable of producing tomographic images of reflective layered structure. The low-cost cameras were tested in LF-FD-OCT. The results were not convincing for OCT but may be good to recommend such systems for sensing and measurement on reflective objects. Using DSLR in LF-FD-OCT is made difficult due to several issues: (i) coating of optical system of LF-FD-OCT is optimised for NIR light above 650 nm, whereas DSLRs are deliberately optimised to have very little QE in NIR; (ii) alignments of DSLRs is difficult on the photography modes without live-view; (iii) technical difficulties in synchronising the camera with extended sources, which brings extra noise into the experiments. However, technology in DSLR cameras is rapidly advancing, and the specification of parameters is still growing steadily. It is foreseeable that the late state-of-art DSLRs are closing the gap between consumer-grade cameras and the expensive detectors for OCT. The experiments with the DSLRs are rather preliminary, however the experiments prove that low-cost consumer-grade cameras can replace expensive scientific cameras in FD-OCT in the near future, at least for some specific applications.

# Chapter 6 Coherence-gated

## Wavefront Sensing

In this chapter, a novel wavefront sensing (WFS) technique combined with detector-array-based low coherence interferometry (LCI) is presented. The LCI techniques are similar to that were described in Chapter 4. Both time-domain and spectral-domain OCT methods have been integrated in a Shack-Hartmann (SH) wavefront sensor (WFS), which allow reducing the depth range of the WFS. For the time-domain method, phase-shifting interferometry (PSI) is employed and 2D SH spots patterns from an *en-face* plane can be generated in a selected depth directly; whereas for the spectral-domain approach, by using swept-source acquisitions, SH spots pattern in a 3D data volume are acquired simultaneously. Both techniques are described in this chapter. Experiments of measuring wavefront aberrations from 5 planes in a multiple-layer target are demonstrated.

### 6.1 Background

#### 6.1.1 Adaptive optics

Adaptive optics (AO) is a wavefront correction method that uses information about medium through which light passes to improve the performance of optical imaging [222, 223]. It was firstly used to improve the performance of astronomical telescopes [224] by reducing the effect of wavefront aberrations due to the atmospheric turbulence. Since 1990s, applications of AO have expanded to ophthalmology [225], microscopy [223] and communications [226]. A typical AO system is composed by a wavefront sensor, a corrector (e.g. a deformable mirror or a liquid crystal array) and a control system. The wavefront sensor measures the wavefront aberrations of incoming light beams and provides real-time information to the control system that instructs the corrector to compensate for such aberrations in an open or a close loop [227].

For biomedical imaging applications, AO has been mainly used in Ocular imaging systems [228] to measure the wave aberrations of human eye by sensing the wavefront emerging from the retinal reflection that is produced by a focused light spot on the fovea [229]. This technique leads to new approaches of ophthalmological diagnosis and treatment, such as *wavefront-guided laser-assisted in situ keratomileusis* (LASIK) [230] and *photorefractive keratectomy* (PRK) [231]. AO has also been used to improve the imaging quality of a wide range of established biomedical imaging techniques, including OCT (both time-domain OCT [232] and Spectral domain OCT [233], even with parallel detection technique [234]), scanning laser ophthalmoscopy (SLO) [235, 236] and microscopy [31, 223, 237]. A brief review of WFS techniques used in biomedical imaging is given below.

### **6.1.2 Shack-Hartmann Wavefront Sensor**

Various wavefront sensing techniques have been used in AO, including spatially resolved refractometry [238], interferometric wavefront sensing [155], laser ray tracing [239], Shack-Hartmann wavefront sensing [229], pyramid wavefront sensing [240] and holographic wavefront sensing [241]. Shack-Hartmann wavefront sensor (SH-WFS) is the most widely used wavefront sensing device in biomedical imaging because it is simple, compact, robust, achromatic (wavelength independent) and relatively vibration insensitive [242]. SH-WFS was firstly used to allow objective measurements of ocular wavefront aberration [229], and later became useful in evaluating laser eye surgeries [243]. SH-WFSs were also used in diagnosis of eye disorder that require high resolution imaging of the retina [244].

#### **6.1.2.1 Structure**

SH-WFS was developed from the concept of Hartmann test by Roland Shack and Ben Platt [245]. A typical unit is composed by a lenslet array (LA) and a 2D detector array (DA). The LA is placed in the path of the incoming light beam and works as a spatial window array that split the incoming beam laterally. Each lenslet sub-aperture intercepts a portion of the incoming wavefront ( Figure 6.1, a) and each individual beamlet was focused by a lenslet onto a DA that

records the position of the focus spot. Altogether, a grid pattern of focal spots is recorded on a 2D image. Assuming the incoming wavefront from a point source is perfectly flat, the recorded spot pattern should be evenly spaced according to the geometry of the LA; however if the incoming wavefront is aberrated, each wavefront-let sampled by a sub-aperture will lead to a lateral shift of its focus position (illustrated in Figure 6.1, b). The displacement of the recorded focal spot from its reference position (recorded beforehand from a perfect wavefront) is related to an average wavefront slope across the sub-aperture. Altogether, information of the wavefront aberration can be work out from all the shifts of the recorded spots pattern.

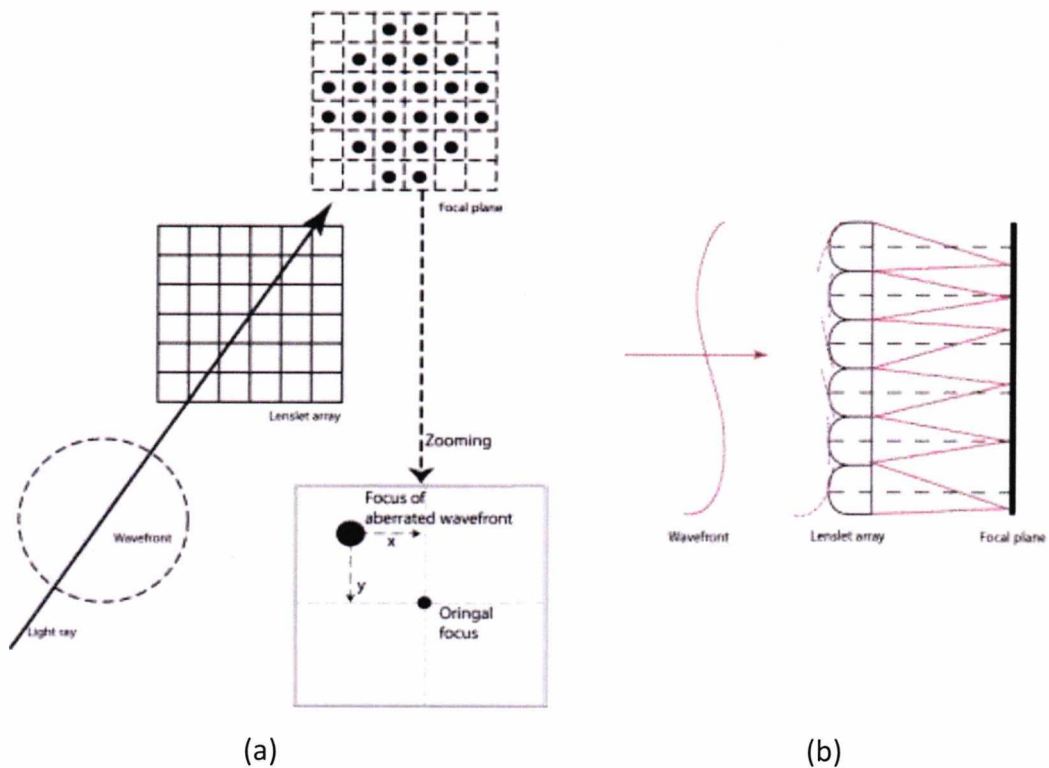


Figure 6.1 (a), Schematic of the principle of SH-WFS; (b), illustration of wavefront tilts produced by the lenslet-array.

### 6.1.2.2 Numeric Processing

A complete procedure of wavefront measurement using SH-WFS can be separated into 3 steps: spots positioning, slopes mapping and wavefront reconstruction. These procedures are illustrated in Figure 6.2.

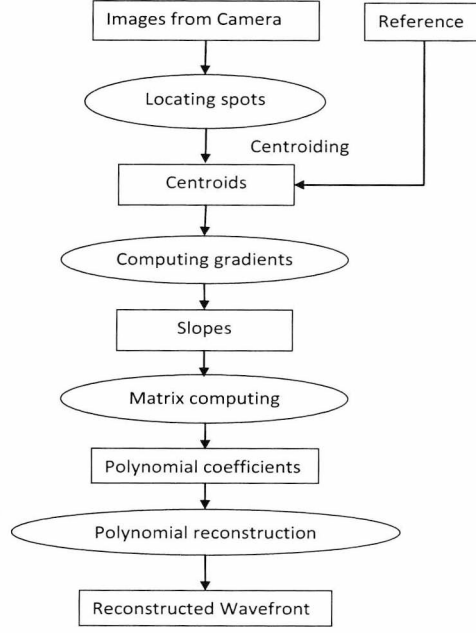


Figure 6.2. Procedures of numeric processing for SH-WFS measurements

To retrieve the lateral positions of the SH spots pattern recorded with good accuracy, the pixel size of the camera should be smaller than the focal spots. The central tendency of each SH spot is then located using a centroiding algorithm. For instance, in a sub-image recorded by a SH-WFS, which has recorded pixel value  $I_{ij}$  at pixel  $(i,j)$ , the centroid position  $(x_{c,k}, y_{c,k})$  is determined using a Center-of-Mass algorithm:

$$\begin{pmatrix} x_c \\ y_c \end{pmatrix}_k = \begin{pmatrix} \frac{\sum_{i,j \in AOI_k} I_{ij} x_i}{\sum_{i,j \in AOI_k} I_{ij}} \\ \frac{\sum_{i,j \in AOI_k} I_{ij} y_i}{\sum_{i,j \in AOI_k} I_{ij}} \end{pmatrix}, \quad (6.1)$$

where  $x$  and  $y$  are the Cartesian coordinates of each pixel;  $k$  denotes the index of lenslet number. The summation is carried out over an area-of-interest  $AOI_k$  that is either the whole area of the corresponding sub-image or a defined area in the sub-image.

The average slope over each lenslet,  $(\partial w / \partial x, \partial w / \partial y)_k$  are simply given by the shift of the measured spot,  $(x_c, y_c)_k$  from the reference location,  $(x_{c,ref}, y_{c,ref})_k$  as

$$\begin{pmatrix} \frac{\partial w}{\partial x} \\ \frac{\partial w}{\partial y} \end{pmatrix}_k \approx \frac{1}{f} \begin{pmatrix} x_c - x_{c,ref} \\ y_c - y_{c,ref} \end{pmatrix}_k, \quad (6.2)$$

where  $f$  is the focal length of the lenslets and  $w$  denotes the local wavefront (phase), which is related to local derivatives of the slopes:

$$\nabla w = \frac{\partial w}{\partial x} \hat{i} + \frac{\partial w}{\partial y} \hat{j}. \quad (6.3)$$

### 6.1.2.3 Zonal Reconstruction

Having the slopes matrix, the wavefront can be reconstructed using zonal or modal approaches. Zonal approaches based on direct numerical integrations of finite-differences, lenslet by lenslet are straightforward [246]. The numerical processing start from an edge of the wavefront slope data and defines the wavefront height (phase) at each integration area as zero; the wavefront in the next adjacent integration area can then be determined according to the local slope and the boundary condition. The measured wavefront slopes can be approximated by the finite difference:

$$\beta_o^x = \frac{1}{2d_x} (w_1 - w_{-1}) \quad (6.4)$$

where  $0, \pm 1$  subscripts describe the wavefront at the adjacent lenslet locations in  $x$  direction. The wavefront therefore can be obtained by:

$$\begin{aligned} w_{i+1,j} &= w_{i-1,j} + 2d_x \beta_{i,j}^x; \\ w_{i,j+1} &= w_{i,j-1} + 2d_y \beta_{i,j}^y. \end{aligned} \quad (6.5)$$

These equations are then solved by least-square fitting or iterative method through the whole data array.

### 6.1.2.4 Modal Reconstruction

The modal approach of wavefront reconstruction describes the wavefront in terms of functions that contain analytic derivatives. Using the measured data to fit the derivatives of these functions, a direct determination of wavefront from the fit coefficients can be attained. By expressing the wavefront  $w(x, y)$  as an expansion of polynomials  $P_m(x, y)$  in the form of:

$$w(x, y) = \sum_{m=1}^M C_m P_m(x, y) \quad (6.6)$$

where  $C_m$  are the polynomial coefficients, the local wavefront slope is written as:

$$\begin{pmatrix} \frac{\partial w}{\partial x} \\ \frac{\partial w}{\partial y} \end{pmatrix}_k = \begin{pmatrix} \sum_{m=2}^M C_m \frac{\partial P_m}{\partial x} \\ \sum_{m=2}^M C_m \frac{\partial P_m}{\partial y} \end{pmatrix} \quad (6.7)$$

The sum-square

$$\chi^2 = \sum_k (\beta_k^x - \sum_{m=2}^M C_m \frac{\partial P_m}{\partial x})^2 + \sum_k (\beta_k^y - \sum_{m=2}^M C_m \frac{\partial P_m}{\partial y})^2 \quad (6.8)$$

can be minimised using  $\partial \chi^2 / \partial C_m = 0$ , which provide the coefficients that are required to reconstruct the wavefront map. Orthogonal polynomials include Zernike [229], Tschebychev [247], Laguerre [248], Hermite-Gaussian polynomials [249] and non-orthogonal polynomials, such as Taylor polynomials [250], are all used in wavefront expression and reconstruction. With the resultant polynomial coefficients, a wavefront map can then be obtained by integrating the polynomials across the whole aperture.

#### 6.1.2.5 Zernike Polynomials

Zernike polynomials is the most widely used polynomials for wavefront analysis because of several advantages:

- a) Zernike polynomials form a complete set of functions (modes) over a circle of unit radius. Because most optical systems have circular pupils, many wavefront analyses use integrations of the pupil functions and aberration functions over a circular pupil.
- b) Data fitting is required due to the finite number of measured SH spots, using Zernike polynomials is convenient to describe aberrations and to apply data fitting.
- c) Zernike polynomials are convenient to be expressed in both polar coordinates and Cartesian coordinates and it allows scaling so that all non-zero order modes could have zero mean and unit variance. This provides a common reference for all modes that allows meaningful comparison between them.
- d) Zernike polynomials are mutually orthogonal, therefore all polynomials are independent and ensure that the variance of all modes equal to the sum of the variance of each individual mode. With normalised Zernike terms, the coefficients of particular term (mode) can be used to evaluate the RMS contribution of that term directly.

The normalised Zernike polynomials in Polar coordinate system are defined as:

$$Z_n^m(r, \theta) = \begin{cases} N_n^m R_n^{|m|}(\rho) \cos(m\theta) & \text{for } m \geq 0, 0 \leq \rho \leq 1, 0 \leq \theta \leq 2\pi \\ -N_n^m R_n^{|m|}(\rho) \sin(m\theta) & \text{for } m < 0, 0 \leq \rho \leq 1, 0 \leq \theta \leq 2\pi \end{cases} \quad (6.9)$$

Non-negative integer 'n' is the order of the polynomial, while Azimuthal frequency 'm' is an integer valued from -n to +n, R is zero when n-m is odd.  $\rho$  and  $\theta$  are the normalised radius and polar angle of Polar coordinate system.  $N_n^m$  is a normalised factor:

$$N_n^m = \sqrt{\frac{2(n+1)}{1+\delta_{m0}}}, \quad \delta_{m0} = \begin{cases} 1 & \text{for } m = 0 \\ 0 & \text{for } m \neq 0 \end{cases} \quad (6.10)$$

The radial polynomial term  $R_n^m(r)$  can be expressed in terms of series:

$$R_n^m(r) = \begin{cases} \sum_{k=0}^{(n-m)/2} \frac{(-1)^k (n-k)!}{k! \left(\frac{n+m}{2} - k\right)! \left(\frac{n+m}{2} + k\right)!} r^{n-2k} & \text{if } (n-m) \text{ is even} \\ 0 & \text{if } (n-m) \text{ is odd} \end{cases} \quad (6.11)$$

The wavefront is then expressed by a weighted definite sum of Zernike polynomials:

$$W(\rho, \theta) = \sum_n^k \sum_{m=-n}^n W_n^m Z_n^m(\rho, \theta) = \sum_n^k \left[ \sum_{m=-n}^{-1} -W_n^m N_n^m R_n^{|m|}(\rho) \sin(m\theta) + \sum_{m=0}^n W_n^m R_n^{|m|}(\rho) \cos(m\theta) \right] \quad (6.12)$$

where  $k$  is the polynomial order of the expansion;  $W_n^m$  is the coefficient of the polynomial mode and equal to the RMS wavefront error for that mode. The first 14 Zernike polynomials are listed in Table 6.1 and the first 10 Zernike polynomials in a circular unit aperture are shown in Fig. 6.3.

Table 6.1. First 14 Zernike polynomials

Mode	Order	Frequency	$Z_n^m(r, \theta)$	Aberration
0	0	0	1	Piston
1	1	-1	$2\rho \sin(\theta)$	Tilt in y, distortion
2	1	1	$2\rho \cos(\theta)$	Tilt in x, distortion
3	2	-2	$\sqrt{6}\rho^2 \sin(2\theta)$	Astigmatism with axis at $\pm 45^\circ$
4	2	0	$\sqrt{3}(2\rho^2 - 1)$	Field curvature, defocus
5	2	2	$\sqrt{6}\rho^2 \cos(2\theta)$	Astigmatism with axis at $0^\circ$ or $90^\circ$
6	3	-3	$\sqrt{8}\rho^3 \sin(3\theta)$	
7	3	-1	$\sqrt{8}(3\rho^3 - 2\rho) \sin(\theta)$	Coma along y axis
8	3	1	$\sqrt{8}(3\rho^3 - 2\rho) \cos(\theta)$	Coma along x axis
9	3	3	$\sqrt{8}\rho^3 \sin(3\theta)$	
10	4	-4	$\sqrt{10}\rho^4 \sin(4\theta)$	
11	4	-2	$\sqrt{10}(\rho^4 - 3\rho^2) \sin(2\theta)$	Secondary astigmatism
12	4	0	$\sqrt{10}(6\rho^4 - 6\rho^2 + 1)$	Spherical Aberration, defocus
13	4	2	$\sqrt{10}(\rho^4 - 3\rho^2) \cos(2\theta)$	Secondary astigmatism
14	4	4	$\sqrt{10}\rho^4 \cos(4\theta)$	

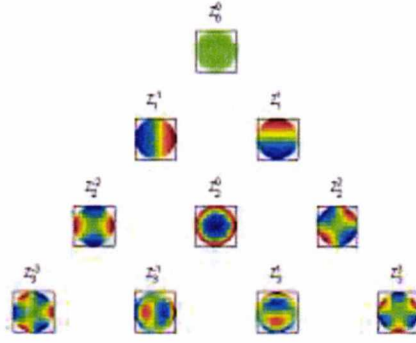


Figure 6.3. First 10 Zernike polynomials in circular unit aperture.

For SH-WFS applications, sometimes it's more convenient to express the expansion in Cartesian coordinates system with single indexing scheme:

$$W(x, y) = \sum_{j=0}^{j_{\max}} W_j Z_j(x, y) \quad (6.13)$$

where  $j$  is the single index mode number. The conversions between  $j$  in single index scheme and  $m, n$  in double index scheme are

$$j = \frac{n(n+2) + m}{2}; \quad (6.14)$$

$$n = \text{roundup} \left[ \frac{\sqrt{9+8j} - 3}{2} \right] \quad \text{and} \quad m = 2j - n(n+2)$$

#### 6.1.2.6 Performance of SH-WFS

The sensitivity of SH-WFS is defined as the minimal wavefront slope  $\theta_{\min}$  that can be recorded by the camera, expressed as

$$\theta_{\min} = \frac{\Delta S_{\min}}{f} \quad (6.15)$$

where  $f$  is the focal length of the lenslet and  $\Delta S_{\min}$  denotes the minimal resolvable displacement of the SH spot, which is related to the centroiding algorithm, the pixel size and signal to noise ratio of the detector. With given  $\Delta S_{\min}$ , the sensitivity of SH-WFS can be improved only by using longer focal length; however, this in return will

affect the dynamic range or the largest measurable wavefront slope, which is inversely proportional to the focal length of the lenslet as

$$\theta_{max} = \frac{D}{2f} \quad (6.16)$$

where  $D$  is the size of the sub-aperture of the lenslet. Eq. (6.15) and Eq. (6.16) show that the sensitivity and dynamic range of the SH-WFS measurement are inversely related.

The precision is defined as the repeatability of the sensor, in the form of the root-mean-square (RMS) deviations of the measured wavefront. Finite precision is a result of pixelisation, planar approximation fitting error, detector noise and other random effects [242]. The sub-aperture size and the number of the lenslets are also related to the accuracy of wavefront measurement, since the local wavefront slopes are approximated by the average over the lenslet sub-aperture that is finite in number.

### **6.1.3 Limitation of SH-WFSs**

Two main limitations of conventional SH-WFS that are related to our interests are the inability of distinguishing aberrations from different depths and the vulnerability to stray reflections [32].

#### **6.1.3.1 Insensitivity to depth variations**

Standard SH-WFS has little sensitivity in depth. For each lenslet, the depth of focus is relatively large due to the limited numerical aperture (NA); therefore the spot positions are deviated from the average of the whole depth of focus. As a result, when SH-WFS targets on a axial position in a scattering samples, lots of backscattering light from layers other than the focal plane will contribute to noises and little sensitivity is obtained; especially for thick-specimen microscopy, because the sample, e.g. brain tissue, is strongly scattering and imaging should be able to go deep to a depth of 3 to 5 mean free paths (MFPs) [251]. With the focus at such depth, the ballistic light from near the focus that is used to determine the wavefront

is only a small fraction of the total backscattered light that reach the sensor detector; therefore shallow layers deteriorate the wavefront measurements for successive deeper layers.

#### **6.1.3.2 Stray reflections**

Stray reflections from the interface optics are common problems in AO system and are difficult to be rejected totally due to the low numeric aperture (NA) of lenslets. In retina imaging, SH-WFS collects light primarily from a point on a single reflective layer. In order to minimise the effect of stray reflections from the other surfaces than the layer of interests, single path correction is preferable that requires a thin beam sent into the eye and the aberrations are picked up by the emerging beam returning from the eye. If the same source is to be used for both imaging and WFS measurement and the imaging operation and measurement of aberrations have to be sequential, thus the wavefront correction cannot be applied dynamically with imaging. Further complication of the system is required to allow simultaneously measurement of aberrations by using lights of two wavelengths separated by dichroic filters. Another solution is to employ off-axis illumination of the retina [252] which make the measuring beam coming from the retina through a different path than the reflection from the cornea; however this separation of imaging and WFS paths usually requires two optical sources [253, 254], which increase the cost and the complexity of the system.

When double-pass correction is required [233], aberrations in both the forward beam and the returning beam are acquired to be corrected together since the same beam is shared by the WFS and imaging facilities. Double-pass WFS allow simultaneous WFS with imaging schemes, such as for SLO and OCT; however curved mirrors must be used instead of lenses between the scanner and the object to avoid the stray lights from the lens surfaces, which leads to a large and bulky layout [236]. Even though, on-axis corneal reflection is still a problem. Supplementary spatial filters are usually needed to reduce the stray light; however, not only the reflection from the cornea are too strong to be entirely eliminated by spatial filters, but also the size of the spatial filter is related to the accuracy of measurement. Since small aperture may stop highly aberrated light from the point of interest at the same

time; therefore the aperture cannot be very small. Other methods have been employed to reduce the effect of the cornea reflections, including moving the lens and mirrors in the optics off axis [255] to reduce the reflection and using polarisation control to eliminate specular reflections [256]. However, off-axis lens or mirrors will induce extra aberrations; polarisation control will lead to signal loss and will make the measurement results sensitive to the polarisation of the samples.

### **6.1.3.3 SH-WFS for Microscopy**

In microscopy, in order to achieve diffraction-limited imaging from deep positions (a few hundreds of microns) inside biological specimens, wavefront aberrations due to refractive-index inhomogeneities in the samples must be compensated. However, there is rarely a 'guide star' or reflective layer to provide reference information in scattering specimens. At the same time multiple reflections from the microscopy slides and multiple facets of multi-elements microscope objectives produce stray light to the SH-WFS [257]. Strong stray light can saturate the detector and even weak light from those layers that are close to near-focal planes creates additional spots to the SH spots of interest, which confuses the WFS calculations. Algorithms to maximise sharpness metrics, such as simulated annealing [258] and genetic algorithms [259, 260] have been devised to assist the correction. Although this is possible because the quality of the focus is controllable when a scanned laser is used as the light source, for example in fluorescence confocal Microscopy, these additional numerical processes are computing-intensive and time consuming, which commonly requires several minutes for each point on the scanning beam [261] to attain optimum corrections. In two-photon microscopy [262], only the aberration for the incoming light beam needs to be corrected. A fast feed-forward correction is required to measure the wavefront directly. Predefined depth-resolved WFS that provide correction information in a single step sufficiently meet the requirement.

### **6.1.4 Coherence Gated SH-WFS**

A solution for eliminating or at least reducing the effect of all limitations discussed above is to introduce a depth gate to the WFS to narrow the depth range of the

wavefront measurement. Coherence gating, the fundamental concept of low coherence interferometry (LCI), has been incorporated in WFS by using either a virtual SH-WFS algorithm [31, 263, 264] or a physical SH-WFS [32].

#### **6.1.4.1 CG/SH-WFS Using Virtual Lenslet**

The first report of depth resolvable WFS measurement was proposed by Feierabend et al.[31]. The motivation was to narrow the depth range of WFS in fluorescence microscopy by using coherence gating to reject out-of-focus light; thereby backscattering light was selected from a shallow layer in scattering samples in the presence of strong background light, which enable direct wavefront measurement. This idea was realised later in a depth resolved WFS assisted Two-Photon Microscopy [263, 264] and successfully corrected wavefront aberrations in imaging forebrain of zebra fish larva. This time-domain PSI method includes 4 steps: a), From the phase shifted interference signal produced by a Mach-Zehnder interferometer, the phase of a 3D distribution of the scattered wave was obtained; b), the 3D complex field was then calculated from the extracted phase; c), the amplitude of complex 3D image data was numerically separated into virtual windows and then analysed using a virtual lenslet algorithm (applying Fourier transformations over each sub-area) to extract the coherence gated SH spots pattern; d) centroiding and wavefront reconstruction.

An advantage of virtual lenslet to a physical counterpart is a larger dynamic range due to lack of light collecting effect of the physical micro-lens. However, the numerical calculations, especially step (b), are computationally intensive; only the last step (d) is required by conventional SH-WFS. As an interferometric approach, the virtual lenslet method has  $2\pi$  ambiguity and therefore requires phase unwrapping [265] which increases the processing time. The procedure was subject to cross-talks between pixels, which alter the phase information and increase phase instability. In fact, the initial development from interferometric WFS to SH-WFS was motivated by the need to avoid phase unwrapping and the phase instability. Using a physical SH-WFS to replace the virtual SH-WFS may be a solution without these deficiencies.

#### 6.1.4.2 Physical CG/SH-WFS Methods

Tuohy and Podoleanu [32] have presented a technique that combines a physical SH-WFS and a Michelson interferometer. Interference was produced by a reference beam and an object beam that passes through a physical lenslet array (LA). Using physical LA eliminates the step (b) and step (c) in the virtual LA method, thus reduces the computation time. This setup proves capable of working in both time domain and spectral domain. The former approach employs a broadband light source and PSI method to extract an *en-face* image that contains SH spots pattern from an axial range of a coherence length around a selected depth, similar to full-field OCT (see Chapter 4). The spectral domain approach uses a wavelength tunable light source to acquire a sequence of images with tuning wavelengths. Fourier transformation is then applied to the spectral data on each pixel, thereby a 3D image volume that contains the SH spots pattern are obtained, similar to (full-field) swept-source OCT (see Chapter 4). The required 2D depth resolved SH spots patterns could be extracted from this 3D volume at required depths. Both approaches have proven to be capable of rejecting the stray reflections and enhancing signal strength. However, both methods exhibited errors in spots positioning compared to that produced by a conventional SH-WFS. One source of possible errors was suggested to be the non-uniform distribution of reference power across the CCD [32]; speckle noise may also act as a limiting factor of the precision.

A design deficiency of the Michelson interferometer based CG/SH-WFS set-up (Figure. 6.4) is a portion of light returning from the object (DM) would reach the camera without passing through the LA, following the 'BS2-BS1-M1-BS3' route. This beam is out of the coherence gate and contributes to noises to the detector. This issue can be solved by replacing the Michelson interferometer with a Mach-Zehnder interferometer. Experiments based on a, improved Mach-Zehnder-interferometer-based CG/SH-WFS system are described in the rest of this chapter. Using this set-up, depth-resolved wavefront aberrations can be measured in real-time.

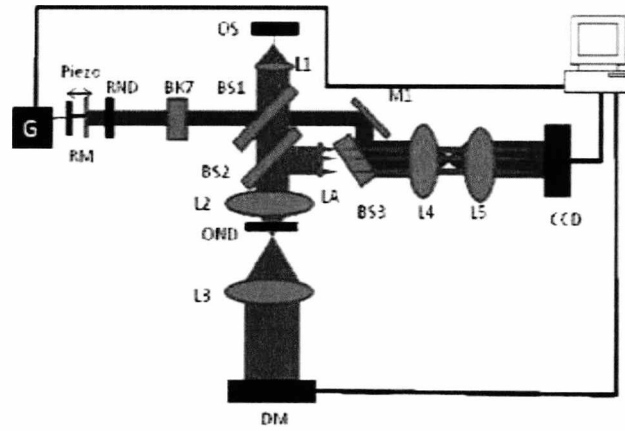


Figure. 6.4. Schematic of the first physical CG/SH-WFS set-up.

(Image courtesy of Dr. Simon Tuohy [32])

## 6.2 Mach-Zehnder Interferometer based CG/SH-WFS

### 6.2.1 Time Domain CG/SH-WFS

The optical set-up of a Mach-Zehnder interferometer based CG/SH-WFS system was built as illustrated in Figure 6.5. It was firstly configured to work with time-domain LCI by using a broadband Superluminescent diode, SLD as the light source (central wavelength at 850 nm and FWHM spectrum bandwidth is about 20 nm). A beam of 10 mm diameter was launched by a collimated lens (CL) to a beam splitter (BS1) and was separated into two paths; each was focused by an achromatic doublet (L1/L2) onto the *object*, *OBJ* and the reference mirror, RM respectively. A pair of neutral density filter (NDF) NDF1 and NDF2 were inserted to balance the optical power in the two interferometric arms. The reference mirror was mounted on a Piezo-actuator (PZT) to introduce phase shifting to the reference beam. After reaching the target/mirror, the light in both arms are reflected to return paths and reflected once more by two other beam splitters (BS2 and BS3). Two reflected light beams then recombine at a fourth beam splitter (BS4). The dispersion due to thickness of the beam splitters are automatically compensated among these four beam splitters themselves. Between BS3 and BS4 in the object path, a lenslet array (LA) (MLA300-14AR, Thorlabs) samples the incoming object beam transversally. The lenslet pitch is

300  $\mu\text{m}$  and focal length of lenslets is 18.6 mm (Other lenslet arrays were also used; details are given in Section 6.3.5.).

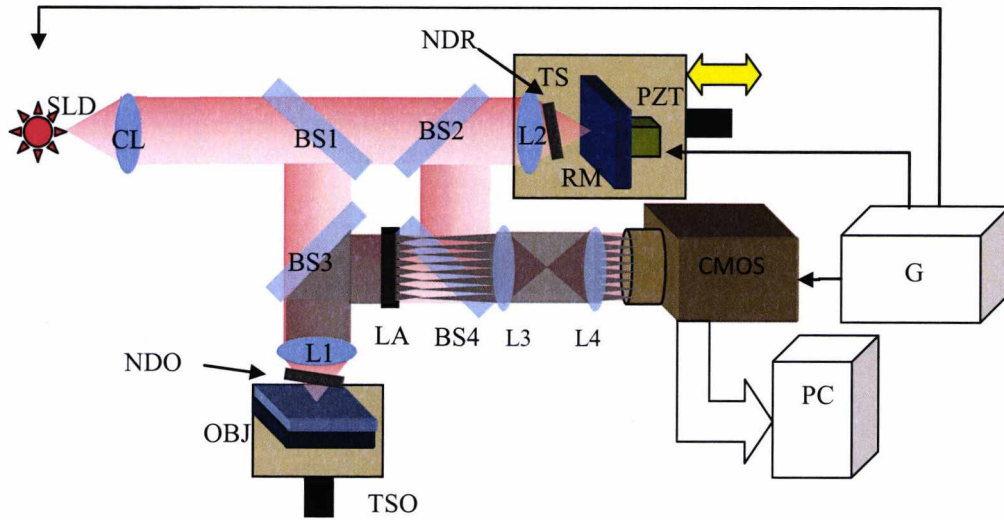


Figure 6.5. Schematic of Mach-Zehnder interferometer based CG/SH-WFS set-up. SLD: SDL-381, (central wavelength: 850 nm, FWHM bandwidth 20 nm); CL: collimating lens, x5 objective; RM: reference mirror; OBJ: object; PZT: Piezo-actuator; G: function generator; NDO and DNR: neutral density filter in object and reference arm respectively; TSR and TSO: translation stage (moving axially) of reference path and object path respectively; L1, L2, L3, L4: achromat doublets with focal length of 30 mm, 30 mm, 75 mm and 100 cm respectively; LA: lenslet array, MLA300-14AR (Thorlabs); CMOS: CMOS camera, Mikrotron EoSens CL (MC1362), resolution: 1280x1024, max frame rate 500 fps, AD bit depth: 8/10 bit.

A fast 2D CMOS camera, Mikrotron EoSens MC1362, is used as the detector. Because the space between the lenslet array and the detector is too small to accommodate BS4, a couple of achromatic lenses were inserted to relay the focus of the lenslet to the surface of the camera. Conventional SH-WFS images can be acquired by simply inserting a screen between BS1 and BS2 to block the reference path. Mikrotron MC1362 is a 10-bit CMOS camera with 1280x1024 pixels and a maximum frame rate of 500 fps. The data are transferred from the CMOS to a PC through a dual-channel frame grabber. Function generators were used to synchronise the CMOS and the light source to perform a stroboscopic illumination scheme, similar to the full-field OCT described in Chapter 4.

When the length of the optical paths of the object arm and the reference arm coincide within a coherence length ( $\sim 16 \mu\text{m}$ ), interference will take place and be recorded by the camera. By applying axial displacement on the Piezo, phase

modulation of the reference beam is introduced; the coherence gated SH spot pattern can be retrieved using 3-step PSI or 4-step PSI (see Chapter 3 and 4). A LabVIEW program was written for setting, imaging calculation, visualisation and recording. Figure 6.6 shows its user interface.

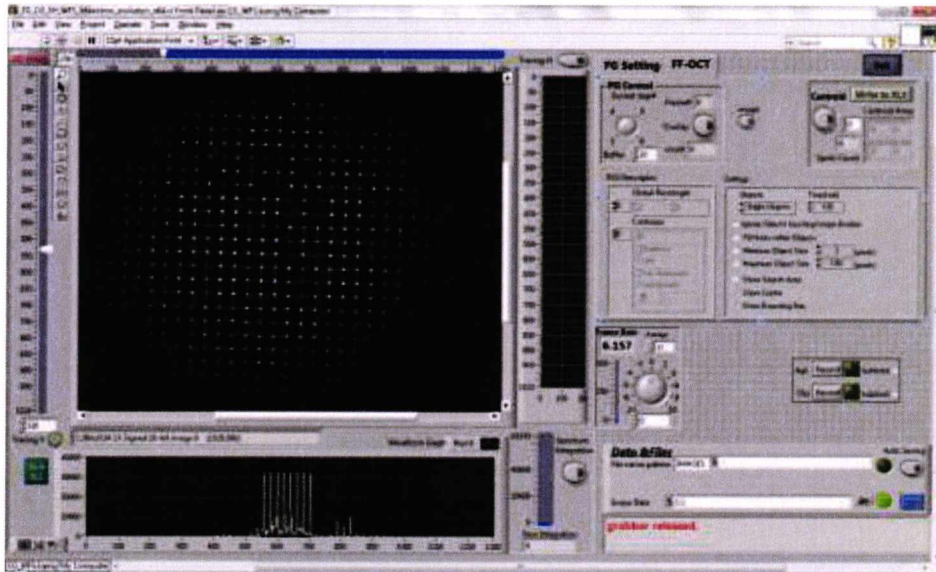


Figure 6.6. User interface of the control software for TD-CG/SH-WFS.

As discussed in the Chapter 4 (Full-field OCT), images obtained by PSI method from a reflective object present inherent residual (parasite) fringes [137, 266]. In Full-field OCT, this is not problematic because there are few reflectors in scattering samples; even with some reflectors in the FOV, it's not difficult to recognise the shape of the reflectors and boundaries between biological features from the images. In Metrologic applications, the residual fringes are usually required to be removed. In the tests of TD-CG/SH-WFS where a reflector is used as the target, the fringes modulate the spots pattern and may interfere the centroiding algorithm. Fringe modulation leads to inconsistent image values of the SH spots. Because these fringes are related to the error of phase stepping, using larger number of phase steps can reduce the contrast of the fringes. Figure 6.7 displays two coherence images obtained with 3-step PSI and 4-step PSI, which confirms the reduction of the phase error and the reduced fringe contrast due to using larger number of phase steps. In the following experiments both 3-step PSI and 4 steps PSI have been used. We refer to this configuration as time-domain Coherence-gated SH-WFS (TD-CG/SH-WFS).

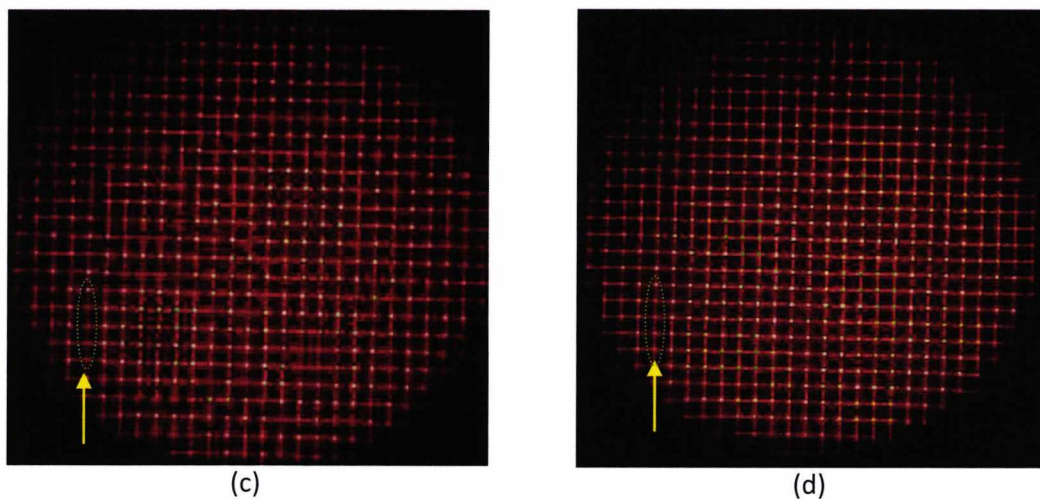


Figure 6.7 TD-CG/SH-WFS images acquired from a single reflector (a point on a mirror) with 3-step PSI (a) and 4-step PSI (b); yellow arrows indicate a region where a fringe valley locates in each image.

### 6.2.2 Swept-source Coherence Gated SH-WFS

Without modifying the optical set-up, the CG/SH-WFS system can also work in spectral domain by replacing the broadband light source with a wavelength tuneable light source, BS-840-1, Superlum. This source was also used in Chapter 4 to acquired full-field swept-source OCT images. The tuning range  $\Delta\lambda$  is about 47 nm (826 nm - 873 nm) with a spectral linewidth of 50 pm. The sweeping rate is up to 200 Hz, corresponding to 9,400 nm/s. Other parts of the system are identical to the time-domain set-up. An I/O board, NI USB-6215 (National Instrument) was used to generate DC voltages to externally tune the wavelength of the light source. The swept-source acquisition is identical to the full-field swept-source OCT, described in Chapter 4 except that the camera works at a much higher rate, usually above 200 fps. The voltages-wavelength response of the source is assumed linear and the voltage values are calibrated to ensure linear  $k$ . Because the wavelength tuning range is small and little dispersion is present in the optical set-up, no data resampling is implemented in post-processing.

The interference images with tuning wavelength are recorded by the CMOS camera and save to PC memory. After the acquisition of the whole spectral-decoded image sequence, spectral data was retrieved on each pixel and fed to Fourier transformation (FT). Each FT produces a depth profile of the corresponding image

pixel; thereby a 3D volume image data can be obtained ultimately. Given a certain FT length, the computing time of a 3D volume rendering is mainly determined by the number of FTs and the pixel number within region of interest (ROI). For a sequence of 256 images with 1M resolution, a volume dataset can be obtained in less than 1 second with CPU rendering. We refer to this configuration as Swept-source Coherence Gated SH-WFS (SS-CG/SH-WFS).

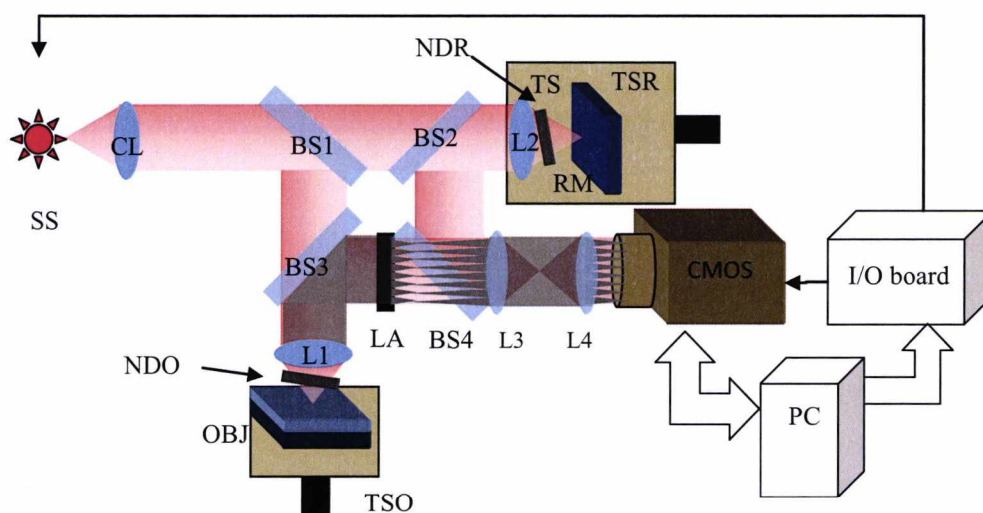


Figure 6.8. Schematic of Mach-Zehnder interferometer based SS-CG/SH-WFS set-up. SS: tunable semiconductor light source BS-840-1; CL: collimated lens, x5 objective; RM: reference mirror; NDF1 and NDF2: neutral density filter or variable optical density; L1, L2: achromatic doublets with focal length of 5 cm; LA: lenslet array, pitch distance 300  $\mu\text{m}$  and focal length 18.6 mm; CMOS: Mikrotron EoSens MC1362.

With a reflective object, all returning light is from the focus of the illumination beam; therefore, only a single SH spot pattern presents in 3D volume. When thick scattering samples are under interrogation with the beam focus inside the sample, the 3D volume may contain more than one SH spots pattern that come from different depth in the focal region. In the following experiment, a reflective surface was tested; therefore only one slice that contained the SH spots pattern was obtained, which was manually selected from the reconstructed 3D volume and fed to post-processing. A control and acquisition software for SS-CG/SH-WFS written in LabView.

### 6.2.3 Centroiding

A single CG/SH-WFS image has a shallow depth range; therefore, in some occasions, due to aberrated wavefronts (in both CG/SH-WFS methods, see Figure 6.10 as an example for TD-CG/SH-WFS) or parasite fringes (in TD-CG/SH-WFS only), only part of the SH spots are obtained in a single coherence image. In these cases, a second coherence-gated image will be added to the incomplete SH spots image. For TD-CG/SH-WFS, this second image is acquired with a slightly shifted OPD (half of the wavelength) or phase ( $\Delta\phi = \pi$ ); for SS-CG/SH-WFS, because a volume of image are obtained in each acquisition sequence, an adjacent image to the selected image is available without extra effort. The sum of these two images produces a complete SH spots pattern, which is ready for the program to register the spots and calculate the centroid coordinates.

For a standard SH-WFS, with good signal-to-noise-ratio (SNR), counting the spots and centroid is straightforward because the bright spots are easy to be distinguished from the background of the image using a simple threshold because all the SH spots present similar pixel values. However, for CG/SH-WFS images, the light pass through the LA interferes with the reference beam that has 2D Gaussian profile. In each spatial window, not only the focus, but also the light due to diffraction (at the lenslet aperture) and transmission (through the space between the lenslets on unmasked LAs) may contribute to the interference. Since the diffraction light and transmission light are not focused, some bright pixels are generated among the SH spots in the coherence image (see examples in Figure 6.7), which are considered as artefacts. These artefacts together with the parasite fringes (for TD-CG/SH-WFS) will make the spots locating and centroiding difficult; therefore a dynamic threshold is used to count the spots; the threshold is automatically adjusted according to a user-defined spot size. For example, a minimal size of 5 pixels and a maximum size of 50 pixels are used to count the spot in each window in most our experiments. The centre-of-mass algorithm was then applied to the counted spots, from which centroid coordinates were obtained using Eq. (6.1). The rest of the numeric processing is the same to conventional SH-WFSs, which was described in section 6.1.2.2.

## 6.3 Results

### 6.3.1 Single Reflector Object

Standard SH-WFS images were acquired firstly as a reference to compare with the CG/SH-WFS results. 100 images, each has a pattern of 225 (15 x 15) spots and each window occupies an area of 21 x 21 pixel<sup>2</sup>, were obtained. The average of the centroid coordinates was used as the reference. The standard deviations of these 100 data were used to represent the precision of the spots centroiding. In the top of Figure 6.9, these deviations were sorted according to the distance to the image centre. The bottom of Figure 6.9 maps the deviation distribution according to the positions in the image; the sizes of the dots are proportional to the deviation values. These results show that the precision of centroiding is random in different regions of the images and the values for x and y are similar. To arrange the results in such way is for the convenience of comparing with the CG/SH-WFS results.

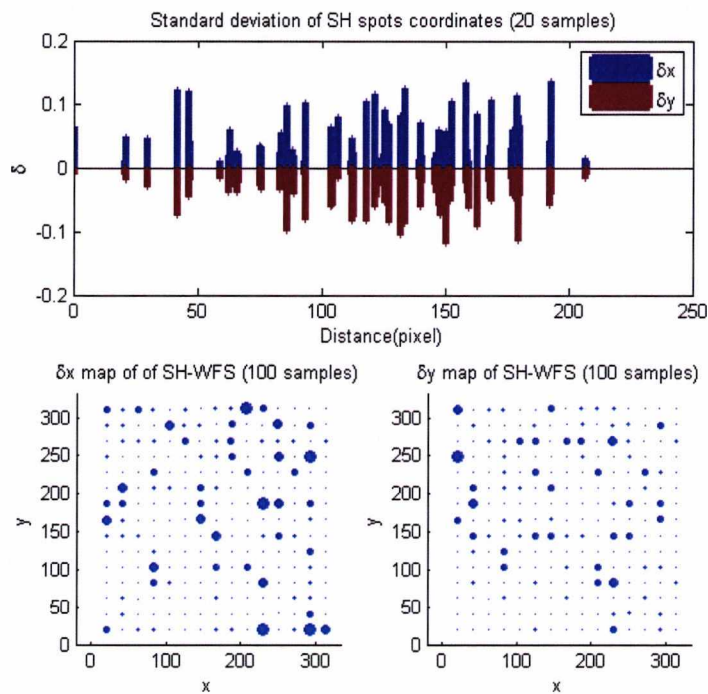


Figure 6.9. Precision of standard SH-WFS spots centroiding; Top: standard deviations of the coordinates,  $\delta x$  (blue) and  $\delta y$  (red) versus the distance to the image centre; bottom: maps of these values in the SH spot pattern image (left:  $\delta x$  and right:  $\delta y$ ).

### 6.3.1.1 TD-CG/SH-WFS

#### 6.3.1.1.1 Coherence gating of TD-CG/SH-WFS

For TD-CG/SH-WFS, the depth resolution is determined by the spectrum FWHM bandwidth  $\Delta\lambda$  of the light sources. The SLD used in our experiments, SDL-381 has a central wavelength at 850 nm and FWHM bandwidth 20 nm. The coherence gate is calculated as

$$L = \frac{2\ln(2)}{n\pi} \frac{\lambda^2}{\Delta\lambda} = \frac{0.44}{n} \frac{850^2}{20} = 16\mu m \quad (6.17)$$

Two TD-CG/SH images with slightly different OPDs displayed in Figure 6.10 show the effect of coherence gating. The left images was acquired with near-zero OPD as majority of the TD-CG/SH spots can be observed; whereas the image on the right that was acquired with about 8  $\mu m$  OPD, shows that the central part of the spots pattern start dimming out. From these two images, it can also be observed that the spots at peripheral locations shows larger value in the right-hand side image than the left-hand side one, this is possibly because the wavefront of the object beam and that of the reference beams are not perfectly parallel; therefore the coherence gate is not in a plane.

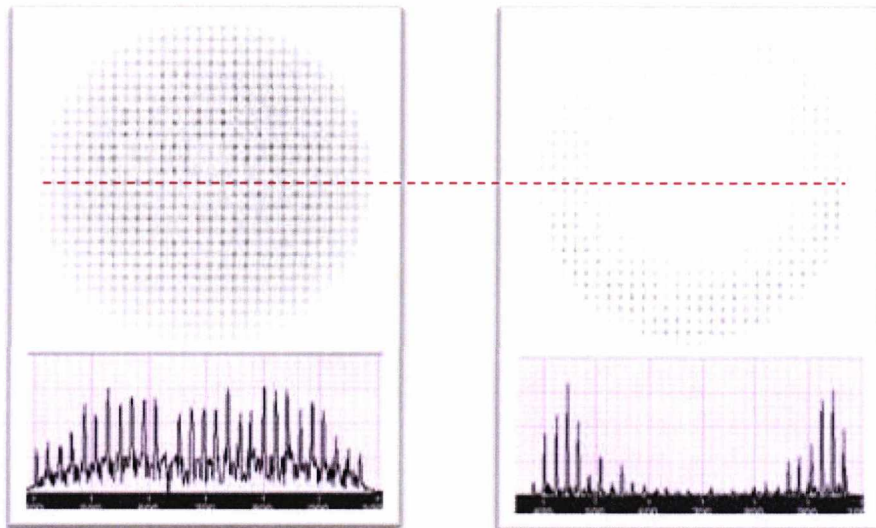


Figure 6.10. TD-CG/SH-WFS images obtained at near-zero OPD (left) and an OPD of approximately 10  $\mu m$  (right); pixel values of an image row that cross a row of SH spots are shown underneath each image.

### 6.3.1.1.2 Rejection of Stray Light

In order to test the rejection of stray lights, the low reflectivity object was mimicked by using a NDF (NDF1 in Figure 6.5) with optical density of about 1.0 in front of a mirror. The NDF is tilted to divert reflection off axis; however, spots due to the reflections from the first surface of NDF1 were still recorded in the top left corner of the image (Figure 6.11. a). This reflection is similar to the reflections from cornea in ophthalmology imaging or from microscopy slides in microscopy. In TD-CG/SH-WFS image (Figure 6.10 b), those spots are totally rejected. Figure 6.10 (c) plots the values of a row that cross the middle of a row of spots. Three spots generated by stray lights can be observed on the left with a higher image value than the other spots of interest; these abnormal peaks are not present in the coherence-gated data. An enhancement of signal strength, about 3 times can also be observed from Figure 6.10 (c). The noise level between the peaks is also higher in the coherence-gated images, because of the diffraction and transmission that fall within the coherence gate.

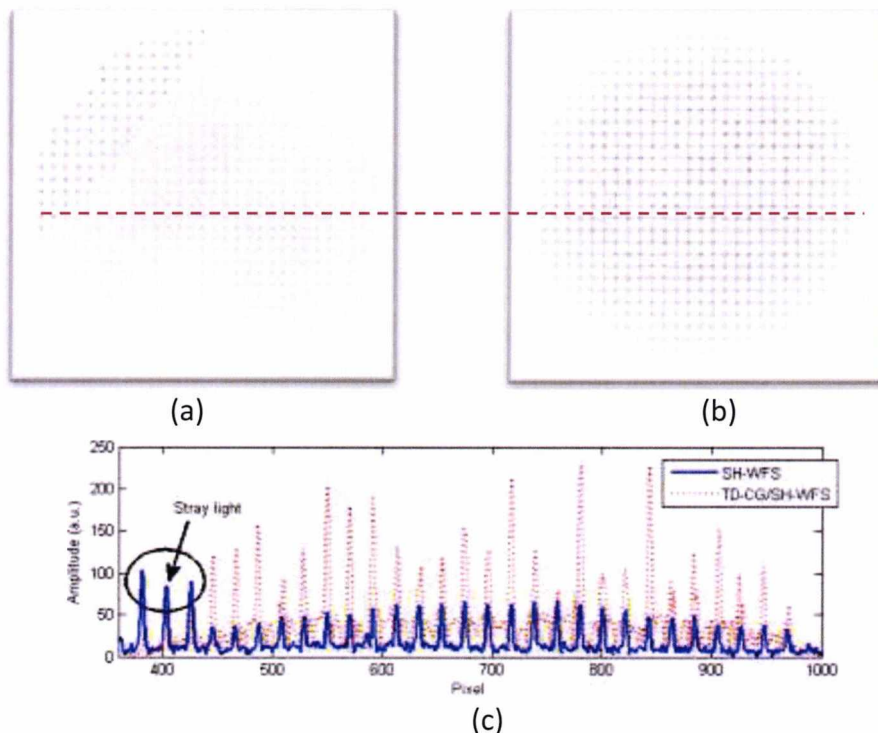


Figure 6.11. Effect of stay light in standard SH-WFS and rejection in TD-CG/SH-WFS: (a), standard SH-WFS image with spots created by stay light present in the top left corner; (b), TD-CG/SH-WFS image; (c) a image row from both (a) and (b) that cross the centre of a row of SH spots, which show the rejection of stray light and enhancement of signal strength in value.

### 6.3.1.1.3 Accuracy of TD-CG/SH-WFS

We know that the number of the PSI phase step is related to the phase error and the contrast of the parasite fringes. It is suggested [32] it may also relate to the accuracy of SH spots positioning. To investigate the relation,  $n = 4, 8, 12$  and  $16$  steps PSI were implemented with the same phase step,  $\pi/2$ . The coherence images were acquired by incorporating ' $n$ ' phase shifted frames from 1, 2, 3, 4 periods of the phase modulation; 4-step PSI uses 1 circle of phase modulation, 8-step PSI requires 2 circles and is equivalent to an average of two 4-step PSI and so on. The error ( $\Delta x_{TD,j}, \Delta y_{TD,j}$ ) for spot ( $j$ ) is calculated using

$$\Delta x_{TD,j} = \frac{|x_{TD,j} - x_{SSH,j}|}{X},$$

$$\Delta y_{TD,j} = \frac{|y_{TD,j} - y_{SSH,j}|}{Y}.$$
(6.18)

where  $(x_{TD,j}, y_{TD,j})$  and  $(x_{SSH,j}, y_{SSH,j})$  are the centroid coordinates acquired with TD-CG/SH-WFS and standard SH-WFS respectively;  $X$  and  $Y$  are the size of the spatial window in  $x$  and  $y$  direction respectively. Spots (a) is at the top-left of the image and spot (c) is at the bottom right, while spot (b) is a spot in the central part of the image. The absolute errors obtained with  $n$ -step PSI from three locations are given in Table 6.2. Average error of all 225 SH spots obtained by TD-CG/SH and the average of the standard deviations of all SH spots obtained by the standard SH-WFS are also listed in Table 6.2.

Table 6.2. Errors of centroid coordinates obtained by TD-CG/SH-WFS using 4, 8, 12, 16 step PSI from three spots at different locations in the coherence image; the average coordinate errors of all 225 TD-CG/SH-WFS spots and the standard deviations of all 225 spots coordinates obtained by the standard SH-WFS.

Step	TD-CG/SH-WFS								SH-WFS	
	Spot (a)		Spot (b)		Spot (c)		Average of all		Average of all	
	$\Delta x$	$\Delta y$	$\Delta x$	$\Delta y$	$\Delta x$	$\Delta y$	$\overline{\Delta x}$	$\overline{\Delta y}$	$\delta x$	$\delta y$
4	0.09612	0.08317	0.08197	0.07506	0.11088	0.05737	0.08520	0.0726	0.04832	0.06446
8	0.07123	0.06614	0.06520	0.07292	0.05090	0.08626	0.06858	0.078789		
12	0.10699	0.08979	0.08274	0.07463	0.07536	0.13980	0.07973	0.09426		
16	0.08166	0.09093	0.06626	0.05399	0.05624	0.06913	0.07938	0.07689		

The errors,  $\sqrt{\Delta x^2 + \Delta y^2}$  at three locations are plotted in Figure 6.12. The results showed no significant improvement of precision by applying more phase steps. The average errors from three chosen spots at different locations show similar errors with different averaging number of PSI.

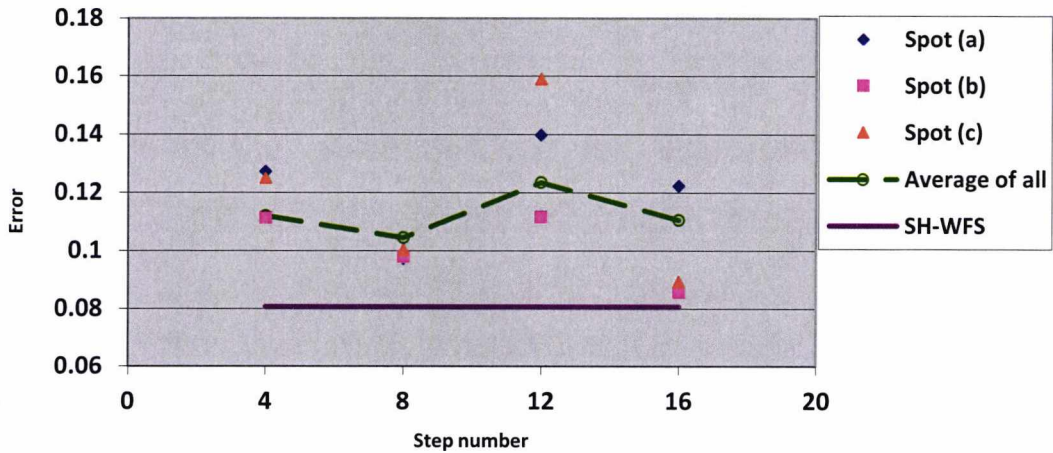


Figure 6.12. Average of absolute errors of spots centroid coordinates obtained with the TD-CG/SH-WFS with  $n$ -step PSI ( $n = 4, 8, 12$  and  $16$ ); in contrast with the stand deviation of the results obtained by the standard SH-WFS (the purple solid line).

#### 6.3.1.1.4 Wavefront Reconstruction

After spots coordinates were extracted from a TD-CG/SH-WFS image, using the Zernike polynomial technique described in section 6.1.2.2, Zernike coefficients, order 0 to 11 are calculated (Figure 6.13 left) and the wavefront is reconstructed on the right. There is little aberration in the measured wavefront; only zero-order piston is present.

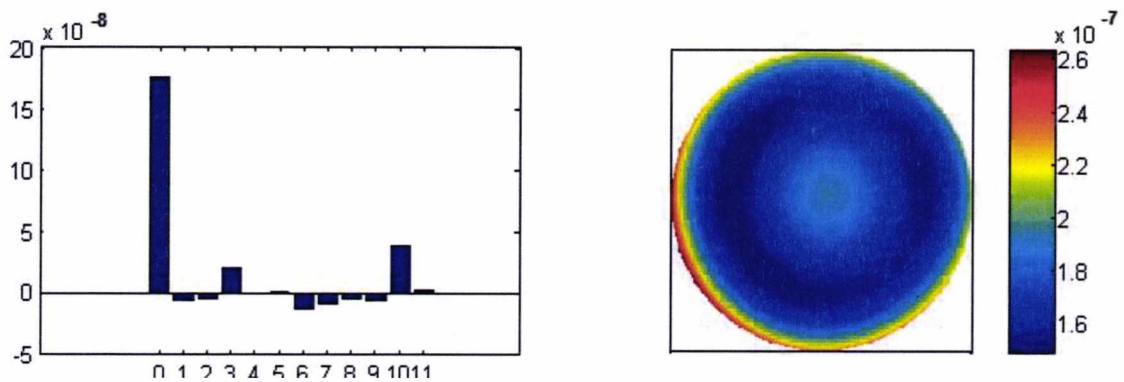


Figure 6.13. Left: Zernike coefficients of TD-CG/SH-WFS measurement; right: reconstructed wavefront from the measurement.

### 6.3.1.2 SS-CG/SH-WFS

For SS-CG/SH-WFS, sequential image acquisitions were carried out as the light source wavelength was sweeping from 826 nm to 873 nm in 256 steps. With the camera working at 250 fps and 300  $\mu$ s integration time each frame, a stack of 256 images were collected. Each pixel in the image stack was extracted along the spectral domain and corresponding to a spectrum of 47 nm, which can produced an axial resolution of 6.8  $\mu$ m at best. The wavelength tuning step is approximately 0.18 nm, much larger than the wavelength linewidth of the source, 0.05 nm; therefore the depth range of the volume is determined by the spectral resolution and is calculated to be  $\sim$  0.92 mm in air. For 256 steps swept-source acquisition, due to the symmetry of Fourier transformation, 128 *en-face* images were obtained in depth; thus each frame is 7.2  $\mu$ m thick (0.92 mm/128), which is close to the best axial resolution. The axial resolution is measured in the experiment by using a mirror as the object. By displacing the translation stage in the reference arm, TSR (Figure 6.8) for 0.381 mm from OPD = 0, a sequence of images were acquired with the tuning wavelength; thus a 3D volume is obtained. Figure 6.14 displays an A-scan at a pixel in the centre of a SH spot that is extracted from the volume. The peak of the A-scan is only achieved in a single frame (the 53rd frame in depth). The axial position of the SH spot was calculated as 0.382 mm ( $53 \times 7.2 \mu\text{m}$ ), which meet the value of the OPD that was applied.

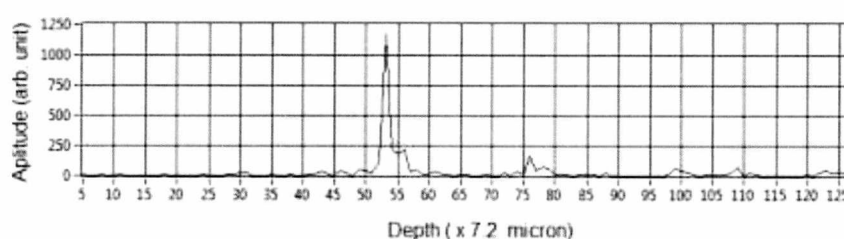


Figure 6.14. An A-scan from a pixel at the centre of a SH spot acquired from an object mirror by the SS-CG/SH-WFS system.

#### 6.3.1.2.1 SH Spots Pattern in 3D

A characteristic of SS-CG/SH-WFS is that the SH spots pattern is distributed in a 3D volume rather than a 2D *en-face* image. The axial location of the spots in the volume, in our experiments, is determined by the OPD between the object beam and the reference beam. If the object beam is so aberrated that the peak-to-valley

wavefront error is greater than the axial resolution of the CG/SH-WFS imaging, a single *en-face* coherence image extracted from the 3D volume will present only a part of the spots pattern, which has already been demonstrated (Figure 6.10) in TD-CG/SH-WFS. Figure 6.15 (a), (b) and (c) presents three *en-face* images extracted from a 3D data volume at three successive axial positions. The distributions of spots in these three frames indicate that the wavefront measured from the object is tilted. The complete SH spots pattern (Figure 6.15, d) can be obtained by summing these three slices, which is required for wavefront analysis and reconstruction.

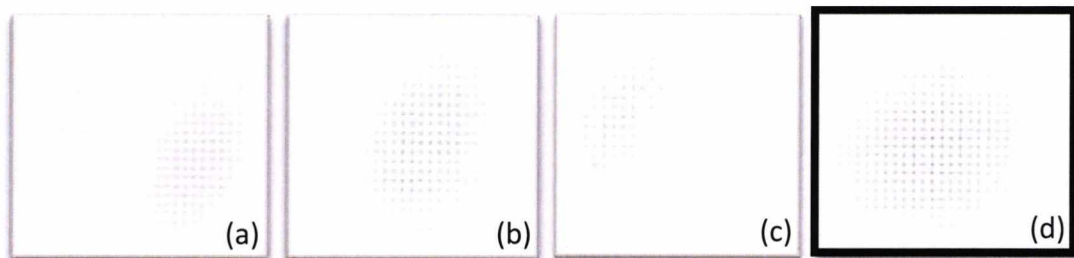


Figure 6.15. Three *en-face* images (a), (b) and (c) from three successive axial position in a 3D volume acquired by the SS-CG/SH-WFS system; the complete SH spots pattern (d) is obtained by summing (a), (b) and (c).

#### 6.3.1.2.2 Rejection to Stray Lights

CG/SH-WFS's capability of rejecting stray light was also confirmed with the SS-CG/SH-WFS method. A similar acquisition, as shown in Figure 6.16, was repeated with SS-CG/SH-WFS. An *en-face* image that contains the SH spots pattern is retrieved from the 3D volume and is compared to the results of the standard SH-WFS and the TD-CG/SH-WFS (Figure 6.16). Clearly, SS-CG/SH-WFS is capable of eliminating the stray reflection (see those spots marked by yellow arrow in the SH-WFS image) similarly to the TD-CG/SH-WFS method does.

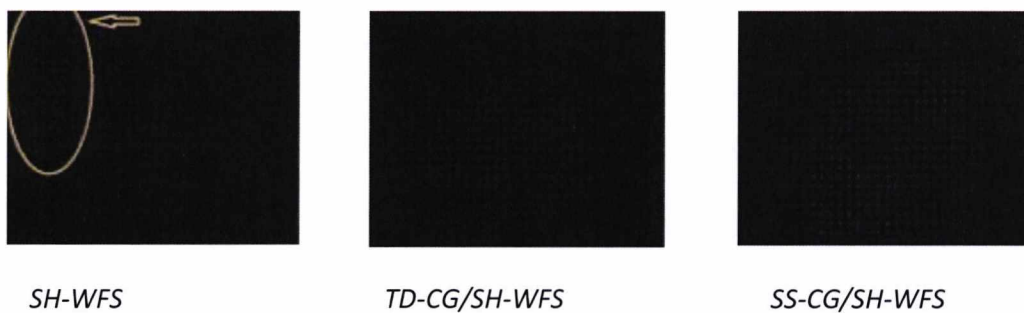


Figure 6.16. SH spot pattern images obtained from a single reflector by the same set-up with three methods: standard SH-WFS (left); TD-CG/SHWFS (middle) and SS-CG/SH-WFS (right).

### 6.3.1.2.3 Accuracy and Precision of SS-CG/SH-WFS

Low accuracy of CG/SH-WFS was suggested [32] possibly related to the non-uniformity of the reference beam profile that is a Gaussian. To investigate the relation, the centroid coordinates from 255 (15 x 15) spots were retrieved from the SS-CG/SH-WFS image; each window occupies an area of about 21 x 21 pixel<sup>2</sup>. An average absolute error  $(\overline{\Delta x_{SS}}, \overline{\Delta y_{SS}}) = (0.0098, 0.01)$  was obtained from all 225 spots. The error of each spot ( $j$ ) is calculated using a similar equation as Eq. (6.18). The distributions of these errors are given in Figure 6.17. On the left two charts, the absolute errors of all 255 spots were sorted according to the distance to the image centre (superposed with the centre of the reference beam) in the ascending order. The absolute errors and the standard deviations are mapped according to the spot locations in the image in middle column and the right column of Figure 6.17 respectively. From these results, the error (accuracy) and the standard deviation (precision) appear randomly in the map.

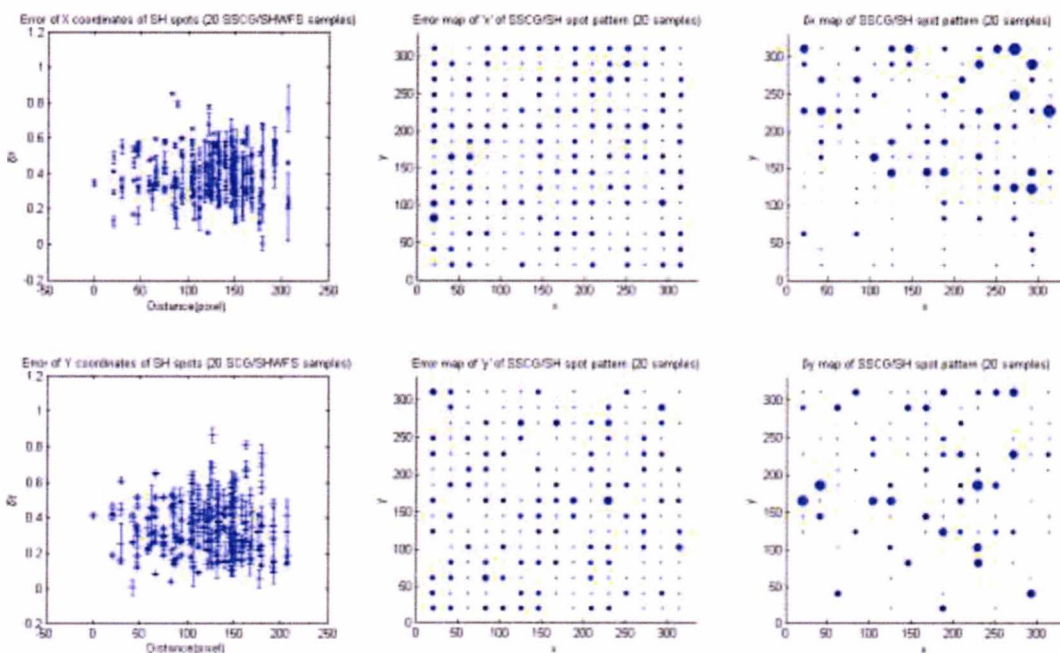


Figure 6.17. Left column: the error of the centroid coordinates of the 255 SH spots acquired with the SS-CG/SH-WFS; middle column and right column: the error maps and the standard deviation maps of the error according to the spot locations in the image, respectively. (Top row is for coordinate x and bottom is for y).

#### 6.3.1.2.4 Wavefront Reconstruction

With extracted SS-CG/SH spots centroid coordinates, Zernike coefficients, order 0 to 11 are obtained (Figure 6.18 left) and the estimated wavefront was reconstructed. We have seen that there is an amount of tilts (order 1 and 2) in Figure 6.15; this is confirmed by the reconstructed wavefront.

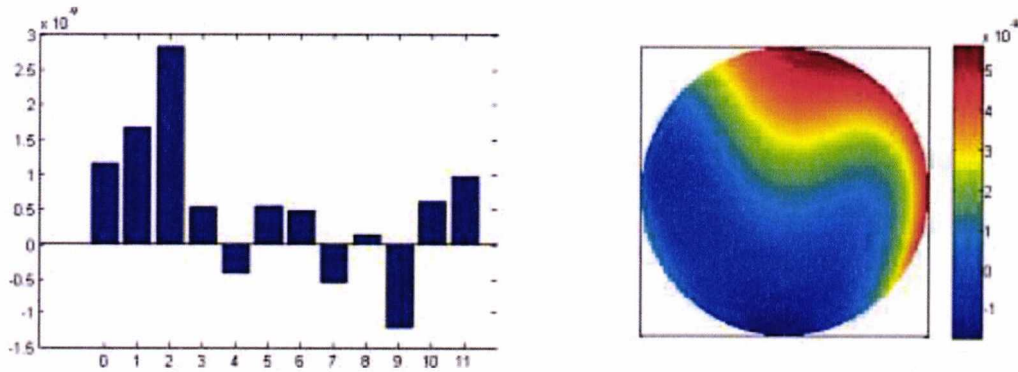


Figure 6.18 Left, Zernike coefficients obtained from the SS-CG/SH-WFS image; right, reconstructed wavefront.

#### 6.3.1.3 Comparisons

Normalised errors of the centroid coordinates obtained with both CG/SH-WFS methods from the reference and the standard deviations of the standard SH-WFS data are listed in Table 6.3 and plotted in Figure 6.19. From the results we can see that the accuracy of both CG/SH-WFS are not as good as the standard SH-WFS, which is expected because the standard SH-WFS image is actually an average of spots patterns from a large depth range, which is defined by the depth of focus of the lenslet; while in CG/SH-WFS, the coherence gating narrows the depth range, thus the spot positions are more sensitive to depth variations, which leads to a greater error.

Both standard SH-WFS and SS-CG/SH-WFS show similar errors in  $x$  and  $y$  directions; in contrast, the TD-CG/SH-WFS present a small difference in errors along two directions, i.e.,  $\Delta x_{TD}$  is larger than  $\Delta y_{TD}$ , which may be because the movement axis of the Piezo-actuator (PZT) was not perfectly parallel to the optical axis. If the angle between the PZT's displacement and the optical axis in  $x$  direction is larger than in  $y$  direction, it may produce a larger error in  $x$  direction.

Table 6.3. Comparison of the accuracy of TD-CG/SH-WFS and SS-CG/SH-WFS to a standard SH-WFS.  $\Delta x$  and  $\Delta y$  represent the error of the spot centroid coordinates along x and y axis.

	$\Delta x$	$\Delta y$
SH-WFS	0.00055	0.00042
TD-CG/SH-WFS	0.00820	0.00570
SS-CG/SH-WFS	0.00980	0.01000

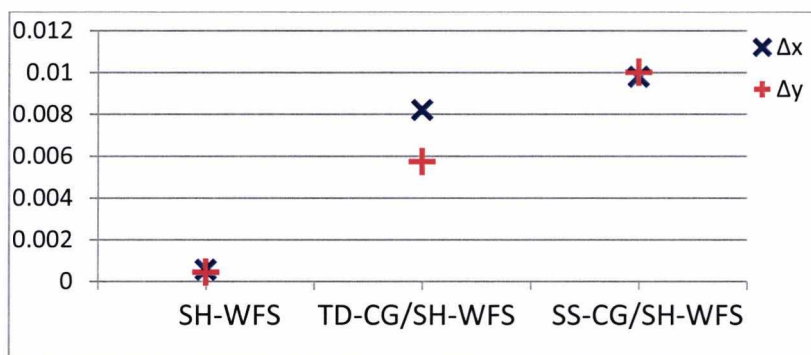


Figure 6.19. Comparison of the errors of TD-CG/SH-WFS, SS-CG/SH-WFS measurements with standard SH-WFS.

### 6.3.2 Multi-layer Targets

To demonstrate the capability of measuring depth-resolved wavefront aberrations in real time, the CG/SH-WFS measurement has been performed in time-domain with a simple multi-layer object that is composed by two thin microscope slides (~1.4 mm thick) and a mirror (Figure 6.20) mounted on the translation stage, TRO. The two slides contribute to 4 interfaces, corresponding to discontinuities in the index of refraction from air to glass, with a 5<sup>th</sup> interface due to the mirror, placed approximately 1.7 mm away. The two slides are deliberately tilted by a small angle (less than 0.025 rad) in relation to each other along horizontal direction (x axis).

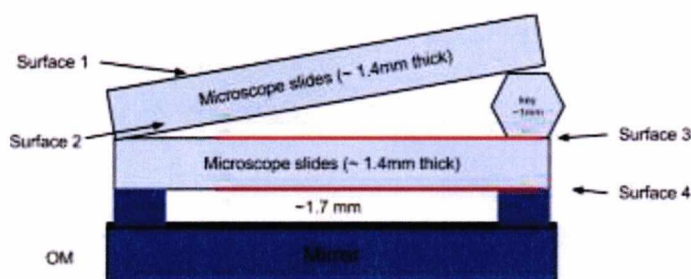


Figure 6.20. A 5 layer target made of two non-parallel microscope slides of 1.4 mm thickness mounted in front of a mirror, OM.

For all the SH spots images acquired in these experiments, matrices of 17 x 17 spots in the central area of the images are used to calculate the aberrations and reconstruct the wavefronts. A window of 22 x 22 pixels<sup>2</sup> is allocated to each spot. Standard SH-WFS images and CG/SH-WFS images were collected by selecting the OPD to match the 5 different depths.

Initially, a direct SH-WFS image (Figure 6.21, a) was acquired from the mirror, OM without the microscope slides in place by placing the OM under the focus of the lens L1. This is considered as a reference of SH spots pattern, which is required to calculate the wavefront slopes for the following measurements. The focus is found by maximising the intensity of the spots while keeping the size of the object beam (the spots pattern) as the same as that of the reference beam. Then the reference path was adjusted to move the axial position of the coherence gate to match the mirror location, i.e. OPD = 0 for the optical lengths measured up to RM and the OM. This adjustment is performed in real time by actuating the TSR until spots are seen in the coherence-gated image. In the following experiments, the reference mirror, RM, is kept in this position and the object position is adjusted by moving TSO to place different planes to OPD=0.

### **6.3.2.1 Rejection of Stray-reflections**

The glass slides were mounted above the OM and the whole object (slides and OM) was moved axially away from the BS3 until interference spots are obtained for the first surface (the farthest from the OM), as shown in Figure 6.21 (d). By blocking the reference path, a standard SH-WFS image was recorded (Figure 6.21 b), which shows several sets of spots patterns, from all 5 planes in the object. There is no way to distinguish among the sets of spots and evaluate the wavefront corresponding to each of them. By inserting a screen between the second slide and the OM, a simpler object of 4 layers reflecting similar strengths was under interrogation, even the image acquired in this occasion without the reflection from OM (Figure 6.21 c) is not suitable for standard SH-WFS numeric processing because each spot in the sub-image is a superposition of four spots from four different axial position in the sample. The centroid evaluation may not work because more than one spots are present in each window with similar image values. A TD-CG/SH-WFS image were

acquired from the same layer with the presence of the reflection from the OM, the image is shown in Figure 6.21 (d). Only one group of SH spots is visible, that are from the axial position at  $OPD = 0$ .

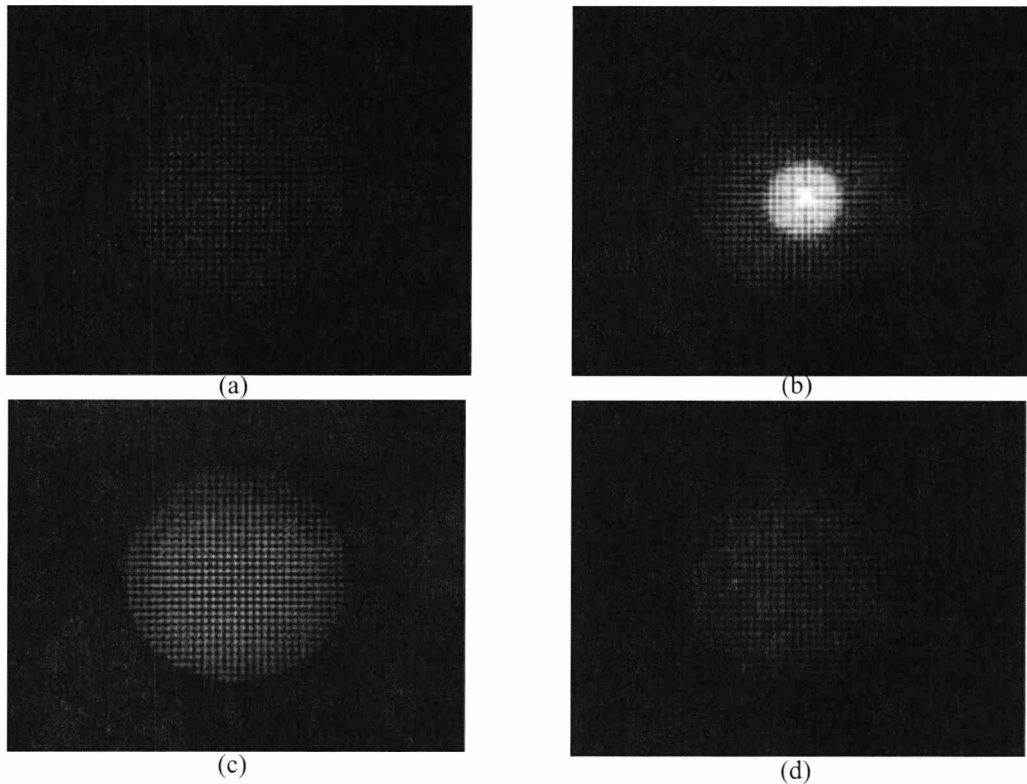


Figure 6.21. (a), SH-WFS image from the object consisting of a mirror, OM only; (b) SH-WFS image from the object with five layers, where the first surface of the slides is at  $OPD = 0$ ; (c) SH-WFS image for the case at (b), where a screen is placed between the 2nd slide and the OM; (d) TD-CG/SH-WFS image, for the case at (b).

As another feature of the CG-SH/WFS, although some parts of the camera are saturated by strong OM reflections, these values are automatically eliminated by the PSI calculation, as there is no difference between the four values recorded in phase-shifted frames. In fact, the experiments show that intentionally increasing the exposure time of the camera to reach saturation may reduce the overall speckle noise in the TD-CG/SH-WFS images, as long as saturation does not occur at the same positions where the spots of interest are.

### 6.3.2.2 Depth-resolved Wavefront Measurements

The measurements are repeated for each of the 5 surfaces in the object by moving the object until the corresponding en-face image of spots pattern is visible, which

produce 5 groups of data. Zoomed images of standard SH-WFS and CG/SH-WFS are displayed in pairs in each column (standard SH-WFS image above CG/SH-WFS images) for each surface in Figure 6.22. The brightest spots in the standard SH-WFS images are due to reflections from the OM, which dominate all other spots from the other 4 layers. In (a), (b), (c) and (d), the spots of interest, whose positions can be located in (f), (g), (h) and (i) respectively, are dim in comparison to bright reflections from the OM. Saturation of the camera occurred in (a), (b) and (c). In (e), however, the spots of interest are those created by the mirror, which can be selected directly from the image though those spots from other layers contribute to noises and thus add error to the result. As it can be seen, the further the plane of interest is away from the mirror, the worse the SH spots image appears. When the surface close to OM is under interrogation (Figure 6.22 d), the spots of interest are so close to those created by the OM, in which case, the retrieved SH spots could be only from the mirror. In thick-specimen microscopy [267], this means if a tissue that has a strongly reflective layer close to some scattering layer features, the wavefront aberration cannot be measured from those scattering layers, and even for the measurement on the reflective layer, large errors are expected due to the spots from those layers nearby. In contrast, only one group of spots is obtained from the axial position  $OPD = 0$ , in all TD-CG/SH-WFS images (Figure 6.22, f to j). The reflections from other surfaces including the OM are totally eliminated.

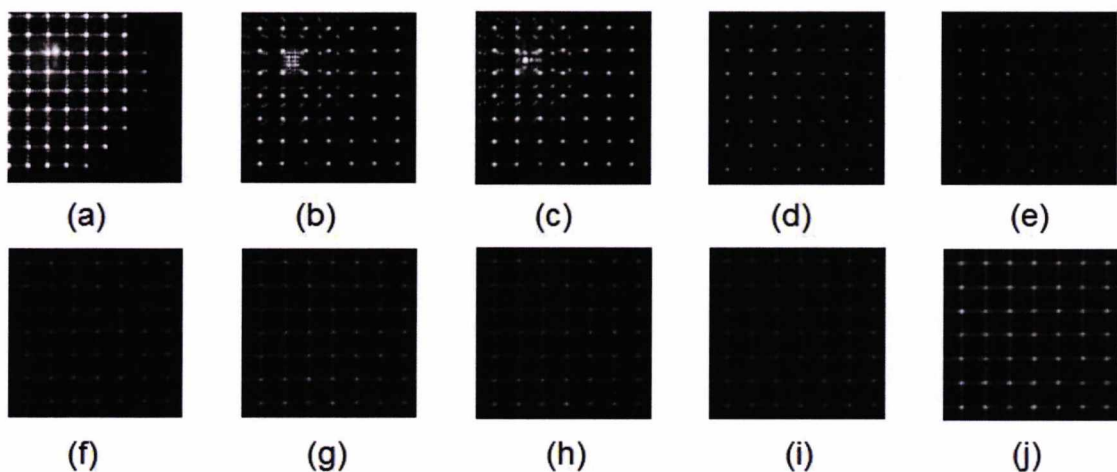


Figure 6.22. Zoom images collected from the SH spots obtained with the standard SH-WFS, (a) to (e) and with the CG/SH-WFS, (f) to (j). In each column, the OBJ was moved until the 1<sup>st</sup>, 2<sup>nd</sup>, 3<sup>rd</sup>, 4<sup>th</sup> surface of the slides and the mirror are at  $OPD = 0$  respectively.

Since each CG/SH-WFS image contains spots from a single layer in the OBJ, the wavefront can therefore be correctly evaluated and its aberrations are calculated and expressed in terms of Zernike polynomials. The coefficients of Zernike expansion are illustrated in the bottom of Figure 6.23. The most important are the 2<sup>nd</sup>, the 3<sup>rd</sup> and the 5<sup>th</sup> coefficients, responsible for tilt along x-axis, tilt along y-axis and defocus respectively. As presented earlier, the OM was aligned in the focus of L1 and the coherence gate was adjusted at the depth of OM initially. Only after that, the two slides were added to the OBJ., therefore the inserted medium of higher refractive index make the focal plane and the coherence gate departed in opposite direction (see Chapter 3, section 3.3.4).

The focus position moves behind the OM, away from BS3, while the coherence gate moves towards BS3. To regain the OPD = 0 at each interface, the whole object was moved axially away from BS3 until the 1<sup>st</sup> interface was placed at OPD = 0, where the OM was initially. Obviously the coherence gate coincides with the focus at here. After that, in order to regain OPD = 0 at the 2<sup>nd</sup> interface, the OBJ is moved towards BS3; therefore for the 2<sup>nd</sup> and 3<sup>rd</sup> interface at OPD = 0, the focus moves away from BS3, inside the glass slide by  $(n^2 - n)t$ , where  $t$  is the slide thickness that is and  $n$  is the index of refraction. For the 4<sup>th</sup> interface and the OM, the focus moves by  $2(n^2 - n)t$ . The 5th Zernike coefficients in Figure 6.23 (f) show the smallest value for the 1<sup>st</sup> interface (where coherence gate was superposed on the focus), while larger values are obtained for the 2<sup>nd</sup> and 3<sup>rd</sup> interface and even larger for the 4<sup>th</sup> and the 5<sup>th</sup> interface. Due to similar differences between the focus position and the coherence gate position when measuring the wavefront for the 2<sup>nd</sup> and 3<sup>rd</sup> interface, similar results for the 5<sup>th</sup> coefficient are obtained. For the same reason, the values of the 5<sup>th</sup> coefficient for the 4<sup>th</sup> and 5<sup>th</sup> interface are also similar. The results in Figure 6.23 also show that aberrations of tilts in x direction (the 2<sup>nd</sup> term of Zernike coefficients) are larger than those in the y-direction (the 3<sup>rd</sup> term) due to the deliberate tilt of the top slide in the OBJ.

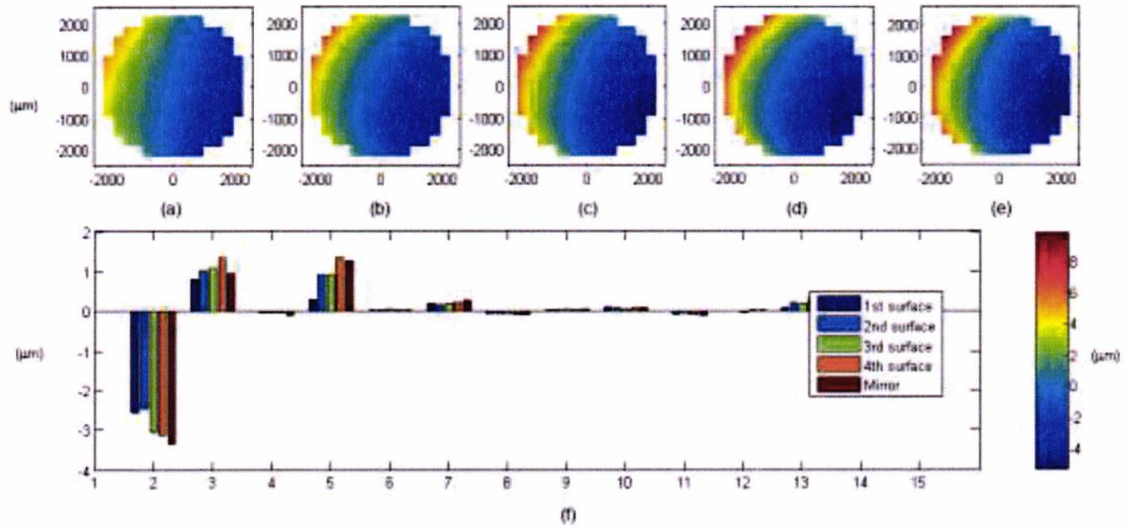


Figure 6.23. Reconstructed wavefronts from all 5 layers of the object: (a), (b) (c) and (d) are the wavefronts measured from the 1st to the 4th surfaces of the slides respectively; (e) is the wavefront measured from the mirror behind the two slides; (f) displays the first 15 Zernike coefficients for all measurements.

### 6.3.3 Scattering Sample

The wavefront was measured from a piece of printing paper. Without applying coherence gating, the wavefront was measured from the top of the paper. The retrieved wavefront slopes, Zernike coefficients and reconstructed wavefront are displayed in Figure 6.24.

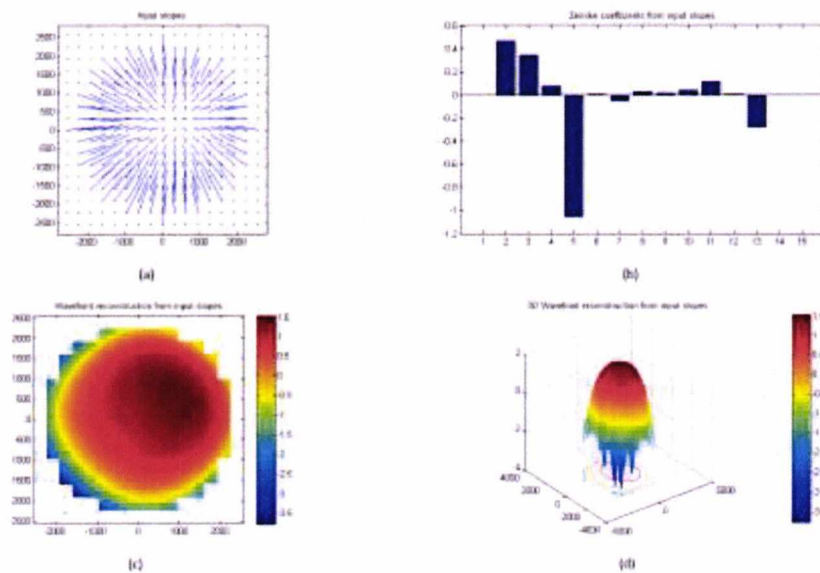
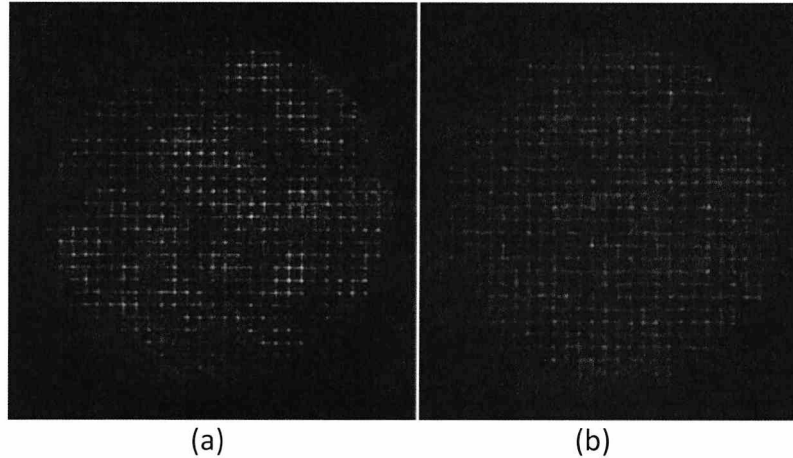


Figure 6.24. Wavefront slopes (a), Zernike coefficients and reconstructed wavefront (c and d) measured from a piece of paper with standard SH-WFS.

With TD-CG/SH-WFS, wavefronts from the paper were measured over a depth range of  $130\ \mu\text{m}$ , which is the limit to the sensitivity of TD-CG/SH-WFS. Over this range, the spots are too dim to be counted and used to retrieve the centroid coordinates. The two images below are acquired at the top and at  $130\ \mu\text{m}$  deep position



*Figure 6.25. SH spots images obtained with TD-CG/SH-WFS method from a point on and in a piece of printing paper at the top (a) and  $130\ \mu\text{m}$  deep (b) positions*

For SS-CG/SH-WFS method,  $N = 128$  was used to tune the wavelength over  $50\ \text{nm}$  range, which produce a depth range of  $460\ \mu\text{m}$ . Image #1 to #15 are selected, which correspond to a depth range of  $115\ \mu\text{m}$ .

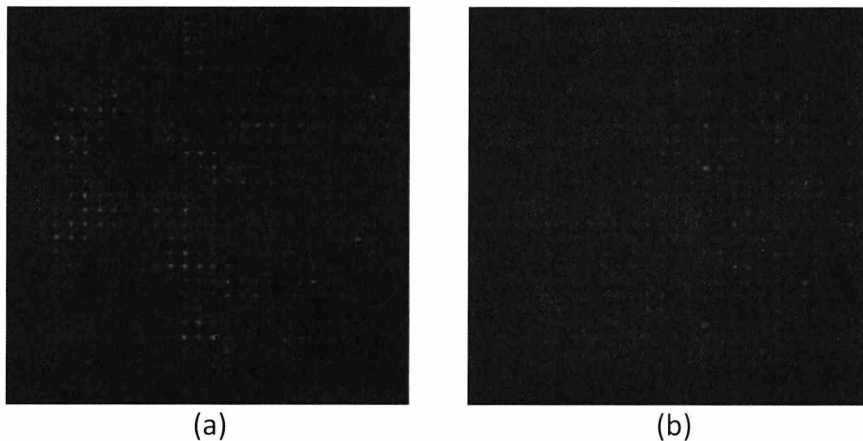


*Figure. 6.26. SH spots images obtained with SS-CG/SH-WFS method from a point on and in a piece of printing paper at the top (a) and  $115\ \mu\text{m}$  deep (b) positions*

Using the spots collected from  $50\ \mu\text{m}$  with TD-CG/SH-WFS and SS-CG/SH-WFS, the wavefront are reconstructed as shown in

Figure 6.27. shows that the results obtained with the two CG/SH-WFS methods meet sufficiently well. Compared with the results acquired by the standard SH-WFS (Figure 6.24), where most signal was acquired from the top of the paper, the measurements from 50  $\mu\text{m}$  inside the paper present larger aberration of 'tilts along  $y'$ ' than 'tilts along  $x'$ ', which is opposite in the results obtained from the top of the paper acquired by the standard SH-WFS.

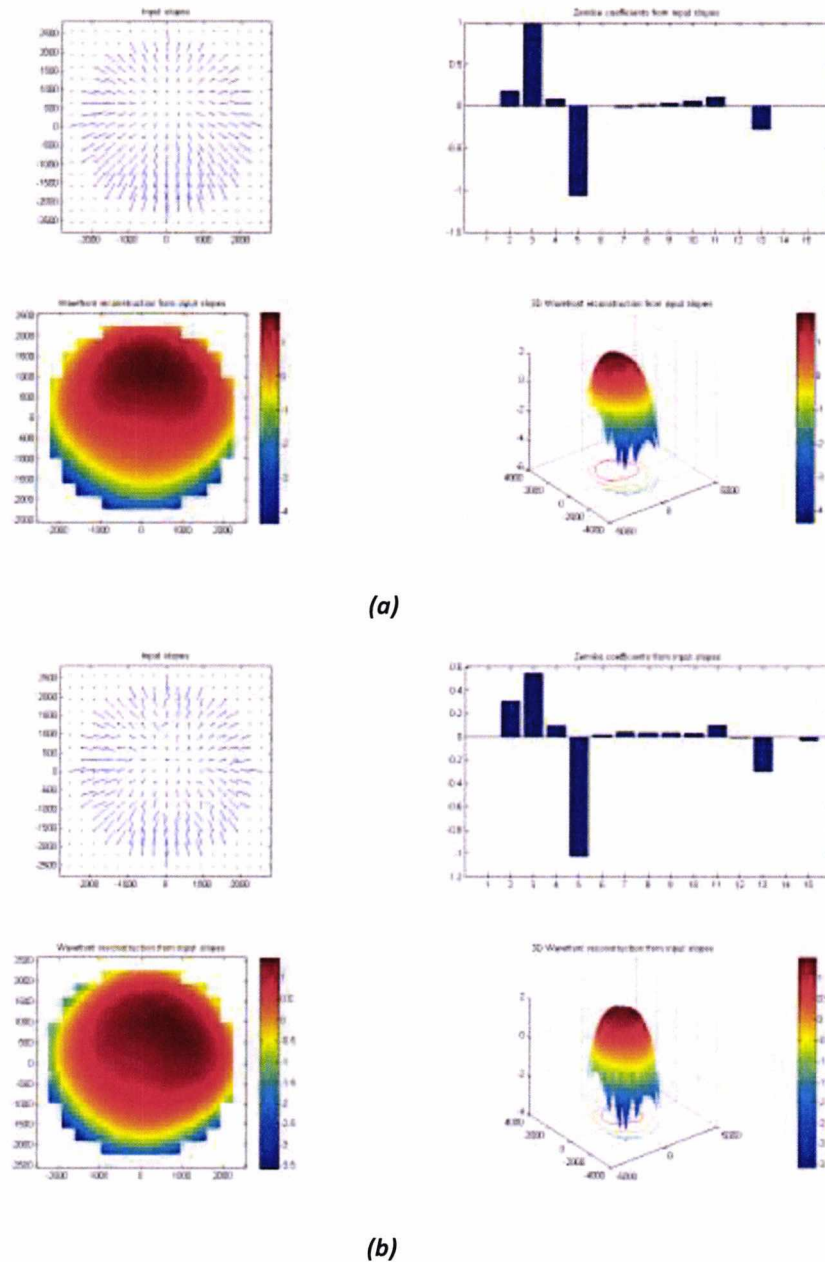


Figure 6.27. Wavefront slopes, Zernike coefficients and reconstructed wavefront measured from 50  $\mu\text{m}$  deep inside the paper with TD-CG/SH-WFS (a) and SS-CG/SH-WFS (b) respectively.

### 6.3.4 Signal Strength

Coherence gate introduces an amplification effect of the weak signal with the strong reference signal. Considering the optical density (OD) of the NDFs in the object and reference arms, NDO and NDR, are  $D_o$  and  $D_r$  respectively, the reflectivity of the object and reference are  $R_o$  and  $R_r$ , the signal in the conventional SH-WFS,  $S_{SH-WFS}$ , is given by

$$S_{SH-WFS} = D_o^2 \cdot R_o \quad (6.19)$$

Given the reflectivity of both OM and RM are close to 1, the amplitude of the interference signal can be expressed as

$$S_{CG/SH-WFS} = \sqrt{D_o^2 \cdot R_o \cdot D_r^2 \cdot R_r} \approx D_o \cdot D_r \quad (6.20)$$

Therefore the ratio of signal strength of CG/SH-WFS to that of conventional SH-WFS can be written as

$$\frac{S_{CG/SH-WFS}}{S_{SH-WFS}} = \frac{D_r}{D_o} \quad (6.21)$$

To compare the signal noise performance in experiments, data were collected with the same  $D_r = 0.3$  (-3dB) and the  $D_o = 0.6$  (-6dB) with both the CG/SH-WFS method and the standard SH-WFS, Figure 6.14 present the signal and noise level from image rows that cross the centre of a spot row. The result from the conventional SH-WFS (blue), present a consistent noise floor and peak values. A signal strength enhancement of 3dB was observed from the results of TD-CG/SH-WFS to that of standard SH-WFS. However both the peak and the noise levels are not as consistent, which is a consequence of residual fringes and high speckle noise.

As described in Chapter 3 and Chapter 4, swept-source OCT provides a larger signal-to-noise ratio in comparison to the time domain OCT approach [74]. With given NDO and NDR, SS-CG/SH-WFS approach should have an extra gain of SNR,  $N/2$ , to the TD-CG/SH-WFS approach, where  $N$  is the spectrum sampling number. In

the experiments, the SNR of the SS-CG/SH-WFS result presents an average 4dB (2.5 x) improvement over that of the TD-CG/SH-WFS. This value is smaller than the theoretical advantage, 15 dB (32 x,  $N = 64$ ), which is possibly due to the lack of spectrum resampling and the imperfect spectrum shape of the source.

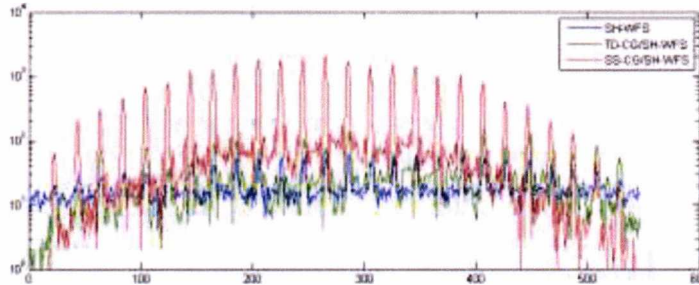


Figure 6.28. Comparison of a image row of the SH spots image acquired with three configuration, conventional SH-WFS (blue), TD-CG/SH-WFS (red) and SS-CG/SH-WFS (green).

### 6.3.5 Challenges

#### 6.3.5.1 Background level

One main challenge to the CG/SH-WFS methods is that the image background value is higher than that of the conventional SH-WFS images due to the effect of signal enhancement to some unwanted light that happen to fall within the coherence gate, including the transmission light passing through the gaps between the circular lenslets and the diffraction occur at the edge of the lenslet aperture. One way to reduce the transmission is employing those lenslet arrays manufactured with chrome apertures that can stop the transmission. Fig. 6.29 shows the difference of zoomed spots images without and with the chromatic apertures. The experiments above use the lenslet array without chrome aperture is because large pitch size is preferred. Specifications of the lenslet arrays that have been tested in our experiments are give in Table 6.4



Fig. 6.29. Comparison of CG/SH-WFS spots without (left, MLA300-14AR ) and with (right, MLA150-5C) chrome apertures; these two images were acquired with TD-Cg/SH-WFS method.

Table 6.4. Parameters of Lenslet arrays used in experiments

Item #	MLA150-5C	MLA150-7AR	MLA300-14AR
Manufacturer	Thorlabs		
Substrate Material	Fused Silica (Quartz)		
Wavelength Range	300 - 1100 nm	400 - 900 nm	
Lenslet Grid Type	Square Grid		
Lenslet Pitch	150 $\mu\text{m}$		300 $\mu\text{m}$
Lens Shape	Round, Plano Convex Spherical		Square, Plano Convex Parabolic
Lens Diameter	146 $\mu\text{m}$		300 $\mu\text{m}$
Chrome Apertures	Yes	No	
Reflectivity	<25%	<1%	<1%
Focal Length	5.2 mm	6.7 mm	18.6 mm

### 6.3.5.2 Spots Shape Variations

A specific problem to TD-CG/SH-WFS is that the shapes of SH spots are very sensitive to the OPD variations. Figure 6.30 illustrates how much the shapes of the SH spots are changing during the acquisitions at two axial positions separated by  $\sim 8 \mu\text{m}$ . This effect is related to the parasite fringes introduced by the PSI and can only be reduced by minimising the phase stepping error. The centroiding accuracy and the repeatability of the measurement suffer when the phase error is large.

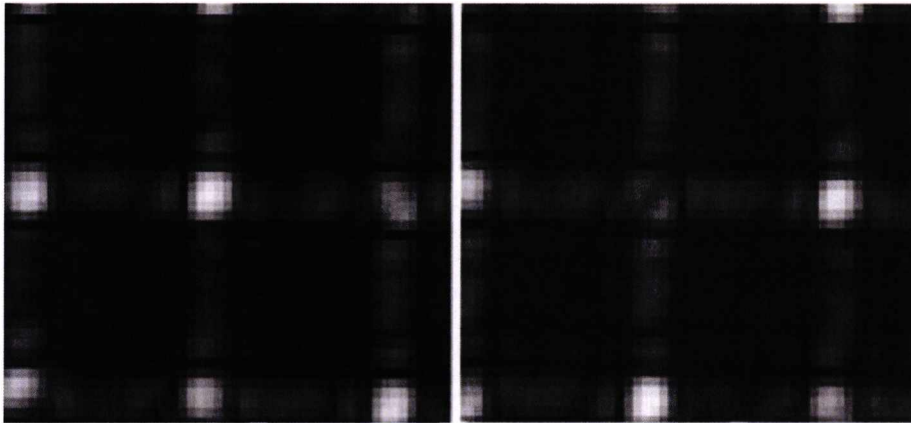


Figure 6.30. SH spots acquired by TD-CG/SH-WFS at two OPDs separated by  $\sim 8 \mu\text{m}$ .

### 6.3.5.3 Spots Pattern

For both CG/SH-WFS, a limitation compared to the conventional SH-WFS is the challenge to obtain a complete SH spots pattern. This deficiency is actually a direct result of the shallow depth range; however, because complete SH spots pattern is

required for modal wavefront analysis and reconstruction, more than one *en-face* CG/SH-WFS images are usually required to produce a complete spots pattern. For SS-CG/SH-WFS, because a 3D volume of images are obtained simultaneously, therefore no extra acquisitions are required; whereas in TD-CG/SH-WFS, in order to obtain real-time wavefront information, a second image is sometimes required, which slow the WFS process and also increase the depth resolution.

## **6.4 Conclusions**

In this chapter, a novel technique, known as coherence gated SH-WFS (CG/SH-WFS) is demonstrated capable of generating similar Shack-Hartmann (SH) spots pattern as a conventional SH-WFS. The advantages of CG/SH-WFS include depth sensitivity as small as the depth resolution of OCT, the capability of eliminating stray reflections and enhancing the signal strength from a low-reflective or scattering target. As a result, wavefront aberrations can be measured from a shallow layer in a selected depth inside a medium.

The depth-resolved wavefront information from different layers were measured from a multi-layer object with TD-CG/SH-WFS method; and the wavefront from a location 50  $\mu\text{m}$  deep inside a piece of paper was measured with SS-CG/SH-WFS method. Both methods have the potential of guiding better wavefront correction in adaptive optics assisted ophthalmology imaging and confocal microscopy systems. CG/SH-WFS can provide direct wavefront measurement from highly scattering tissue in Microscopy which is not possible with standard SH-WFS due to the presence of large amount of background light. In ophthalmology, the capability of rejecting stray light may allow CG/SH-WFS to be integrated with imaging systems with lens rather than curved mirrors, thus reduce the system-induced aberrations and the size of the optical layout.

# Chapter 7 Conclusions

Parallel-detection OCT is an alternative OCT method that allows reducing or eliminating mechanical scanning. Three approaches of parallel OCT based on 2D detector arrays have been demonstrated in the thesis.

Both time-domain full-field OCT (FF-OCT) and full-field swept-source OCT (FF-SS-OCT) employ flood-illumination in a 2D field of view and use a 2D detector array to acquire OCT images in *en-face* planes without the need of scanning the object beam in transversal plane. FF-OCT allows acquiring *en-face* OCT images from a shallow depth directly; while FF-SS-OCT acquires a 3D data volume from a sequence of wavelength-resolved images. In chapter 4, a coherence radar set-up is demonstrated allow obtaining topography images with high axial resolution in *en-face* plane. Based on this set-up, a novel method of curvature measurement from spherical objects was presented by employing multiple optical delay lines. Multiple depth-resolved contours are acquired simultaneously from a single *en-face* image, which allow better stability and higher rate of the measurements.

The coherence radar set-up was later modified by using high NA optics to allow acquiring FF-OCT images from biological samples. FF-OCT provides *en-face* OCT images with high spatial resolution. FF-OCT images of my fingers and fruit fly larvae have been acquired. Extending the imaging regime from time domain to spectral domain, by employing a wavelength-tuneable source, the same system has been used to deliver 3D image volumes. Measurements in both the time-domain and spectral-domain using the same set-up were performed to demonstrate that the signal-to-noise ratio of SS-OCT is superior to that of TD-OCT, which is expected from mathematical treatments.

Line-field Fourier-domain OCT (LF-FD-OCT) is another parallel-detection OCT technique, which is based on the principle of Fourier-domain OCT. In Chapter 5, spectrometer-based Fourier domain-OCT (FD-OCT) was implemented in parallel. A line-field on the target is illuminated and an array of channelled spectra is acquired by a 2D detector array. By arranging the optical paths differently in two directions,

the multi-channel spectrometer allows acquiring depth related modulation of interference signal from a line-field simultaneously, which produces a B-scan OCT image from a single camera shot. B-scan images acquired from my fingers and other biological samples including fruit fly larvae and human teeth from patients are shown. The structure of the LF-FD-OCT system is comparatively simple and compact. The imaging process is straightforward and highly iterative which inspired me to evaluate the possibility of using extended light sources in FD-OCT. The results have shown good depth resolution, but low brightness limits the applications of such sources. The line-field FD-OCT set-up was also modified to equip commercial digital cameras. The ability of the DSLR camera to resolve the channelled spectrum from the spectrometer and to produce OCT images from reflective layered structure are demonstrated. The performances of the low-cost cameras were compared with the expensive counterparts. The experiments with the DSLR are rather preliminary, however the results show that low-cost consumer-grade cameras have the potential to replace expensive scientific cameras in FD-OCT.

The principle of low coherence interferometry (LCI) has been used to assist wavefront sensing (WFS). In Chapter 6, a physical Shack-Hartmann wavefront sensor (SH-WFS) is shown combined with a LCI set-up, which allows the depth range of WFS to be narrowed down to the scale of the axial resolution of the LCI. The acquisition methods of FF-OCT and FF-SS-OCT have been applied here, which allow distinguishing wavefront aberrations introduced by different layers in a multi-layer object. Wavefront information was obtained from weak signal that was collected from 50  $\mu\text{m}$  deep inside a scattering medium (paper). This technique is promising to allow direct WFS in thick-tissue microscopy, which is difficult with the conventional SH-WFS techniques.

The advantages of all the three parallel OCT techniques are similar. Because the OCT signals from different transversal positions are acquired simultaneously, the imaging rates are only dependent on the frame rate of the detector array. Many modern CMOS cameras present a frame rate of 1K fps with 1 Megapixel, which corresponds to approximately 1 GHz OCT data rate.

FF-OCT has a unique advantage that allow using high NA optics to acquire high transverse resolution without affecting the depth range; therefore it has been used widely as a supplement to the conventional microscopy. By using incoherent light sources that have large wavelength bandwidths, FF-OCT can achieve high spatial resolution in both axial and lateral direction at the same time. Due to the signals are acquired in parallel simultaneously, all parallel OCT present good stability in the lateral direction, which make them useful in phase mapping, Doppler tomography and material analysis.

For LF-FD-OCT, if thin line-shape extended sources with relative high brightness are available, it is possible to replace expensive SLDs with low-cost optical sources and the imaging quality may be improved due to reduced cross-talks. With the advance of digital camera technology, it is also promising to have industrial cameras in the FD-OCT be replaced by smart commercial cameras.

As for the depth-resolved wavefront sensing, works has been ongoing to equip this technique onto an AO-assisted ophthalmology imaging system and a microscopy system to guide better wavefront correction.

# Reference

1. A. F. Fercher, W. Drexler, C. K. Hitzenberger, and T. Lasser, "Optical coherence tomography-principles and applications," *Reports on progress in physics* **66**, 239-303 (2003).
2. R. H. Webb, and G. W. Hughes, "Scanning Laser Ophthalmoscope," *Biomedical Engineering, IEEE Transactions on BME-28*, 488-492 (1981).
3. S. R. Arridge, and J. C. Hebden, "Optical imaging in medicine: II. Modelling and reconstruction," *Physics in Medicine and Biology* **42**, 841 (1997).
4. E. A. Swanson, J. A. Izatt, M. R. Hee, D. Huang, C. P. Lin, J. S. Schuman, C. A. Puliafito, and J. G. Fujimoto, "In vivo retinal imaging by optical coherence tomography," *Opt. Lett.* **18**, 1864-1866 (1993).
5. D. Huang, E. A. Swanson, C. P. Lin, J. S. Schuman, W. G. Stinson, W. Chang, M. R. Hee, T. Flotte, K. Gregory, C. A. Puliafito, and et al., "Optical coherence tomography," *Science* **254**, 1178-1181 (1991).
6. M. R. Hee, J. A. Izatt, E. A. Swanson, D. Huang, J. S. Schuman, C. P. Lin, C. A. Puliafito, and J. G. Fujimoto, "Optical Coherence Tomography of the Human Retina," *Arch Ophthalmol* **113**, 325-332 (1995).
7. C. A. Puliafito, M. R. Hee, C. P. Lin, E. Reichel, J. S. Schuman, J. S. Duker, J. A. Izatt, E. A. Swanson, and J. G. Fujimoto, "Imaging of macular diseases with optical coherence tomography," *Ophthalmology* **102**, 217-229 (1995).
8. J. A. Izatt, M. R. Hee, E. A. Swanson, C. P. Lin, D. Huang, J. S. Schuman, C. A. Puliafito, and J. G. Fujimoto, "Micrometer-Scale Resolution Imaging of the Anterior Eye In Vivo With Optical Coherence Tomography," *Arch Ophthalmol* **112**, 1584-1589 (1994).
9. S. Radhakrishnan, J. Goldsmith, D. Huang, V. Westphal, D. K. Dueker, A. M. Rollins, J. A. Izatt, and S. D. Smith, "Comparison of Optical Coherence Tomography and Ultrasound Biomicroscopy for Detection of Narrow Anterior Chamber Angles," *Arch Ophthalmol* **123**, 1053-1059 (2005).
10. J. A. Goldsmith, Y. Li, M. R. Chalita, V. Westphal, C. A. Patil, A. M. Rollins, J. A. Izatt, and D. Huang, "Anterior chamber width measurement by high-speed optical coherence tomography," *Ophthalmology* **112**, 238-244 (2005).
11. J. Welzel, E. Lankenau, R. Birngruber, and R. Engelhardt, "Optical coherence tomography of the human skin," *Journal of the American Academy of Dermatology* **37**, 958-963 (1997).
12. J. Welzel, "Optical coherence tomography in dermatology: a review," *Skin Research and Technology* **7**, 1-9 (2001).
13. M. C. Pierce, J. Strasswimmer, B. H. Park, B. Cense, and J. F. de Boer, "Advances in Optical Coherence Tomography Imaging for Dermatology," *J Investig Dermatol* **123**, 458-463 (2004).
14. T. Gambichler, G. Moussa, M. Sand, D. Sand, P. Altmeyer, and K. Hoffmann, "Applications of optical coherence tomography in dermatology," *Journal of Dermatological Science* **40**, 85-94 (2005).
15. D. Fried, J. Xie, S. Shafi, J. D. B. Featherstone, T. M. Breunig, and C. Le, "Imaging caries lesions and lesion progression with polarization sensitive optical coherence tomography," *Journal of Biomedical Optics* **7**, 618-627 (2002).

16. J. B. W. Colston, M. J. Everett, L. B. Da Silva, L. L. Otis, P. Stroeve, and H. Nathel, "Imaging of Hard- and Soft-Tissue Structure in the Oral Cavity by Optical Coherence Tomography," *Appl. Opt.* **37**, 3582-3585 (1998).
17. W.-C. Kuo, N.-K. Chou, C. Chou, C.-M. Lai, H.-J. Huang, S.-S. Wang, and J.-J. Shyu, "Polarization-sensitive optical coherence tomography for imaging human atherosclerosis," *Appl. Opt.* **46**, 2520-2527 (2007).
18. J. A. Izatt, M. D. Kulkarni, S. Yazdanfar, J. K. Barton, and A. J. Welch, "In vivo bidirectional color Doppler flow imaging of picoliter blood volumes using optical coherence tomography," *Optics Letters* **22**, 1439-1441 (1997).
19. S. Yazdanfar, M. Kulkarni, and J. Izatt, "High resolution imaging of in vivo cardiac dynamics using color Doppler optical coherence tomography," *Optics Express* **1**, 424-431 (1997).
20. D. C. Adler, R. Huber, and J. G. Fujimoto, "Phase-sensitive optical coherence tomography at up to 370,000 lines per second using buffered Fourier domain mode-locked lasers," *Opt. Lett.* **32**, 626-628 (2007).
21. G. J. Tearney, M. E. Brezinski, B. E. Bouma, S. A. Boppart, C. Pitris, J. F. Southern, and J. G. Fujimoto, "In vivo endoscopic optical biopsy with optical coherence tomography," *Science* **276**, 2037-2039 (1997).
22. D. C. Adler, C. Zhou, T.-H. Tsai, J. Schmitt, Q. Huang, H. Mashimo, and J. G. Fujimoto, "Three-dimensional endomicroscopy of the human colon using optical coherence tomography," *Opt. Express* **17**, 784-796 (2009).
23. M. Atif, H. Ullah, M. Y. Hamza, and M. Ikram, "Catheters for optical coherence tomography," *Laser Physics Letters* **8**, 629-646 (2011).
24. L. P. Hariri, G. T. Bonnema, K. Schmidt, A. M. Winkler, V. Korde, K. D. Hatch, J. R. Davis, M. A. Brewer, and J. K. Barton, "Laparoscopic optical coherence tomography imaging of human ovarian cancer," *Gynecologic Oncology* **114**, 188-194 (2009).
25. X. Li, C. Chudoba, T. Ko, C. Pitris, and J. G. Fujimoto, "Imaging needle for optical coherence tomography," *Opt. Lett.* **25**, 1520-1522 (2000).
26. A. Bradu, L. Ma, J. W. Bloor, and A. Podoleanu, "Dual optical coherence tomography/fluorescence microscopy for monitoring of *Drosophila melanogaster* larval heart," *Journal of Biophotonics* **2**, 380-388 (2009).
27. L. Ma, A. Bradu, A. G. Podoleanu, and J. W. Bloor, "Arrhythmia Caused by a *Drosophila* Tropomyosin Mutation Is Revealed Using a Novel Optical Coherence Tomography Instrument," *PLoS ONE* **5**, e14348 (2010).
28. A. A. Moayed, S. Hariri, E. S. Song, V. Choh, and K. Bizheva, "In vivo volumetric imaging of chicken retina with ultrahigh-resolution spectral domain optical coherence tomography," *Biomed. Opt. Express* **2**, 1268-1274 (2011).
29. E. Alarousu, L. Krehut, T. Prykäri, and R. Myllylä, "Study on the use of optical coherence tomography in measurements of paper properties," *Measurement Science and Technology* **16**, 1131 (2005).
30. R. K. Tyson, and M. Dekker, *Adaptive Optics Engineering Handbook* (Marcel Dekker Incorporated, 1999).
31. M. Feierabend, M. Rückel, and W. Denk, "Coherence-gated wave-front sensing in strongly scatteringsamples," *Opt. Lett.* **29**, 2255-2257 (2004).
32. S. Tuohy, and A. G. Podoleanu, "Depth-resolved wavefront aberrations using a coherence-gated Shack-Hartmann wavefront sensor," *Opt. Express* **18**, 3458-3476 (2010).

33. J. G. Fujimoto, S. De Silvestri, E. P. Ippen, C. A. Puliafito, R. Margolis, and A. Oseroff, "Femtosecond optical ranging in biological systems," *Optics Letters* **11**, 150 (1986).
34. R. C. Youngquist, S. Carr, and D. E. N. Davies, "Optical coherence-domain reflectometry: a new optical evaluation technique," *Optics Letters* **12**, 158-160 (1987).
35. A. A. Michelson, "The Relative Motion of the Earth and the Luminiferous Ether," *American Journal of Science* **22**, 120-129 (1881).
36. O. Svelto, *Principles of Lasers* (Springer, 1998).
37. J. W. Goodman, and A. H. Levesque, *Statistical optics* (1985).
38. M. Born, E. Wolf, A. B. Bhatia, P. C. Clemmow, D. Gabor, A. R. Stokes, A. M. Taylor, P. A. Wayman, and W. L. Wilcock, "Elements of the theory of interference and interferometers," in *Principles of Optics: Electromagnetic Theory of Propagation, Interference and Diffraction of Light* (Cambridge University Press, 2000), p. 290.
39. Y.-Y. Cheng, and J. C. Wyant, "Multiple-wavelength phase-shifting interferometry," *Appl. Opt.* **24**, 804-807 (1985).
40. M. R. Hee, "Optical Coherence Tomography: Theory," in *Handbook of Optical Coherence Tomography*, B. E. Bouma, ed. (Basel, New York, 2002).
41. M. A. Duguay, and J. W. Hansen, "AN ULTRAFAST LIGHT GATE," *Applied Physics Letters* **15**, 192-194 (1969).
42. A. F. Fercher, K. Mengedocht, and W. Werner, "Eye-length measurement by interferometry with partially coherent light," *Opt. Lett.* **13**, 186-188 (1988).
43. H. C. Fercher AF, Drexler W, Kamp G, Sattmann H. . , and 8328536., "In vivo optical coherence tomography," *Am J Ophthalmol.* **116**, 113-114 (1993).
44. T. D. Visser, and E. Wolf, "Potential scattering with field discontinuities at the boundaries," *Physical Review E* **59**, 2355-2360 (1999).
45. Superlum, "SLDs Product Overview," ([http://www.superlumdiodes.com/slds\\_overview.htm](http://www.superlumdiodes.com/slds_overview.htm), 2009), [http://www.superlumdiodes.com/slds\\_overview.htm](http://www.superlumdiodes.com/slds_overview.htm), Accessed 12th June 2009.
46. B. E. Bouma, and G. J. Tearney, "Optical Sources," in *Handbook of Optical Coherence Tomography*, B. E. Bouma, ed. (Basel, New York, 2002).
47. R. Tripathi, N. Nassif, J. S. Nelson, B. H. Park, and J. F. de Boer, "Spectral shaping for non-Gaussian source spectra in optical coherence tomography," *Optics Letters* **27**, 406-408 (2002).
48. T. Wilson, *Confocal microscopy* (Academic Press, 1990).
49. Inoue, "Foundations of confocal scanned imaging in light microscopy," in *Handbook of biological confocal microscopy, 3rd ed.*, J. B. Pawly, ed. (Springer, 2006).
50. W. Drexler, U. Morgner, F. X. Kärtner, C. Pitris, S. A. Boppart, X. D. Li, E. P. Ippen, and J. G. Fujimoto, "In vivo ultrahigh-resolution optical coherence tomography," *Opt. Lett.* **24**, 1221-1223 (1999).
51. L. Vabre, A. Dubois, E. Beaurepaire, and C. Boccara, "Optical coherence microscopy for high resolution biological imaging," *Photon Migration, Diffuse Spectroscopy and Optical Coherence Tomography: Imaging and Functional Assessment* **1**, 24-30 (2000).
52. R. K. Wang, J. Izatt, and M. D. Kulkarni, "Optical Coherence Microscopy," in *Handbook of Optical Coherence Tomography*, B. E. Bouma, ed. (Basel, New Yoek, 2002).

53. A. Rollins, and J. Azatt, "Reference Optical Delay Scanning," in *Handbook of Optical Coherence Tomography*, B. E. Bouma, and G. J. Tearney, eds. (Basel, New York, 2002).
54. J. Szydlo, N. Delachenal, R. Gianotti, R. Wälti, H. Bleuler, and R. P. Salathe, "Air-turbine driven optical low-coherence reflectometry at 28.6-kHz scan repetition rate," *Optics Communications* **154**, 1-4 (1998).
55. A. Rollins, S. Yazdanfar, M. Kulkarni, R. Ung-Arunyawee, and J. Izatt, "In vivo video rate optical coherence tomography," *Optics Express* **3**, 219-229 (1998).
56. N. Nassif, B. Cense, B. Park, M. Pierce, S. Yun, B. Bouma, G. Tearney, T. Chen, and J. de Boer, "In vivo high-resolution video-rate spectral-domain optical coherence tomography of the human retina and optic nerve," *Optics Express* **12**, 367-376 (2004).
57. F. Feldchtein, V. M. Gelikonov, and G. V. Gelikonov, "Design of OCT Scanners," in *Handbook of Optical Coherence Tomography*, B. E. Bouma, and G. J. Tearney, eds. (Basek, New York, 2002).
58. G. J. Tearney, S. A. Boppart, B. E. Bouma, M. E. Brezinski, N. J. Weissman, J. F. Southern, and J. G. Fujimoto, "Scanning single-mode fiber optic catheter-endoscope for optical coherence tomography," *Optics Letters* **21**, 543-545 (1996).
59. A. Ahmad, S. G. Adie, E. J. Chaney, U. Sharma, and S. A. Boppart, "Cross-correlation-based image acquisition technique for manually-scanned optical coherence tomography," *Optics Express* **17**, 8125 (2009).
60. J. A. Izatt, M. R. Hee, G. M. Owen, E. A. Swanson, and J. G. Fujimoto, "Optical coherence microscopy in scattering media," *Optics Letters* **19**, 590-592 (1994).
61. A. Podoleanu, J. Rogers, D. Jackson, and S. Dunne, "Three dimensional OCT images from retina and skin," *Optics Express* **7**, 292-298 (2000).
62. E. Beaurepaire, A. C. Boccara, M. Lebec, L. Blanchot, and H. Saint-Jalmes, "Full-field optical coherence microscopy," *Opt. Lett.* **23**, 244-246 (1998).
63. E. A. Swanson, D. Huang, M. R. Hee, J. G. Fujimoto, C. P. Lin, and C. A. Puliafito, "High-speed optical coherence domain reflectometry," *Optics Letters* **17**, 151-153 (1992).
64. A. G. Podoleanu, "Unbalanced versus balanced operation in an optical coherence tomography system," *Applied Optics* **39**, 173-182 (2000).
65. A. E. Siegman, *Lasers* (University Science Books, 1986).
66. C. K. Hitzenberger, A. Baumgartner, and A. F. Fercher, "Dispersion induced multiple signal peak splitting in partial coherence interferometry," *Optics Communications* **154**, 179-185 (1998).
67. C. K. Hitzenberger, A. Baumgartner, W. Drexler, and A. F. Fercher, "Dispersion effects in partial coherence interferometry: implications for intraocular ranging," *Journal of Biomedical Optics* **4**, 144 (1999).
68. A. Fercher, C. Hitzenberger, M. Sticker, R. Zawadzki, B. Karamata, and T. Lasser, "Numerical dispersion compensation for partial coherence interferometry and optical coherence tomography," *Optics Express* **9**, 610-615 (2001).
69. C. K. Hitzenberger, "Absorption and dispersion in OCT," in *Handbook of Coherent Domain Optical Methods*, V. V. Tuchin, ed. (Kluwer, 2004).
70. E. D. J. Smith, A. V. Zvyagin, and D. D. Sampson, "Real-time dispersion compensation in scanning interferometry," *Optics Letters* **27**, 1998-2000 (2002).
71. G. J. Tearney, B. E. Bouma, and J. G. Fujimoto, "High-speed phase-and group-delay scanning with a grating-based phase control delay line," *Opt. Lett* **22**, 1811-1813 (1997).

72. Y. Chen, and X. Li, "Dispersion management up to the third order for real-time optical coherence tomography involving a phase or frequency modulator," *Optics Express* **12**, 5968-5978 (2004).
73. J. F. De Boer, B. Cense, B. H. Park, M. C. Pierce, G. J. Tearney, and B. E. Bouma, "Improved signal-to-noise ratio in spectral-domain compared with time-domain optical coherence tomography," *Optics Letters* **28**, 2067-2069 (2003).
74. M. Choma, M. Sarunic, C. Yang, and J. Izatt, "Sensitivity advantage of swept source and Fourier domain optical coherence tomography," *Optics Express* **11**, 2183-2189 (2003).
75. M. Wojtkowski, V. Srinivasan, T. Ko, J. Fujimoto, A. Kowalczyk, and J. Duker, "Ultrahigh-resolution, high-speed, Fourier domain optical coherence tomography and methods for dispersion compensation," *Optics Express* **12**, 2404-2422 (2004).
76. R. Leitgeb, M. Wojtkowski, A. Kowalczyk, C. K. Hitzenberger, M. Sticker, and A. F. Fercher, "Spectral measurement of absorption by spectroscopic frequency-domain optical coherence tomography," *Optics Letters* **25**, 820-822 (2000).
77. M. A. Choma, A. K. Ellerbee, C. Yang, T. L. Creazzo, and J. A. Izatt, "Spectral-domain phase microscopy," *Optics Letters* **30**, 1162-1164 (2005).
78. R. Leitgeb, L. Schmetterer, W. Drexler, A. Fercher, R. Zawadzki, and T. Bajraszewski, "Real-time assessment of retinal blood flow with ultrafast acquisition by color Doppler Fourier domain optical coherence tomography," *Optics Express* **11**, 3116-3121 (2003).
79. R. K. Wang, and Z. Ma, "A practical approach to eliminate autocorrelation artefacts for volume-rate spectral domain optical coherence tomography," *Physics in Medicine and Biology* **51**, 3231-3240 (2006).
80. M. Bail, G. Haeusler, J. M. Herrmann, M. W. Lindner, and R. Ringler, "Optical coherence tomography with the "Spectral Radar"-Fast optical analysis in volume scatterers by short coherence interferometry," *Optics Letters* **21**, 1087-1089 (1996).
81. M. Wojtkowski, R. Leitgeb, A. Kowalczyk, T. Bajraszewski, and A. F. Fercher, "In vivo human retinal imaging by Fourier domain optical coherence tomography," *Journal of Biomedical Optics* **7**, 457 (2002).
82. A. F. Fercher, C. K. Hitzenberger, G. Kamp, and S. Y. El-Zaiat, "Measurement of intraocular distances by backscattering spectral interferometry," *Optics Communications* **117**, 43-48 (1995).
83. G. Häusler, and M. W. Lindner, "'Coherence Radar' and 'Spectral Radar'—New Tools for Dermatological Diagnosis," *Journal of Biomedical Optics* **3**, 21 (1998).
84. B. Cense, N. Nassif, T. Chen, M. Pierce, S. H. Yun, B. Park, B. Bouma, G. Tearney, and J. de Boer, "Ultrahigh-resolution high-speed retinal imaging using spectral-domain optical coherence tomography," *Optics Express* **12**, 2435-2447 (2004).
85. R. Leitgeb, C. Hitzenberger, and A. Fercher, "Performance of fourier domain vs. time domain optical coherence tomography," *Optics Express* **11**, 889-894 (2003).
86. C. S. Williams, and O. A. Becklund, *Introduction to the optical transfer function* (SPIE Press, 2002).
87. V. N. Kumar, and D. N. Rao, "Interferometric Measurement of the Modulation Transfer Function of a Spectrometer by Using Spectral Modulations," *Appl. Opt.* **38**, 660-665 (1999).

88. Z. Hu, Y. Pan, and A. M. Rollins, "Analytical model of spectrometer-based two-beam spectral interferometry," *Applied Optics* **46**, 8499-8505 (2007).
89. T. Bajraszewski, M. Wojtkowski, M. Szkulmowski, A. Szkulmowska, R. Huber, and A. Kowalczyk, "Improved spectral optical coherence tomography using optical frequency comb," *Opt. Express* **16**, 4163-4176 (2008).
90. S. Yun, G. Tearney, B. Bouma, B. Park, and J. de Boer, "High-speed spectral-domain optical coherence tomography at 1.3  $\mu$ m wavelength," *Opt. Express* **11**, 3598-3604 (2003).
91. J. A. Izatt, and M. Choma, "Theory of OCT," in *Optical Coherence Tomography*, W. Drexler, and J. G. Fujimoto, eds. (Springer, 2008).
92. W. A. Traub, "Constant-dispersion grism spectrometer for channeled spectra," *Journal of the Optical Society of America A* **7**, 1779-1791 (1990).
93. S. Vergnole, D. Lévesque, and G. Lamouche, "Experimental validation of an optimized signal processing method to handle non-linearity in swept-source optical coherence tomography," *Opt. Express* **18**, 10446-10461 (2010).
94. S. Makita, T. Fabritius, and Y. Yasuno, "Full-range, high-speed, high-resolution 1 $\mu$ m spectral-domain optical coherence tomography using BM-scan for volumetric imaging of the human posterior eye," *Optics Express* **16**, 8406-8420 (2008).
95. M. Mujat, B. H. Park, B. Cense, T. C. Chen, and J. F. de Boer, "Autocalibration of spectral-domain optical coherence tomography spectrometers for in vivo quantitative retinal nerve fiber layer birefringence determination," *Journal of Biomedical Optics* **12**, 041205 (2007).
96. E. J. Fernández, B. Hermann, B. Považay, A. Unterhuber, H. Sattmann, B. Hofer, P. K. Ahnelt, and W. Drexler, "Ultrahigh resolution optical coherence tomography and pancorrection for cellular imaging of the living human retina," *Optics Express* **16**, 11083-11094 (2008).
97. B. Liu, and M. E. Brezinski, "Theoretical and practical considerations on detection performance of time domain, Fourier domain, and swept source optical coherence tomography," *Journal of Biomedical Optics* **12**, 044007 (2007).
98. K. Zheng, B. Liu, C. Huang, and M. E. Brezinski, "Experimental confirmation of potential swept source optical coherence tomography performance limitations," *Applied Optics* **47**, 6151 (2008).
99. S. R. Chinn, E. A. Swanson, and J. G. Fujimoto, "Optical coherence tomography using a frequency-tunable optical source," *Optics Letters* **22**, 340-342 (1997).
100. M. Yamanari, S. Makita, and Y. Yasuno, "Polarization-sensitive swept-source optical coherence tomography with continuous source polarization modulation," *Opt. Express* **16**, 5892-5906 (2008).
101. S. H. Yun, C. Boudoux, G. J. Tearney, and B. E. Bouma, "High-speed wavelength-swept semiconductor laser with a polygon-scanner-based wavelength filter," *Optics Letters* **28**, 1981-1983 (2003).
102. W. Y. Oh, S. H. Yun, G. J. Tearney, and B. E. Bouma, "115 kHz tuning repetition rate ultrahigh-speed wavelength-swept semiconductor laser," *Optics Letters* **30**, 3159-3161 (2005).
103. R. Huber, M. Wojtkowski, K. Taira, J. Fujimoto, and K. Hsu, "Amplified, frequency swept lasers for frequency domain reflectometry and OCT imaging: design and scaling principles," *Optics Express* **13**, 3513-3528 (2005).

104. R. Huber, M. Wojtkowski, and J. G. Fujimoto, "Fourier Domain Mode Locking (FDML): A new laser operating regime and applications for optical coherence tomography," *Optics Express* **14**, 3225-3237 (2006).
105. T. Klein, W. Wieser, C. M. Eigenwillig, B. R. Biedermann, and R. Huber, "Megahertz OCT for ultrawide-field retinal imaging with a 1050nm Fourier domain mode-locked laser," *Opt. Express* **19**, 3044-3062 (2011).
106. C. Hauger, M. Worz, and T. Hellmuth, "Interferometer for optical coherence tomography," *Applied Optics* **42**, 3896-3902 (2003).
107. J. Rosen, and M. Takeda, "Longitudinal Spatial Coherence Applied for Surface Profilometry," *Appl. Opt.* **39**, 4107-4111 (2000).
108. J. F. De Boer, T. E. Milner, M. J. C. van Gemert, and J. S. Nelson, "Two-dimensional birefringence imaging in biological tissue by polarization-sensitive optical coherence tomography," *Optics Letters* **22**, 934-936 (1997).
109. S. Guo, J. Zhang, L. Wang, J. S. Nelson, and Z. Chen, "Depth-resolved birefringence and differential optical axis orientation measurements with fiber-based polarization-sensitive optical coherence tomography," *Opt. Lett.* **29**, 2025-2027 (2004).
110. J. M. Stephen, C. P. Winlove, and V. G. Sergei, "The collagen structure of bovine intervertebral disc studied using polarization-sensitive optical coherence tomography," *Physics in Medicine and Biology* **49**, 1295 (2004).
111. A. F. Zuluaga, and R. Richards-Kortum, "Spatially resolved spectral interferometry for determination of subsurface structure," *Opt. Lett.* **24**, 519-521 (1999).
112. B. Povazay, A. Unterhuber, B. Hermann, H. Sattmann, H. Arthaber, and W. Drexler, "Full-field time-encoded frequency-domain optical coherence tomography," *Opt. Express* **14**, 7661-7669 (2006).
113. A. Dubois, J. Moreau, and C. Boccara, "Spectroscopic ultrahigh-resolution full-field optical coherence microscopy," *Opt. Express* **16**, 17082-17091 (2008).
114. B. B. Garcia, A. J. Moore, C. Perez-Lopez, L. Wang, and T. Tschudi, "Spatial phase-stepped interferometry using a holographic optical element," *Optical Engineering* **38**, 2069-2074 (1999).
115. A. Hettwer, J. Kranz, and J. Schwider, "Three channel phase-shifting interferometer using polarization-optics and a diffraction grating," *Optical Engineering* **39**, 960-966 (2000).
116. C. W. See, R. K. Appel, and M. G. Somekh, "Scanning differential optical profilometer for simultaneous measurement of amplitude and phase variation," *Applied Physics Letters* **53**, 10 (1988).
117. A. Dubois, A. C. Boccara, and J. G. Fujimoto, "Full-Field Optical Coherence Tomography," in *Optical Coherence Tomography: Technology and Applications* W. Drexler, and J. G. Fujimoto, eds. (Springer, 2008).
118. L. Vabre, A. Dubois, and A. C. Boccara, "Thermal-light full-field optical coherence tomography," *Opt. Lett.* **27**, 530-532 (2002).
119. M. V. Sarunic, S. Weinberg, and J. A. Izatt, "Full-field swept-source phase microscopy," *Opt. Lett.* **31**, 1462-1464 (2006).
120. D. Choi, H. Hiro-Oka, H. Furukawa, R. Yoshimura, M. Nakanishi, K. Shimizu, and K. Ohbayashi, "Fourier domain optical coherence tomography using optical demultiplexers imaging at 60,000,000 lines/s," *Opt. Lett.* **33**, 1318-1320 (2008).
121. J. M. Schmitt, "Array detection for speckle reduction in optical coherence microscopy," *Physics in Medicine and Biology* **42**, 1427 (1997).

122. G. C. Holst, "CCD arrays, cameras, and displays," (JCD Publishing, 1998).
123. S. K. Saha, "Diffraction-Limited Imaging With Large and Moderate Telescopes," (World Scientific, 2007), p. 628.
124. P. J. Shaw, "Comparison of Widefield/Deconvolution and Confocal Microscopy for Three-Dimensional Imaging," in *Handbook Of Biological Confocal Microscopy*, J. B. Pawley, ed. (Springer, 2006), p. 460.
125. P. C. D. Hobbs, "Building Electro-Optical Systems: Making It All Work," (John Wiley & Sons, 2011).
126. G. C. Holst, "Solid State Arrays," in *CCD arrays, cameras, and displays*(JCD Publishing, 1998).
127. D. J. Denvir, E. Conroy, D. Sinha, and P. A. Laplante, "Electron-multiplying CCD: the new ICCD," in *Society of Photo-Optical Instrumentation Engineers (SPIE) Conference Series*, C. B. Johnson, ed. (2003), pp. 164-174.
128. S. Middelhoek, and S. A. Audet, *Silicon sensors* (Acad. Pr., London, 1989).
129. M. S. Robbins, "Electron Multiplying Charge Coupled Devices - EMCCDs," in *Single-Photon Imaging* P. Seitz, and A. J. P. Theuwissen, eds. (Springer, 2011), p. 104.
130. K. A. Parulski, and P. H. Jameson, "Enabling technologies for a family of digital cameras," C. N. Anagnostopoulos, M. M. Blouke, and M. P. Lesser, eds. (SPIE, San Jose, CA, USA, 1996), pp. 156-163.
131. J. Ohta, "Smart CMOS Image Sensors And Applications," (CRC Press, 2008).
132. T. Dresel, G. Häusler, and H. Venzke, "Three-dimensional sensing of rough surfaces by coherence radar," *Appl. Opt.* **31**, 919-925 (1992).
133. P. Gleyzes, A. C. Boccara, and H. Saint-Jalmes, "Multichannel Nomarski microscope with polarization modulation: performance and applications," *Opt. Lett.* **22**, 1529-1531 (1997).
134. L. Kay, A. Podoleanu, M. Seeger, and C. J. Solomon, "A new approach to the measurement and analysis of impact craters," *International Journal of Impact Engineering* **19**, 739-753 (1997).
135. I. Gurov, E. Ermolaeva, and A. Zakharov, "Analysis of low-coherence interference fringes by the Kalman filtering method," *J. Opt. Soc. Am. A* **21**, 242-251 (2004).
136. B. Laude, A. De Martino, B. Drévilion, L. Benattar, and L. Schwartz, "Full-Field Optical Coherence Tomography with Thermal Light," *Appl. Opt.* **41**, 6637-6645 (2002).
137. A. Dubois, K. Grieve, G. Moneron, R. Lecaque, L. Vabre, and C. Boccara, "Ultrahigh-resolution full-field optical coherence tomography," *Applied Optics* **43**, 2874-2883 (2004).
138. A. Dubois, L. Vabre, A.-C. Boccara, and E. Beaurepaire, "High-Resolution Full-Field Optical Coherence Tomography with a Linnik Microscope," *Appl. Opt.* **41**, 805-812 (2002).
139. S. Bourquin, V. Monterosso, P. Seitz, and R. P. Salathé, "Video-rate optical low-coherence reflectometry based on a linear smart detector array," *Opt. Lett.* **25**, 102-104 (2000).
140. S. Bourquin, P. Seitz, and R. P. Salathé, "Optical coherence topography based on a two-dimensional smart detector array," *Opt. Lett.* **26**, 512-514 (2001).
141. M. Ducros, M. Laubscher, B. Karamata, S. Bourquin, T. Lasser, and R. P. Salathé, "Parallel optical coherence tomography in scattering samples using a two-dimensional smart-pixel detector array," *Optics Communications* **202**, 29-35 (2002).

142. M. Laubscher, M. Ducros, B. Karamata, T. Lasser, and R. Salathe, "Video-rate three-dimensional optical coherence tomography," *Opt. Express* **10**, 429-435 (2002).
143. W. Y. Oh, B. E. Bouma, N. Iftimia, S. H. Yun, R. Yelin, and G. J. Tearney, "Ultra-high-resolution full-field optical coherence microscopy using InGaAs camera," *Opt. Express* **14**, 726-735 (2006).
144. A. Dubois, G. Moneron, and C. Boccara, "Thermal-light full-field optical coherence tomography in the 1.2  $\mu\text{m}$  wavelength region," *Optics Communications* **266**, 738-743 (2006).
145. D. Sacchet, J. Moreau, P. Georges, and A. Dubois, "Simultaneous dual-band ultra-high resolution full-field optical coherence tomography," *Opt. Express* **16**, 19434-19446 (2008).
146. A. Dubois, "Spectroscopic polarization-sensitive full-field optical coherence tomography," *Opt. Express* **20**, 9962-9977 (2012).
147. A. Dubois, G. Moneron, K. Grieve, and A. C. Boccara, "Three-dimensional cellular-level imaging using full-field optical coherence tomography," *Physics in Medicine and Biology* **49**, 1227 (2004).
148. K. Grieve, A. Dubois, M. Simonutti, M. Paques, J. Sahel, J.-F. Le Gargasson, and C. Boccara, "In vivo anterior segment imaging in the rat eye with high speed white light full-field optical coherence tomography," *Opt. Express* **13**, 6286-6295 (2005).
149. M. Akiba, J. Yan, C. Reisman, Z. Wang, Y. Fukuma, M. Hangai, N. Yoshimura, and K. Chan, "Ultra-high Resolution Full-field Optical Coherence Tomography for Visualizing Human Photoreceptor Cells in vivo," (Optical Society of America, 2010), p. BSuC2.
150. H. Makhoulouf, K. Perronet, G. Dupuis, S. Lévêque-Fort, and A. Dubois, "Simultaneous optically sectioned fluorescence and optical coherence microscopy with full-field illumination," *Opt. Lett.* **37**, 1613-1615 (2012).
151. P. Carré, "Installation et utilisation du comparateur photoélectrique et interférentiel du Bureau International des Poids et Mesures," *Metrologia* **2**, 13 (1966).
152. Y.-Y. Cheng, and J. C. Wyant, "Phase shifter calibration in phase-shifting interferometry," *Appl. Opt.* **24**, 3049-3052 (1985).
153. H. Schreiber, and J. H. Bruning, "Phase Shifting Interferometry," in *Optical Shop Testing* (John Wiley & Sons, Inc., 2006), pp. 547-666.
154. P. Hariharan, B. F. Oreb, and T. Eiju, "Digital phase-shifting interferometry: a simple error-compensating phase calculation algorithm," *Appl. Opt.* **26**, 2504-2506 (1987).
155. J. H. Bruning, D. R. Herriott, J. E. Gallagher, D. P. Rosenfeld, A. D. White, and D. J. Brangaccio, "Digital Wavefront Measuring Interferometer for Testing Optical Surfaces and Lenses," *Appl. Opt.* **13**, 2693-2703 (1974).
156. K. Creath, "Phase-shifting holographic interferometry," *Holographic Interferometry*, in *Holographic interferometry: principles and methods*, P. K. Rastogi, ed. (Springer, 1994), pp. 109-150.
157. J. E. Greivenkamp, and J. H. Bruning, "Phase shifting interferometry," in *Optical Shop Testing*, D. Malacara, ed. (Wiley-Interscience, 2007), pp. 501-598
158. M. Roy, P. Svahn, L. Chereil, and C. J. R. Sheppard, "Geometric phase-shifting for low-coherence interference microscopy," *Optics and Lasers in Engineering* **37**, 631-641 (2002).

159. S.-H. Lu, C.-Y. Wang, C.-Y. Hsieh, K.-Y. Chiu, and H.-Y. Chen, "Full-field optical coherence tomography using nematic liquid-crystal phase shifter," *Appl. Opt.* **51**, 1361-1366 (2012).
160. Y. Watanabe, and M. Sato, "Three-dimensional wide-field optical coherence tomography using an ultrahigh-speed CMOS camera," *Optics Communications* **281**, 1889-1895 (2008).
161. A. Dubois, "Phase-map measurements by interferometry with sinusoidal phase modulation and four integrating buckets," *J. Opt. Soc. Am. A* **18**, 1972-1979 (2001).
162. J. Novak, "Five-step phase-shifting algorithms with unknown values of phase shift," *Optik - International Journal for Light and Electron Optics* **114**, 63-68 (2003).
163. C. Dunsby, Y. Gu, and P. French, "Single-shot phase-stepped wide-field coherence-gated imaging," *Opt. Express* **11**, 105-115 (2003).
164. M. Akiba, C. Kin Pui, and N. Tanno, "Video-rate optical coherence imaging by two-dimensional heterodyne detection," in *Lasers and Electro-Optics, 2001. CLEO '01. Technical Digest. Summaries of papers presented at the Conference on(2001)*, p. 380.
165. M. Akiba, K. P. Chan, and N. Tanno, "Full-field optical coherence tomography by two-dimensional heterodyne detection with a pair of CCD cameras," *Opt. Lett.* **28**, 816-818 (2003).
166. D. Sacchet, M. Brzezinski, J. Moreau, P. Georges, and A. Dubois, "Motion artifact suppression in full-field optical coherence tomography," *Appl. Opt.* **49**, 1480-1488 (2010).
167. P. Groot, "Derivation of algorithms for phase-shifting interferometry using the concept of a data-sampling window," *Appl Opt* **34**, 4723-4730 (1995).
168. J. Schwider, R. Burow, K. E. Elssner, J. Grzanna, R. Spolaczyk, and K. Merkel, "Digital wave-front measuring interferometry: some systematic error sources," *Appl. Opt.* **22**, 3421-3432 (1983).
169. J. Schwider, O. Falkenstoerfer, H. Schreiber, A. Zoeller, and N. Streibl, "New compensating four-phase algorithm for phase-shift interferometry," *Optical Engineering* **32**, 1883-1885 (1993).
170. Y. Surrel, "Design of algorithms for phase measurements by the use of phase stepping," *Appl. Opt.* **35**, 51-60 (1996).
171. Y. Zhu, and T. Gemma, "Method for designing error-compensating phase-calculation algorithms for phase-shifting interferometry," *Appl Opt* **40**, 4540-4546 (2001).
172. K. Kinnstaetter, A. W. Lohmann, J. Schwider, and N. Streibl, "Accuracy of phase shifting interferometry," *Appl. Opt.* **27**, 5082-5089 (1988).
173. P. L. Wizinowich, "Phase shifting interferometry in the presence of vibration: a new algorithm and system," *Appl. Opt.* **29**, 3271-3279 (1990).
174. C. Rathjen, "Statistical properties of phase-shift algorithms," *J. Opt. Soc. Am. A* **12**, 1997-2008 (1995).
175. W. Y. Oh, B. E. Bouma, N. Iftimia, R. Yelin, and G. J. Tearney, "Spectrally-modulated full-field optical coherence microscopy for ultrahigh-resolution endoscopic imaging," *Opt. Express* **14**, 8675-8684 (2006).
176. B. Karamata, M. Laubscher, M. Leutenegger, S. Bourquin, T. Lasser, and P. Lambelet, "Multiple scattering in optical coherence tomography. I. Investigation and modeling," *J. Opt. Soc. Am. A* **22**, 1369-1379 (2005).
177. B. Karamata, M. Leutenegger, M. Laubscher, S. Bourquin, T. Lasser, and P. Lambelet, "Multiple scattering in optical coherence tomography. II. Experimental

- and theoretical investigation of cross talk in wide-field optical coherence tomography," *J. Opt. Soc. Am. A* **22**, 1380-1388 (2005).
178. Y. Abraham, N. A. W. Holzwarth, and R. T. Williams, "Electronic structure and optical properties of CdMoO<sub>4</sub> and CdWO<sub>4</sub>," *Physical Review B* **62**, 1733-1741 (2000).
179. E. Bordenave, E. Abraham, G. Jonusauskas, N. Tsurumachi, J. Oberl, C. Rullière, P. E. Minot, M. Lassègues, and J. E. S. Bazeille, "Wide-field optical coherence tomography: imaging of biological tissues," *Appl. Opt.* **41**, 2059-2064 (2002).
180. B. Karamata, P. Lambelet, M. Laubscher, R. P. Salathé, and T. Lasser, "Spatially incoherent illumination as a mechanism for cross-talk suppression in wide-field optical coherence tomography," *Opt. Lett.* **29**, 736-738 (2004).
181. H. AMBAR, Y. AOKI, N. TAKAI, and T. ASAKURA, *Relationship of speckle size to the effectiveness of speckle reduction in laser microscope images using rotating optical fiber* (Elsevier, Reutlingen, ALLEMAGNE, 1986).
182. H. AMBAR, Y. AOKI, N. TAKAI, and T. ASAKURA, *Fringe contrast improvement in speckle photography by means of speckle reduction using vibrating optical fiber* (Elsevier, Reutlingen, ALLEMAGNE, 1986).
183. J. Kim, D. T. Miller, E. Kim, S. Oh, J. Oh, and T. E. Milner, "Optical coherence tomography speckle reduction by a partially spatially coherent source," *Journal of Biomedical Optics* **10**, 064034-064039 (2005).
184. J.-H. Han, J. Lee, and J. U. Kang, "Pixelation effect removal from fiber bundle probe based optical coherence tomography imaging," *Opt. Express* **18**, 7427-7439 (2010).
185. V. J. Srinivasan, "Ultrahigh-Speed Optical Coherence Tomography for Three-Dimensional and En Face Imaging of the Retina and Optic Nerve Head," *Investigative ophthalmology & visual science* **49**, 5103-5110 (2008).
186. A. F. Fercher, "Inverse Scattering, Dispersion, and Speckle in Optical Coherence Tomography," W. Drexler, and J. G. Fujimoto, eds. (Springer Berlin Heidelberg, 2008), pp. 119-146.
187. D. L. Marks, "Inverse scattering for frequency-scanned full-field optical coherence tomography," *Journal of the Optical Society of America. A, Optics, image science, and vision* **24**, 1034 (2007).
188. T. Anna, V. Srivastava, C. Shakher, and D. S. Mehta, "Transmission Mode Full-Field Swept-Source Optical Coherence Tomography for Simultaneous Amplitude and Quantitative Phase Imaging of Transparent Objects," *Photonics Technology Letters, IEEE* **23**, 899-901 (2011).
189. D. Satish Kumar, M. Dalip Singh, A. Arun, and S. Chandra, "Simultaneous topography and tomography of latent fingerprints using full-field swept-source optical coherence tomography," *Journal of Optics A: Pure and Applied Optics* **10**, 015307 (2008).
190. S. K. Dubey, T. Anna, C. Shakher, and D. S. Mehta, "Fingerprint detection using full-field swept-source optical coherence tomography," *Applied Physics Letters* **91**, 181106-181106-181103 (2007).
191. D. Hillmann, T. Bonin, C. Lühns, G. Franke, M. Hagen-Eggert, P. Koch, and G. Hüttmann, "Common approach for compensation of axial motion artifacts in swept-source OCT and dispersion in Fourier-domain OCT," *Opt. Express* **20**, 6761-6776 (2012).

192. A. E. Desjardins, B. J. Vakoc, G. J. Tearney, and B. E. Bouma, "Speckle Reduction in OCT using Massively-Parallel Detection and Frequency-Domain Ranging," *Opt. Express* **14**, 4736-4745 (2006).
193. Y. Y. Takashi Endo, Frederic Truffer, Gouki Aoki, Shuichi Makita, Masahide Itoh and Toyohiko Yatagai, "Line-field Fourier-domain optical coherence tomography," *Proc. SPIE* , **5690**, 168 (2005).
194. M. Bashkansky, and J. Reintjes, "Statistics and reduction of speckle in optical coherence tomography," *Opt. Lett.* **25**, 545-547 (2000).
195. B. Grajciar, Y. Lehareinger, A. F. Fercher, and R. A. Leitgeb, "High sensitivity phase mapping with parallel Fourier domain optical coherence tomography at 512 000 A-scan/s," *Opt. Express* **18**, 21841-21850 (2010).
196. Z. Yaqoob, T. Yamauchi, W. Choi, D. Fu, R. R. Dasari, and M. S. Feld, "Single-shot Full-field reflection phase microscopy," *Opt. Express* **19**, 7587-7595 (2011).
197. J. Wu, Z. Yaqoob, X. Heng, X. Cui, and C. Yang, "Harmonically matched grating-based full-field quantitative high-resolution phase microscope for observing dynamics of transparent biological samples," *Opt. Express* **15**, 18141-18155 (2007).
198. Z. Yaqoob, W. Choi, S. Oh, N. Lue, Y. Park, C. Fang-Yen, R. R. Dasari, K. Badizadegan, and M. S. Feld, "Improved phase sensitivity in spectral domain phase microscopy using line-field illumination and self phase-referencing," *Opt. Express* **17**, 10681-10687 (2009).
199. Y. Watanabe, I. Wakaki, T. Niizuma, and M. Sato, "Time-gated full-field optical coherence tomography using optical Hilbert transformation," in *Biophotonics, 2004. APBP 2004. The Second Asian and Pacific Rim Symposium on(2004)*, pp. 10-11.
200. C. Wirbelauer, C. Scholz, H. Hoerauf, G. O. Bastian, R. Engelhardt, R. Birngruber, and H. Laqua, "[Examination of the cornea using optical coherence tomography]," *Der Ophthalmologe : Zeitschrift der Deutschen Ophthalmologischen Gesellschaft* **98**, 151-156 (2001).
201. T. Swartz, L. Marten, and M. Wang, "Measuring the cornea: the latest developments in corneal topography," *Current opinion in ophthalmology* **18**, 325-333 (2007).
202. L. Plesea, M. Gomez, and A. G. Podoleanu, "Cornea curvature measurement using single shot C-scan OCT," in *Society of Photo-Optical Instrumentation Engineers (SPIE) Conference Series(2007)*, p. 17.
203. L. Plesea, and A. G. Podoleanu, "Direct corneal elevation measurements using multiple delay en face optical coherence tomography," *J Biomed Opt* **13**, 054054 (2008).
204. Y. Yasuno, V. D. Madjarova, S. Makita, M. Akiba, A. Morosawa, C. Chong, T. Sakai, K.-P. Chan, M. Itoh, and T. Yatagai, "Three-dimensional and high-speed swept-source optical coherence tomography for in vivo investigation of human anterior eye segments," *Opt. Express* **13**, 10652-10664 (2005).
205. M. Takeda, H. Ina, and S. Kobayashi, "Fourier-transform method of fringe-pattern analysis for computer-based topography and interferometry," *J. Opt. Soc. Am.* **72**, 156-160 (1982).
206. A. F. Fercher, C. K. Hitzenberger, M. Sticker, E. Moreno-Barriuso, R. Leitgeb, W. Drexler, and H. Sattmann, "A thermal light source technique for optical coherence tomography," *Optics Communications* **185**, 57-64 (2000).

207. R. N. Graf, W. J. Brown, and A. Wax, "Parallel frequency-domain optical coherence tomography scatter-mode imaging of the hamster cheek pouch using a thermal light source," *Opt. Lett.* **33**, 1285-1287 (2008).
208. CHEN, #160, Yuping, ZHAO, Hong, and WANG, *Investigation on Spectral-Domain Optical Coherence Tomography Using a Tungsten Halogen Lamp as Light Source* (Springer, Heidelberg, ALLEMAGNE, 2009).
209. K. Grieve, M. Paques, A. Dubois, J. Sahel, C. Boccara, and J.-F. Le Gargasson, "Ocular Tissue Imaging Using Ultrahigh-Resolution, Full-Field Optical Coherence Tomography," *Investigative ophthalmology & visual science* **45**, 4126-4131 (2004).
210. A.-H. Dhalla, "Crosstalk rejection in parallel optical coherence tomography using spatially incoherent illumination with partially coherent sources," *Optics Letters* **35**, 2305 (2010).
211. G. Kate, M. Gael, D. Arnaud, G. Jean-François Le, and B. Claude, "Ultrahigh resolution ex vivo ocular imaging using ultrashort acquisition time en face optical coherence tomography," *Journal of Optics A: Pure and Applied Optics* **7**, 368 (2005).
212. G. Moneron, A. C. Boccara, and A. Dubois, "Stroboscopic ultrahigh-resolution full-field optical coherence tomography," *Opt. Lett.* **30**, 1351-1353 (2005).
213. X. Liu, and P. Xue, "Ultrahigh resolution parallel Fourier domain optical coherence tomography using xenon flash lamp," in *Society of Photo-Optical Instrumentation Engineers (SPIE) Conference Series*(2007), p. 97.
214. Y. Chen, H. Zhao, and Z. Wang, "Investigation on spectral-domain optical coherence tomography using a tungsten halogen lamp as light source," *Optical Review* **16**, 26-29 (2009).
215. D. J. Darling, "The universal book of astronomy: from the Andromeda Galaxy to the zone of avoidance," (Wiley, 2004), p. 570.
216. D. Gabor, "A new microscopic principle," *Nature (London)* **161**, 777 (1948).
217. D. S. Mehta, K. Saxena, S. K. Dubey, and C. Shakher, "Coherence characteristics of light-emitting diodes," *Journal of Luminescence* **130**, 96-102 (2010).
218. M. N. J. V. P. Janardan Prasad, "Display Devices and Recorders," in *Instrumentation And Process Control* (I.K. International Publishing House Pvt. Limited, 2009), p. 329.
219. T. Gebel, M. Voelskow, W. Skorupa, G. Mannino, V. Privitera, F. Priolo, E. Napolitani, and A. Carnera, "Flash lamp annealing with millisecond pulses for ultra-shallow boron profiles in silicon," *Nuclear Instruments and Methods in Physics Research Section B: Beam Interactions with Materials and Atoms* **186**, 287-291 (2002).
220. K. F. McDonald, R. D. Curry, and P. J. Hancock, "Comparison of pulsed and CW ultraviolet light sources to inactivate bacterial spores on surfaces," *Plasma Science, IEEE Transactions on* **30**, 1986-1989 (2002).
221. B. E. Bayer, "Color imaging array," (Eastman Kodak Company (Rochester, NY), United States, 1976).
222. F. Roddier, *Adaptive Optics in Astronomy* (2004).
223. M. J. Booth, "Adaptive optics in microscopy," *Philosophical Transactions of the Royal Society A: Mathematical, Physical and Engineering Sciences* **365**, 2829-2843 (2007).
224. J. M. Beckers, "Adaptive optics for astronomy - Principles, performance, and applications," *Annual Review of Astronomy and Astrophysics* **31**, 13-62 (1993).

225. J. Porter, *Adaptive Optics for Vision Science: Principles, Practices, Design, and Applications* (Wiley-Interscience, 2006).
226. R. K. Tyson, "Bit-error rate for free-space adaptive optics laser communications," *J. Opt. Soc. Am. A* **19**, 753-758 (2002).
227. R. Tyson, *Principles of Adaptive Optics* (Taylor & Francis, 2010).
228. T. O. Salmon, L. N. Thibos, and A. Bradley, "Comparison of the eye's wavefront aberration measured psychophysically and with the Shack-Hartmann wavefront sensor," *J. Opt. Soc. Am. A* **15**, 2457-2465 (1998).
229. J. Liang\*, B. Grimm, S. Goelz, and J. F. Bille, "Objective measurement of wave aberrations of the human eye with the use of a Hartmann-Shack wavefront sensor," *J. Opt. Soc. Am. A* **11**, 1949-1957 (1994).
230. M. Sharma, B. S. Wachler, and C. C. Chan, "Higher order aberrations and relative risk of symptoms after LASIK," *Journal of refractive surgery* (Thorofare, N.J. : 1995) **23**, 252-256 (2007).
231. Z. Z. Nagy, I. Palagyi-Deak, E. Kelemen, and A. Kovacs, "Wavefront-guided photorefractive keratectomy for myopia and myopic astigmatism," *Journal of refractive surgery* (Thorofare, N.J. : 1995) **18**, S615-619 (2002).
232. B. Hermann, E. J. Fernández, A. Unterhuber, H. Sattmann, A. F. Fercher, W. Drexler, P. M. Prieto, and P. Artal, "Adaptive-optics ultrahigh-resolution optical coherence tomography," *Opt. Lett.* **29**, 2142-2144 (2004).
233. R. Zawadzki, S. Jones, S. Olivier, M. Zhao, B. Bower, J. Izatt, S. Choi, S. Laut, and J. Werner, "Adaptive-optics optical coherence tomography for high-resolution and high-speed 3D retinal in vivo imaging," *Opt. Express* **13**, 8532-8546 (2005).
234. Y. Zhang, J. Rha, R. Jonnal, and D. Miller, "Adaptive optics parallel spectral domain optical coherence tomography for imaging the living retina," *Opt. Express* **13**, 4792-4811 (2005).
235. R. H. Webb, G. W. Hughes, and F. C. Delori, "Confocal scanning laser ophthalmoscope," *Appl. Opt.* **26**, 1492-1499 (1987).
236. A. Roorda, F. Romero-Borja, I. I. I. W. Donnelly, H. Queener, T. Hebert, and M. Campbell, "Adaptive optics scanning laser ophthalmoscopy," *Opt. Express* **10**, 405-412 (2002).
237. O. Albert, L. Sherman, G. Mourou, T. B. Norris, and G. Vdovin, "Smart microscope: an adaptive optics learning system for aberration correction in multiphoton confocal microscopy," *Opt. Lett.* **25**, 52-54 (2000).
238. R. H. Webb, C. M. Penney, and K. P. Thompson, "Measurement of ocular local wavefront distortion with a spatially resolved refractometer," *Appl. Opt.* **31**, 3678-3686 (1992).
239. R. Navarro, and E. Moreno-Barriuso, "Laser ray-tracing method for optical testing," *Opt. Lett.* **24**, 951-953 (1999).
240. S. R. Chamot, C. Dainty, and S. Esposito, "Adaptive optics for ophthalmic applications using a pyramid wavefront sensor," *Opt. Express* **14**, 518-526 (2006).
241. G. P. Andersen, "Holographic wavefront sensor," *Optical Engineering* **48**, 085801 (2009).
242. D. R. Neal, J. Copland, D. A. Neal, and B. Singh, "Shack-Hartmann wavefront sensor precision and accuracy," in *Society of Photo-Optical Instrumentation Engineers (SPIE) Conference Series*, A. Duparré, ed. (2002), pp. 148-160.
243. T. Oshika, S. D. Klyce, R. A. Applegate, H. C. Howland, and M. A. El Danasoury, "Comparison of corneal wavefront aberrations after photorefractive

- keratectomy and laser in situ keratomileusis," *American journal of ophthalmology* **127**, 1-7 (1999).
244. M. Wojtkowski, B. Kaluzny, and R. J. Zawadzki, "New Directions in Ophthalmic Optical Coherence Tomography," *Optometry & Vision Science* **89**, 524-542 10.1097/OPX.1090b1013e31824eecb31822 (2012).
245. R. V. Shack, "Production and use of a lenticular Hartmann screen," *Journal of the Optical Society of America. B, Optical physics* **61**, 656 (1971).
246. W. H. Southwell, "Wave-front estimation from wave-front slope measurements," *J. Opt. Soc. Am.* **70**, 998-1006 (1980).
247. L. Fox, and I. B. Parker, *Chebyshev polynomials in numerical analysis* (Oxford U.P., 1968).
248. L. Allen, M. W. Beijersbergen, R. J. C. Spreeuw, and J. P. Woerdman, "Orbital angular momentum of light and the transformation of Laguerre-Gaussian laser modes," *Physical Review A* **45**, 8185-8189 (1992).
249. A. E. Siegman, "Hermite-gaussian functions of complex argument as optical-beam eigenfunctions," *Journal of the Optical Society of America* (1930) **63**, 1093 (1973).
250. H. C. Howland, and B. Howland, "A subjective method for the measurement of monochromatic aberrations of the eye," *J. Opt. Soc. Am.* **67**, 1508-1518 (1977).
251. P. Theer, M. T. Hasan, and W. Denk, "Two-photon imaging to a depth of 1000 microm in living brains by use of a Ti:Al<sub>2</sub>O<sub>3</sub> regenerative amplifier," *Opt Lett* **28**, 1022-1024 (2003).
252. H. Hofer, P. Artal, B. Singer, J. L. Aragon, and D. R. Williams, "Dynamics of the eye's wave aberration," *J Opt Soc Am A Opt Image Sci Vis* **18**, 497-506 (2001).
253. M. Glanc, E. Gendron, F. Lacombe, D. Lafaille, J. F. Le Gargasson, and P. Léna, "Towards wide-field retinal imaging with adaptive optics," *Optics Communications* **230**, 225-238 (2004).
254. L. Diaz-Santana, C. Torti, I. Munro, P. Gasson, and C. Dainty, "Benefit of higher closed-loop bandwidths in ocular adaptive optics," *Opt. Express* **11**, 2597-2605 (2003).
255. D. U. Bartsch, M. H. El-Bradey, A. El-Musharaf, and W. R. Freeman, "Improved visualisation of choroidal neovascularisation by scanning laser ophthalmoscope using image averaging," *The British journal of ophthalmology* **89**, 1026-1030 (2005).
256. J. Liang, D. R. Williams, and D. T. Miller, "Supernormal vision and high-resolution retinal imaging through adaptive optics," *J. Opt. Soc. Am. A* **14**, 2884-2892 (1997).
257. M. J. Booth, M. A. A. Neil, R. Juškaitis, and T. Wilson, "Adaptive aberration correction in a confocal microscope," *Proceedings of the National Academy of Sciences* **99**, 5788-5792 (2002).
258. J. R. Fienup, and J. J. Miller, "Aberration correction by maximizing generalized sharpness metrics," *J. Opt. Soc. Am. A* **20**, 609-620 (2003).
259. M. A. A. Neil, R. Juškaitis, M. J. Booth, T. Wilson, T. Tanaka, and S. Kawata, "Adaptive aberration correction in a two-photon microscope," *Journal of Microscopy* **200**, 105-108 (2000).
260. L. Sherman, J. Y. Ye, O. Albert, and T. B. Norris, "Adaptive correction of depth-induced aberrations in multiphoton scanning microscopy using a deformable mirror," *Journal of Microscopy* **206**, 65-71 (2002).
261. P. Marsh, D. Burns, and J. Girkin, "Practical implementation of adaptive optics in multiphoton microscopy," *Opt. Express* **11**, 1123-1130 (2003).

262. W. Denk, J. Strickler, and W. Webb, "Two-photon laser scanning fluorescence microscopy," *Science* **248**, 73-76 (1990).
263. M. Rueckel, J. A. Mack-Bucher, and W. Denk, "Adaptive wavefront correction in two-photon microscopy using coherence-gated wavefront sensing," *Proceedings of the National Academy of Sciences* **103**, 17137-17142 (2006).
264. J. Wang, J.-F. Léger, J. Binding, C. Boccara, S. Gigan, and L. Bourdieu, "Measuring known aberrations in rat brain slices with Coherence-Gated Wavefront Sensor based on a Linnik interferometer," (Optical Society of America, 2012), p. BTu3A.83.
265. M. Rueckel, and W. Denk, "Properties of coherence-gated wavefront sensing," *J. Opt. Soc. Am. A* **24**, 3517-3529 (2007).
266. S. Chang, X. Liu, X. Cai, and C. P. Grover, "Full-field optical coherence tomography and its application to multiple-layer 2D information retrieving," *Optics Communications* **246**, 579-585 (2005).
267. M. J. Booth, M. A. A. Neil, and T. Wilson, "Aberration correction for confocal imaging in refractive-index-mismatched media," *Journal of Microscopy* **192**, 90-98 (1998).